

UNIVERSITY OF NAPLES

“FEDERICO II”



PhD in Chemical Sciences

XXXI Cycle

2015-2018

*Synthesis, optoelectronic properties and
processing of bio-inspired soft materials:
Toward new "green" electronic devices*

Dr Carmela Tania Prontera

Supervisors

Dr Paola Manini

Dr Maria Grazia Maglione

Assessor

Pro. Roberto Centore

PhD Coordinator

Prof. Luigi Paduano

~CONTENTS~

⊕ ABSTRACT	4
⊕ INTRODUCTION	12
⊕ AIMS OF THE THESIS WORK	34
• References	40
⊕ SECTION 1:	
<i>Processing techniques for the fabrication of ITO-free substrates based on the standard PEN and the biodegradable PLA for flexible OLED devices</i>	
• INTRODUCTION	43
• RESULTS AND DISCUSSION	50
• CONCLUSIONS	64
• EXPERIMENTAL SECTION	65
• REFERENCES	69
⊕ SECTION 2:	
<i>Synthesis and electrical properties of eumelanin thin films: towards the design of polymeric anode for ITO-free devices</i>	
• INTRODUCTION	71
• RESULTS AND DISCUSSION	83
• CONCLUSIONS	108
• EXPERIMENTAL SECTION	109

• REFERENCES	111
⊕ SECTION 3:	
<i>Synthesis of nature-inspired electroluminescent materials for OLED applications</i>	
• INTRODUCTION	114
• RESULTS AND DISCUSSION	126
• CONCLUSIONS	167
• EXPERIMENTAL SECTION	169
• REFERENCES	192
⊕ SECTION 4:	
<i>Synthesis and processing techniques of biocompatible and low cost materials for encapsulating layers in OLED devices</i>	
• INTRODUCTION	194
• RESULTS AND DISCUSSION	209
• CONCLUSIONS	227
• EXPERIMENTAL SECTION	229
• REFERENCES	232
⊕ LIST OF PUBLICATIONS	234
⊕ COMMUNICATIONS AT MEETINGS	235
⊕ COURSES AND SCHOOLS	238

~ABSTRACT~

"Green electronics" represents an emerging research area, within the field of organic electronics, aimed at exploiting the potentiality of natural compounds and their derivatives as functional materials for innovative, low-cost and sustainable electronic devices (Figure 1).

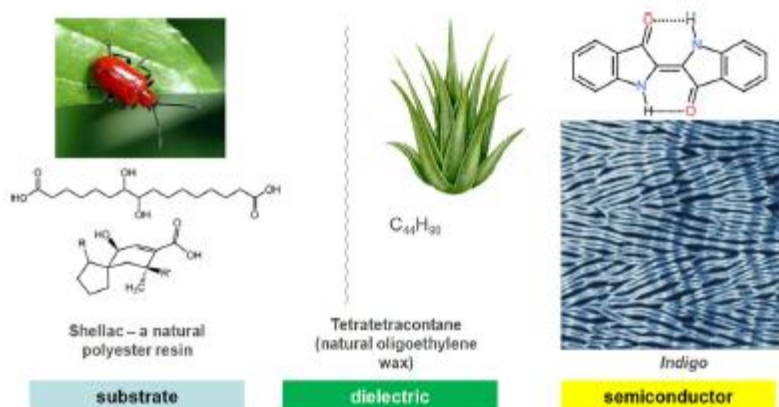


Figure 1: Example of materials set for a nature-inspired organic field effect transistor

Main goals of "green electronics" are: 1) the considerable reduction of the cost of production of the devices by using highly abundant and low cost bio-materials; 2) the fabrication of efficient bio-degradable materials for more sustainable electrical devices; 3) the increase of the bio-compatibility of the devices for a more efficient integration in human, animal and plant tissues (Figure 2).

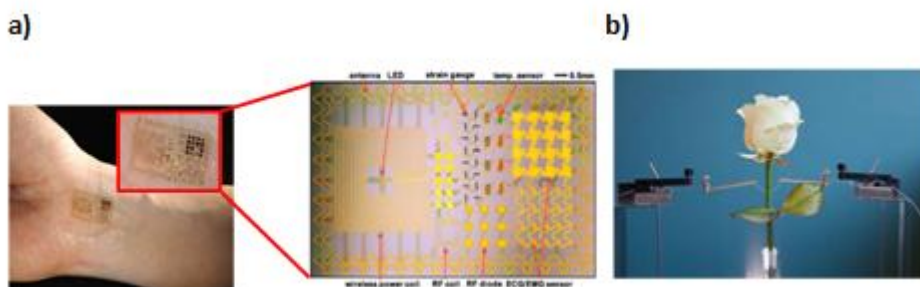


Figure 2: a) Skin integrated device for physiological measurements and stimulation; b) Electronic rose: plant integrated device for physiology regulation, energy harvesting from photosynthesis, and plant optimization beyond genetic modifications.

Starting from this background, the research activity of my PhD has been aimed at the design, synthesis, characterization of the opto-electronic properties and processing of natural and/or Nature-inspired materials for organic light emitting diodes (OLEDs).

This work has been planned into different research activities all concurring to the design of a “green” OLED device. In detail, the attention has been focused on the following topics:

- 1) processing techniques for the fabrication of ITO-free substrate based on the standard PEN and the biodegradable PLA for flexible OLED devices;
- 2) synthesis and electrical properties of eumelanin thin films: towards the design of polymeric anode for ITO-free devices;
- 3) synthesis of nature-inspired organic electroluminescent materials for the emitting layer in OLED applications;
- 4) synthesis and processing techniques of biocompatible and low cost materials for encapsulating layers in OLED devices.

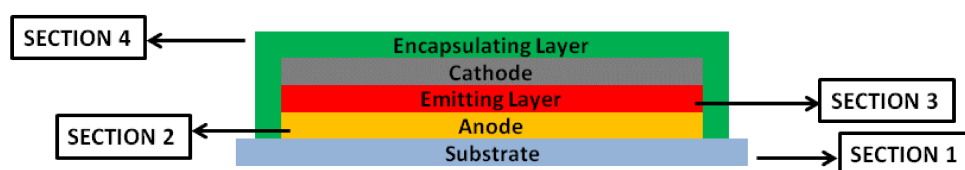


Figure 3: OLED device structure and thesis sections

The research activity was been carried out in the laboratories of Dr Manini, Dept. Chemical Sciences – University of Naples Federico II (**DCS-UniNA**), in the laboratories of Dr Maglione, Lab. Nanomaterials and Devices – ENEA C.R. Portici (**ENEA**) and in the Laboratories of Prof. Santato, Dept. Engineering Physics - Polytechnique Montréal (**DEP-PM**).

1) Processing techniques for the fabrication of ITO-free substrate based on the standard PEN and the biodegradable PLA for flexible OLED devices.

In the field of flexible OLED fabrication, two issues have been faced in the last decade, device flexibility and ITO (mixed oxide of indium and tin) substitution.

ITO is the most used anode layer in OLED manufacturing, because of high cost and limited supply of indium and the fragility and lack of flexibility of ITO layers, alternative materials are being investigated. In this connection, PEDOT:PSS (poly(3,4-ethylenedioxythiophene) polystyrene sulfonate) has been selected as valid substitute to ITO. During my PhD, a first research line was devoted to the fabrication of flexible OLED devices by using PEDOT:PSS as anode.

The most promising flexible substrate for organic electronics applications is PEN (polyethylene naphthalate); so in a first set of experiments PEN was used to fabricate a white PLED (polymer light emitting diode) device with a gravure printed PEDOT:PSS film as ITO-free anode. Printing techniques represent the best opportunity for scaling-up the OLED manufacturing. In particular, a multilayer gravure printed high conductive PEDOT:PSS was realized, and its potential as anode for OLED devices was tested. Even if the registered performances proved quite low if compared to typical ITO/glass based

OLED devices, this approach may be largely rewarded by the demonstrated opportunity of processing flexible ITO-free devices by using the most attractive printing technology for roll-to-roll large area manufacturing.

In a second set of very preliminary experiments, the potential of PLA (polylactic acid) as innovative biodegradable substrate for OLED devices was tested for the first time. Also in this case there are some problems that need to be overcome, such as the sensibility of PLA to the high temperatures and to many common organic solvents; further experiments are still in due course.

2) Synthesis and electrical properties of eumelanin thin films: towards the design of polymeric anode for ITO-free devices

This section has been developed within the frame of a research line aimed at testing the potential of eumelanins, the brown-black pigments that hold important functions in human body, as materials for organic electronics devices.

a) Analysis of factors governing the solid state polymerization process

The ammonia induced solid state polymerization (AISSP) is an innovative technique allowing the deposition of quite homogeneous melanin thin films on different kind of substrates.

Herein is reported a study aimed at assessing the role of temperature, oxygen and water in the solid state polymerization process of 5,6-dihydroxyindole (DHI), the monomer melanin precursor.

To this aim the process was studied by following the evolution of the transmission spectrum over the time under different ambient conditions.

Since the polymerization process consists in a series of oxidative reactions, the oxygen flux is fundamental for the determination of the process rate; water and temperature further accelerate the oxidation.

In another set of experiments it was also evaluated how the ambient conditions can influence the morphology of the melanin thin film. Eumelanin thin films obtained at higher temperatures and oxygen flows show higher roughness and heterogeneity. On the contrary, although water can accelerate the oxidative process leading to melanin thin films, it is also able to give a surface solubilization effect of the material with a consequent smoothing and homogenizing effect.

b) Study on the electric conductivity of eumelanin thin films

The electrical characteristics of eumelanin thin films realized by ammonia induced solid state polymerization (AISSP) were also studied. Both monomers, DHI (5,6-dihydroxyindole) and DHICA (5,6-dihydroxyindole-2-carboxylic acid) were used in the thin film fabrication to evaluate the effect of the chemical composition on the electrical property of the material.

In the first set of experiments, the current-voltage measurements of a device fabricated by using eumelanin thin films as semiconductors among two planar platinum electrodes

were performed. The work was carried out in association with Prof. Clara Santato at the Polytechnique of Montreal (CA) (from 01/09/2016 to 23/12/2016).

In the second set of experiments, the electronic and protonic current of eumelanin materials was evaluated by using Pd and PdHx electrodes under different humidity conditions.

The experimental results confirm the capability of the eumelanin materials to act as hybrid ionic-electronic conductors under humidity conditions. The presence of traps, the morphology and the chemical composition further influence the electric properties as observed for most of the disorder organic materials. The right synergy between morphology, chemical composition and electric properties is still an open issue for the researchers.

3) Synthesis of Nature-inspired organic electroluminescent materials for the emitting layer in OLED applications

This section has been aimed at the design and the synthesis of a series of Nature-inspired electroluminescent complexes for OLED applications.

a) Synthesis of electroluminescent dopamine-inspired iridium(III) complexes

In this work the attention was focused on the synthesis and characterization of new dopamine-inspired iridium(III) complexes as electroluminescent materials for organic light emitting diodes (OLEDs). In particular a set of new iridium(III) complexes was prepared, namely a series of 1-phenyl-6,7-dimethoxy-3,4-dihydroisoquinoline (PHQ) derivatives (Figure 4).

OLEDs based on phosphorescent transition-metal complexes are attracting great attention since they can improve electroluminescence performances as compared with the conventional fluorescent OLEDs. According to spin statistics, electroluminescence from fluorescent molecules can reach a maximum quantum yield of 25%, but in phosphorescent complexes it can theoretically achieve quantum yields up to 100%, since both triplet and singlet excitons can be harvested for the emission. Among all the phosphors, cyclometalated iridium(III) complexes are acquiring a mainstream position in the field of organic displays because of their highly efficient emission properties, relatively short excited state lifetime and excellent colour tunability over the entire visible spectrum.

For the synthesis of PHQ ligands a similar procedure was followed. This consisted in the reaction of the selected benzoic acid with ethylchloroformate and *O,O*-dimethyldopamine to form the intermediate amide derivative, followed by the intramolecular cyclization with POCl₃ to give the desired compounds (Figure 4).

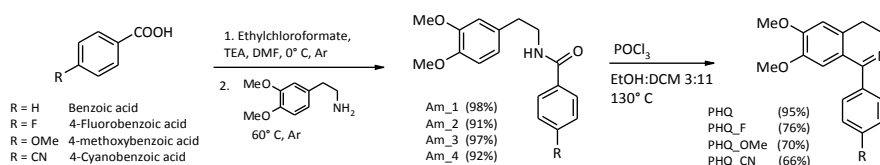


Figure 4: Synthesis of PHQ derivatives

All the synthesized compounds were fully characterized by ^1H and ^{13}C NMR analysis confirming the structures. ^{19}F NMR spectroscopy was also used to confirm that the *fac* isomers of the homoleptic iridium complexes tri-substituted with PHQ-type ligands were formed.

The photo-physical properties of the iridium complexes were investigated in diluted solutions in DCM. It is possible to note that parameters such as the structure of the complex and the nature of the substituents on the phenyl ring induced shifts of both the absorption and emission maxima.

OLED devices were fabricated with the synthesized iridium(III) complexes used as guests at different percentages (2%, 6% and 12% w/w) in the 4,4'-bis(*N*-carbazolyl)-1,1'-biphenyl (CBP), selected as the host. The selected OLED configuration was the following: ITO/PEDOT:PSS/Ir:CBP/BCP/Alq₃/Ca/Ag.

All the fabricated devices exhibited a red electroluminescence with significant shift of the emission maximum observed by changing the nature of the substituents on the phenyl ring of the iridium complexes.

The best devices in terms of luminance and turn-on voltage resulted those prepared by using a 2% wt of the iridium(III) complex, reaching maximum luminances of 1092 cd/m² and 2474 cd/m².

b) Synthesis of transition metal complexes with natural β -diketones

In this section the potential of curcumin (1) and 6-dehydrogingerdione (2), two naturally occurring β -diketones, as ligands in transition metal complexes, such as Ir(III) and Zn(II) complexes, were tested.

Well known for their antioxidant, anti-inflammatory and anticancer properties, curcumin is obtained from the rhizome of *Curcuma longa* and is the main component of turmeric, and 6-dehydrogingerdione is obtained from the rhizome of *Zingiber officinale* and is the main component of ginger.

The use of the easily accessible zinc(II) in addition to iridium(III) is a deliberate choice towards a green approach to OLED fabrication.

Both ligands and the corresponding transition metal complexes were synthesized in good yields and on large scale, and were subjected to spectroscopic characterization. A comparative investigation of their photo-physical properties were carried out both in dilute solutions and on thin films by UV-visible and emission spectroscopy: all the complexes exhibited a green emission (from 480 to 524 nm) and quantum efficiencies up to 1.7% for iridium complexes and up to 78% for zinc complexes.

The iridium and zinc complexes synthesized by using nature-inspired β -diketone ligands, respectively curcumin and 6-dehydrogingerdione showed photoluminescence in the green region.

OLED devices realized with the iridium complexes showed limited performance due to aggregation phenomena in thin film. Zinc complexes show very poor solubility in the common used organic solvents. They were tested as fluorescent emitters in a standard device structure (ITO/PEDOT:PSS/Zn complex/BCP/Alq₃/Ca/Ag). Deposition of the zinc complexes were performed from solution (dimethyl sulfoxide) and with a thermal vacuum deposition, unfortunately in both cases, although devices show a diode electrical

behavior, the emission of the zinc complexes was not observed. As future development, the synthesized zinc complexes can be structural modified to improve the solubility and/or they can be tested as host and/or electron transport material.

These data pointed out the potentiality of these new nature-based complexes as organic materials for optoelectronic application and represent the good starting point toward the development of more sustainable OLED devices.

4) Synthesis and processing techniques of biocompatible and low cost materials for encapsulating layers in OLED devices

In the last section of the thesis, low-cost encapsulation methods for flexible OLED devices have been studied. The permeation process is a very complex phenomena and different mechanisms are involved. As a consequence, different approaches can be used to realize a barrier layer.

The use of oxides materials is one of the most used solution for the realization of high performances barrier layers by using vacuum deposition techniques. On the contrary, vacuum techniques are expensive and often very slow.

In this work ceramic, hydrophobic and water absorbing thin film were realized to test the possibility to realize a barrier multilayer for electronic devices.

ZnO nanoparticles deposited by solution based processes were used as an alternative to inorganic barrier films realized by vacuum techniques. The obtained ceramic thin film showed different permeation mechanisms in relation to the used deposition technique and to its microstructure. The impossibility to use high temperatures to proceed with sintering process is the main obstacle to further improve the barrier properties.

An “active” multilayer approach is proposed to reduce the water permeability of the solution-based ZnO layer; in particular, the adsorption phase of the permeation process can be slow down by reducing the surface interactions between the penetrant and the barrier materials. Hydrophobic and/or oleophobic treatments of surface reduce its wettability and slow down the adsorption process.

Hydrophobic layers were prepared by using functionalized ZnO nanoparticles with stearic acid deposited on PEN substrates. An improvement of the barrier properties with respect to the only ZnO nanoparticles layer was observed and it was demonstrated how the hydrophobicity is capable to slow down the permeation process and improve the multilayer barrier performances. It was also demonstrated that it is possible to merge the use of a ceramic and hydrophobic material in a single step deposition process.

Moreover, a water absorbing interlayer can be introduced for further improve barrier performances and a hydrogel thin film was realized to test this hypothesis.

It is reported that a double layer hydrogel/ZnO nanoparticles shows better barrier properties with respect to the sole ZnO nanoparticles layer and comparable performances with the hydrophobic layers.

Although the hydrophobic and the hydrogel layers act according to different mechanisms, both solutions can be exploited to improve the ceramic layer barrier properties.

Different functional thin film were realized by using solution based deposition techniques, demonstrating how is possible to easily confer the desired characteristics to a layer. The

proposed methods can be used for preparing multilayer structures that can be very attractive for packaging applications and encapsulation of moisture sensitive devices.

~INTRODUCTION~

In our lives we are constantly surrounded by electronic devices and it is impossible to imagine ourselves without using such devices. The market demand for electronic devices is growing every day from both the points of view of the quantity and the performances. In this context, inorganic semiconductors remain fundamentals. Nevertheless, at present, the energy efficiency of these devices is not able to balance the economic and energy costs needed in the production phase.¹ Furthermore, the huge demand of electronics is leading to a massive amount of electronic waste and to a great demand of rare elements such as gallium and indium.²

From these premises, the use of organic semiconductors and materials to prepare electronic devices can be seen as an answer to the problems posed by the inorganic counterparts. The interest in what is currently called "organic electronics" was born with the discovery of the electrical conduction properties of some organic materials. The first organic conductive material (polyaniline) was reported by Henry Letheby in 1862 by anodic oxidation of aniline in sulfuric acid.³ Successfully, in 1954, high conductivity of 0.12 S/cm was reported in perylene-iodine complex.⁴

In 1977, Shirakawa et al. reported the high electrical conductivity of iodine-doped polyacetylene⁵ a research that was awarded in 2000 with the Nobel prize in Chemistry for "The discovery and development of conduction polymers". In the same period, highly conductive polypyrrole was also discovered.⁶ These kind of materials led to a huge interest in organic electronics.

In the early stages, the term "organic" was referred to the typology of semiconductor materials employed in this new kind of devices; with the evolution of the technology, the term "organic" has acquired a wider meaning referring also

to the other materials than constitute the electronic devices such as dielectrics, substrates, etc.

Nowadays, when we talk about organic electronics we refer to that set of technologies and materials that allow us to obtain light and flexible devices with the possibility of realizing them on large areas thanks to the peculiar mechanical properties of the organic materials.⁷ With organic materials it is indeed possible to use easy and low cost solution-based processing techniques such as printing techniques.⁸ Another advantage of the organic materials is the possibility of tuning their properties at molecular level, to modulate the characteristics and performances in a detailed way to meet the devices requirements. Organic materials can be tailored: for example by varying functional groups and/or the polymer length with the aim of changing the band gap and allowing the electronic tunability.⁹

On the other hand, poor crystallinity, low mobility and degradation susceptibility of organic materials represent today the greatest obstacles to the commercialization of organic devices.

Among organic electronic devices, organic light emitting diodes (OLEDs), organic photovoltaics (OPVs) and organic field-effect transistors (OFETs) are the most known.

An OLED mainly consists of an electroluminescent organic material sandwiched between two electrodes (Figure 1).

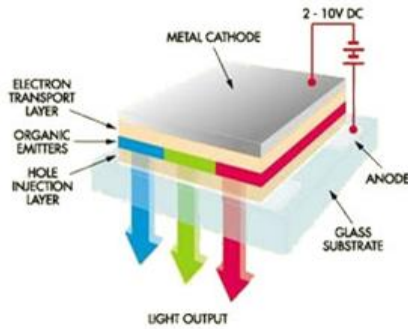


Figure 1: Structure organic light emitting diode

OLED devices find application in different fields from civil lighting to electronics, from automotive industry to biomedical devices, from interior design to light art and fashion industry. Now mobile telephones and laptop displays, TV sets and design lamps based on the OLED technologies are largely diffused on the market (Figure 2).

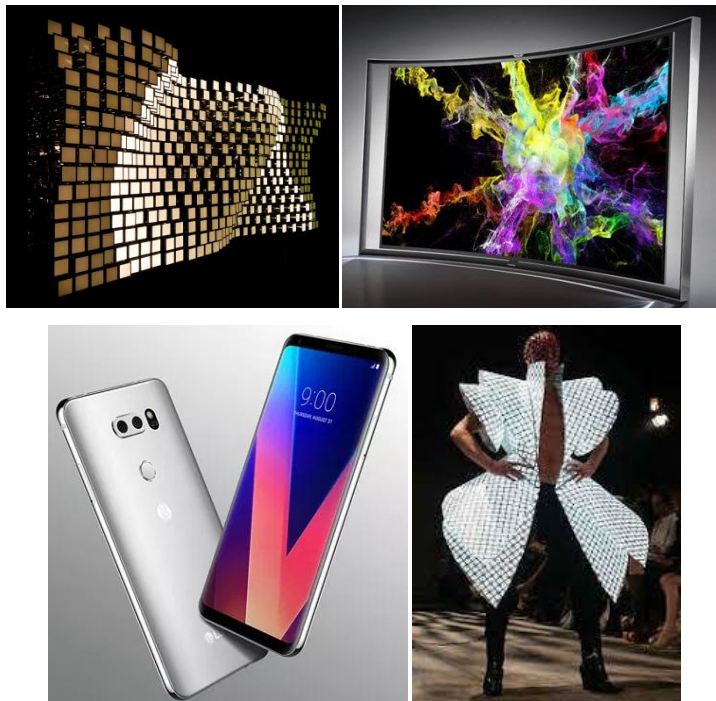


Figure 2: Examples of OLED application

An organic solar cell or plastic solar cell is a type of photovoltaic device that uses organic materials for light absorption and charge transport to produce electricity from sunlight exploiting the photovoltaic effect.¹⁰

A typical OPV device consists of one or several photoactive materials sandwiched between two electrodes (Figure 3). The molecules most commonly used in organic solar cells are solution-processable, as they are cheap allow high throughput, resulting in low production costs to fabricate potentially cost-effective large volume photovoltaic devices. The optical absorption coefficient of organic molecules is high, so a large amount of light can be absorbed with a small thickness of the materials (usually on the order of hundreds of nanometers). The main disadvantages associated with organic photovoltaic cells are the low efficiency, low stability and low strength compared to inorganic photovoltaic cells such as silicon solar cells. Polymer solar cells, as other organic electronic devices, can be lightweight, potentially disposable and flexible, and customizable at the molecular level. Polymer solar cells also have the potential to exhibit transparency, suggesting applications in smart windows, walls, flexible electronics, etc. The disadvantages of the polymer solar cells are also serious: they offer about 1/3 of the efficiency of the hard materials, and experience substantial photochemical degradation.¹¹ As a result, polymer solar cells efficiency and stability problems are the main topics in the solar cell research.

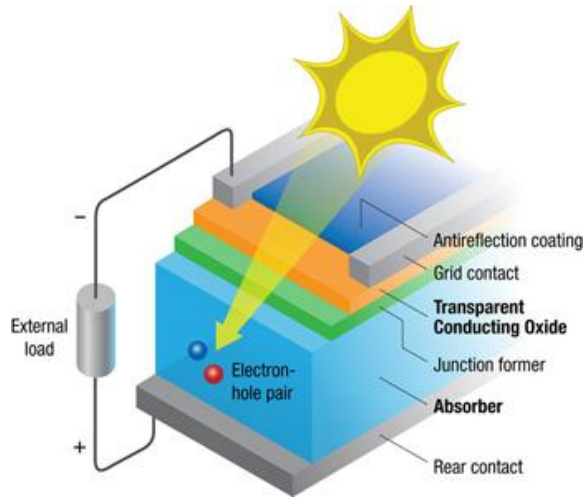


Figure 3: Structure organic solar cell

An organic field effect transistor is realized with a layered structural design consisting of a thin film of organic semiconductor, an insulator, and three electrodes named source (S), drain (D), and gate(G) as shown in Figure 4. The source and drain electrodes inject and extract the charge carriers, respectively, and are in contact with the active layer. On the other hand, the gate is separated from the semiconductor film by the insulator. The voltage applied to the gate controls the conductivity of the semiconductor between source and drain (channel). The channel in a transistor is formed by the accumulation of the charge in the semiconductor.¹² The field-effect transistor was first proposed by J.E. Lilienfeld, who received a patent for his idea in 1930.¹³ He discovered that a field-effect transistor behaves as a capacitor with a conducting channel between a source and a drain electrode. Applied voltage on the gate electrode controls the amount of charge carriers flowing through the system. The first field-effect transistor was designed and prepared in 1960 by Kahng and Atalla using a metal-oxide-semiconductor structure (MOSFET).¹⁴ As previously mentioned, the rising of the materials and manufacturing costs and the interest in the use of more

environmentally friendly electronic materials have supported the development of organic electronic devices, and in 1987 Koezuka and co-workers reported the first organic field-effect transistor based on a conjugated polymer of thiophene molecules.¹⁵

Many OFETs are now designed based on the thin-film transistor (TFT) model, which allows the devices to use less materials.

OTFTs are the fundamental unit for basic circuits and are now widely used in active matrix displays, RFID (Radio-Frequency Identification) tags, sensors and actuators conditioning.

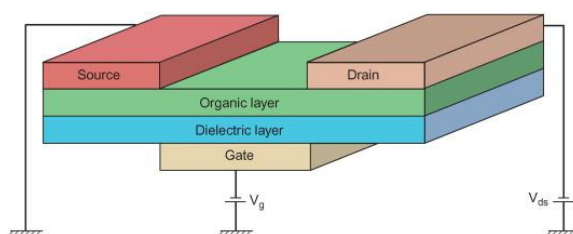


Figure 4: Structure of organic field effect transistor

➤ The lighting evolution

With the discovery of fire, people had the possibility to illuminate an area, firstly with campfire or torches and thanks to the technological evolution with oil lamps and candles. With the advent of electricity, electric lighting became predominant. The first electric light was created by Humphry Davey in the first decade of 1800; he realized the first incandescent light using a bank of batteries and two charcoal rods (arc light).

In 1879 Thomas Edison invented a long-lasting electric light bulb that could compete with gas lighting. In particular with a carbonized bamboo filament was possible to have light for 1200 hours. Incandescent bulbs would go on to dominate the world of lighting until fluorescent lights were commercially introduced by Daniel McFarlan Moore in 1904. Although fluorescent light required

high voltage and non-standard connectors to operate, their higher efficiency, compared to incandescent lights, led the major incandescent manufacturer General Electric to improve upon their incandescent technology by introducing the tungsten filament. The 20th century was the century of high density discharge (HID) lamps. The most popular types of HID lamps are the fluorescent, the mercury-vapor, the high-pressure sodium, and the metal-halide lamps. All of these lamps exploit a technology based on a visible light generated via an electrical current between two metal electrodes through a glass tube filled with inert gas.

The lighting technology change substantially with the birth of the solid state lighting (SSL) era. In this emerging concept for illumination, selected semiconducting materials can produce visible light under the action of an electrical field (electroluminescence) in suitably engineered devices where the transport of charge occurs in one specific direction (diodes). Through this approach, the primary product of these lighting devices is the photon itself, unlike traditional sources where visible light is essentially a by-product of other processes, such as heating or discharging. As a result, SSL produces visible light with reduced heat generation and energy dissipation, while its solid-state nature provides greater resistance and lifetime, with limited impact on the environment. First examples of SSL devices are LEDs (Light Emitting Diodes), an inorganic-based semiconductor device that emits visible light of a defined color when a voltage is applied. The first LED was invented in the 1960 by General Electric scientist Nick Holonyak. From 1960 to nowadays, LED technology has evolved in terms of emission spectra, cost and efficiency so that now such technology represent the undisputed leader in lighting industry.

Thanks to the discovery of the semiconducting and electroluminescence properties of organic materials,¹⁶ in the last 30 years the Organic Light Emitting

Diode (OLED) technology was introduced as possible alternative to LED technology.



Figure 5: Technology evolution of the lighting

➤ Fluorescence and Phosphorescence

Typically, organic molecules in their ground state have paired electrons in all the orbitals, thus a total spin equal to zero gives a singlet state (S_0). Upon the absorption of an incident radiation of a given energy, an electron from the outer orbital can be promoted to an unoccupied high energy orbital leading the molecule to an excited state (S_n).

Within the S_n states, there are several energy levels. The bigger gap between the second and first excited state is overcome by internal conversion (IC) and during this conversion the spin of electrons is maintained (Figure 6). After that, the electrons can relax vibrationally until they reach the lowest energy level of the S_1 state. The electrons could relax even further in a non-radiative way until they eventually reach the ground state again, but it can be the case that the last amount of energy is too large to be released to the surroundings, because the surrounding molecules cannot absorb this much energy. In this case, fluorescence occurs with emission of photons of a specific wavelength.

The light emitted by radiative relaxation has a longer wavelength and a lower energy than the absorbed light because a part of the energy has already been released in a non-radiative decay process. This shift towards a longer wavelength is called Stokes shift (Figure 6). The emission lasts only until the electrons are back in the ground state. Since during all those transitions the electron spin is kept the same, they are described as spin-allowed

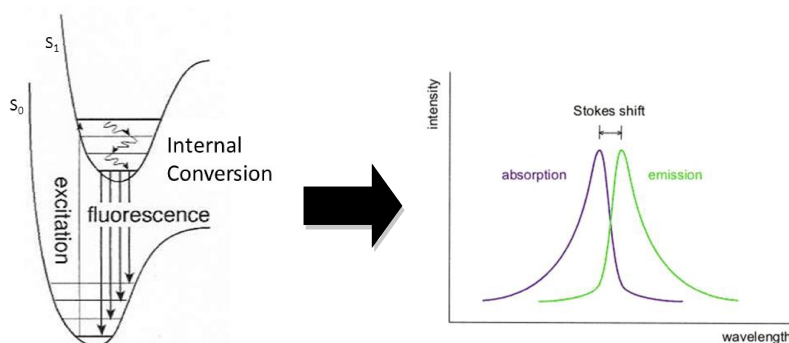


Figure 6: Radiative energy decay and Stokes shift

According to the selection rules, triplet states (T) cannot be populated by direct absorption of a radiation. Nevertheless, for some materials the T_1 state can be populated from the lowest excited S_1 state through an intersystem crossing conversion (ISC) (Figure 7). This ISC is an electronic transition between two excited states generally associated with a spin inversion. Even if the ISC process is described as "spin-forbidden", it occurs thanks to a phenomenon called "spin-orbit coupling".

The relaxation process from the triplet state to the S_0 state ($T_1 \rightarrow S_0$) is also spin forbidden; for this reason the photon emission is weak and slow (phosphorescence). Phosphorescence emission is more favorable for organic transition metal complexes, in which the central metal ion induces significant spin-orbit coupling (SOC). It also depends on the properties of so-called quenchers that are surrounding molecules and are able to take up larger amounts of energy.

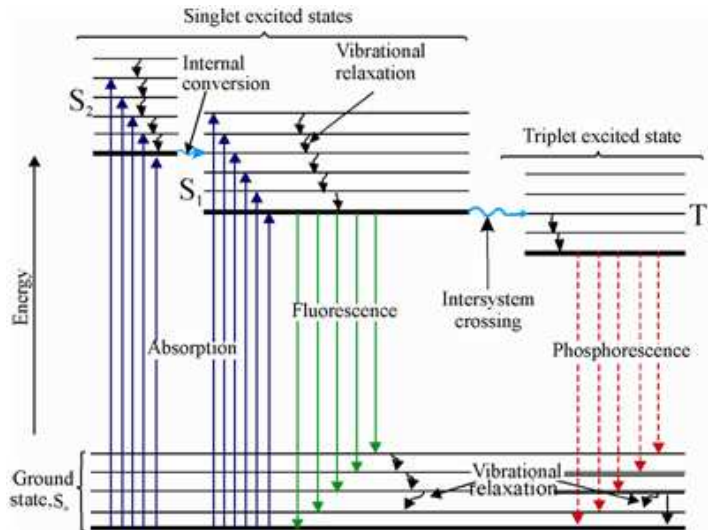


Figure 7: Jablonski diagram

➤ OLED devices

An organic light emitting diode (OLED) is an optoelectronic device in which an organic electroluminescent material is sandwiched between two electrodes, with at least one of the two contacts being transparent to allow light emission. The physical process is based on the electroluminescence (EL). With voltage application, anode and cathode inject respectively holes and electrons that move through the layers and recombine in the emitting layer with exciton formation. Relaxation of the exciton produce light emission (electroluminescence) with a wavelength strictly dependent on the electronic properties of the emitting material.

High photo-luminescence is a necessary but not sufficient condition for electroluminescence.

In the simplest version, an OLED device is composed of a single organic emitting layer between an anode and a cathode (monolayer device); since the HOMO and LUMO of the emitting layer, in the most of the cases, are set at energy levels very different from those of the two electrodes, organic multilayer structures have

been developed in order to improve the device performances. This can help holes and electrons movements supporting the recombination in the emissive layer. A typical multilayer structure is composed by: anode, HIL (hole injection layer), HTL (hole transport layer), EML (emitting layer), ETL (electron transport layer), EIL (electron injection layer) and cathode as reported in Figure 8, and it can be designed to perfectly balance charge injection and transport with the aim of optimizing the recombination process.

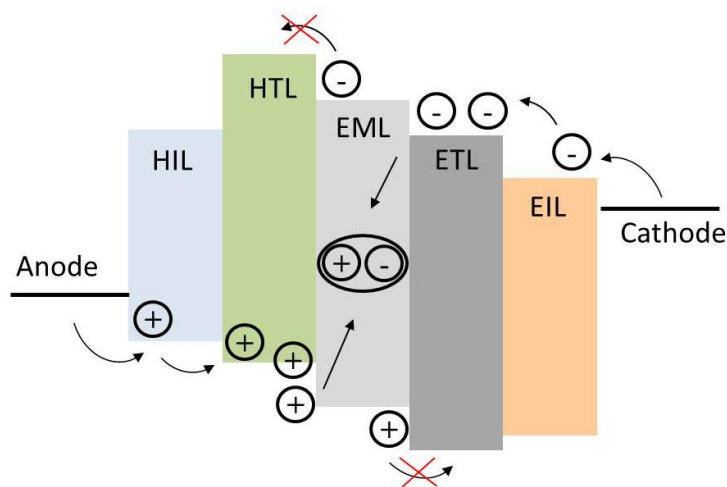


Figure 8: OLED multilayer structure

The anode component typically used is indium tin oxide (ITO). This material is transparent to visible light, it show good electrical conductivity ($\sim 10^4$ S/cm) and it has a high work function which promotes injection of holes into the HOMO level of the organic layers. Due to the high costs and the limited availability of indium, the fragility and lack of flexibility of the indium-tin oxide layers, and the high costs of deposition techniques that require high temperatures and sometimes high vacuum levels, researcher are working on alternative anode materials.

A typical conductive layer behaving as a transparent electrode that replace the traditionally used ITO is PEDOT:PSS , a blend of the two polymers poly(3,4-

ethylenedioxythiophene and poly(styrenesulfonate) (Figure 9).¹⁷ PEDOT:PSS is a transparent and conductive blend (>200 S/cm) with high flexibility, and since its HOMO level lies between the work function of ITO and the HOMO of other commonly used polymers, it is able to reduce the energy barriers for hole injection.

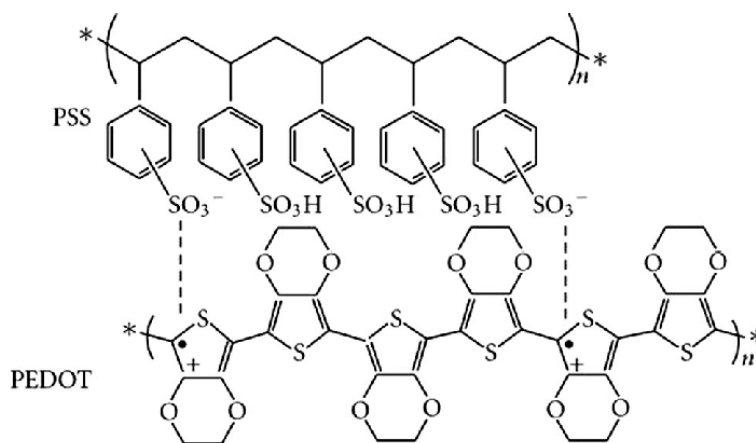


Figure 9: PEDOT:PSS structure

The hole injection layer (HIL) improves the electrical properties of the device and it is able to smooth the ITO surface.¹⁸ A typical HIL is constituted by PEDOT:PSS. The electron transport layer (ETL) and/or the electron injection layer (EIL) are necessary to help electrons injection and transport from the cathode layer. Typical electron transport materials are: tris-(8-hydroxyquinoline)aluminum (Alq₃), 3-(Biphenyl-4-yl)-5-(4-*terz*-butylphenyl)-4-phenyl-4H-1,2,4-triazole (TAZ) and 2,2',2''-(1,3,5-Benzinetriyl)-tris(1-phenyl-1-*H*-benzimidazole) (TPBi) (Figure 10).¹⁹

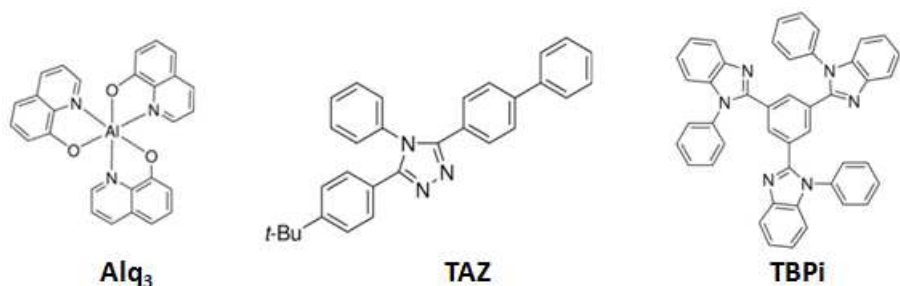


Figure 10: Electron transport materials

Both hole and electron blocking layers are used to confine charges. Typical hole and electron blocking materials are bathocuproine (BCP) and tris(4-carbazoyl-9-ylphenyl)amine (TcTa) respectively (Figure 11).^{20,21}

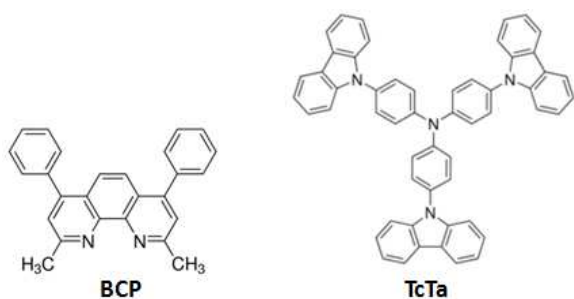


Figure 11: Hole and electron transport materials

Of course, all materials of the multilayer structure must be chosen to reduce charge injection barriers.

The cathode component depends on the type of OLED required. Noteworthy, even a transparent cathode can be used. Usually metals like barium, calcium and aluminum are used as cathodes because they have work functions lower than anodes, which helps in injecting electrons into the LUMO level of the different layers.²²

The emitting layer is the main component of an OLED device and it is constituted by an electroluminescent material. This can be a small molecule, a transition metal complex and a polymer.

Small molecules such as pentaphenylcyclopentadiene and transition metal complexes involving zinc, beryllium, copper and barium have been widely used as emitting layer in small molecule organic light emitting diode devices (SM-OLED) (Figure 12).²³ Devices prepared with such materials result in moderately low bias voltages and attractive luminance efficiency. Fluorescent small molecules can be easily synthesized and designed to obtain all the primary colors. The production of small molecule devices and display usually involves thermal evaporation in a vacuum, since insolubility of this kind of materials. This makes the production process more expensive and of limited use for large area devices, than other processing techniques. Nevertheless, vacuum deposition enables the construction of very complex multi layer structures to optimize devices performances.

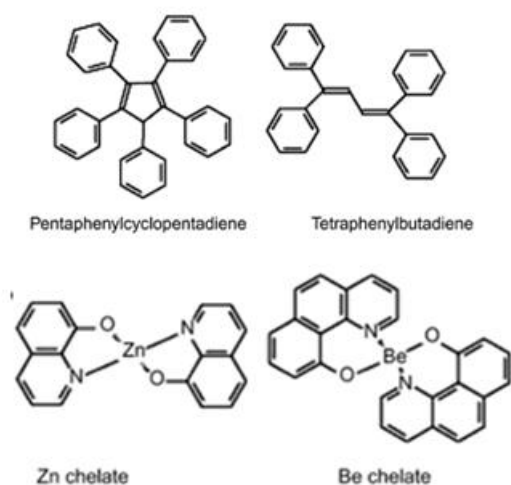


Figure 12: Small molecules used as emitting materials

Fluorescent conjugated polymers represent the ideal candidate for commercial applications. Polymer OLED (P-OLED)²⁴ materials do not perform as good as SM-

OLED in terms of lifetime and efficiency. This can be explained considering that they have higher hole conductivity than electron conductivity and so excitons form usually close to the cathode and often tend to relax non radiatively via energy transfer.

Anyway, devices based on this kind of polymer exhibit efficiencies around 20 lm/W, close to those of inorganic LEDs. Polymers are soluble and available as inks for printable electronics applications, they show good flexibility and it is usually required a relatively small quantity of material for large area deposition so they are more suitable for the realization of large-screen displays. On the contrary, it is not possible to realize complex multilayer structures since with solution based deposition process there are problem of compatibility between solvents used for deposition and materials already deposited to realize the device (perpendicularity); this is another reason why P-OLED devices show limited efficiency. Typical polymers backbones used include derivates of poly(*p*-phenylene vinylene) and polyfluorene (Figure 13). This kind of materials offer many opportunities for the control of electronic, chemical, morphological and rheological properties. Substitution of side chains onto the polymer backbone or variation of the backbone structure may determine the stability and solubility of the polymer and the color of emitted light.

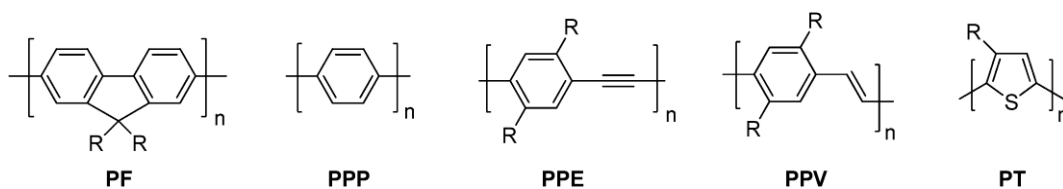


Figure 13: Polymeric backbone used as emitting materials in P-OLED

In order to improve the performances and the brightness of the devices, OLED based on phosphorescent emitting molecules²⁵ (PH-OLEDs) are becoming predominant.

Phosphorescent organic light emitting diodes use the principle of electrophosphorescence to convert electrical energy into light in a highly efficient manner.²⁶

According to spin statistics, in PH-OLED all the four different combinations of excited states are possible, one combination of antiparallel spin giving a singlet (accounting for the 25% of excitons), and three combinations of parallel spin giving a triplet (accounting for the 75% of excitons)²⁷ so by harvesting both singlet and triplet excitons, PH-OLEDs overcame the limit of SM-OLEDs due to low efficiencies, approaching a theoretical internal quantum efficiency of 100%.

Efficient phosphorescence is rare at room temperature, and few materials emit efficiently in homogenous films due to the quenching effects by surrounding molecules. The solution to these demands is found by doping the luminescent material into a charge transport host material.²⁸ Emission then occurs by direct carrier trapping and exciton formation on the luminescent dye, or by exciton formation in the host and energy transfer to the luminescent guest.

The energy transfer mechanism is not completely clear and understood. Two mechanisms are possible: the Dexter transfer and the Förster transfer (Figure 14).²⁹ The Dexter electron transfer is a fluorescence quenching mechanism in which an excited electron is transferred from one molecule (a donor) to a second molecule (an acceptor) due to hopping of the electrons. The process requires an overlap of the wavefunctions between the donor and the acceptor, which means it can only occur at short distances (typically within 10 Å). The excited state may be exchanged in a single step, or in two separate charge exchange steps.

In the Förster mechanism (FRET), transfer occurs through non radiative dipole-dipole coupling. The efficiency of this energy transfer is inversely proportional to the sixth power of the distance between donor and acceptor, so this process is

extremely sensitive to small changes in the distance. FRET occurs over large distance as compared to Dexter energy transfer (10-100 Å).

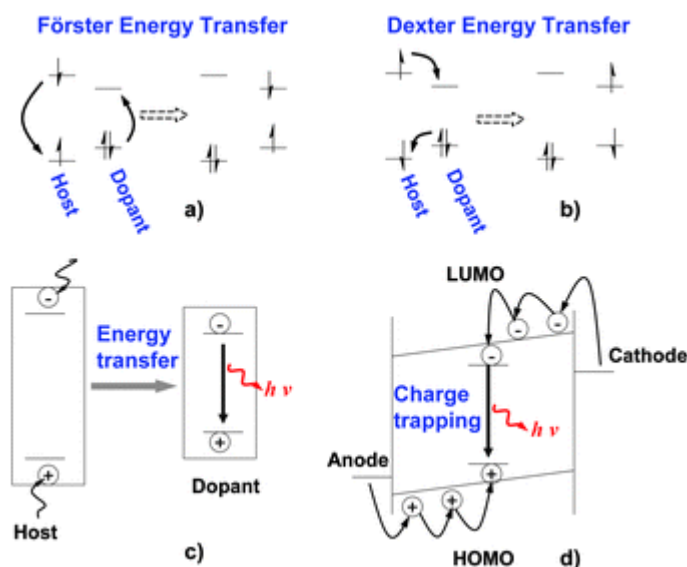


Figure 14: Energy transfer mechanisms in host-guest systems

➤ Device fabrication

Deposition techniques are a fundamental aspect in the organic electronic device fabrication.

Inorganic and metallic materials are deposited usually by e-beam, sputtering, thermal deposition, ecc.

Organic semiconductors can be deposited either from vapor or solution phase, depending on their vapor pressure and solubility. Of course, device performances are greatly influenced by the deposition conditions, that influence the resulting molecular structure and the morphology of the thin film.³⁰

Vacuum thermal evaporation is a process that consist in the heating of the organic semiconductor using a resistive heating source under a pressure in the range of 10^{-8} to 10^{-6} torr (Figure 15). Organic small molecules and oligomers are usually deposited by vacuum thermal evaporation due to their insolubility. By using

vacuum thermal evaporation it is possible to obtain with a good reproducibility films with high uniformity. Multilayer deposition and co-deposition of several organic semiconductors are possible without the concerns of delamination and/or dissolution of the previous layers during subsequent deposition steps. On the other hand, vacuum techniques are time expensive and require a relatively high amount of material, without considering the initial cost for the equipment setup. Furthermore, there is a limitation in the dimensions of the device due to the relatively small dimensions of the vacuum deposition chamber.

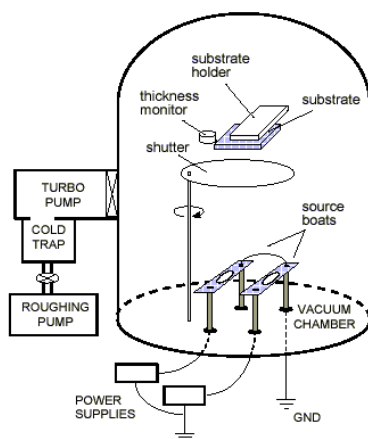


Figure 15: Vacuum thermal evaporation chamber

Solution based deposition techniques show few advantages such as: they are not limited by the size of the vacuum chamber, no pumping down time is required, low cost of production.

Both spin coating and solution casting are commonly used for solution deposition. In the spin coating process, a liquid precursor or a solid dissolved in a proper solvent is deposited on a smooth and flat substrate which is subsequently spun at a high rate to centrifugally spread the solution over the substrate. The desired thickness can be reached by acting on the speeding rate, the time of spinning and by performing repeated deposition. In the spin coating method, the solvent dries

relatively fast allowing less time for molecular ordering, as a consequence an annealing treatment is often carried out in order to crystallize the amorphous spin coated film. Dip coating is another solution deposition technique, in this case the substrate is completely submerged in the solution and then withdrawn under controlled conditions. By controlling the withdrawal speed, the evaporation conditions (i.e. humidity, temperature) and the volatility and viscosity of the solvent, the film thickness, homogeneity and morphology can be controlled. Since the evaporation of the solvent is slower than in the spin coating process, with dip coating it is possible to obtain a good molecular order, although the film uniformity is usually better for spin-coated films.

The Langmuir-Blodgett (LB) technique is another possible solution method to deposit organic thin films. LB film consists in an ordered array of amphiphilic molecules deposited from the surface of a liquid onto a solid by immersing the solid substrate into (or from) the liquid. The molecules in the LB film are usually well-aligned.

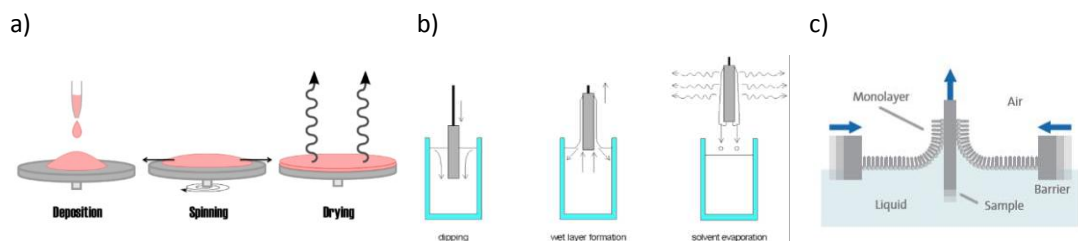


Figure 16: a) spin coating deposition; b) dip coating deposition; c) Langmuir-Blodgett deposition

In the device fabrication it is not only important the thin film deposition process but also the patterning of both conductor and semiconductor layers. The distances and the specific overlap between different layers and materials need to be specifically designed in order to reach the best device performances. As in all the steps of the fabrication process, cost, achievable feature size and materials

compatibility need to be considered. There are three main types of patterning procedures: optical lithography,³¹ shadow masking³² and printing.³³

Optical lithography or photolithography is a conventional technique for patterning and realization of components for microelectronics and photonic devices (Figure 17). This technique is based on the deposition of a photoresist layer that is subsequently exposed to UV light through a mask. UV light exposition induces chemical changes in the exposed regions making the photoresist more soluble (positive resist) or less soluble (negative photoresist) in a specific solution. The soluble portion is so removed leaving a photoresist pattern. If the resist is deposited directly on the layer that is necessary to pattern, the patterning is followed by an etching process of the region not covered with photoresist. The subsequent removal of photoresist residues leave a patterned layer. This kind of process is called direct photolithography and is very used in the field of the organic electronic devices for the pattern of the ITO layer. Another photolithographic technique consists in the deposition of the thin film on top of a patterned photoresist layer and subsequent dissolution of the photoresist, leaving a pattern of the substrate of the deposited material (lift-off).

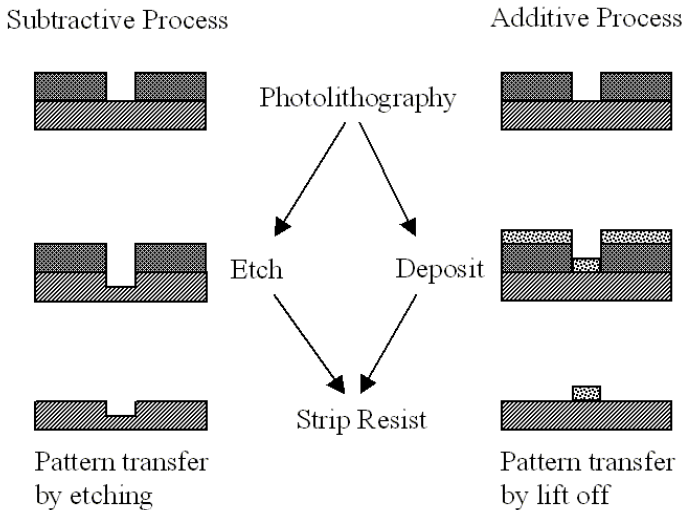


Figure 17: Subtractive and additive photolithographic processes

Photolithography generally has relatively high cost per unit area, the substrate size is limited by the size of the exposure tools and the resolution is around 80 nm, for such reasons this technique is usually used for realization of high added value components.

Materials can also be patterned directly in the deposition phase by using a shadow mask. Shadow mask is often used in the vacuum thermal evaporation process. The device size is limited by the size of the mask and the resolution is around 25-40 μm .

Driven by the necessity to have low cost, large area and flexible devices, significant progress has been made by printing methods. The main printing techniques used for device fabrication are: ink jet printing, screen printing, flexography and gravure printing (Figure 18).

Ink jet printing consists in the deposition of liquid droplets on a substrate with a specific pattern that can be easily changed. Since inkjet deposits material by jetting droplets from a nozzle that is scanned relative to the substrate, in order to achieve high throughput, a large number of nozzles must be used, which increases the risk of nozzle clogging. Furthermore, minimum feature size is limited by the nozzle size and drop placement accuracy especially at high print speeds. Thus, non-digital printing methods such as screen printing, flexography and gravure are more promising for scaled-up of the devices manufacturing.

In the screen printing, a specially formulated ink is squeezed through a screen mask onto the substrate surface to form a desired pattern. Screen printing requires inks with high viscosity and so it is ideally suitable for thick films deposition. The limitation with screen printing is the feature size it can print: 75 μm is the smallest feature size that is reproducible unless surface patterning is used, so that the printed ink does not spread.

Both flexography and gravure printing use a roll that is inked, from which patterned ink is transferred to the substrate. They differ in how the pattern is created on the roll. In flexography the pattern consists of raised features that are inked from an anilox roller. The resolution of flexography is limited by the low stiffness of the material from which the patterned roll is fabricated. Gravure is most promising in terms of resolution and print speed. In gravure printing the pattern is made up of recessed cells below the roll surface. These cells are filled with ink and excess ink is removed from the land areas in between the cells using a doctor blade. Gravure cylinders are typically made from metals such as copper with a chromium coating. This results in excellent dimensional stability, roll durability and pattern fidelity and also compatibility with a wide range of solvents.

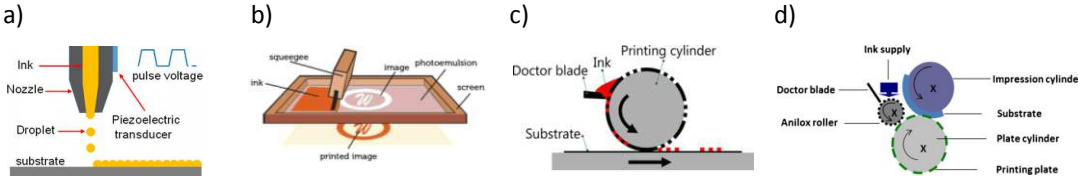


Figure 18: a) ink-jet printing; b) screen-printing; c) Gravure-printing; d) flexography

~AIMS OF THE THESIS WORK~

What discussed till this point represents the background from which I have started my PhD work that has been focused on synthesis, optoelectronic properties and processing of bio-inspired soft materials: toward new «green» electronic devices.

"Green electronics" represents an emerging research area, within the field of organic electronics, aimed at exploiting the potentiality of natural compounds and their derivatives as functional materials for innovative, low-cost and sustainable electronic devices.³⁴

Main goals of "green electronics" are: 1) the considerable reduction of the cost of production of the devices by using highly abundant and low cost bio-materials; 2) the fabrication of efficient bio-degradable materials for more sustainable electrical devices; 3) the increase of the bio-compatibility of the devices for a more efficient integration in human, animal and plant tissues.

All the different components of an electronic device can be thought in a "green" electronic vision, from the substrate to the encapsulating layer, from the electrode to the semiconductor (Figure 19).

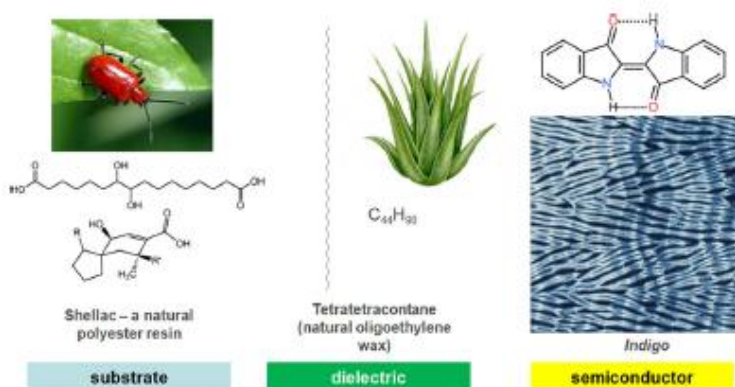


Figure 19: Example of materials set for a nature-inspired organic field effect transistor.

Different natural and synthetic biodegradable and biocompatible substrates have been successfully used for electronic devices. Paper is employed in devices for storage, generation and harvesting of energy^{35,36} and recently it was demonstrated that the performances of an all-organic paper supercapacitor based on nanocellulose and PEDOT:PSS is enhanced by incorporating lignin, another abundant and natural biopolymer (Figure 20).³⁷

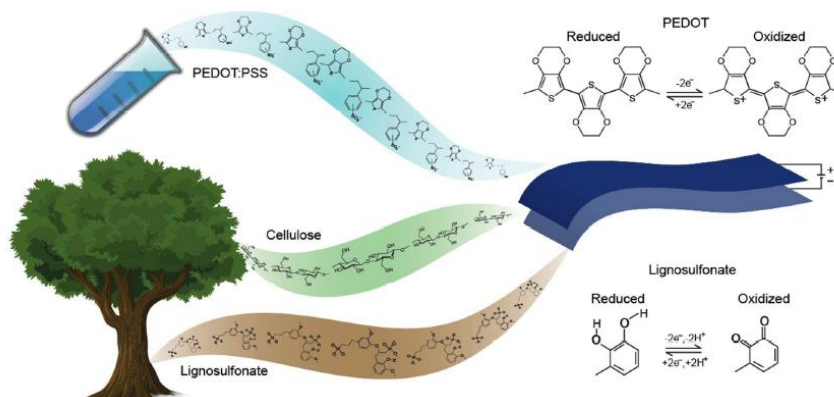


Figure 20: Schematic of the paper supercapacitor with the molecular structures of its constituents

PDMS (polydimethylsiloxane), PVA (polyvinyl alcohol) and PLA (polylactic acid) are examples of biocompatible synthetic polymers used as substrate in electronic devices (Figure 21).^{38,39,40}

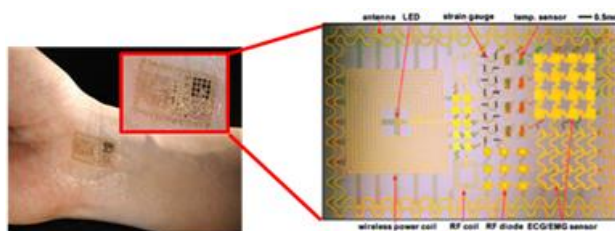


Figure 21: PVA-based skin integrated device for physiological measurements and stimulation

Fully biocompatible and biodegradable substrates are also of great interest. Silk was employed as a platform for the fabrication of sensing devices for the food industry.⁴¹

Recently, also inorganic scaffolds have been used such as biosilica from living diatoms used in photonics and electronics (Figure 22)⁴² and the carbonate microstructures from sand dollars converted into perovskite semiconductors (Figure 23).⁴³

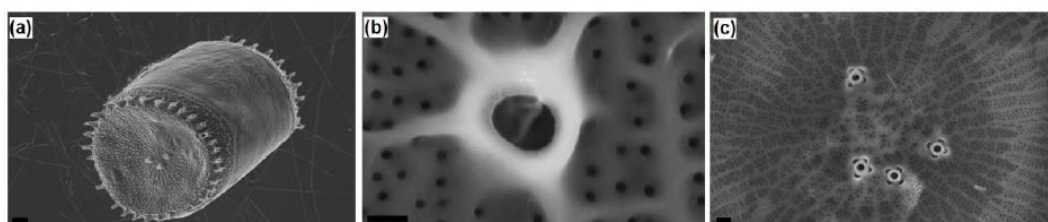


Figure 22: Scanning electron microscopy images of a *Thalassiosira weissflogii* frustules: a) after soft acid treatment the whole structure is preserved; (b,c) after hard acidic oxidative treatment, the intricate pattern of pores is clearly visible. Markers: (a) 1 μm ; (b) 100 nm; (c) 200 nm

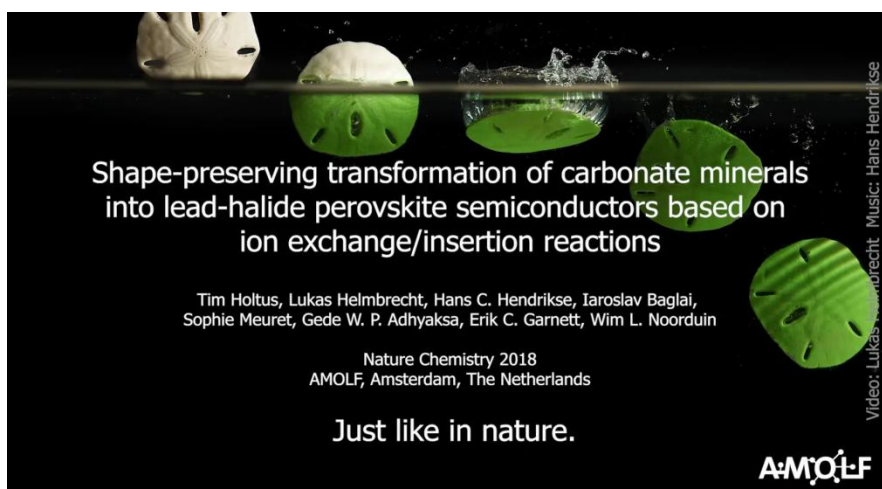


Figure 23: From sea urchin skeleton to semiconductor

The "green" electronics developed parallelly with bio-electronics because the biocompatibility and the biodegradability are requirements for electronic devices to be interfaced with biological systems.

OFETs (organic field effect transistors) were used as selective sensors by incorporating receptors molecules. The receptors are able to selectively bind analytes of interest with a modification of the electric signal of the device.⁴⁴

The group of Prof. Malliaras reported on the use of an EOCT (Organic electrochemical transistor) device for in vivo recording of brain activity in rats.⁴⁵

The group of Prof. Rolandi realized for the first time an OFET based on proton charge transport by using maleic-chitosan proton conducting layer as semiconducting material and PdH_x as proton conductors.⁴⁶

An important contribution was given by the group of Prof. Berggren with the introduction of two innovative devices that can be used as logic gates and delivery systems, respectively the ion bipolar junction transistors (IBJT_s) and the organic electronic ion pumps (OEIP_s) (Figure 24).⁴⁷

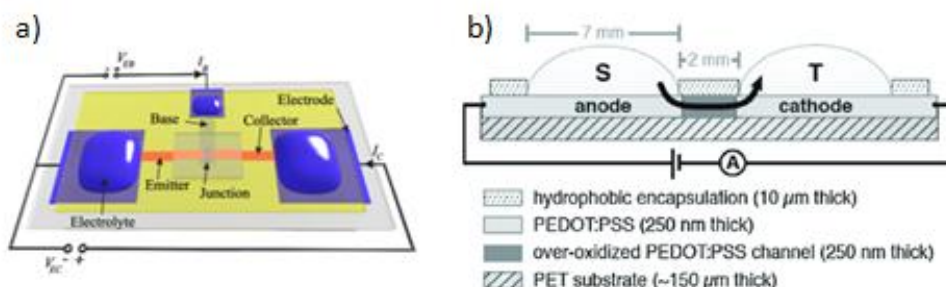


Figure 24: device structures of a) ion bipolar junction transistors (IBJT_s); b) organic electronic ion pumps (OEIP_s)

In particular, ion pumps were successfully used in vitro, in vivo and in plantae with few examples reported in Figure 25.⁴⁸

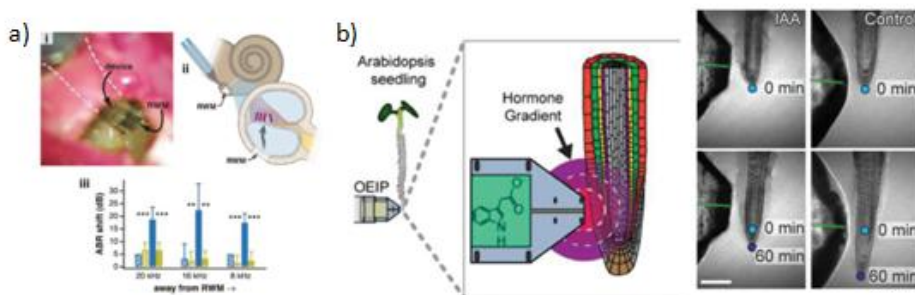


Figure 25: Application of ionotronic devices: a) affecting auditory response in guinea pigs in vivo; b) Regulation of growth rate in plants by controlled delivery of a plant hormone gradient

With its electronic rose prof. Berggren demonstrates for the first time the integration of a plant's "circuitry" with electronics and how this can lead to a selective control of plant physiology (Figure 26).⁴⁹



Figure 26: Electronic rose, plant integrated device for physiology regulation, energy harvesting from photosynthesis, and plant optimization beyond genetic modifications.

In this scenario is set my work that has been aimed at the design of a "green" OLED device.

In particular I focused the attention on four main components of the device:

1) the substrate; 2) the anode; 3) the emitting layer; 4) the encapsulating layer (Figure 27).

The research activity has been reported in the following four sections:

SECTION 1- processing techniques for the fabrication of ITO-free substrate based on the standard PEN and the biodegradable PLA for flexible OLED devices;

SECTION 2- synthesis and electrical properties of eumelanin thin films: towards the design of polymeric anode for ITO-free devices;

SECTION 3- synthesis of nature-inspired electroluminescent materials for OLED applications;

SECTION 4- synthesis and processing techniques of biocompatible and low cost materials for encapsulating layers in OLED devices.

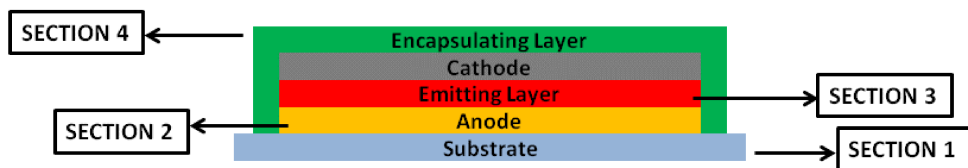


Figure 27: OLED device structure and thesis sections

REFERENCES

- ¹ E.D. William et al, *IEEE Int. Symp. Electr. Environ.*, 2004, 0-7803-8250-1/04
- ² B.C.J. Zoeteman et al, *Int. J. Adv. Manuf. Technol.*, 2010, 47, 415-436
- ³ H. Letheby, *J. Chem. Soc.*, 1862, 15, 161–163
- ⁴ H. Akamatu et al, *Nature*, 1954, 173, 168
- ⁵ H. Shirakawa et al, *J.C.S. CHEM. COMM.*, 1977, 16, 578
- ⁶ Dall'olio et al, *CR Acad. Sci. Paris*, 1968, 267, 433–435
- ⁷ A.C. Arias et al, *Chem. Rev.*, 2010, 110, 3-24
- ⁸ M. Berggren et al, *Nature Materials*, 2007, 6, 3-5
- ⁹ J. Rivnay et al, *Chem. Mater.*, 2014, 26, 679-685
- ¹⁰ D. Wöhrle et al, *Adv. Mater.*, 1991, 3, 129-138
- ¹¹ Q. L. Song et al, *Appl. Phys. Lett.*, 2006, 89, 251118
- ¹² G. Horowitz, *Adv. Mater.*, 1998, 10, 365-377
- ¹³ J.E. Lilienfeld, *US 1745175* (1930) "Method and apparatus for controlling electric currents"
- ¹⁴ J. Atalla and D. Kahnq, *US 3102320* (1963) "Metal Oxide Semiconductor (MOS) Transistor"
- ¹⁵ H. Koezuka et al, *Synthetic Metals*, 1987, 18, 699-704
- ¹⁶ A. Bernanose et al, *J. Chim. Phys.*, 1953, 50: 64
- ¹⁷ S. A. Carter et al, *Appl. Phys. Lett.*, 1997, 70, 2067-2069
- ¹⁸ T.-C. Li et al, *Int. Journal of Precision Engineering and manufacturing-Green Technology*, 2014, 1, 4, 329-334
- ¹⁹ Y. Karzazi, *J. Mater. Environ. Sci.*, 2014, 5, 1-12
- ²⁰ A. Uniyal et al, "Improvement in Performance of OLED by introducing additional hole blocking layer", 2017, Springer Singapore
- ²¹ C. Murawski et al, *MRS Proceedings*, 2012, 1402
- ²² R.H. Friend et al, *Nature*, 1999, 397, 121
- ²³ Z.D. Popovic et al, *Journal on Selected Topics in Quantum Electronics*, 2002, 8
- ²⁴ J.H. Burroughes et al, *Nature*, 1990, 347, 539-541
- ²⁵ R.C. Evans et al, *Coord. Chem. Rev.*, 2006, 250, 2093-2126
- ²⁶ H. Yersin, *Top. Curr. Chem.*, 2004, 241, 1-26
- ²⁷ H. Yersin et al, *Coordination Chemistry Reviews*, 2011, 255, 2622– 2652
- ²⁸ E. Holder et al, *Adv. Mater.*, 2005, 17, 1109
- ²⁹ X. Yang et al, *Wiley-VCH: Weinheim*, 2006, 333
- ³⁰ M.M. Ling et al, *Chem. Mater.*, 2004, 16, 4824-4840
- ³¹ L. F. Thompson et al, *Introduction to Microlithography*, 2nd ed.; American Chemical Society: Washington, DC, 1994
- ³² C. Bartic et al, *Org. Electron.*, 2002, 3, 65-72

- ³³ Z. Bao et al, *J. Mater. Chem.*, 1999, 9, 1895-1904
- ³⁴ M. Irimia-Vladu, *Chem. Soc. Rev.*, 2014, 43, 588-610
- ³⁵ M. M. Pérez-Madrigal et al, *Green Chemistry*, 2016, 18, 5930-5956
- ³⁶ Y. Z. Zhang et al, *Chemical Society reviews*, 2015, 44, 5181-5199
- ³⁷ J. Edberg et al, *J. of Mat. Chem. A.*, 2018, 6(1), 145-152
- ³⁸ D. H. Kim et al, *Science*, 2011, 333, 838-843
- ³⁹ C. J. Bettinger et al, *Adv. Mater.*, 2010, 22, 651-655
- ⁴⁰ E. Delivopoulos et al, *Lab Chip*, 2012, 12, 2540-2551
- ⁴¹ H. Tao et al, *Adv. Mater.*, 2012, 24, 1067-1072
- ⁴² S. R. Cicco et al, *Bioengineering*, 2016, 3, 35
- ⁴³ T. Holtus et al, *Nature Chemistry*, 2018, 10, 740-745
- ⁴⁴ M. Magliulo et al, *Adv. Mater.*, 2013, 25, 2090-2094
- ⁴⁵ D. Khodagholy et al, *Nat. Commun.*, 2013, 4, 575
- ⁴⁶ C. Zhong et al, *Nat. Commun.*, 2011, 2, 476
- ⁴⁷ K. Tybrandt et al, *Nat. Commun.*, 2012, 3, 871
- ⁴⁸ T. A. Sjöström et al. *Adv. Mater. Technol.*, 2018, 1700360
- ⁴⁹ E. Stavrinidou et al, *Sci. Adv.*, 2015, 1, e1501136

SECTION 1

PROCESSING TECHNIQUES FOR THE FABRICATION OF ITO-FREE SUBSTRATES BASED ON THE STANDARD PEN AND THE BIODEGRADABLE PLA FOR FLEXIBLE OLED DEVICES

~INTRODUCTION~

OLED based on glass substrates have been improved to achieve commercial application standard in terms of lifetime (longer than 200 khr)¹ and efficacies (larger than 100 lm/W).² Flexible electronic devices are desired in order to realize cheaper, lightweight, portable and wearable applications such as displays, lighting and sensors. With the interest in flexible electronics, roll to roll manufacturing processes are becoming accessible.

The prospects for flexible devices are very promising but still some technical issues need to be overcome for the future commercialization. The individuation of all the device components and their suitability for flexible devices are the main topics.

Polymers, thanks to their transparency, lightness, flexibility and robustness are the perfect candidates for the design of flexible devices, from transparent substrates to active materials, coating materials, etc.

Among materials for flexible substrate we can find: thin glass, metal foils and plastics.

Thin glass is at the same time bendable, resistant to temperatures and chemical agents and it shows low roughness. All these characteristics make thin glass a good candidate for the realization of flexible electronic devices, but unfortunately it is extremely brittle.

Metal foils are flexible, resistant to temperatures and various solvents and not easily breakable, but they can be used only for application in which transparency is not required; they are also expensive. Low cost plastics are the key materials thanks to their mechanical, optical and chemical properties.

According to the glass transition temperature, plastic substrates for electronic devices can be divided into three classes: semi-crystalline polymers (PET, PEN and

PEEK), amorphous thermoplastic polymers (PC and PES) and amorphous polymers that cannot be melted (PAR, PCO, PI).

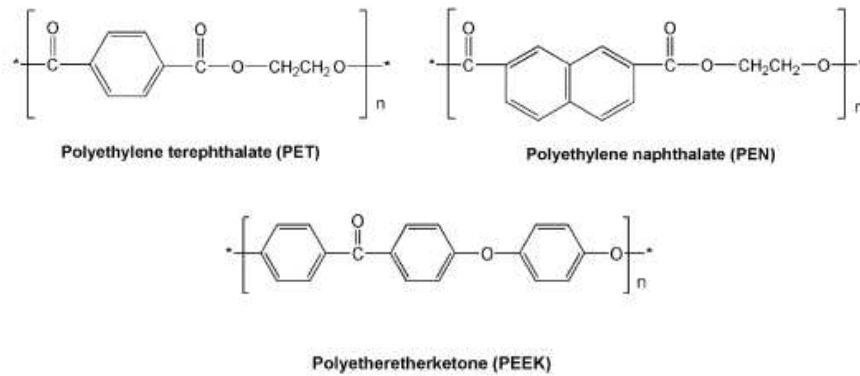


Figure 1: PET, PEN and PEEK structures

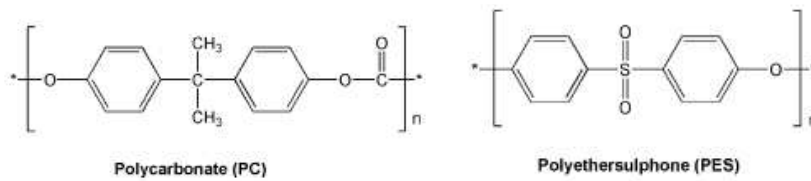


Figure 2: PC and PES structures

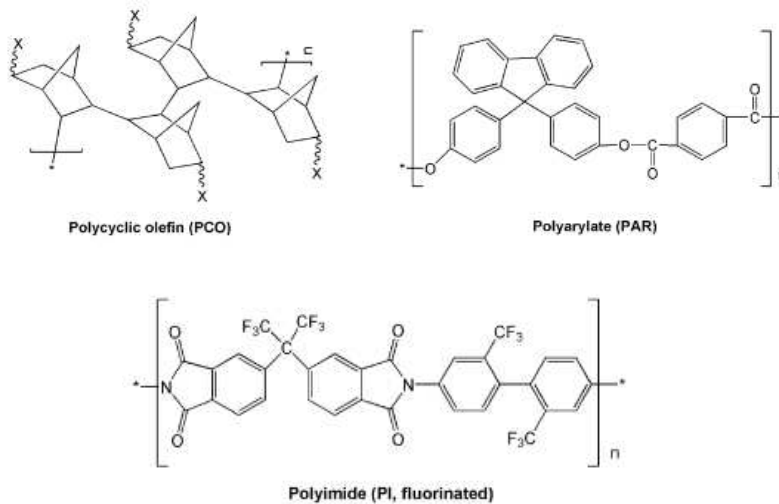


Figure 3: PCO, PAR and PI structures

The perfect plastic substrate for electronic devices should mimic the glass properties such as, transparency, dimensional and thermal stability, barrier properties, chemical resistance, low coefficient of thermal expansion and smooth surface.

In Table 1 is reported a classification of the principal plastic substrates according to the quality criteria just mentioned.³

Table 1: Comparison of polymer materials for flexible substrates

	PET	PEN	PC	PAR	PES	PI
Optical clarity	○	○	●	○	○	X
Upper operating temperature	△	○	△	●	○	●
Dimensional stability	○	○	△	△	△	○
Surface roughness	X	X	○	○	○	○
Solvent resistance	○	○	X	X	X	○
Moisture absorption	○	○	△	△	X	X
Young's modulus	○	○	△	△	△	△

●:Excellent ○:Good △:Fair X:Poor

As you can see, PET and PEN show good transparency, dimensional stability, solvent resistance, moisture absorption and low price, while the upper operating temperature represent a limit especially for PET. The surface roughness of PET and PEN is another problem for applications in electronic devices.

PES has good optical transparency and high operating temperature, but the low resistance to solvent and the price are the two main disadvantages.

PI shows the best thermal stability and mechanical and chemical properties. On the other hand, PI is usually orange-colored but some chemical modification can

give a colorless material. The price of PI remains a problem for its large volume of applications.

Nowadays, PEN represents the most used plastic substrate for flexible circuits and devices,⁴ despite the surface features. PEN belongs to the family of aromatic polyester, the presence of two condensed aromatic rings in the main chain gives it a series of advantages with respect to the well known PET. PEN shows improved mechanical and barrier properties and a better resistance to chemical agents, temperature and UV light with respect to PET.

PET and PEN, as other petrochemical based polymers, show good mechanical and chemical properties and they can be produced with fast and relatively low cost processes. On the other hand synthetic polymers show different disadvantages: reduction of the oil and gas resources, increase of the oil and gas prices, environmental concerns due to their degradation or disposal, recycling costs and toxicity risks. Recycling and disposal issues need to be negligible for biodegradable and biocompatible materials.

Biodegradable and biocompatible materials exist as natural occurring or synthetic materials and some aliphatic polyesters show these properties⁵ (i.e. PLA (polylactic acid)).

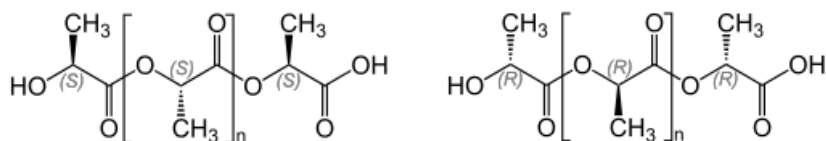


Figure 4: Poly(L-lactic acid) and Poly(D-lactice acid) structures

PLA is a thermoplastic biopolymer derived from renewable resources, such as corn starch, cassava roots, chips or starch, or sugarcane. The polymer derives from the polymerization of the lactide acid unit; since such building block is a chiral compound, several distinct forms of PLA exist. PLLA is the product resulting from

polymerization of L,L-lactide. It has a glass transition temperature around 60-65°C and a melting temperature of 160-180°C. It is soluble in chlorinated solvents, hot benzene, THF and dioxane. It can be processed like most thermoplastic materials into fibers and films. PLA has mechanical properties similar to PET, but has a significantly lower resistance to temperature.⁶ The melting temperature of PLLA can be increased by 40-50°C by physically blending the polymer with PDLA.⁷ PDLA and PLLA form a highly regular stereocomplex with increased crystallinity. The temperature stability is maximized when a 1:1 blend is used, but even at lower concentration of PDLA (3-10%), there is still a substantial improvement. In this case PDLA acts as nucleating agent.

The biodegradation of PDLA is slower than PLLA due to the higher crystallinity. Considering all the mentioned characteristics, PLA is a promising alternative as a “green” polymer for application in bioelectronic devices.

An important step toward the realization of a flexible device is the individuation of the electrode materials. High transparency and low sheet resistance are the two most desirable characteristics for a transparent conductive film. As previously discussed, ITO is a commonly used transparent conducting electrode having high transmittance and low sheet resistance. Unfortunately, such material is extremely brittle and this characteristic represents a problem of compatibility with flexible substrates; fractures of the anode can occur which can increase the sheet resistance of the ITO or disrupt the layer and the OLED structure.⁸

Some studies were carried out to study the effect of the bending process on OLED devices realized with ITO and good results were reported with preservation of about the 90% of the original efficiency.⁹

Nevertheless, other materials proved suitable as anode for flexible applications representing also a green alternative to ITO, since the ITO price is not negligible (US\$ 800/kg) and indium is a scarce nonrenewable resource.

Transparent conducting oxides, conducting polymers, metal nanowires and graphene have been explored as alternative to ITO.¹⁰

Binary compounds of transparent conducting oxides (TCOs) are usually doped to improve the electrical conductivity. CdO, SnO₂ and ZnO based transparent conducting oxides have shown interesting properties, but exhibited also some problems¹¹. Cadmium is a toxic element, SnO₂ derivatives showed limited success in real application and in all cases the brittleness remains an obstacle for their use in flexible devices.

Metal nanowires and graphene are other two candidates for ITO substitution, but they are too expensive and not suitable for the market.

Now, conducting polymers represent the only convenient alternative to ITO for mass and flexible devices fabrication. Conducting polymers are light in weight, flexible and show excellent compatibility with plastic substrates.

Polyaniline (PANI),¹² polypyrrole (PPY)¹³ and poly(3,4-ethylenedioxythiophene):poly(4-styrenesulfonate) (PEDOT:PSS)¹⁴ are the three most important conducting polymers.

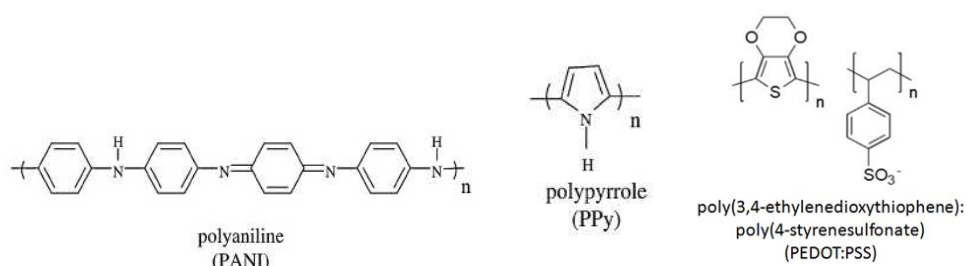


Figure 5: PANI, PPY and PEDOT:PSS structures

Among these, PEDOT:PSS is actually the most used conducting polymer for flexible optoelectronic device fabrication, thanks to its conductivity, transparency and ductility.¹⁵

PEDOT:PSS dispersions for solution processing are commercially available and they are composed by gel-like particles comprising a polyanion (PSS⁻)-rich shell which helps to stabilize the PEDOT-enriched particles in aqueous solvents.^{16,17}

PEDOT:PSS structure has been intensely studied by a variety of techniques including electron microscopy, X-ray scattering, elemental and surface-sensitive scanning probes,^{18,19,20,21} largely with the goal of understanding and enhancing hole transport to make better electrodes for optoelectronic devices. Changes in formulation content, processing or post-processing have led to enhancements in hole conductivity, by inducing morphological re-arrangements, minimizing excess dopant phase (insulating PSS) or both.

Physical treatments, like temperature and light, can improve conductivity of PEDOT:PSS. Organic compound and high boiling solvents like methylpyrrolidone, dimethyl sulfoxide (DMSO), sorbitol, ionic liquids and surfactants can be added or used in post-treatment phases to improve conductivity of many order of magnitude.²²

- AIMS

Starting from this background, flexible ITO-free OLED devices were realized.

Gravure printing was used as high throughput technique for the realization of a conductive PEDOT:PSS layer on a PEN substrate. The suitability of the anode/substrate selected were tested by analyzing the performances of the OLED device.

In a second set of experiments, ITO-free flexible OLED devices were realized for the first time on the biodegradable substrate PLA.

~RESULTS AND DISCUSSION~

○ GRAVURE PRINTED PEDOT:PSS AS ANODE FOR FLEXIBLE ITO-FREE ORGANIC LIGHT EMITTING DIODE

Here is reported about the realization of an high conductive (HC) PEDOT:PSS layer and subsequent DMSO post treatment completely by gravure printing technique for application as anode in flexible OLED devices.

Highly conductive PEDOT:PSS was obtained by adding DMSO (5% v/v) to the commercial Clevios PH1000 solution, as also suggested by the supplier.²³ Solution was diluted with isopropyl alcohol in order to test the effects of the ink concentration on the resulting PEDOT:PSS layer. A multilayer approach was also used as further improvement of the anode layer characteristics. By this way we obtained an increase of the conductivity of the HC PEDOT:PSS layer thanks to the decrease of the sheet resistance with increasing the number of the overlapped layers, keeping high transparency.

Multilayer deposition of inks at decreasing concentration gives the best result; in fact the increase in the solvent content of the consecutive printed layers allowed to achieve values of conductivity higher than the multilayer printed at the same ink concentration.²⁴ The multilayer approach allows a better spreading of the material in the successive printed layers and a smoothing effect of the previous printer layers; just three layers successively printed with a decreasing concentration profile are sufficient to realize a conductive layer suitable for applications as electrode.

Polyethylene naphthalate (PEN) was selected as flexible substrate for the realization of the printed anode layer. PEN is, infact, one of the most promising substrate for flexible electronic thanks to its physical-chemical properties.

Furthermore, It is an interesting material from an environmental point of view since it can be easily reused and recycled.

In Table 2 the characteristics of the printed anodes on a PEN substrate are showed and compared with the ones of the anode obtained by spin coating.

Table 2: Anode characteristics on PEN substrates

Anode preparation technique	Thickness [nm]	Sheet resistance [Ω/sq]	Conductivity [S/cm]	Surface roughness [nm]
Spin coating	162 \pm 8	137 \pm 8	451	11 \pm 1
Multilayer gravure printing	157 \pm 10	146 \pm 10	436	21 \pm 3
Multilayer gravure printing + DMSO post treatment	151 \pm 6	125 \pm 5	530	18 \pm 2

In Figure 6 the transparency of the layers is proved by UV transmittance measurements. The properties of the printed and spin coated layers are quite similar, despite the great differences between the fabrication techniques; the gravure printing is in fact discontinuous being applied through a multi-step process and it is intrinsically less uniform than the spin coating. This demonstrated the possibility to obtain layers by gravure printing of comparable quality to the widely used spin coating technique. The use of the printing technique in all these applications may be an advantage for industrially scalable processes. As expected, the roughness of the gravure printed anodes is higher than the one of the spin coated layers, mainly due to the overlapping process.

To further improve the characteristics of the gravure printed anode, a solvent printing post treatment was tested. As reported in the introduction, post treatment of the HC PEDOT:PSS layer with DMSO leads to an improvement of the overall conductivity of the layer, thanks to the removal of the insulating PSS

components promoting the connection among the conducting PEDOT grains^{25,26,27}. Here, DMSO post treatment was carried out by gravure printing in order to realize a complete process with a single technique.

As expected, the post-treatment was found to increase the conductivity (plus 20%) of the printed layer; the effect of the solvent post-treatment causes also a slightly smoothing effect on the surface roughness of the pre-printed layer and an increase in its uniformity (see Table 2).

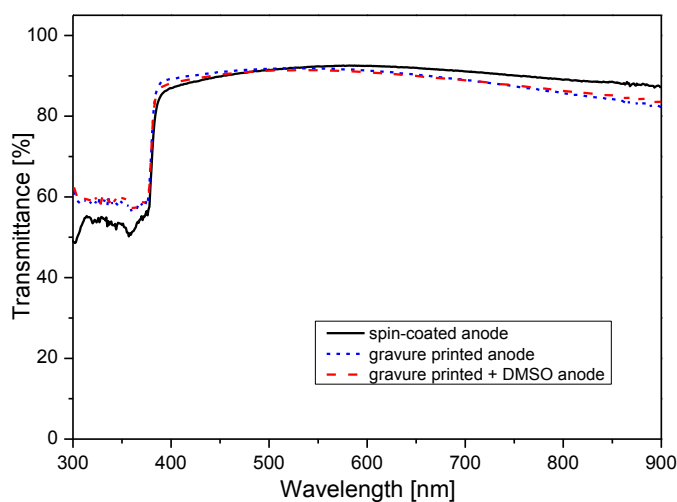


Figure 6: UV transmittance measurements of the spin coated and gravure printed layers on the PEN substrate

SEM analysis confirms an increase of the quantity of the PEDOT grains and a higher uniformity of the grain size in the printed sample treated with DMSO (Figure 7c) with respect to the untreated one (Figure 7b). A low homogeneous distribution of the domains with very different size is detectable in the gravure printed sample, while the post treated sample shows an uniformity in the PEDOT domains similar to the spin coated sample.

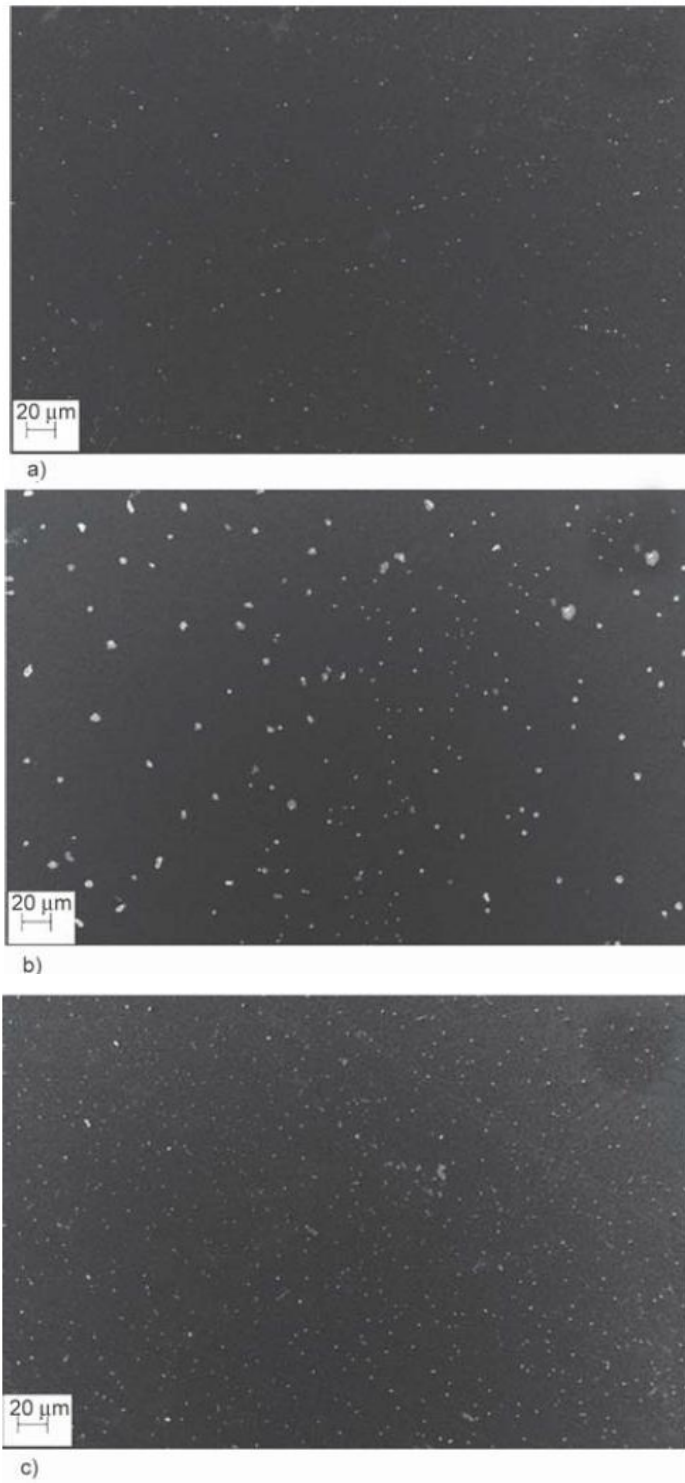


Figure 7: SEM images of the spin coated (a), gravure printed (b) and gravure printed with DMSO post-treatment (c) HC PEDOT:PSS

The HC PEDOT:PSS layer on PEN was tested in OLEDs with the following structure: PEN/HC PEDOT:PSS/Emitting polymer/Ca/Ag.

The current density vs voltage (J - V) curves and the luminance vs voltage characteristics are reported in Figure 8 and fFigure 9. As expected, the performances of the OLEDs with the gravure printed and the spin coated anodes are similar, since the characteristics of their electrodes are similar. Considering the obtained luminance values, it does not appear possible to detect significant differences in the behavior of the anodes in the devices. Anyway, the slightly observed differences can be related to the differences in the anodes and devices fabrication.

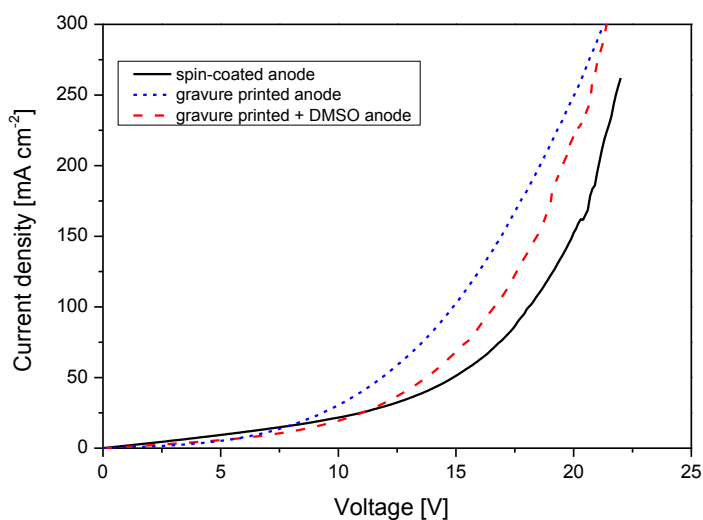


Figure 8: J - V curves of the flexible OLED devices

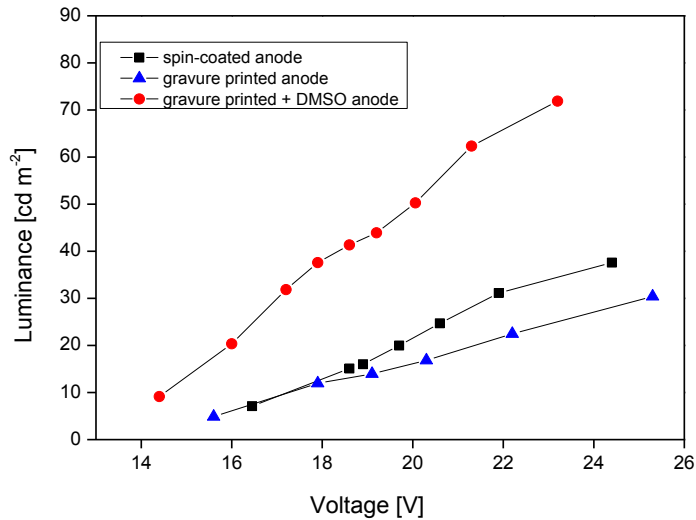


Figure 9: L-V curves of the flexible OLED devices

○ PLA SUBSTRATES FOR ITO-FREE FLEXIBLE OLED DEVICES

In this work the potential of PLA as innovative and biodegradable flexible substrate in ITO-free OLED devices was tested.

PLA films were realized by hot press (PLAhp) and extrusion (PLAex) processes and were characterized to test the suitability as substrate for OLED devices. For the realization of ITO-free OLED devices, the commercial Clevious PH1000 aqueous solution was used to deposit a PEDOT:PSS film as anode. The wettability of the substrate is an important parameter to deposit the PEDOT:PSS solution and to obtain a layer with a good quality. Oxygen plasma treatment was applied in order to optimize the surface wettability of the PLA films. Different combinations of oxygen flow rate, treatment time and plasma power were tested and the optimal combination (10 sccm, 30', 15 W) was selected. The water contact angles (WCA) before and after the plasma treatment are reported in Figure 10.

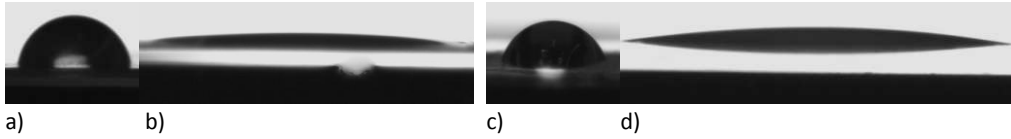


Figure 10: WCA of PLAhp film before (86°, a) and after (18°, b) O₂ plasma; WCA of PLAex film before (80°, c) and after (20°, d) O₂ plasma.

In order to assess how the plasma treatment modify the optical transmission of the PLA substrate, transmission spectra together with reflectance and diffusion spectra, before and after the plasma treatment, were registered (Figure 11).

The plasma treatment do not compromise the transmittance (transparency) of the substrate but it involves a slight increase in diffused and reflected light.

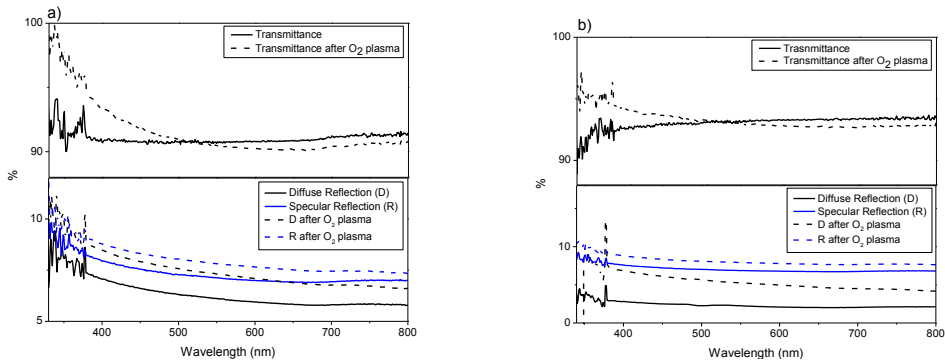


Figure 11: Optical characteristics of PLAhp before and after O₂ plasma treatment (a) and PLAex before and after O₂ plasma treatment (b).

The PLAhp films show always a lower transmittance value than the PLAex (before and after the plasma treatment), imputable to a higher crystalline degree of the PLAhp. Such hypothesis is confirmed by the differential scanning calorimetry of the two substrates (Figure 12). No relevant differences are found between PLAhp and PLAex for what concerns the glass transition (T_g) as shown in Table 3, while an increase of about 13°C of the melting temperature (T_m) is observed for PLAhp, confirming the higher crystallinity.

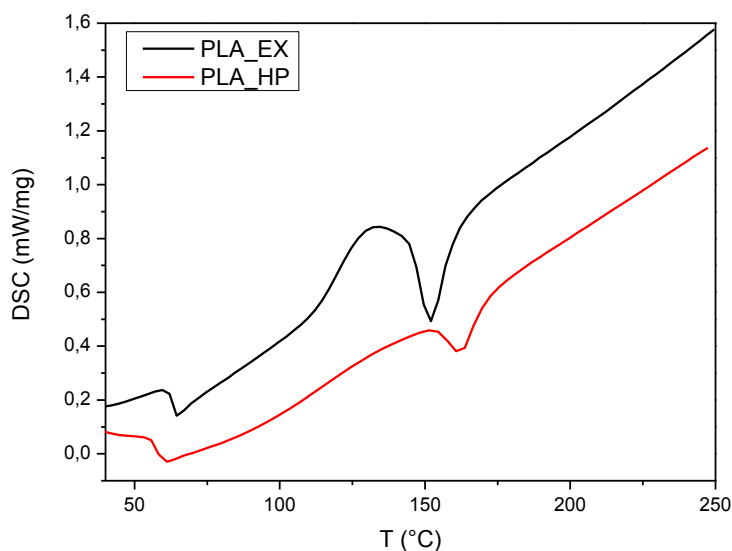


Figure 12: DSC curves of PLAhp and PLAex

Table 3: DSC data of PLAhp and PLAex

	Tg (°C)	Tm (°C)	Area (J/g)
PLAhp	59.2	162.5	-9.57
PLAex	62.0	152.0	-25.29

HC PEDOT:PSS layers were obtained by adding DMSO (5% v/v) to the commercial Clevious PH1000 solution and by spin coating such solution on the plasma treated PLA substrates followed by annealing overnight at 45°C. The sheet resistance of the two anodes was measured (Table 4). Unfortunately, due to the high roughness of the PLA substrates, it wasn't possible to obtain an accurate measure of the thickness of the anode necessary to calculate the conductivity value of the layer. By assuming that the thickness of PEDOT:PSS on PLA is similar to that on PEN it has been possible to measure a thickness (135 nm) and to estimate a conductivity

value. Despite the extremely low temperature used in the annealing phase of the PEDOT:PSS, a good conductivity was observed for both substrates.

Table 4: Anode characteristics on PLA substrates

Anode preparation technique	Sheet resistance [Ω/sq]	Conductivity [S/cm]
PLAht	108 ± 6	686
PLAex	115 ± 5	644

Transmittance spectra of the anode layers are reported in Figure 13 and they are compared with the transmittance of the neat substrates.

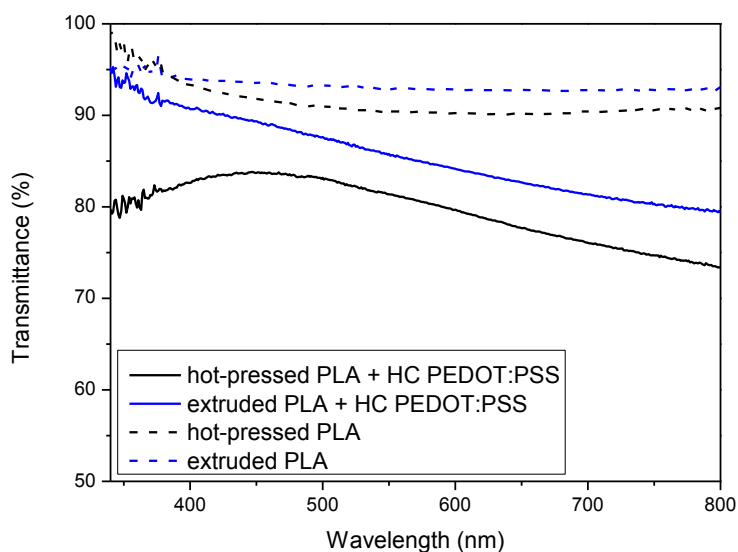


Figure 13: Transmittance spectra of anode on PLA films

To test the performances of the anode layer on PLA substrates, OLED devices with the following configurations were selected: *HC PEDOT:PSS/White Emitting Polymer/Ca/Ag* and *HC PEDOT:PSS/HIL/White Emitting Polymer/Ca/Ag*.

The HIL layer based on a commercial solution of PEDOT:PSS was realized both by dip coating and by spin coating. The dip coating process was performed after the thermal annealing of the anode layer, viceversa the spin coating process of the HIL was performed after 2-5 minutes from the anode deposition (Table 5). The water content in the HC PEDOT:PSS layer is able to improve the wettability and to facilitate the HIL deposition to obtain a layer with higher quality (wet-on-wet technique). An overnight annealing treatment at 45°C was carried out after the HIL deposition.

Table 5: HIL deposition parameters

	Deposition parameters
Dip coating	Dip speed: 5000 $\mu\text{m/s}$ Dip duration: 2s Extraction speed: 2000 $\mu\text{m/s}$ Waiting time: 15 s (before the subsequent dip) Number of dip cycle: 5
Spin coating 1	500 rpm x 500 rpm/s x 30s
Spin coating 2	1000 rpm x 500 rpm/s x 30s

The electroluminescent polymer was also deposited by spin coating from a toluene solution and the multilayer structure HC PEDOT:PSS/HIL/emitting polymer was annealed overnight at 45°C.

The cathode layer was finally deposited by vacuum thermal evaporation.

In Table 6 are summarized all the devices.

Table 6: Devices

Device	PLA	HIL deposition
1a	Hot-pressed	≡
1b	Hot-pressed	Dip-coating
2a	Extruded	≡

2b	Extruded	Dip-coating
1c	Hot-pressed	Spin coating (500 rpm)
1d	Hot-pressed	Spin coating (1000 rpm)

The characteristics of the OLED devices are reported in figures Figure 14-Figure 16. Only the devices fabricated by using the dip-coated HIL layer exhibited light emission. In both cases, the J - V curves of the devices without HIL show higher current densities. The J - V curve of the device 1b shows higher current density with respect to the device 2b, with the light emission for the device 1b occurring at lower voltage values.

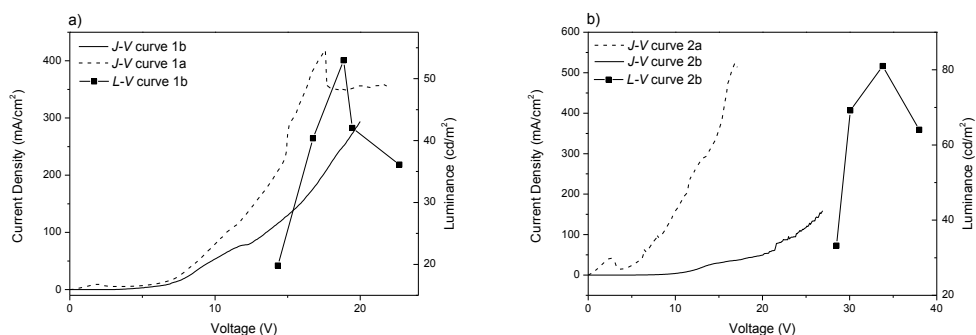


Figure 14: J - V and L - V curves of 1a and 1b devices (a), and of 2a and 2b devices (b).

From the electroluminescence spectra of the 1b and 2b devices is also possible to observe an higher voltage values, a deterioration process of the emitting materials and a modification of the spectrum shape with a shift of the CIE coordinates.

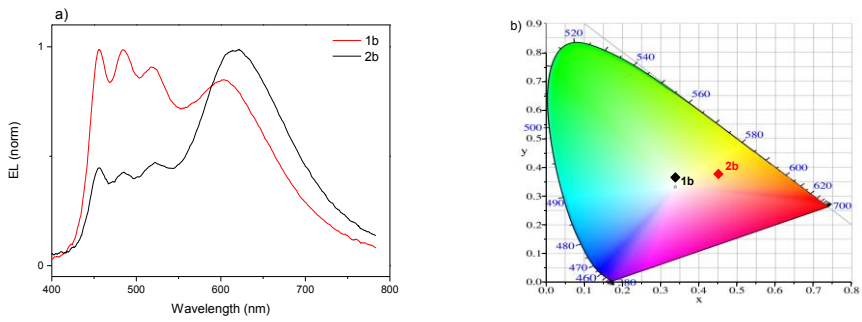


Figure 15: a) Electroluminescence spectra of 1b and 2b devices; b) CIE coordinates of 1b and 2b devices

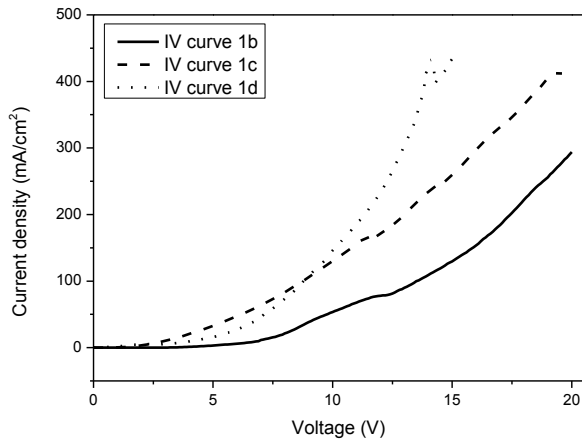


Figure 16: J-V curves of 1b, 1c and 1d devices

To deeply understand the observed electro-optical behavior of the realized devices, a morphological analysis of the different layers was carried out by AFM analysis.

The analysis of both PLA substrates after oxygen plasma treatment show a granular surface with an average grain size of 35 nm and an R_q of 12.5 nm.

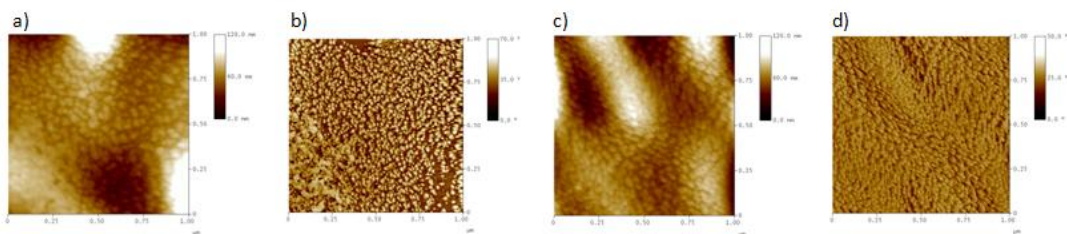


Figure 17: AFM topographical and phase-contrast images of hot pressed PLA film (a)(b) and extruded PLA film (c)(d)

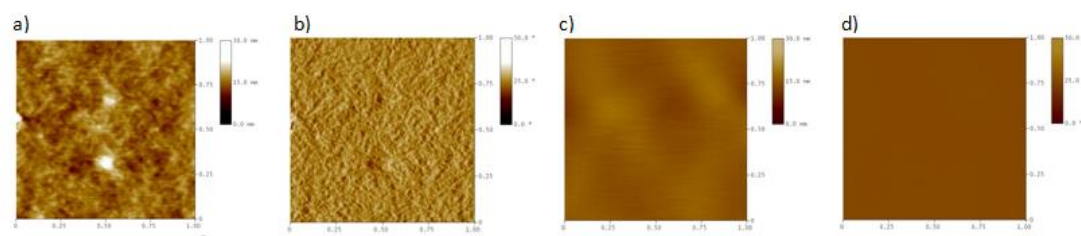


Figure 18: AFM topographical and phase-contrast images of hot pressed PLA/HC PEDOT:PSS ($R_q \sim 2\text{nm}$) (a)(b) and extruded PLA/HC PEDOT:PSS ($R_q \sim 0.9\text{nm}$) (c)(d)

After the deposition of the HC PEDOT:PSS layer, it is possible to observe a change in the surface morphology with a reduction of the surface roughness and an homogenizing effect (Figure 18). Nevertheless, the HC PEDOT:PSS layer shows poor compactness and adhesion to the extruded PLA substrate.

Finally, AFM analysis was carried out also after deposition of the HIL layer. When the HIL layer has been deposited by dip coating, the surface is flat and homogeneous. On the other hand, samples realized by wet-on-wet deposition techniques denoted highly irregular morphology with the formation of aggregates of different shape and size. Although macroscopically the deposition proves to be of good quality, probably the lack of the drying process of the underlying layer leads to dramatic consequences on the microscopic quality of the film.

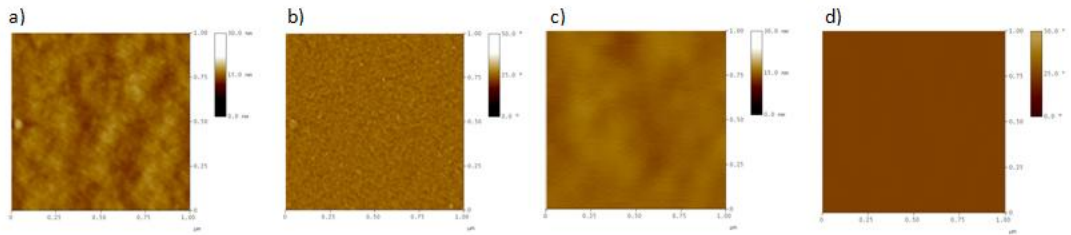


Figure 19: AFM topographical and phase-contrast images of hot pressed PLA/HC/HIL (dip) ($R_q \sim 0.9\text{nm}$) (a)(b) and extruded PLA/HC/HIL (dip) ($R_q \sim 0.6\text{nm}$) (c)(d)

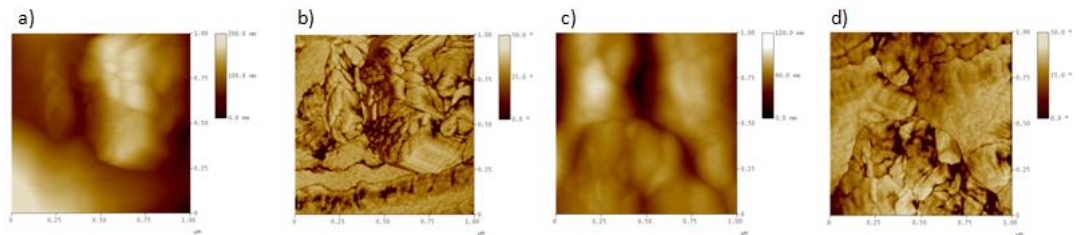


Figure 20: AFM topographical and phase-contrast images of hot pressed PLA/HC/HIL (spin 500 rpm) (a)(b) and pressed PLA/HC/HIL (spin 1000 rpm) (c)(d)

As expected it is possible to conclude that the morphology characteristics affect the device performances.

The good adhesion and low roughness of the HC/HIL(dip) bilayer on the PLAhp explain the good performances observed in the device 1b.

The low adhesion of the HC layer on the PLAex substrate and the low homogeneity of the HC/HIL(spin) layers on the PLAhp are the causes of the low performances observed in the devices 2b, 1c and 1d.

~CONCLUSIONS~

This section reports on the realization of flexible ITO-free OLED devices.

In the first part a multilayer gravure printed HC PEDOT:PSS was realized with increasingly dilution profile stacking and it was used as anode for OLEDs fabrication, expanding the possibilities for future developments of optoelectronic devices, partly or entirely, industrially produced by gravure printing. The obtained performances, relatively poor if compared to typical ITO and glass based OLEDs, are therefore largely rewarded by the demonstrated opportunity for processing flexible ITO-free devices using the most attractive printing technology for roll-to-roll large area manufacturing.²⁸

In the second part, a biodegradable PLA substrate was characterized and tested as innovative and green alternative to classic polyester substrates for OLED applications. PLA is very sensitive to high temperatures and to many common organic solvents, nevertheless the possibility to use a biodegradable plastic material as substrate for electronic devices has been proven.

~EXPERIMENTAL SECTION~

○ MATERIALS AND METHODS

Polyethylene naphthalate (PEN) (Teonex® Q65FA) substrate was purchased from DuPont Teijin Films provided in A4 sheet, having a thickness of 125 μm .

PLA (Ingeo™ Biopolymer 4043D) was supplied as pellets by NatureWorks LLC.

PEDOT:PSS PH1000 and PVP Al 4083 (HIL) were purchased from HeraeusClevios.

The electroluminescent polymer (Livlux SPW 111) was purchased from Merck.

Oxygen Plasma treatments have been carried out with the Tucano RIE (Gambetti).

An OCA20 (Dataphysics) system was used for the contact angle measurements.

The thickness and surface roughness of the coated/ printed layers were investigated by interferometry based optical profilometer (Talysurf CCI HD, Taylor Hobson, Leicester, UK). The root mean square surface roughness was obtained according to the ISO 25178 standard; the reported values are the average results of the measurements made.

DSC measurements have been carried out by using a DSC/TGA Jupiter STA449F3 instrument (Netzsch).

The electrical conductivity of the anodes was evaluated by sheets resistance measurements performed by a four points probe instrument (Resistest RT 8A coupled with Resistage RG 8, Napson, Tokyo, Japan) applying a current of 1 μA and the reported values are the average results of the measurements made.

The produced films were also characterized by performing UV-visible transmission measurements (Lambda 900, Perkin Elmer, Waltham MA, USA) and by scanning electron microscopy (1530, LEO Elektronenmikroskopie GmbH, Oberkochen, Germany), respectively.

The surface morphology of the films has been analyzed by atomic force microscopy (AFM) measurements carried out in tapping mode by the Veeco Dimension Digital Instruments Nanoscope IV system.

Electrical and optical characteristics of the devices were measured using respectively a sourcemeter (Keithley 2400, Tektronix, Beaverton OR, USA) and spectroradiometer (OL770, Gooch&Housego, Ilminster Somerset, UK) coupled with an integrating sphere.

Some devices (4-5 per type) were tested to verify the reproducibility of the results and the reported data are related to the best results obtained.

○ PLA FILM PREPARATION

Films from the PLA polymer were obtained by molding the pellets, previously dried at 40°C overnight, in a Carver Laboratory Press, between two PTFE sheets and holding them at 180°C for 10 min to destroy any memory of previous processing. The molded materials were rapidly quenched into an ice-water bath at 0 °C. About 100 µm thick films were obtained and named PLAhp.

PLA pellets were dried at 80 °C for 4 h before the extrusion process. PLA film extrusion was performed in a HAAKE Rheomex 19/25 QC single screw extruder with a PolyLab QC drive unit and chill roll system, using a screw speed of 30 rpm, and with a temperature of the water entering the chill roll of 40 °C. During the PLA film extrusion the temperature was 180 °C in the feeding zone and in the die. The lip of the sheet die and speed of the chill roll system were arranged to obtain an average thickness of the film of about 100 µm (PLAex).

○ DEVICE FABRICATION

About devices realized on PEN substrates, all the inks were realized and gravure printed or spin coated in air at room temperature. The inks to realize the anode

were prepared using a commercially available aqueous PEDOT:PSS dispersion and the dimethylsulfoxide (DMSO) was added (5% by volume) in order to enhance its conductivity, this pristine solution, suitable for spin-coating deposition, was diluted by 1,2-isopropyl alcohol (IPA) in different weight ratios to decrease the viscosity and the surface tension, obtaining inks gravure printable without the use of any substrate pre-treatment. The reference anodic layers were obtained spin coating the pristine solution at 800 rpm for 60 sec on PEN treated with UV-ozone to improve the wettability. The films were subsequently annealed at 140 °C for all night.

The employed gravure was a lab-scale printer (G1-5, IGT, Amsterdam, The Netherlands) equipped with a cylinder having line density of 40 lines/cm, stylus angle of 120°, cell depth of 72 µm and screen angle of 53°. The diluted inks were gravure printed using a printing force of 1000 N at a speed of 60 m/min. The multilayer structure was obtained by drying each layer at 140°C for 5 min before printing the next one.

In order to further improve the conductivity of the printed layer, in some cases, a post-treatment was performed by gravure printing DMSO solvent on the printed anode, before the final annealing, using a printing force of 500 N at a speed of 12 m/min; the layer was then annealed at the same process temperature after a slow solvent evaporation (70°C for 5 min). Concerning the devices preparation, the active layer was obtained through spin coating a solution containing 10 mg/mL of a commercial white emitting polymer in toluene at 3000 rpm for all the prepared devices. The active layers had a thickness of ≈100 nm as measured by profilometer. The Ca/Ag cathode (20 and 80 nm respectively) was deposited by thermal evaporation in ultra-high vacuum (10^{-7} mbar) using a shadow mask to define the active area of the device (0.07 cm²).

About devices on PLA substrates, anode layer was obtained by spin coating (800 rpm for 60s) a commercially available aqueous PEDOT:PSS dispersion with addition of DMSO (5%). HIL layers were realized by dip coating and spin coating using the commercial available solution (PEDOT:PSS PVP Al 4083).

Deposition condition of electroluminescent polymer and Ca/Ag are the same reported for devices on PEN substrates.

REFERENCES

- ¹ M. Hack et al, *7th International Conference on Electroluminescence of Molecular Materials and Related Phenomena*, 2008
- ² S. Forrest, *7th International Conference on Electroluminescence of Molecular Materials and Related Phenomena*, 2008.
- ³ M.-C. Choi et al, *Prog. Polym. Sci.*, 2008, 33, 581-630
- ⁴ W. A. MacDonald et al, *Journal of the SID*, 2007, 15/12
- ⁵ Khalid Mahmood Zia et al, *Int J Biol Macromol.*, 2016, 82, 1028
- ⁶ S. Farah et al, *Advanced Drug Delivery Reviews*, 2016, 107,367–392
- ⁷ A. Jiménez et al, " *Poly(lactic acid) Science and Technology : Processing, Properties, Additives and Applications*", The Royal Society of Chemistry, 2014
- ⁸ C. Y. Lim, *J. Int. Counc. Electr. Eng.*, 2012, 2, 237–241
- ⁹ C.-J- Chiang et al, *Organic Electronics*, 2010, 11 1870-1875
- ¹⁰ S. Sharma et al, *Opto-Electronics Review*, 2018, 26, 223-235
- ¹¹ Q. Zheng et al, *Graphene for Transparent Conductors: Synthesis, Properties and Applications*, Springer, 2015
- ¹² Y. Cao et al, *Appl. Phys. Lett.*, 1992, 60(22), 2711–2713.
- ¹³ L. Swathiha Priyadharshni et al, *Int. J. Polym.Mater. Polym. Biomater.*, 2014, 64, 47–53.
- ¹⁴ M. Nishii et al, *SID 09 DIGEST*, 2009, 768–771
- ¹⁵ A. Elschener et al, " *PEDOT: Principles and Applications of an Intrinsically Conductive Polymer*", CRC Press, 2010
- ¹⁶ X. Crispin et al., *Chem. Mater.*, 18, 2006, 4354–4360
- ¹⁷ G. Greczynski et al, *Thin Solid Films*, 354, 1999, 129–135
- ¹⁸ D. Alemu Mengistie et al, *J. Mater. Chem. A*, 1, 2013, 9907–9915
- ¹⁹ A. M. Nardes et al, *Adv. Funct. Mater.*, 18, 2008, 865–871
- ²⁰ T. Takano et al, *Macromolecules*, 45, 2012, 3859–3865
- ²¹ C. M. Palumbiny et al, *J. Phys. Chem. C*, 118, 2014, 13598–13606
- ²² H. Shi et al, *Adv. Electron. Mater.*, 1, 2015, 1500017
- ²³ A. De Girolamo Del Mauro et al, *Thin Solid Films*, 520, 2012, 5386–5391
- ²⁴ G. Sico et al, *Organic Electronics*, 28, 2016, 257-262
- ²⁵ K. Sun et al, *Journal of Materials Science: Materials in Electronics*, 26, 2015, 4438-4462.
- ²⁶ J. S. Yeo et al, *Solar Energy Materials and Solar Cells*, 114, 2013, 104–109
- ²⁷ M. Wang et al, *Solar Energy*, 129, 2016, 175–183
- ²⁸ M. Montanino et al, *EXPRESS Polymer Letters*, 11, 6, 2017, 518–523

SECTION 2

SYNTHESIS AND ELECTRICAL PROPERTIES OF EUMELANIN THIN FILMS: TOWARDS THE DESIGN OF POLYMERIC ANODE FOR ITO-FREE DEVICES

~INTRODUCTION~

Among the broad variety of biopolymers found in nature, few have such profound and fascinating interdisciplinary implications at the crossroads of physics, chemistry, biology, and medicine as melanins do. The reasons for this are rooted in the role of these pigments as the key components of the human pigmentary system, their important socio-economic impact and clinical relevance in relation to pigmentary disorders, such as malignant melanoma, the most aggressive of the skin cancers, and in their photo-protecting action.

There are two main types of melanin: eumelanins, which are brown-black pigments, and pheomelanins, which are yellow-red pigments. Eumelanins are the most abundant type of human melanins and hold important functions in the human body including photo-protection, coloration of skin, hair and eyes, free radical scavenging, metal ion chelation, thermo-regulation, and is also involved in the neuronal signal transmission.^{1,2,3}

Eumelanins and pheomelanins share a common biosynthetic origin in the amino acid L-tyrosine. With the formation of the common key-intermediate dopaquinone, which is formed by the action of the enzyme tyrosinase in epidermal melanocytes, two different pathways depart. The first one leads to the formation of 1,4-benzothiazine intermediates, the monomer precursors of pheomelanins, whereas the second one leads to the formation of 5,6-dihydroxyindole (DHI) and its 2-carboxylic acid (DHICA), the monomer precursors of eumelanins (Figure 1).⁴ The oxidative polymerization of these precursors leads to the formation of dimers, trimers and superior oligomers forming eumelanins.

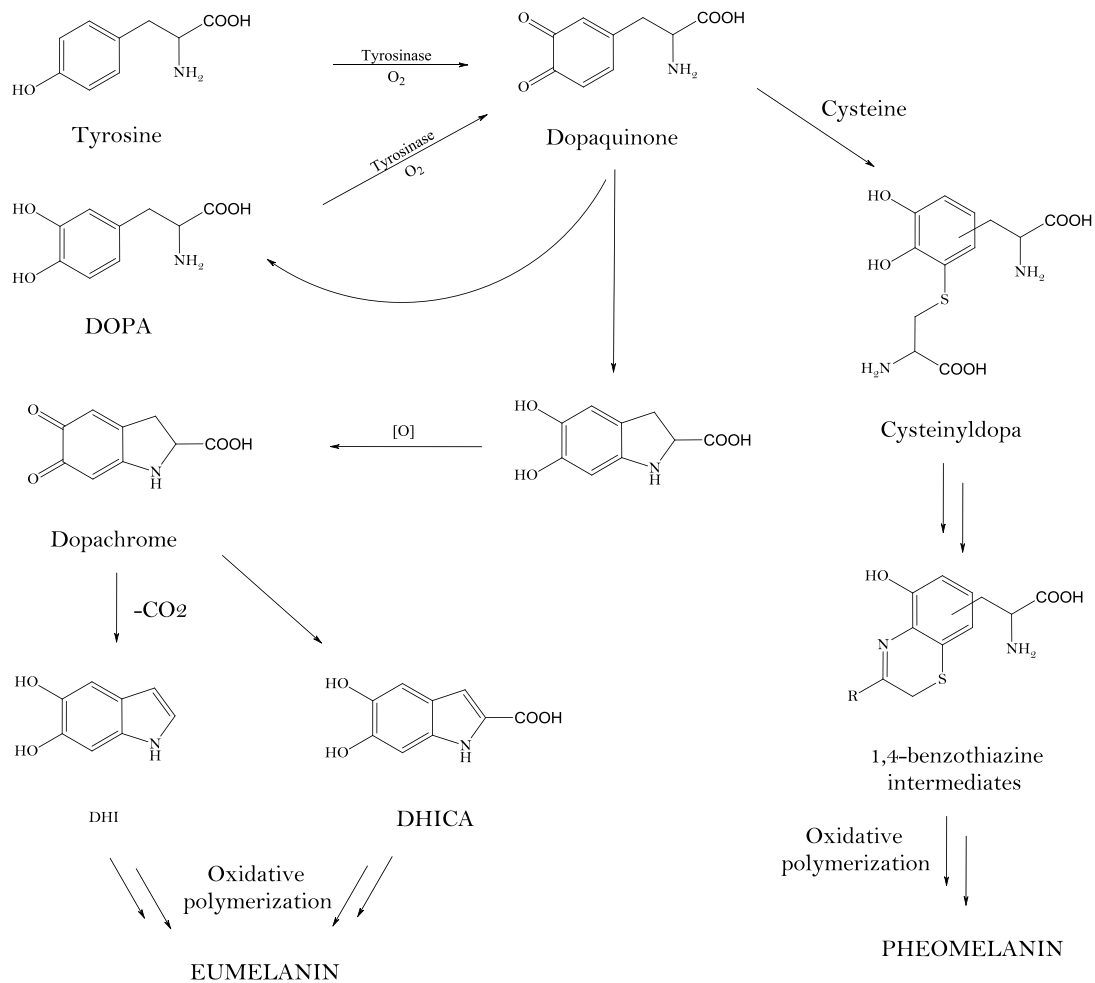


Figure 1: Biosynthetic pathways leading to eumelanins and pheomelanins

The way the monomers are connected is important to understand deeply the chemical structure of eumelanins. The oxidative polymerization of DHI led to the formation of dimers, trimers and other oligomers linked through 2,2'-2,4' and 2,7' bonding (Figure 2).^{5,6,7,8,9}

In the case of DHICA, the oxidative polymerization is conditioned by the presence of the carboxylic acid group in the 2 position. This led to the formation of

oligomers in which the DHICA units are linked through the 4 and 7 positions (Figure 3).¹⁰

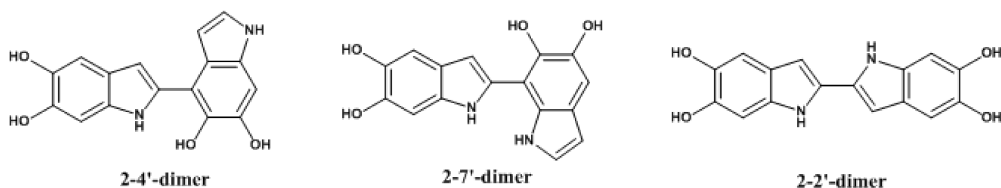


Figure 2: DHI dimers

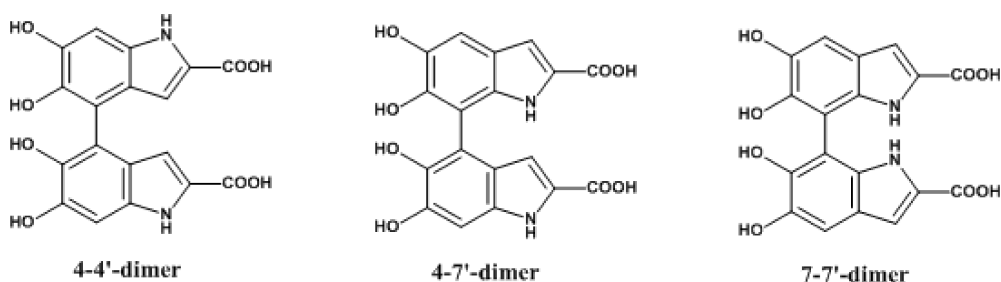


Figure 3: DHICA dimers

For this reason DHI-melanins are characterized structurally by planar portion of the polymer backbone denoting an efficient inter-unit- π -conjugation. This led to the formation of nanoaggregates via π -stacking interactions. Nanoaggregates can then cluster together via side on interactions.^{11,12,13,14} DHI-melanins usually show a strong optical absorption in the visible region.¹⁵

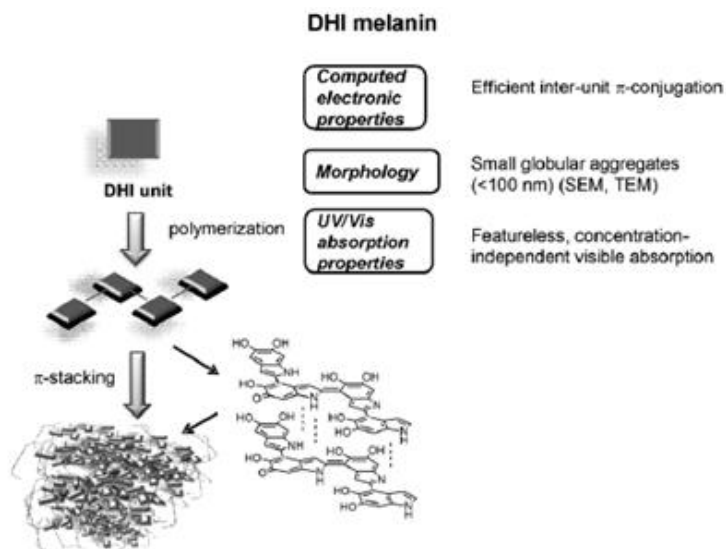


Figure 4: Structure–property relationships proposed for DHI melanins

DHICA oligomers exhibit a linear backbone with a stacked configuration.^{16,17,18} This led to the formation of rod-like assembly.

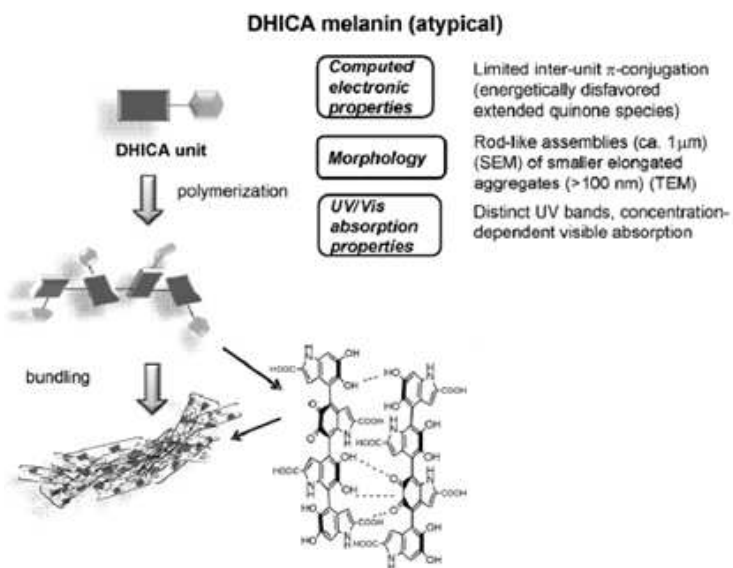


Figure 5: Structure–property relationships proposed for DHICA melanins

Eumelanins that derive from the polymerization of both DHI and DHICA have a typical broadband featureless optical absorption throughout the entire UV-visible spectrum, accounting for their black colour.

It has been shown that the absorption spectrum can result from the superposition of the absorption of eumelanin oligomers of different size and structure.¹⁹ Pezzella et al. further reported that the coexistence of oxidized and reduced monomers contributes to the broad-band absorption.²⁰ Stacking of the sheets and environmental factors also broaden and shift the peaks. It is proposed that with enough of this chemical disorder, the overlapping individual peaks would be smeared into the monotonic absorption spectrum observed experimentally (Figure 6).

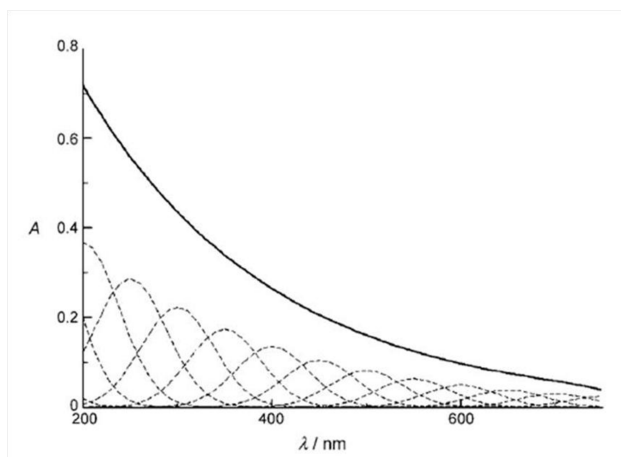


Figure 6: Broad band absorption spectrum of eumelanin materials

Other important physico-chemical characteristics that make eumelanins a unique material are:²¹

- a) the nearly quantitative non radiative conversion of absorbed photon energy;
- b) the photoconductivity in the solid state;
- c) the hydration-dependent electronic-ionic hybrid conduction properties;

- d) H-atom donor, antioxidant and free radical scavenger properties;
- e) metal ion-binding properties;
- f) the redox behavior.

The conduction properties of eumelanin materials were observed for the first time by McGinnes and his associates in the 1970s²² and from that moment the electrical conductivity of such material was explained with the amorphous organic semiconductor model. This model was also considered an explanation for the observed broad optical absorbance, indicating that eumelanin shows an extended π -conjugation. A critical point of the McGinness observation is that conductivity of eumelanin materials was observed only in hydrated state.

Jastrzebska et al reported one of the most exhaustive investigation of the eumelanin conductivity as function of the relative humidity and temperature.²³ He reported that the electrical conductivity of synthetic dopa melanin rises from 10^{-13} to 10^{-5} S/cm from a dry to a fully hydrated state.

Water could affect the electron transfer processes in two complementary ways: by modifying the local dielectric constant of the material or by ionization of acidic and basic groups. When amorphous materials absorb water molecules onto their surface, water can be distributed throughout the bulk of the solid. The absorption of water induce a variation of the dielectric constant leading to a lower activation energy for electron hopping. The modified dielectric theory^{24,25} was the first explanation to the conductivity behavior of eumelanins and it is also in accordance with the amorphous organic semiconductor theory. According to the modified dielectric theory, conductivity can be calculates as:

$$\sigma = \sigma_0 \exp\left(-\frac{E_D}{2RT}\right) \exp\left(\frac{e^2}{2RT\epsilon} \left(\frac{1}{k} - \frac{1}{k'}\right)\right) \quad (1)$$

where σ_0 is the dry electronic conductivity in the infinite temperature limit, E_D is the band gap of the material in the dry state, R is the molar gas constant, T is the temperature, r is the screening length, k is the dielectric constant in the dry state and k' is the dielectric constant at the relevant hydration.

This theory was questioned by different experimental evidences and by the chemical disorder theory²⁶ that explain the broad band UV-Vis spectrum in contradiction with the amorphous semiconductor theory. The presence of different ionizable groups in the eumelanin structures is another evidence to doubt on the amorphous semiconductor theory.

In fact, water can greatly affect the conductivity by reacting with ionizable groups of the materials with alteration of the their energy levels. In the last decade, a more detailed model was also proposed to explain the water dependent conductivity of eumelanins. According to the water dependent electronic ionic conductor model, free carriers are produced from the comproportionation reaction (Figure 7), which drives the production of extrinsic free radicals (electrons) and hydronium ions (protons).²⁷ According to this model, eumelanin is not a simply electronic conductors but it is also an hybrid ionic-electronic conductor; this explains the peculiar electrical properties of melanin.

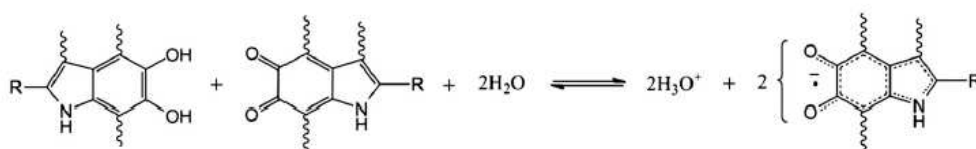


Figure 7: Comproportionation reaction of eumelanin materials

The works of Wünsche reported investigations about eumelanin conduction as a function of the hydration states and confirmed the mixed ionic-electronic transport in eumelanin thin films.^{28,29} In this context, any electrochemical

phenomena at the interface between melanin and electrode³⁰ must be taken into account to understand correctly the experimental information.

Thanks to the peculiar optical, electric and redox properties of eumelanins, different work are reported in literature about their application in electronic devices.

A bulk heterojunction of porous silicon and eumelanin was proposed in 2012 as a new organic-inorganic hybrid material for photovoltaic applications.³¹

Different works were reported about the realization of eumelanin-based electrochemical transistors (EOCTs).^{32,33} Among sensors, a pH sensor based on an extended gate field effect transistors (EGFETs)³⁴ and an ultrasensitive and fast moisture sensor^{35,36} were realized by using eumelanins as active material.

In 2010, Ambrico demonstrated that a Au/eumelanin/ITO/glass device is able to act as a read-only memory, pointing out the possible integration of eumelanin layers in electro-optical charge storage based memory device.³⁷ In 2011, for the first time, metal insulator semiconductor (MIS) devices with melanin layers directly on pSi and nSi substrates were realized³⁸ and a memory like behavior was observed.³⁹ The redox activity of the eumelanin building blocks and the capability of functionalities to reversibly bind cations constitutes the principles for the use of melanin in energy storage systems. In 2016 Kumar realized a flexible micro-supercapacitors based on the melanin pigment.⁴⁰

In 2017 Migliaccio demonstrated the integration of eumelanin with a standard commercial PEDOT:PSS solution.⁴¹ The realized blend represent a water stable transparent thin film that is able to operate as electrode for organic devices. Since eumelanin materials still represent a challenge for researcher, the deep knowledge of its properties is mandatory to be able to integrate it with other material for electronic applications.

The lacking of a crystalline structure, the insolubility in any solvents, the sensitivity to acid and bases, the high chemical heterogeneity and the lacking of an exhaustive conduction mechanism represent the main reasons why eumelanins have not been so far used for organic electronic applications.

In particular, the realization of uniform and reproducible thin film is an important aspect for device applications. Due to insolubility of eumelanins, the thin film is usually realized by direct deposition of the pigment; this can be done by suspending the pigment in DMSO or by a chemical pretreatment to obtain a partial solubilization.⁴² With the first method, good quality eumelanin films were obtained only from commercial synthetic eumelanin by spin coating process. In the second case, the pretreatment consists in an aqueous alkaline treatment with a consequent modification of the pigment backbone, modification of the chemical properties and increase of the chemical disorder.⁴³

The variation of the chemical properties of the pigments is of course undesired in order to study the structure-property relationship of the materials and to realize reproducible eumelanin thin films. For a detailed design of eumelanin based devices is mandatory the control of the material structure and of its chemical-physical properties.

In order to obtain an eumelanin thin film with a better quality and a deeply chemical control, a new method has been developed based on the deposition of the monomer precursors DHI and DHICA. DHI and DHICA have the advantage to be completely soluble in all the common organic solvents.

The method consists in the deposition of the monomer precursor by spin coating and a subsequent oxidative process by exposing the film of the monomer to gaseous ammonia in an air-equilibrated atmosphere (ammonia induced solid state polymerization, AISSP).⁴⁴ DHI thin films exposed to ammonia vapour, rapidly (a

few minutes) become dark brown suggesting that the polymerization process has occurred; DHICA films required longer time (hours) due to its lower reactivity. The evolution of the UV-vis spectra during the AISSP process of a DHI thin film is reported in Figure 8; after 120 s the typical monotonic profile of eumelanins is clearly visible.

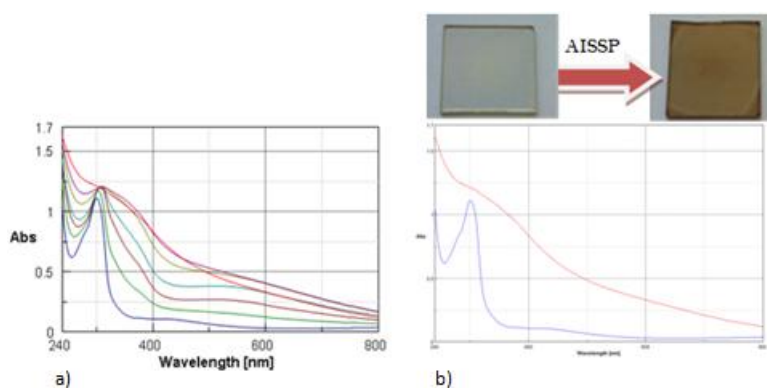


Figure 8: a) UV-vis profiles of a DHI thin film fabricated by AISSP. Plots are taken at 5, 15, 30, 45, 60 and 180 min after exposition to a polymerization inducing atmosphere; b) UV-vis plots of DHI and DHI melanin (120 min AISSP time) films on quartz substrates are showed with the corresponding substrate picture: DHI, left and eumelanin right.

The matrix-assisted laser desorption ionization (MALDI) mass spectrometry characterization confirms the formation of the DHI melanin films. In particular, by comparing the MALDI-MS data of a reference dopa-melanin sample prepared by auto-oxidation in an alkaline medium and the AISSP DHI-eumelanin, it is possible to appreciate several important chemical and technological advantages of the AISSP method.

AISSP DHI films exhibited greater structural integrity, as evidenced by the regular clusters of peaks centered around the expected pseudomolecular ion peak, and a limited degree of polymerization (the highest oligomer detected at the hexamer-eptamer stage, to be compared with the 30-mer identified in the polymerization mixture of DHI) (Figure 9B).⁴⁵

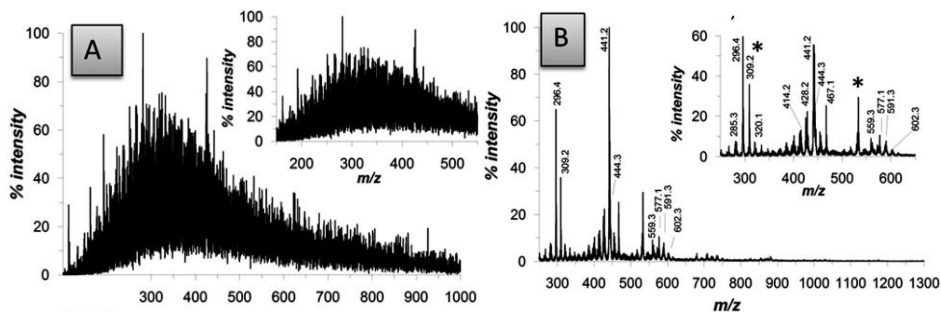


Figure 9: MALDI-MS spectra of eumelanin thin films on a standard MALDI plate. (A) Dopa melanin prepared by alkaline autoxidation. (B) DHI melanin prepared by the AISSP methodology. Asterisks denote impurities.

In contrast, preformed eumelanins proved to be highly heterogeneous as a consequence of the disordered polymerization of the different units, higher molecular weight dispersion and extensive post-synthetic degradation under the solution conditions of the polymerization processes (Figure 9A).

About the morphology, AFM images denoted that the film surface is characterized by a very smooth matrix where the only specific morphological feature is the presence of some columnar structures having heights of a few nm. On a $2 \mu\text{m} \times 2 \mu\text{m}$ scale, the average roughness is found to be lower than 0.3 nm, while it increases up to about 1 nm when larger scales are considered (Figure 10). The film shows also good adhesion to the substrate.

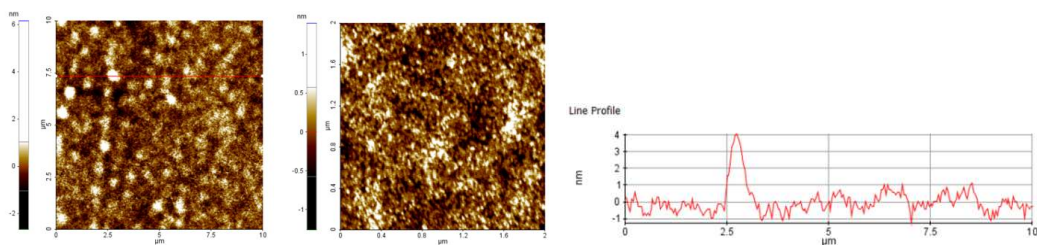


Figure 10: AFM topographical maps on different scales of a DHI melanin thin film grown by AISSP ($2 \times 2 \mu\text{m}$, $10 \times 10 \mu\text{m}$) and height profile caught from the red line on map (red line).

- AIMS

This research work is aimed at testing the potential of eumelanins as new conductors for organic electronic devices.

In the first part, the solid state polymerization process of the DHI monomer was studied by following the evolution of the transmission spectrum over the time under different ambient conditions (i.e. temperature, oxygen and water vapour).

In the second part, the electrical conductivity of eumelanin thin films was studied. Both monomers, DHI and DHICA, were used in the thin film fabrication to evaluate the effect of the chemical composition of the film on the electrical property of the material.

To this aim current-voltage measurements of eumelanin materials were performed as a function of the relative humidity. This work was carried out in association with Prof. Clara Santato during my stage at the Polytechnique of Montreal (CA) (from 01/09/2016 to 23/12/2016 - FRQSC scholarship)

~RESULTS AND DISCUSSION~

○ FACTORS GOVERNING THE SOLID STATE POLYMERIZATION PROCESS OF DHI

Aim of this work is to understand the effect of various ambient factors on the solid state polymerization process of the DHI monomer.

As preliminary test, the oxidative process of DHI as thin film was monitored in ambient conditions (25°C-50RH) by evaluating the evolution of the transmittance spectrum during the time. In Figure 11 it is reported the UV-vis spectrum of the just deposited DHI film and at t_{final} , corresponding to the time after which the spectrum does not change further. t_{final} can be considered as the time at which the polymerization process is completed.

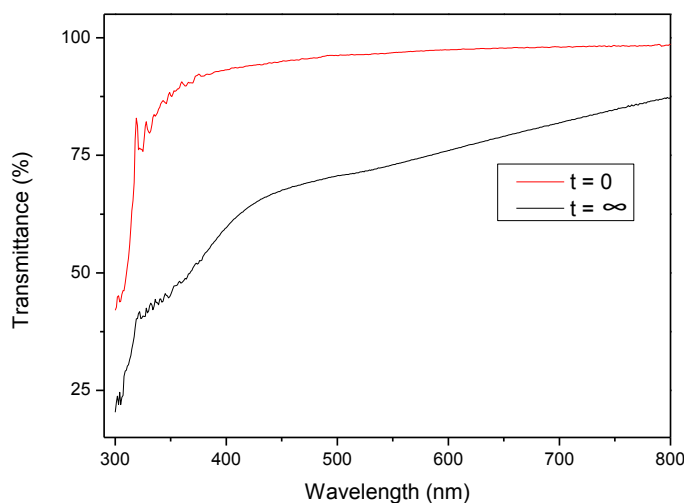


Figure 11: Evolution of the DHI thin film transmittance spectra exposed to air

From the comparison of the two spectrum it is possible to observe that the polymerization process involves a more significant decrease in transmittance in the range 350-650 nm and for such reason the variation of the transmittance value at 400 nm has been considered as our reference for the kinetic study of the

process. In Figure 12 it is reported the transmittance value at 400 nm as function of the time.

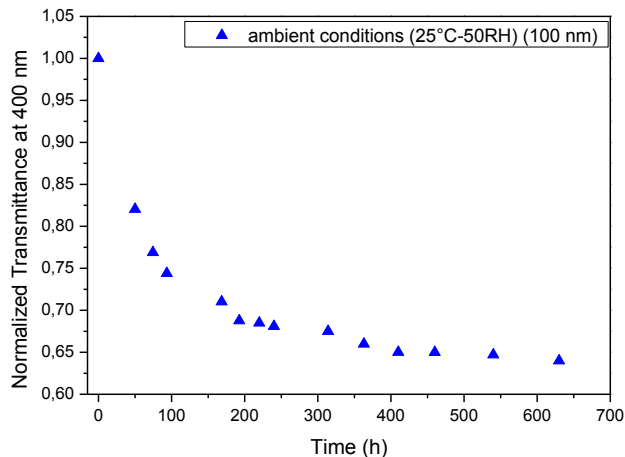


Figure 12: Time evolution of the transmittance value at 400 nm of a DHI thin film exposed to air

The transmittance value at 400 nm decreases during the time until it reaches a plateau after approximately 500 hours; in this case the polymerization can be considered completed.

In order to evaluate the effect of temperature and humidity on the rate of the polymerization process, other experiments were carried out. The polymerization process at 38°C-50RH is very fast and it stops after 1-2 days. Under these conditions it is difficult to evaluate the effect of the temperature and humidity on the polymerization process.

For this reason it was designed an experimental setup to slow down the polymerization process. This consists in the deposition of a DHI thin film on a glass substrate that is sealed with a plastic barrier film in a nitrogen atmosphere (Figure 13). Afterwards, the sealed sample is placed in a climate chamber in which is possible to control temperature and relative humidity.

Thanks to the use of the plastic barrier it is possible to regulate the oxygen and water vapour flows that can interact with the DHI sample and so to slow down the polymerization process. Known the temperature, the relative humidity, the oxygen transmission rate (OTR) and the water vapour transmission rate (WVTR) of the barrier layer, it is possible to study the rate of the polymerization process. In Table 1 are reported all the used experimental conditions.

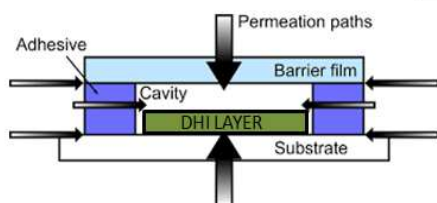


Figure 13: Experimental setup with plastic barrier layer

Table 1: Experimental conditions of DHI solid state polymerization study

Sample	Ambient conditions	Barrier	OTR (cc/m ² /day)	WVTR (g/m ² /day)
1	65°C - 90 RH	Polystyrene (PS)	≈ 100000	920
2	65°C - 70 RH	Polystyrene (PS)	≈ 100000	716
3	65°C - 50 RH	Polystyrene (PS)	≈ 100000	512
4	38°C - 90 RH	Polystyrene (PS)	> 10000	140
5	38°C - 70 RH	Polystyrene (PS)	> 10000	110
6	38°C - 50 RH	Polystyrene (PS)	> 10000	78
7	65°C - 90 RH	Polyethylene terephthalate (PET)	370	28.40
8	65°C - 70 RH	Polyethylene terephthalate (PET)	280	22.10
9	65°C - 50 RH	Polyethylene terephthalate (PET)	240	15.80
10	38°C - 90 RH	Polyethylene terephthalate (PET)	18.70	4.32
11	38°C - 70 RH	Polyethylene terephthalate (PET)	16.80	3.36

12	38°C - 50 RH	Polyethylene terephthalate (PET)	12.30	2.40
13	65°C - 90 RH	PET-SiO _x	15.46	5.95
14	65°C - 70 RH	PET-SiO _x	11.74	4.63
15	65°C - 50RH	PET-SiO _x	9.42	3.30
16	38°C - 90 RH	PET-SiO _x	2.12	1.05
17	38°C - 70 RH	PET-SiO _x	1.76	0.82
18	38°C - 50 RH	PET-SiO _x	1.45	0.59

The reported WVTR and OTR values were estimated by assuming an Arrhenius behavior starting from known values at 38°C and 90% of relative humidity measured by MOCON permeabilimeter.

The transmission spectrum of all the samples has been measured over time until t_{final} (polymerization completed).

About samples with PS barrier, t_{final} is comparable to the t_{final} values observed without the barrier layer, suggesting that the oxygen flow is not a limiting factor for the polymerization process. By plotting the t_{final} and the WVTR it is possible to observe a linear correlation, demonstrating the effect of water in promoting the oxidative polymerization of DHI (Figure 14).

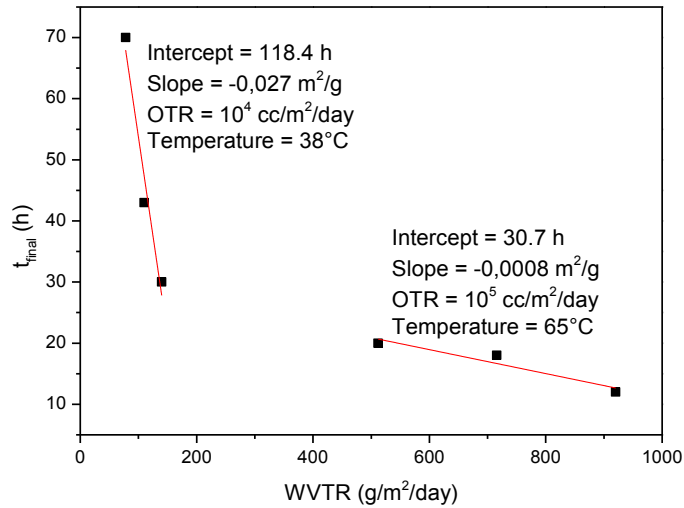


Figure 14: t_{final} vs WVTR plot for samples with PS

Moreover, the slope of the linear regression decreases from 65 ° C to 38 ° C as a demonstration of the catalytic effect of the temperature.

A reduction in the oxygen and water vapour flows is achieved by using PET and PET-SiO_x as a barrier layers. The t_{final} values under these conditions are bigger than those observed without barrier layer, suggesting that the oxygen flow is able to limit the rate of the process. A linear correlation between t_{final} and the water vapour flows exists and the slope varies according to the combined effects of oxygen flow and temperature (Figure 15-Figure 16).

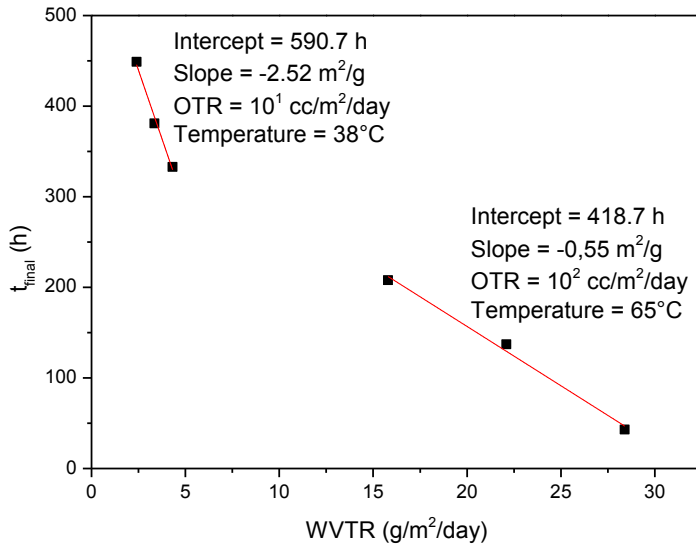


Figure 15: t_{final} vs WVTR plot for samples with PET

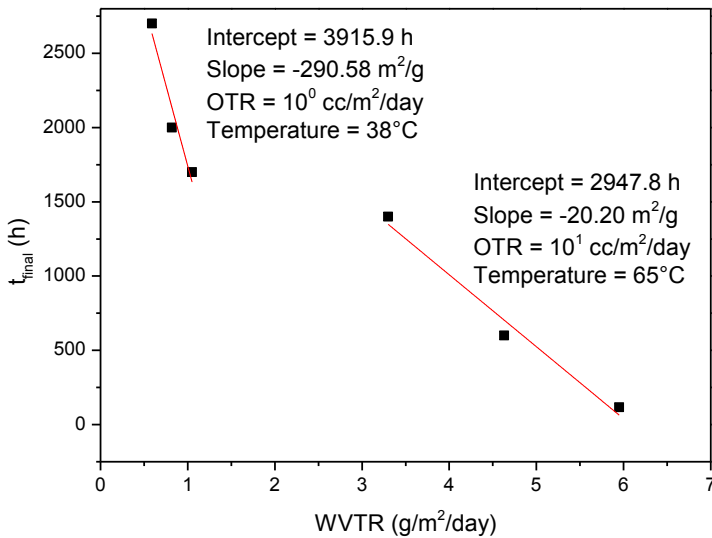


Figure 16: t_{final} vs WVTR plot for samples with PET-SiO_x

On the basis of these results, it is possible to conclude that the oxidative process slows down by reducing the quantity of oxygen that can interact with the DHI film.

Specifically, in the case in which PS is used as barrier layer, oxygen is not a limiting reagent and the reaction proceeds with the typical characteristic time of the polymerization process. The rate of the polymerization process is affected by the catalytic effect of temperature and water vapour. By using PET and PET-SiO_x, oxygen became a limiting reactant of the process and the reaction is dramatically slowed down.

It can be supposed that the material disorder and the defectiveness can be influenced by the rate of the polymerization process and so by ambient conditions. As a consequence, the control of the polymerization variables can be the key to realize more ordered and reproducible thin films.

To investigate how the polymerization conditions can influence the morphology of the eumelanin thin films, a surface characterization with an optical profilometer was carried out.

By comparing the 2-dimension maps and in particular the roughness of the films obtained by using the same barrier layer (group), it is evident that, although the samples of the same group have quite different characteristics, there is a trend between surface features and barrier properties. An increase of the roughness with the decrease of the barrier properties it is observed and in Figure 17 there are reported some representative maps.

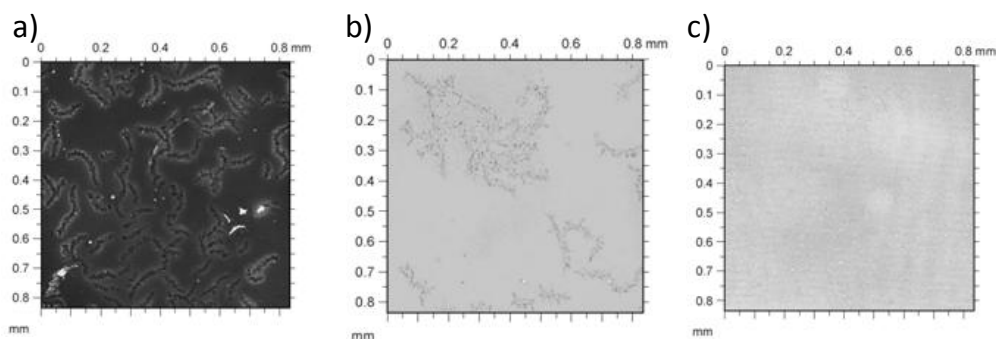


Figure 17: 2-dimension map of eumelanin with a) PS barrier $S_q=86$ nm (Samples average $S_q = 71 \pm 32$ nm) ; b) PET barrier $S_q = 42$ nm (Samples average $S_q = 42 \pm 22$ nm); c) PET-SiO_x $S_q= 22$ nm (Samples average $S_q = 24 \pm 10$ nm)

Another factor that seems to affect the thin film morphology is the water vapour transmission rate accounting for the quantity of water that can interact with the thin film. With the same type of barrier and temperature, films of melanins with a higher degree of relative humidity appear smoother and less defective. This evidence maybe can be imputable to a local solubilization effect of the water vapour which promotes a rearrangement of the molecules during the polymerization and so promoting a more ordered process. In Figure 18-Figure 20 are reported the 2-D maps of samples obtained by using different barrier layers at 38°C under two different values of relative humidity.

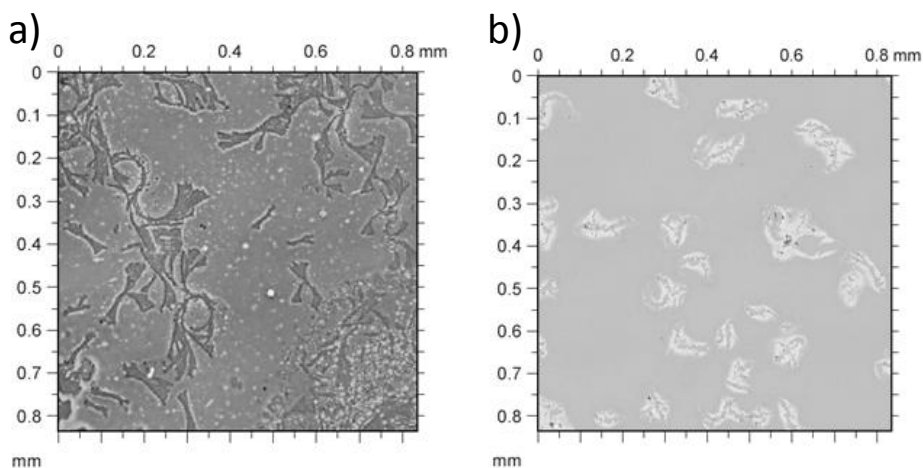


Figure 18: 2-dimenson map of eumelanin with PS barrier at a)38°C-50RH PS $S_q=85$ nm; b) 38°C-70RH $S_q=70$ nm

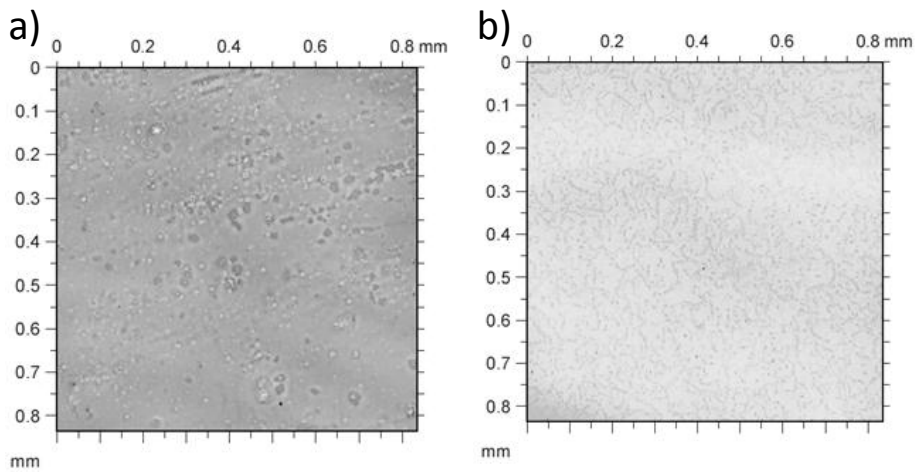


Figure 19: 2-dimenson map of eumelanin with PET barrier at a)38°C-50RH PS $S_q=50$ nm; b) 38°C-70RH $S_q=28$ nm

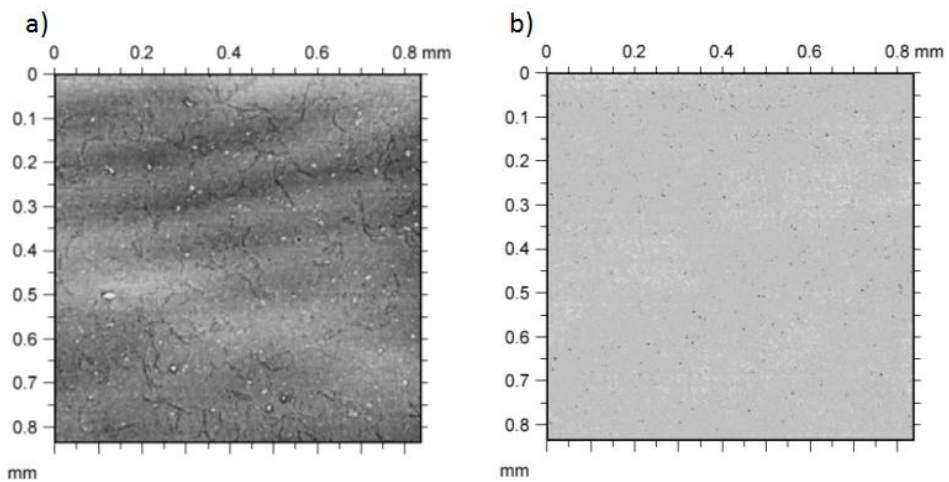


Figure 20: 2-dimenson map of eumelanin with PET_SiO_x barrier at a)38°C-50RH PS $S_q=34.3$ nm; b) 38°C-70RH $S_q=23$ nm

A deeper investigation between the reaction conditions and the thin film morphology is of course necessary, but this work represent a good starting point for the realization of eumelanin thin films with controlled features.

○ ELECTRONIC CONDUCTION IN DISORDERED ORGANIC MATERIALS

The absence of a crystalline structure in most of the organic semiconductors leads to a different conduction mechanism. The principal characteristic making the difference between disorder materials and crystalline materials is the absence of a well defined band structure. All electronic states in organic disordered systems are localized (sites), with the electronic wavefunction set in a certain volume. Efficient charge transport requires that the charges are able to move from one site to another and not trapped or scattered. Therefore, charge carrier motilities are influenced by many factors⁴⁶ including molecular packing, disorder, presence of impurities, temperature, electric fields, charge carrier density, size-molecular weight etc. In particular, the synthesis and deposition of the organic semiconductors can dramatically change the structural properties thus influencing the charge carrier properties.

The passage of the charge carrier from one site to another occurs through successive incoherent hopping. The Miller-Abrahams⁴⁷ (M-A) expression define the rate of carrier transitions from an occupied site i with energy ϵ_i to an empty site j with energy ϵ_j , separated by distance r_{ij} as follow:

$$v_{ij} = v_0 \exp(-2r_{ij}/\alpha) \begin{cases} 1 & \text{if } \epsilon_i < \epsilon_j \\ \exp[-(\epsilon_i - \epsilon_j)/kT] & \text{otherwise} \end{cases} \quad (1)$$

The best way to describe the hopping transport in disordered systems is based on the percolation theory.⁴⁸ According to this theory, the charge hopping can be considered as a percolation process through a resistor network, in which every site is replaced by an electrical node distributed randomly in the space. A pair of neighboring nodes i and j is connected via a resistor R_{ij} , that is inversely proportional to the M-A hopping probability.

$$R_{ij} = \left(\frac{k_B T}{q^2} \right) \left(\frac{1}{v_{ij}} \right) \quad (2)$$

Very large resistance values do not contribute to transport because they can be bypassed through paths with much lower resistances. Low resistances values serve simply as short-cuts between higher resistances. This leads to a critical value R_{crit} for the resistance that is representative for the whole system and needs to be overcome to form a continuous percolation pathway through the sample.

In a more intuitive way, the percolation problem can be also considered from a geometrical point of view by considering d -dimensional spheres around every site with radii r_i . In this situation, the threshold for percolation is then found by increasing r until an infinite cluster is found at $r=r_{crit}$ (Figure 21).

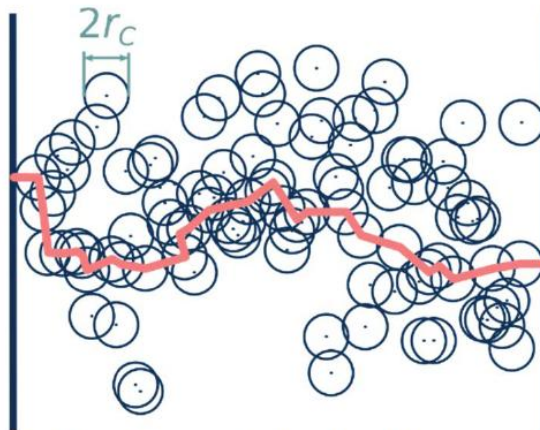


Figure 21: Percolation criterium interpreted with spheres

Since the hopping is a thermally activated process, at high temperature, the energy dependent terms in the M-A equation do not play any significant role and the hopping rates are determined solely by the spatial terms. In this situation the hopping process will occur on the nearest neighbour sites (NNH) (Figure 22). At low thermal energies, it becomes energetically favorable for carriers to tunnel to non nearest sites with lower site energies. This hopping regime is referred to as

variable range hopping (VRH) and can be implemented into the percolation formalism by assuming percolation in 4 dimensions (3D space + 1D energy).

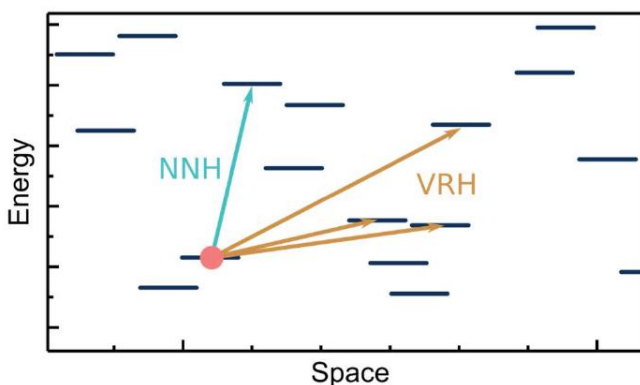


Figure 22: Nearestneighbour hopping (NNH) and variable range hopping (VRH)

In these conditions, an optimal hopping distance-energy combination can be obtained, which energy is called transport energy (E_t)⁴⁹ and represent the final site energy for which the upwards hopping rate from an initial site i is highest.

The charge relaxation process is another important difference between organic disordered materials and crystalline materials. The time that is needed for the charge carriers to equilibrate is called relaxation time (τ_{rel}). Within time of the order τ_{rel} , transport is dispersive with a time dependent mobility. At $t > \tau_{rel}$ mobility acquires a time-independent well defined value.

When a constant mobility is observed in experiments, the relaxation process cannot play an important role for charge transport. It must therefore be much shorter that the time that a single charge carrier needs to traverse through the sample. Otherwise, the time dependent dispersive transport would be mirrored in the experimental data. Usually the relaxation process is particularly slow for organic materials and is also profoundly affected from the traps and their energy.⁵⁰ Carriers in the shallow trapping situations tends to transport by a multiple trapping and release processes, which result in larger energetic disorder;

on the contrary, carriers in the deep trapping situations are nearly immobilized once trapped and act as scattering centers, thus leading to decreased carrier density and slightly decreased mobility. It can be deduced that, shallow traps greatly decrease the mobility by orders of magnitude and increase the relaxation time whereas deep traps mainly decrease the collected carrier quantity without significantly affecting the mobility (Figure 23).

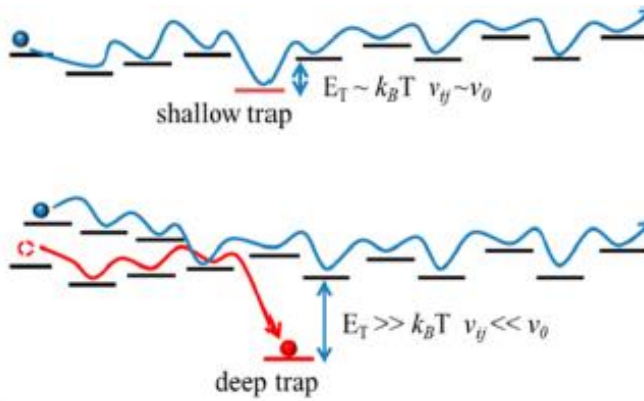


Figure 23: Trap energy effect on the charge transport

Different models have been developed to explain the effects of all the extrinsic factors, like trapping, electric field and temperature in disordered materials. One of the most popular and complete formulation derive from the work of Bassler et al.⁵¹ The resulting equation is:

$$\mu(T, \Sigma, E) = \mu_0 \exp \left[- \left(\frac{2\sigma}{3k_B T} \right)^2 \right] \begin{cases} \exp \left[C \left(\left(\frac{\sigma}{k_B T} \right)^2 - \Sigma^{1/2} \right) E^{1/2} \right] & \Sigma \geq 1.5 \\ \exp \left[C \left(\left(\frac{\sigma}{k_B T} \right)^2 - 2.25 \right) E^{1/2} \right] & \Sigma < 1.5 \end{cases} \quad (3)$$

where μ_0 is a field-independent prefactor, σ is the energetic disorder which represent the standard deviation of the DOS (density of state), C is a constant and Σ is the positional disorder referring to the relative positions and orientations.

All the developed models represent a guideline to understand the charge transport in organic disordered materials. It's not always easy to quantify the disorder of a system and the presence of traps and how these factors can be connected with the chemical composition and morphology, every material represent a new issue and a new challenge.

Eumelanin is a very disorder material that show electronic-ionic conduction in hydrated state and it represent a further obstacle in the determination of a charge transport mechanism. The specific experimental conditions and the used precursors greatly affect the electrical characteristics of eumelanins and a direct comparison between all the literature data is not useful and exhaustive.

The identification of a deposition process that give reproducible and good quality thin film and the individuation of the chemical composition that can improve the conduction properties are two key points that need to be faced to successfully implement eumelanins in electronic devices.

○ SOLID STATE PROTONIC CONDUCTION

Ionic and in particular protonic species play an important role in charge transport in a variety of materials, from ceramic to organics. Protons are extremely reactive and for such reason they do not exist independently in condensed matter.

There are two accepted proton-conducting mechanisms: vehicle-type⁵² and Grotthus-type⁵³ mechanisms (Figure 24).

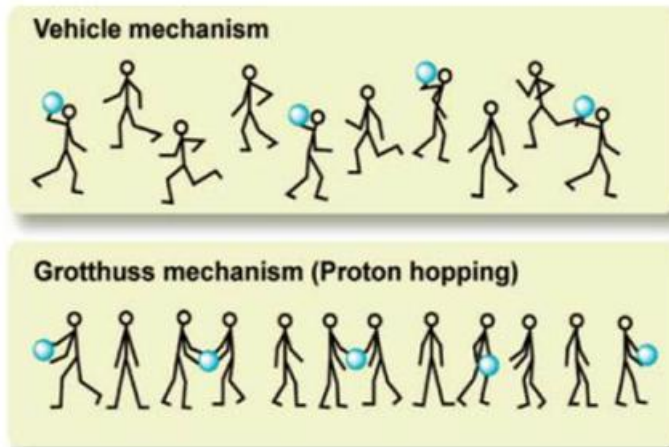


Figure 24: Vehicle and Grotthuss mechanisms for proton transport

In the vehicle mechanism, protons migrate through the medium with a "vehicle", in this case the conductivity is dependent on the diffusion rate of the vehicle. The process is described by the Einstein-Stokes equation for charged particles:

$$\mu = \frac{Dq}{k_B T} \quad (4)$$

where D is the diffusion constant and q the charge.

In the Grotthuss mechanism (also known as hopping), protons are transferred from one site to another through the continuous formation and breaking of hydrogen bonds. In this kind of process, reorientation and reorganization is necessary and the proton conductivity is directly affected by the proton transfer rate and the reorganization rate. This mechanism of conduction is most efficient when a continuous hydrogen-bonded network exists.

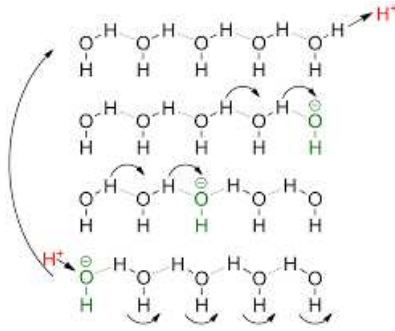


Figure 25: Grotthus mechanism for proton hopping

These mechanisms are not independent and often could make cooperative contributions to proton conductivity. The overall conductivity for proton transport can be described by the following equation:

$$\sigma = \frac{A}{T} \exp\left(\frac{-E_A}{k_B T}\right) \quad (5)$$

where the first part of the equation captures centre of mass diffusion and the exponential captures the tunneling, heat activated process.

A factor that can further influence the proton conductivity is the hydration state of the material, since the mobility of protons in water is extremely high. In the case of the vehicular mechanism water can act as vehicle for the proton conduction. In the Grotthus type mechanism it is necessary to have a continuous H-bonded network. The continuous network can be related with the peculiar chemical and morphological structure of the material; in this case the proton conduction occurs in dry state and the material hydration can further improve the phenomenon. When the material doesn't show a continuous hydrogen-bonded network, absorbed water can constitute such network and the Grotthus mechanism can occur.

The increase in conductivity with adsorbed water can also be explained through the percolation theory by considering the absorbed molecules of water able to

create a continuous percolation path for proton transport. By considering the percolation theory, the hopping process of protons in organic material can be easily treated as the electron hopping in organic disordered systems.

○ ELECTRONIC vs PROTONIC CONDUCTION IN EUMELANIN THIN FILMS

The aim of the reported measurements is the evaluation of the effect of relative humidity and the chemical composition on the electrical properties of eumelanin thin films.

The experimental setup is constituted by a two platinum electrodes in a planar configuration as reported in Figure 26.

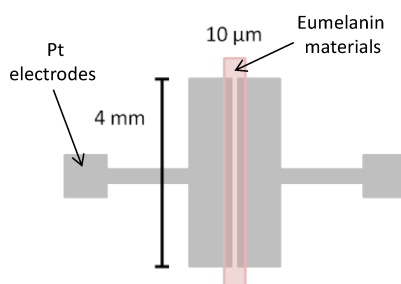


Figure 26: *I-V* measurements device

The eumelanin thin films were realized by using the AISSP processing technique starting from DHI or DHICA, as monomer precursors, individually or by combining them in a 1:1 ratio. For comparison, a device realized by using the commercial melanin (Sigma melanin) was also characterized. The electrical characterization was carried out by performing three *I-V* cycle scans (0 → 0.6 → 0 V).

In Figure 27 and Figure 28 are reported the *I-V* curves of the Sigma melanin, the DHI_melanin, the DHICA_melanin and the DHI/DHICA_melanin at different relative humidity values (second cycle reported).

The first evidence is that for all the samples at all the relative humidity values it is visible a significant hysteresis. Specifically, the current measured in the backward scan being lower than those measured in the forward cycle (clockwise hysteresis). This effect is usually due to the presence of charge trapping phenomena and it is typical of disordered materials. For ionic conductor materials, hysteresis can be also caused by ionic space charge accumulation at the interface with the electrode.

About the shape of the I - V curves, Sigma melanin and DHI/DHICA_melanin samples show a different behavior with respect to DHI_melanin and DHICA_melanin. In particular, in the I - V curves of Sigma melanin and DHI/DHICA_melanin is possible to distinguish two different regions: 1) the region at potential $< 0.2/0.3$ V is characterized by a weak dependence of the current with the voltage and it is usually due to the formation of a double layer capacitance; 2) the region at potential > 0.3 V, showing a quasi-exponential dependence on voltage, suggesting a non-capacitive behavior. On the other hand, I - V curves for DHI_melanin and DHICA_melanin seem to obey to the Ohm law. A possible explanation may be the similar chemical composition of Sigma melanin and DHI/DHICA_melanin deriving from the oxidative polymerization of both DHI and DHICA units.

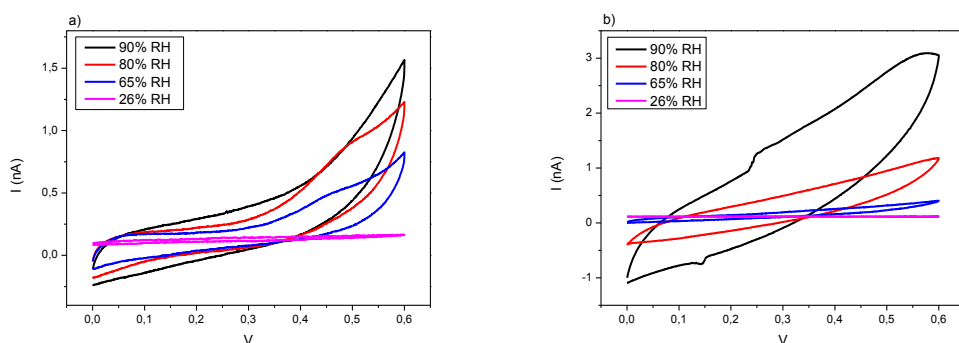


Figure 27: IV curves at different relative humidity values of device with a) sigma melanin and b) DHI_melanin

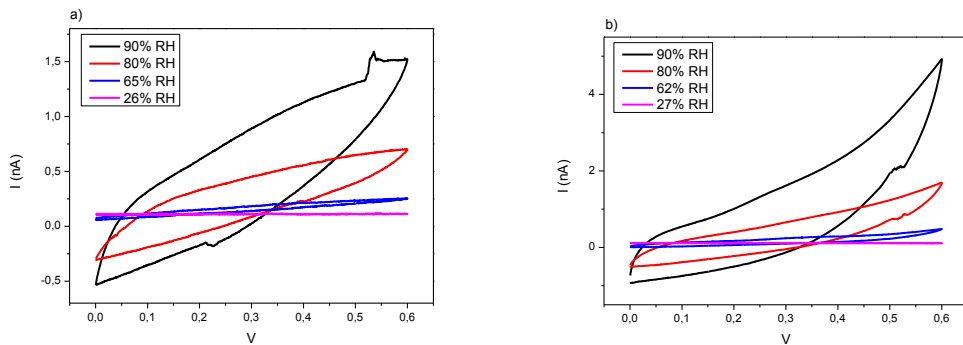


Figure 28: IV curves at different relative humidity values of device with a)DHICA_melanin and b) DHI/DHICA_melanin

By evaluating the different I - V cycles for all the devices, it is visible a reduction of the current values with each cycle (Figure 29), that is imputable to an irreversible redox process. It was demonstrated by Wünsche²⁹ that redox processes occurring at the Pt/eumelanin interface can cause the depletion of redox species or the formation of an insulating layer with a consequent decrease of the current from one cycle to another.

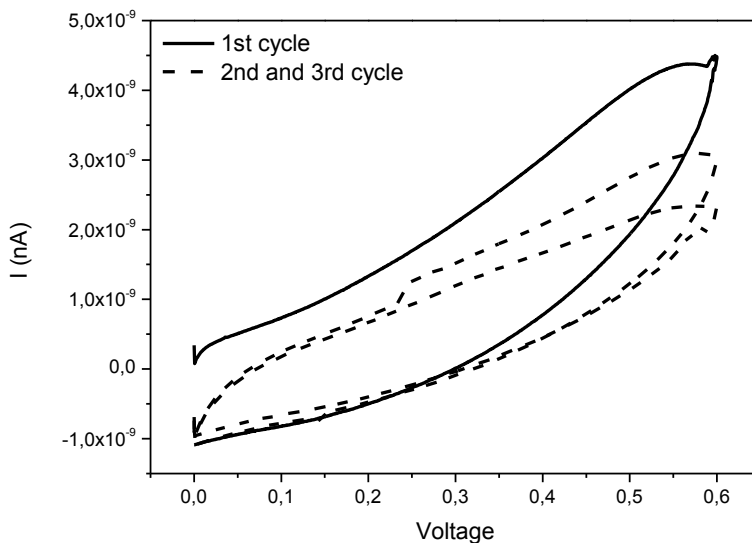


Figure 29: IV cycles for Pt-eumelanin devices

To evaluate the effect of the humidity on the electrical properties of eumelanin materials, the conductivity was calculated by using the Ohm law at 0.6 V and in Figure 30 is reported the conductivity as function of the relative humidity.

As expected, all the samples show an increase in conductivity with the increase of the relative humidity (Figure 30). In particular, melanin films realized by using the AISSP technique show higher conductivity with respect to the commercial melanin. The highest conductivity values are observed for the DHI/DHICA_melanin as a demonstration of the importance of both monomers in determining the peculiar electrical characteristics of eumelanins.

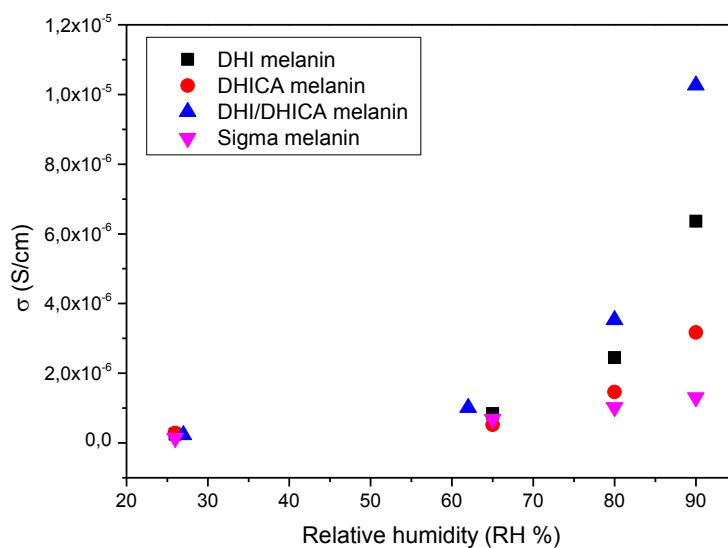


Figure 30: Conductivity values calculated for the commercial melanin (50 nm thickness) and for the eumelanin deriving from the AISSP (20 nm thickness)

In order to understand how electrons and protons contribute to the electrical current of eumelanin materials, transient current measurements were carried out by using palladium and palladium hydride (PdH_x) electrodes.

PdH_x derive from the exposition of palladium to gaseous hydrogen; when the hydrogen is absorbed into the palladium electrode it is almost completely ionized

and it is able to modify the electronic structure of the material with the formation of an hydrogen-saturated palladium.⁵⁴ Rolandi at all demonstrated that PdH_x can be easily used as proton-transparent electrode in bioprotonic devices,⁵⁵ infact PdH_x electrodes inject and drain protons into and from the proton-conducting material and for each proton injected an electron is collected (Figure 31).

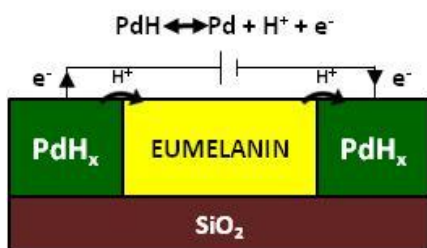


Figure 31: device with PdH_x working principle

In 2014 an eumelanin/PdH_x device was realized by using commercial melanin (Sigma melanin) and an ionic conductivity of 2×10^{-5} S/cm was reported (RH 90%). Here eumelanin devices with Pd and PdH_x electrodes were realized by using the AISSP method allowing a better control on the chemical composition of the material. To improve the accuracy of the measurement, the alternating polarity method was used for the determination of the resistance. Insulating materials, polymers and plastics typically exhibit background currents due to piezoelectric effect, capacitive elements charged by static electricity, and polarization effects. These background currents are often equal to or greater than the current stimulated by the applied voltage. In these cases, the result is often unstable, inaccurate resistance or resistivity readings or even erroneous negative values. The alternating virtually eliminates the effect of any background currents in the sample. First and second order drifts of the background currents are also canceled out. The Alternating Polarity method consists in applying a voltage of positive polarity, then the current is measured after a specified delay (Measure Time); next

the polarity is reversed and the current measured again by using the same delay. This process is repeated continuously, and the resistance is calculated based on a weighted average of the four most recent current measurements. This method typically produces highly reproducible, accurate measurements of the resistance. After some preliminary tests, the measure time was fixed at 30s and the number of cycles was 5 for all the samples.

In Figure 32 is reported an example of the alternating polarity measurement on eumelanin-based devices.

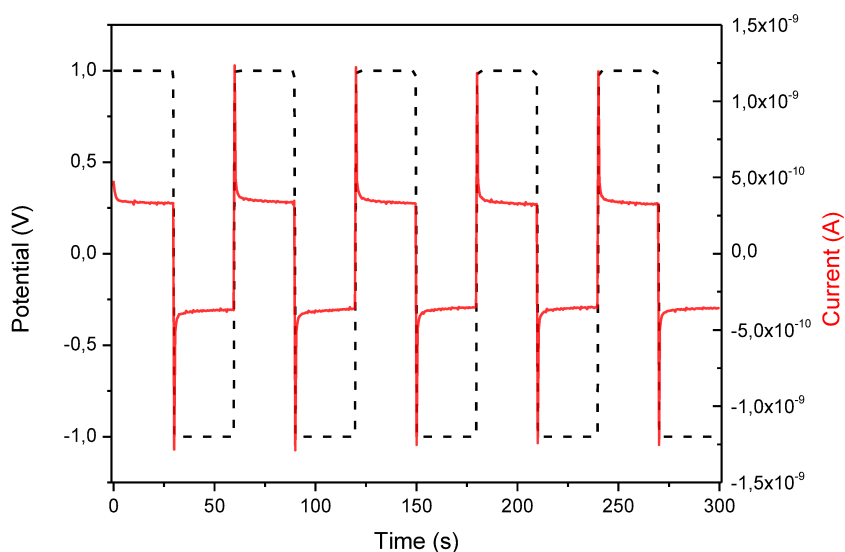


Figure 32: Alternating polarity measurement on a 2-electrode DHI-eumelanin device

DHI_melanin, DHICA_melanin and DHI/DHICA_melanin devices realized by using the AISSP method were characterized from 45 to 72% of relative humidity in nitrogen and hydrogen atmosphere.

In Figure 33 are reported the conductivity values at the different humidity values for all the experimental conditions.

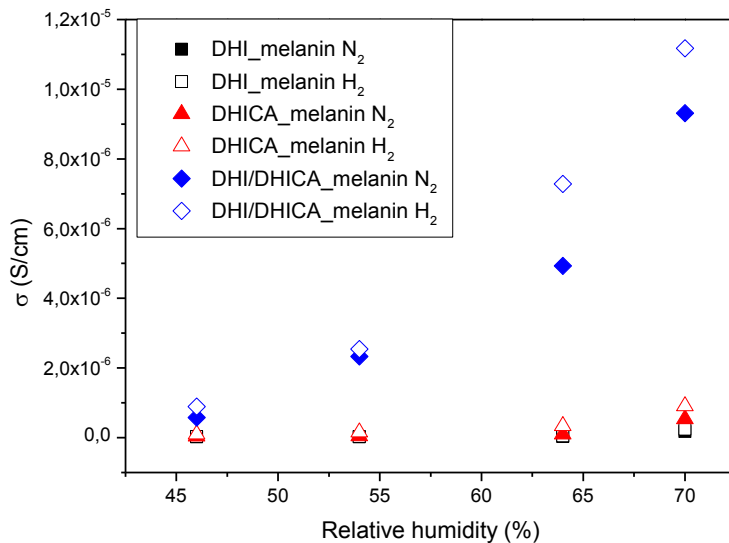


Figure 33: Conductivity values evaluated by the alternating polarity method by using the Ohm law

For all the samples the conductivity increases with the humidity and the hydrogen flux. Under hydrogen flux, palladium electrodes became PdH_x that can act as electrodes for protons and so the higher current is imputable to an additional protonic component. As observed in the previous paragraph, the material with highest conductivity is the DHI/DHICA_melanin.

The time dependence of the transient current was also analyzed to get more informations. A typical current vs time curve is reported in Figure 34.

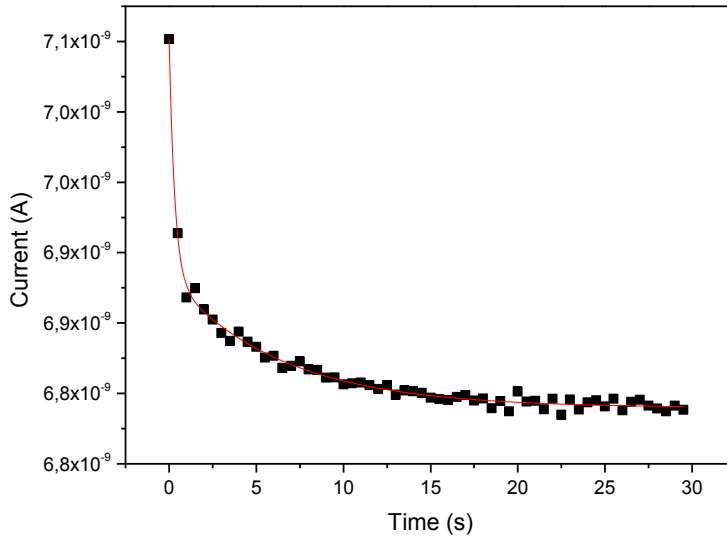


Figure 34: Typical current vs time curve for the eumelanin devices

The experimental curves can be fitted by using the following double exponential decay (eq. 6).

$$I(t) = I_{\infty} + I_1 \exp\left(-\frac{t}{\tau_1}\right) + I_2 \exp\left(-\frac{t}{\tau_2}\right) \quad (6)$$

in which is possible to distinguish two different time constants τ_1 and τ_2 , with $\tau_1 \approx 1$ and $4s < \tau_2 < 15s$. The double exponential decay is usually employed to describe a transport mechanism in which two different species are involved. Since eumelanins are considered hybrid ionic-electronic conductors, the two different time constants probably account for the movement of electrons and protons; protons are heavier than electrons with a consequent slower decay. Charge trapping phenomena and the proton accumulation at the eumelanin/Pd interface can further influence the time constants. Furthermore, measurements with PdH_x electrodes show a smaller τ_2 with respect to the corresponding samples with Pd. Since Pd is a proton blocking electrode, it causes the accumulation of charges at

the eumelanin/electrode interface and this effect can slow down the proton transport. The proton accumulation doesn't occur with the PdH_x electrodes.

All the experimental evidences confirm that eumelanins act as hybrid ionic-electronic conductors and that the humidity enhances this characteristic. The conductivity values observed for the different samples confirm again the importance of the chemical composition in the determination of the material properties.

~CONCLUSIONS~

The thin film fabrication and the electric conduction properties are two important aspects to be explored when we think to eumelanins in organic electronics.

In this section, the solid state polymerization of the DHI monomer under controlled ambient conditions was studied. It was evaluated the effect of the oxygen, water and temperature on the kinetic of the polymerization process and on thin film morphology.

Since the polymerization consists in a series of oxidative reactions, the oxygen flux is fundamental for the determination of the process rate; water vapour and temperature further accelerate the oxidation. The morphology of the final eumelanin thin film is also influenced by the polymerization conditions. Eumelanin thin films obtained at higher temperatures and oxygen flows show higher roughness and heterogeneity. About the water vapour effect on the eumelanin thin film, although it accelerate the oxidative process, it is also able to give a solubilization effect of the material during the polymerization with a smoothing effect.

About the conduction properties, electric measurements of eumelanin thin films realized by AISSP were carried out. The experimental results confirm the capability of the eumelanin materials to act as hybrid ionic-electronic conductors under humidity conditions. The presence of traps, the morphology and the chemical composition further influence the electric properties as observed for most of the disordered organic materials. The right synergy between morphology, chemical composition and electric properties is still an open issue.

~EXPERIMENTAL SECTION~

- DHI and Eumelanin thin film deposition via AISSP

DHI and DHICA were synthesized according to protocols reported in 2006 by Edge et al.⁵⁶ DHI thin films were prepared by spin coating starting from a methanol solution.

For the study of the solid state polymerization process, DHI was deposited in the inner of a glass lid starting from a 20 mg/ml (spinning program: 2000 rpm x 1000 rpm/s x 30s). The glass lids were sealed in a glove-box by using the UV-curable epoxy resin ZEOGLUE-HV/SEU10 (SAES GETTERS) and a plastic barrier layer (PS, PET, PET/SiOx).

For the electrical measurements, DHI was deposited starting from a 10 mg/ml methanol solution (spinning program: 2500 rpm x 1200 rpm/s x 30s) on two different kind of substrates and contact. For the IV measurements, Si/SiO₂ substrates with 50 nm thick coplanar Pt patterned by photolithography were used and they were wet-cleaned and UV-ozone treated before the DHI deposition.

For the alternating polarity measurements, glass substrates with interdigitated palladium electrodes were used. In both cases, after the DHI deposition, substrates were exposed to a ammonia vapors (AISSP).

- Solid state polymerization and Morphological measurements

UV-visible transmission measurements were carried out by using a Lambda 900, Perkin Elmer, Waltham MA, USA. The reported polymerization time values are the average on three samples.

The surface roughness of the layers were investigated by interferometry based optical profilometer (Talysurf CCI HD, Taylor Hobson, Leicester, UK). The root mean square surface roughness was obtained according to the ISO 25178

standard and the reported values are the average results of the measurements made.

- Electrical characterization of eumelanin thin films

I-V measurements were performed in a chamber with controlled RH in air. The Pt electrodes were contacted with micromanipulated tungsten probes. A software-controlled source/measure unit (Agilent B2902A) was used for *I-V* measurements. *I-t* measurements were performed in a chamber with controlled RH and temperature under N₂ or N₂+5%H₂ flow.

The Pd and PdH_x electrodes were contacted with micromanipulated tungsten probes and the electrical measurements were performed with a Keithley 2400 SourceMeter.

Three devices per type were tested to verify the reproducibility of the results.

REFERENCES

- ¹ G. Prota et al, *Medicinal Research Reviews*, 1988, 8, 4, 525-556.
- ² P. Riley et al, *International Journal of Biochemistry and Cell Biology*, 1997, 29, 11, 1235-1239
- ³ F. A. Zucca et al, *Pigment Cell Research*, 2004, 17, 6, 610-617
- ⁴ E. Land et al, *Acc. Chem. Res.*, 2003, 36, 300–308
- ⁵ M. d'Ischia et al, *Adv. Heterocycl. Chem.*, 2005, 89, 1-63
- ⁶ M. d'Ischia et al, *Eur. J. Org. Chem.*, 2011, 28, 5501-5516
- ⁷ L. Panzella et al, *Org. Lett.*, 2007, 9, 1411-1414
- ⁸ A. Pezzella et al, *J. Org. Chem.*, 2007, 72, 9225-9230
- ⁹ M. G. Corradini et al, *Tetrahedron*, 1986, 42, 2083-2088
- ¹⁰ A. Pezzella et al, *Tetrahedron*, 1996, 52, 7913-7920
- ¹¹ J. Cheng et al, *Pigm. Cell. Res.*, 1994, 7, 63
- ¹² J. Cheng et al, *Pigm. Cell. Res.*, 1994, 7, 255
- ¹³ G. W. Zajac et al, *Biochim. Biophys. Acta Gen. Subj.*, 1994, 1199, 271-278
- ¹⁴ K. C. Littrell et al, *Photochem. Photobiol.*, 2003, 77, 115-120
- ¹⁵ A. Pezzella et al, *J. Am. Chem. Soc.*, 2006, 128, 15490 – 15498
- ¹⁶ A. Pezzella et al, *Tetrahedron*, 2002, 58, 3681-3687
- ¹⁷ A. Pezzella et al, *Tetrahedron Asymmetry*, 2003, 14, 1133-1140
- ¹⁸ A. Pezzella et al, *J. Org. Chem.*, 2009, 74, 3727 – 3734
- ¹⁹ M. L. Tran et al, *Biophys. J.*, 2006, 90, 743-752
- ²⁰ A. Pezzella et al, *J. of Am. Chem. Soc.*, 2009, 131, 15270-15275
- ²¹ P. Meredith et al, *Pigment Cell Research*, 2006, 19, 572-594
- ²² J. McGinness et al, *Science*, 1974, 183, 853–855
- ²³ M.M. Jastrzebska et al, *J. Biomater. Sci. Polymer*, 1995, 7(7), 577-586
- ²⁴ B. Rosenberg et al, *Ann NY Acad Sci*, 1969, 158, 161–190
- ²⁵ M. R. Powell et al, *Bioenergetics*, 1970, 1, 493–509
- ²⁶ M. Linh Tran et al, *Biophysical Journal*, 2006, 90(3), 743-752
- ²⁷ A. B. Mostert et al, *PNAS*, 2012, 109, 8943–8947
- ²⁸ J. Wünsche et al, *Journal of Material Chemistry B*, 2013, 1, 3836-3842
- ²⁹ J. Wünsche et al, *Chem. Mater.*, 2015, 27, 2, 436-442
- ³⁰ J. Wünsche et al, *Adv. Func. Mater.*, 2013, 23, 5591-5598
- ³¹ G. Mula et al, *Nanoscale Research Letters*, 2012, 7:377
- ³² G. Tarabella et al, *Chemical Science*, 2013, 4(4), 1395
- ³³ M. Sheliakina, *Materials Horizons*, 2018, 5(2), 256-263
- ³⁴ M. Piacenti da Silva et al, *AIP Advances*, 2014, 4, 037120
- ³⁵ T.-F. Wu et al, *Sensors and Actuators B Chemical*, 2016, 224, 178-184
- ³⁶ T.-F. Wu et al, *Adv. Mater. Interfaces*, 2015, 2, 1500203

- ³⁷ M. Ambrico et al, *Organic Electronics*, 2010, 11(11), 1809-181
- ³⁸ M. Ambrico et al, *Adv. Mater.*, 2011, 23(29), 3332-3336
- ³⁹ M. Ambrico et al, *Applied Physics Letters*, 2012, 100, 253702
- ⁴⁰ P. Kumar et al, *J. of Mater. Chem. C*, 2016, 4, 9516-9525
- ⁴¹ L. Migliaccio et al, *Advanced Electronic Materials*, 2017, 3, 1600342
- ⁴² J. P. Bothma et al, *Adv. Mater.*, 2008, 20, 3539–3542
- ⁴³ N. F. Della Vecchia et al, *Adv. Funct. Mater.*, 2013, 23, 1331–1340
- ⁴⁴ A. Pezzella et al, *Mater. Horiz.*, 2015, 2, 212–220
- ⁴⁵ S. Reale et al, *J. Mass Spectrom.*, 2012, 47, 49–53
- ⁴⁶ V. Coropceanu et al, *Chem. Rev.*, 2007, 107, 926-952
- ⁴⁷ A. Miller et al, *Phys. Rev.*, 1960, 120, 745
- ⁴⁸ J.O. Oelerich (Master Thesis), "Theoretical Description of Charge Transport in Organic Semiconductors", 2012
- ⁴⁹ S.D Baranovskii et al, *J. Phys. C*, 1997, 9, 2699
- ⁵⁰ Chen Li et al, *J. Phys. Chem. C*, 2014, 118, 10651-10660
- ⁵¹ H. Bassler, *Phys. Status Solidi. B*, 1993, 175, 15-56
- ⁵² K.-D. Kreuer et al, *Angewandte Chemie*, 1982, 21(3), 208-209
- ⁵³ N. Agmon, *Chemical Physics Letters*, 1995, 244, 456-462
- ⁵⁴ H. Morgan et al, *J. Phys. E: Sci. Instrum.*, 1986, 19
- ⁵⁵ C. Zhong et al, *Nature Communications*, 2011, 2, 476
- ⁵⁶ R. Edge et al, *Pigment Cell Research*, 2006, 19, 443-450

SECTION 3

SYNTHESIS OF NATURE-INSPIRED ELECTROLUMINESCENT MATERIALS FOR OLED APPLICATIONS

~INTRODUCTION~

○ TRANSITION METAL COMPLEXES

Transition metal complexes have been extensively studied in the past decades due to their wide range of applications.¹ Coordination compounds have been traditionally used as (photo)catalysts in a large number of organic reactions (i.e. the first and second generation of Grubbs' catalysts for metathesis reactions), but also find use as drugs in cancer treatment (i.e. cisplatin), as photosensitizers in photodynamic therapy, as contrast agents in bio-imaging and as bio-sensors (Figure 1).

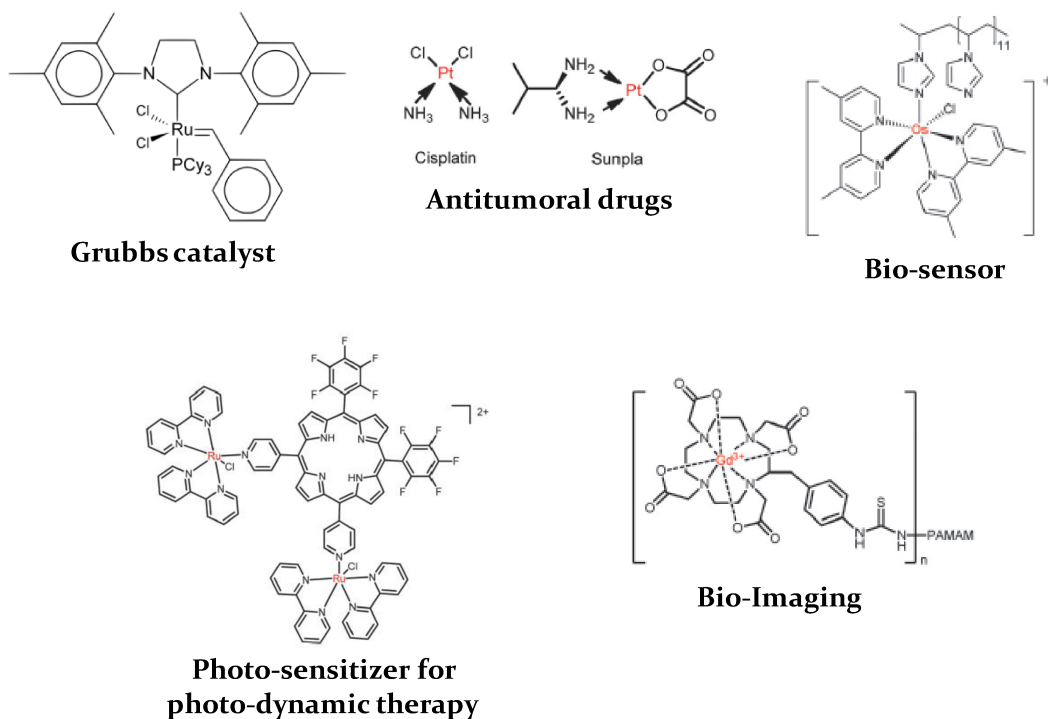


Figure 1: Examples of transition metal complexes applications

With the rise of organic electronics transition metal complexes have been object of new interest in particular for the applications in the optoelectronic field. Now

phosphorescent transition metal complexes are commonly used as emitting materials in OLED devices.

There are three kind of electronic transitions exhibited by these kind of complexes:

- Metal-Centered (MC) transitions between molecular orbitals localized on the metal centre. Since $d \rightarrow d$ transitions are forbidden according to the Laporte rule, their probability is very low;
- Ligand-Centered (LC) transitions between molecular orbitals localized on the ligands (es $\pi \rightarrow \pi^*$);
- Charge Transfer (CT) transitions between molecular orbitals of difference localization. Charge transfer transitions can be LMCT (ligand to metal charge transfer), MLCT (metal to ligand charge transfer) and LL'CT (ligand to ligand charge transfer).

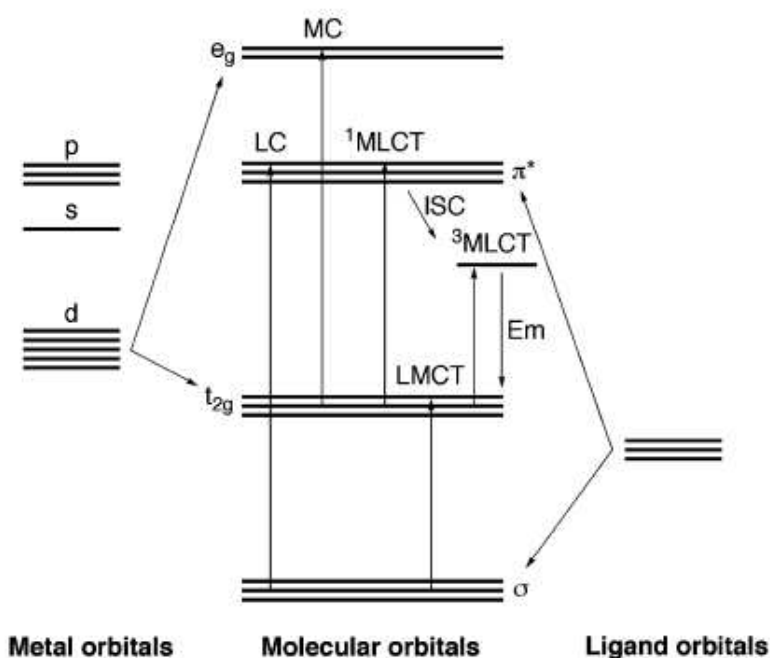


Figure 2: Schematic diagram for an octahedral d^6 metal complex involving 2-phenylpyridine (C_3 symmetry)-type ligands in which various possible transitions are indicated

Among transition metal complexes used as emitters in OLEDs, iridium (III) complexes have attracted much more attention for a series of properties making them suitable for applications in highly efficient devices. These are: 1) the quasi-octahedral geometry that allows the introduction of specific ligands in a controlled manner; 2) the photo-physical and electrochemical properties that are tunable in a predictable way; 3) the stable and easily accessible oxidation and reduction states; 4) the highest triplet quantum yields; 5) the strong spin-orbit coupling.

In 1984, Watts isolated the tris(2-phenylpyridine)iridium(III) complex ($\text{Ir}(\text{ppy})_3$) and reported a general protocol for its synthesis in higher yields.²

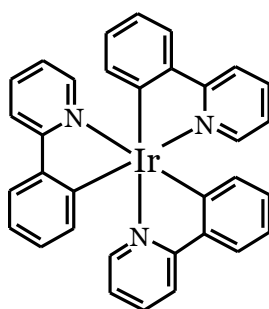


Figure 3: $\text{Ir}(\text{ppy})_3$ structure

$\text{Ir}(\text{ppy})_3$ is also the first and also one of the most popular phosphorescent green-emitter used in OLED devices. From that moment a number of scientific researchers have dedicated their work to the synthesis of variously substituted iridium(III) complexes. Key ligands for the synthesis of iridium complexes are generally derivatives of 2-phenylpyridine, 2,2'-bipyridine, picolinate or acetylacetonate, that are referred to as $\text{C}^{\wedge}\text{N}$, $\text{N}^{\wedge}\text{N}$, $\text{N}^{\wedge}\text{O}$ or $\text{O}^{\wedge}\text{O}$, respectively. Ligands can give rise to homoleptic ($[\text{Ir}(\text{L})_3]$) or heteroleptic $[\text{Ir}(\text{L})_2(\text{L}')]$ tris-cyclometalated complexes.

The tris-cyclometalated iridium(III) complexes exhibit a quasi-octahedral geometry and are always chiral (Figure 4). To distinguish the two enantiomers, the octahedron is viewed down a 3-fold axis. The enantiomer with left-handedness is labelled Λ , and that with right-handedness is Δ . Moreover, the tris-cyclometalated iridium(III) complexes are available in two different isomers, namely facial (fac) and meridional (mer) complexes (Figure 4). The facial isomers usually exhibit longer lifetimes and higher quantum efficiencies compared to the meridional isomer.³ In general, meridional isomers display a red-shifted emission compared to the facial ones. The formation of facial isomers is favored under high reaction temperatures due to their thermodynamic stability, whereas the kinetically favored mer-isomers can be isolated by performing the reactions at lower temperatures.⁴

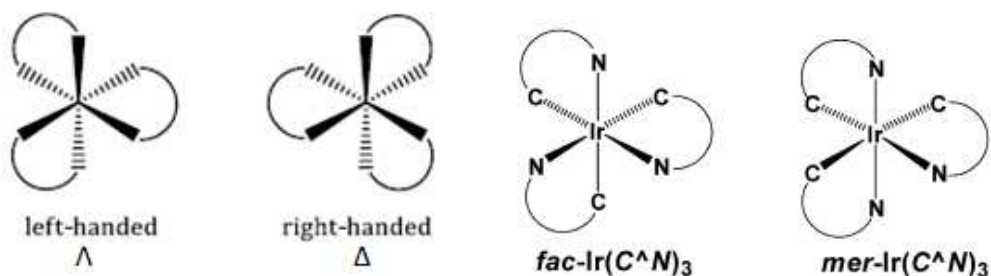


Figure 4: Λ -/ Δ -handedness enantiomers (left side) and facial/meridional isomers (right side) of cyclometalated iridium complexes.

In heteroleptic complexes, such as $[\text{Ir}(\text{C}^{\wedge}\text{N})_2(\text{O}^{\wedge}\text{O})]$, the ligands can arrange leading to cis and trans isomers (Figure 5).

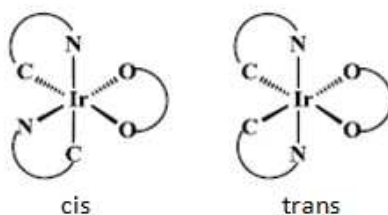


Figure 5: Cis and Trans isomers of neutral $[\text{Ir}(\text{C}^{\wedge}\text{N})_2(\text{O}^{\wedge}\text{O})]$ complexes

Light emission of iridium complexes depends on the structures of both cyclometalating and ancillary ligands. Therefore, it is possible to design a complex with specific photo-physical and electrochemical properties by a rational choice of the ligands. In particular, the maximum emission wavelength of iridium complexes depend on their HOMO-LUMO gap.

The color emission can be tuned by stabilizing or destabilizing the HOMO and/or LUMO levels of the complex through the insertion of electron-withdrawing or electron releasing substituents.

Specifically, DFT calculations were carried out for Ir(ppy)₃ to determine where are located the HOMO and LUMO levels in the complex.⁵ It is reported that the HOMO is mainly composed of π -orbitals of the phenyl ring and the d-orbitals of the metal, while the pyridine is the major contributor to the LUMO. Electron-withdrawing substituents on the phenyl ring will stabilize the metal-base HOMO, whereas electron-releasing substituents will lead to a destabilization of the HOMO level. On the other hand, the presence of electron-acceptor and electron-releasing substituents on the pyridine rings induce respectively a stabilization and a destabilization of the LUMO level. The position of the substituents on the phenyl and pyridine rings is another factor that can influence the HOMO or LUMO levels. The selection of a different heterocyclic backbone is another tool to properly induce a variation in the HOMO-LUMO levels. In Figure 6 it is shown how it is possible to tune the color emission of iridium complexes (in this case from green to red) by passing from 2-phenylpyridine to 1-phenylisoquinoline ligands.⁶

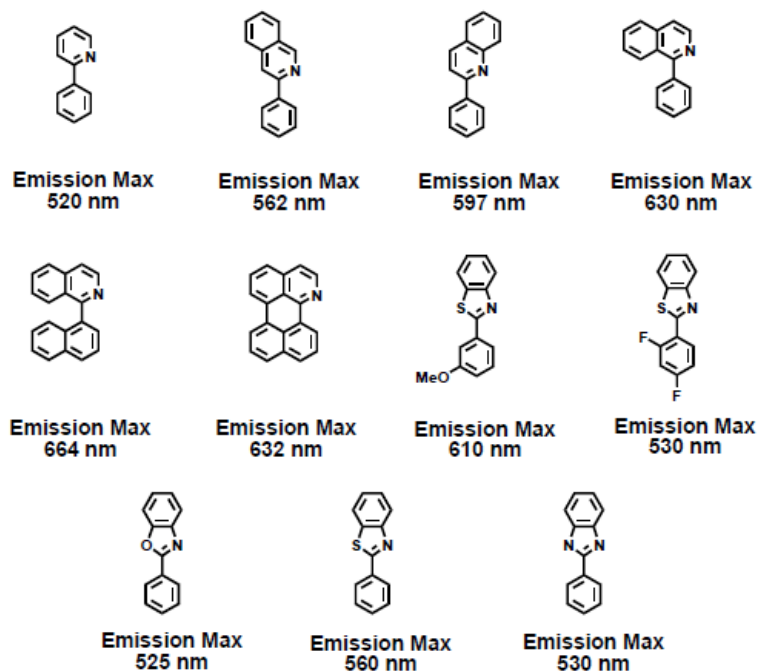


Figure 6: Tuning of color emission of iridium(III) complexes with different cyclometalating ligand

A vastness of different iridium complexes are now commercial available for the realization of OLED with all the primary colors as reported in Figure 7.

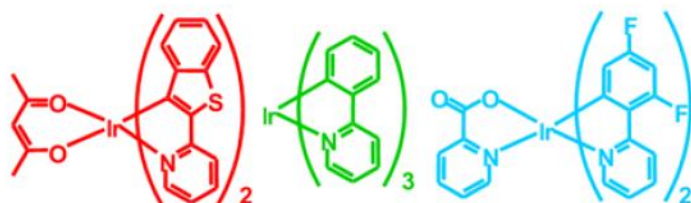


Figure 7: Example of iridium based phosphorescent dopants for RGB emitters

To achieve mass market, it is important to consider not only the device efficiency but also the manufacturing costs. Heavy metals are often expensive and not available on a large scale. On the contrary, zinc complex precursors are about 1400 times cheaper than the corresponding iridium complex precursors. Furthermore, reaction yields for the synthesis of iridium complexes are around

20%, while for Zn-complexes yields vary from 50 to 90%. In a low cost approach, Zn complexes represent very promising materials for cheaper OLED devices.

Zinc(II) complexes were studied in OLED devices for three main applications: emitting molecules, hosts for fluorescent and phosphorescent materials and electron transport materials.⁷ First of all, zinc complexes were mostly investigated as single emitters and/or emitters for bilayer devices (Figure 8).⁸ By using this approach, it is conceivable that the overall cost can be reduced through a more simplified device fabrication, although all reports clearly evidence that devices made by single-emitting layer are less efficient.

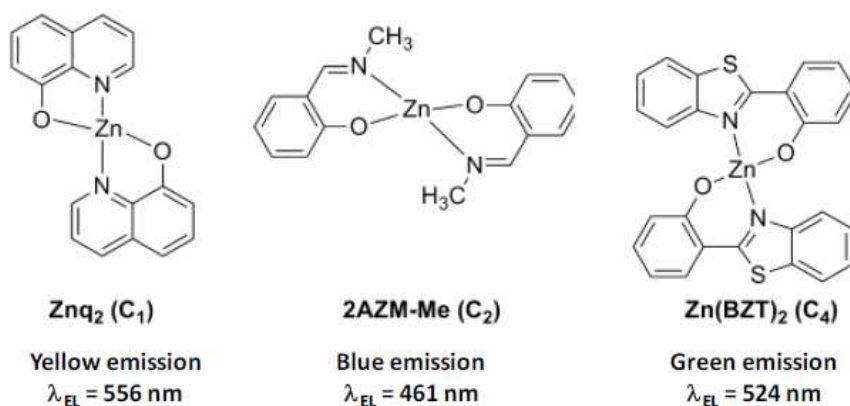


Figure 8: Zinc(II) complexes used in OLED devices as emitting layer

Recently, zinc complexes were studied as hosts for fluorescent and phosphorescent dopants (Figure 9).^{9,10} Metal complexes by their rigid molecular structures and improved thermal stabilities make these hosts of higher interests than conventional purely organic hosts. The results obtained in terms of improvement of external quantum efficiency (EQE) definitely proved the viability of this approach.

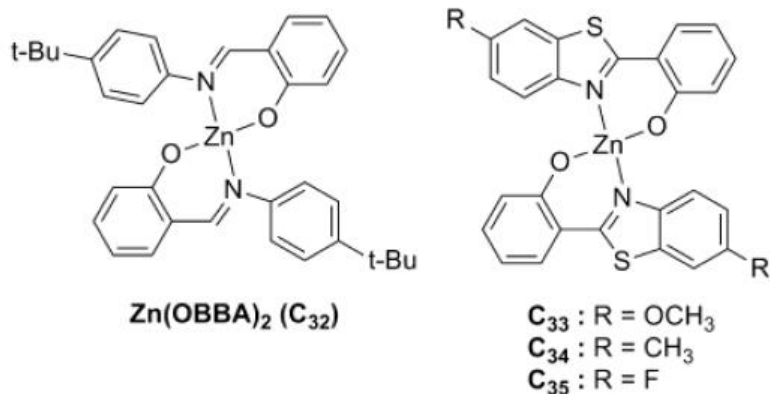


Figure 9: Zinc(II) complexes used in OLED devices as hosts

Finally zinc complexes were explored for electron transport layer due to their higher electron-transport ability over conventional electron-transport layers such as Alq₃ (Figure 10).¹¹

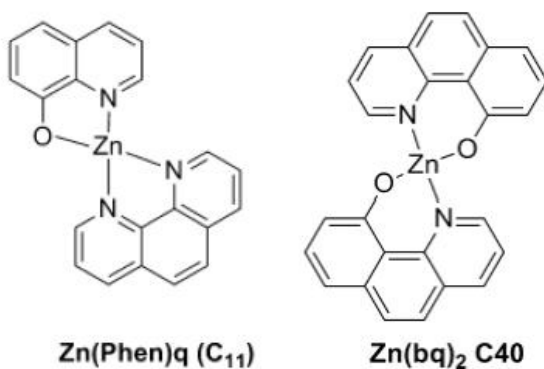


Figure 10: Zinc(II) complexes used in OLED devices as electron-transport layer

- AIMS

Starting from this background, my work has been aimed at the synthesis of Ir(III) and Zn(II) complexes featuring natural and nature-inspired ligands. In particular, the attention has been focused on dopamine, curcumin and 6-dehydrogingerdione.

Dopamine is a catecholic neurotransmitter, precursor of neuromelanin and monomer precursor of polydopamine. For our purposes dopamine was used as building block for the synthesis of C^N and N^O ligands for iridium complexes (Figure 11).

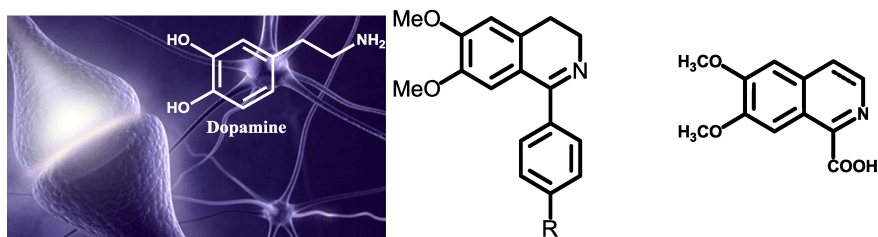


Figure 11: Dopamine inspired C^N and N^O ligands

Curcumin¹² and 6-dehydrogingerdione¹³ are β -diketones ligands extracted from plants of the Ginger family.

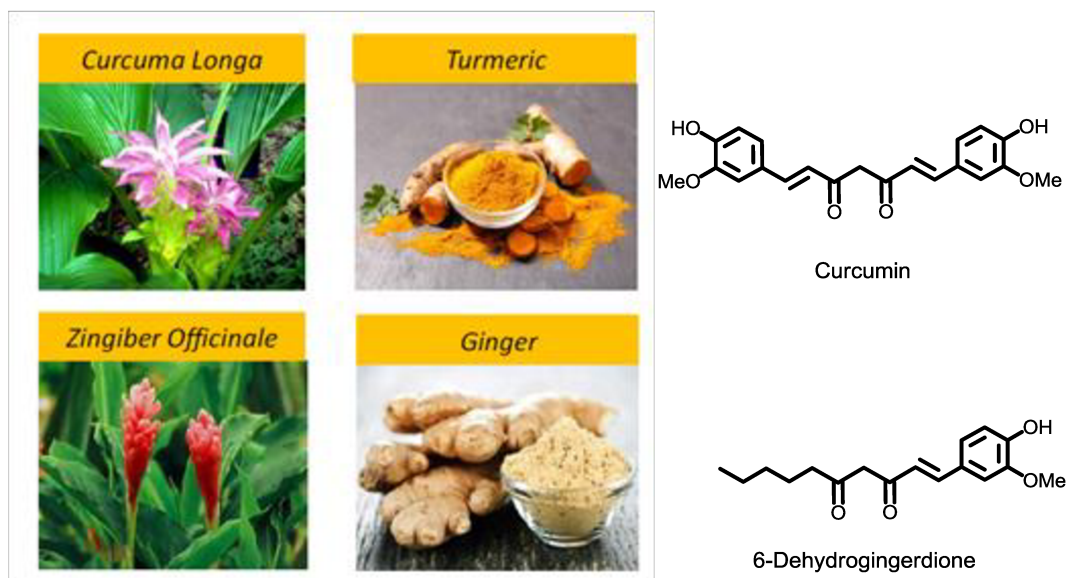


Figure 12: Natural β -diketones selected as ligands for TMCs

Curcumin is a component of the spice turmeric manufactured from the rhizomes of the plant *Curcuma Longa*, that is widely cultivated in tropical countries of South East Asia, especially in China and India.¹⁴

Besides its widespread use as food, flavor and colorant, turmeric has been used in traditional Chinese and Ayurvedic medicine for around 4000 years.

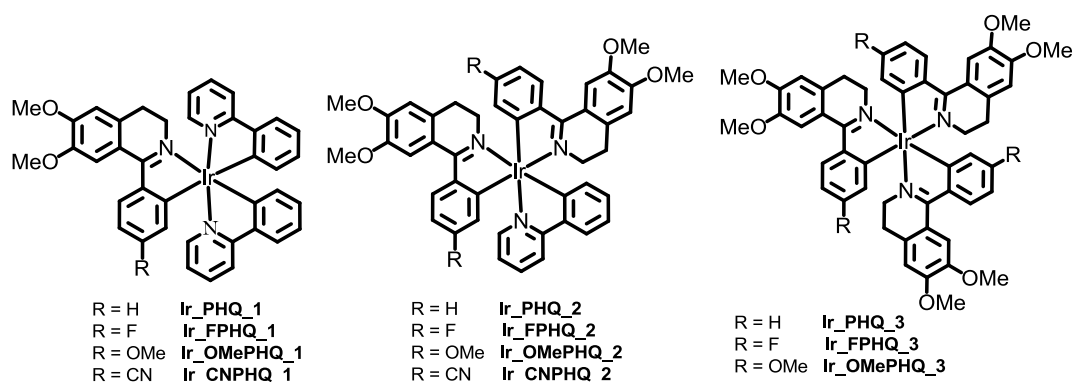
Over the past few decades, the medicinal properties of turmeric and curcumin, including antitumoral, antimicrobial, anti-inflammatory, antioxidant, antihepatotoxic, antihyperlipidemic, antiviral, and anti-Alzheimer's disease have been explored in numerous studies.¹⁵

6-Dehydrogingerdione is obtained from the rhizome of *Zingiber Officinale* belonging, together with *Curcuma Longa*, to the Zingiberaceae family.

6-Dehydrogingerdione is one of the major components of dietary ginger, used worldwide both as a spice and as a medicinal herb. 6-Dehydrogingerdione has received extensive attention due to its multiple pharmacological activities, including anti-inflammatory, analgesic, anti-tumoral and anti-oxidant activity.¹⁶

Curcumin and 6-dehydrogingerdione thanks to their keto-enol functionality can act as ligands for metal complex synthesis.

In detail, iridium and zinc complexes were synthesized by using the dopamine-inspired ligands, curcumin and 6-dehydrogingerdione which structures are reported in Figure 13 and Figure 14.



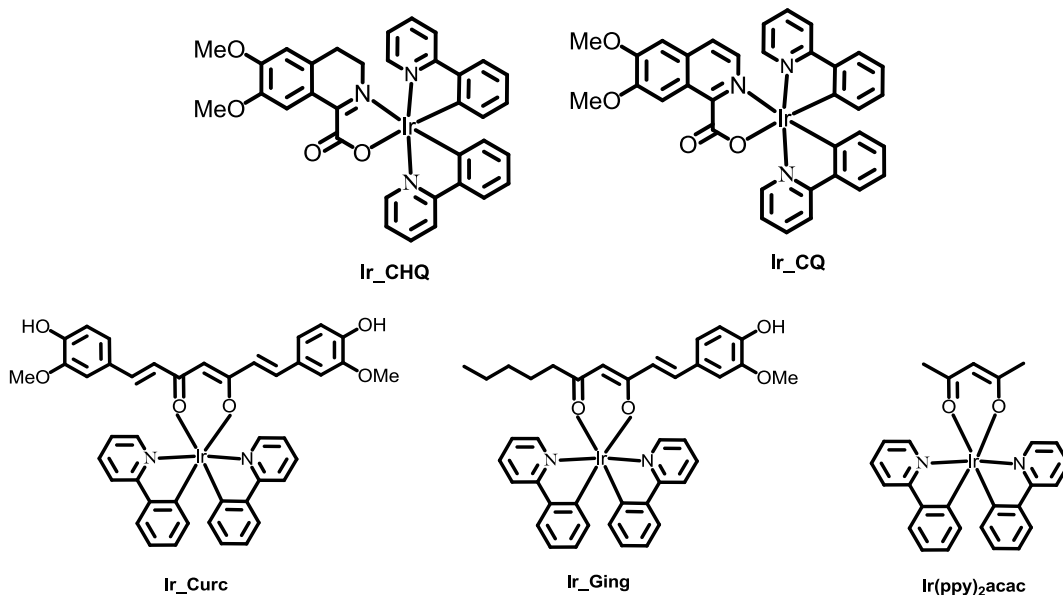


Figure 13: Synthesized Ir(III) complexes

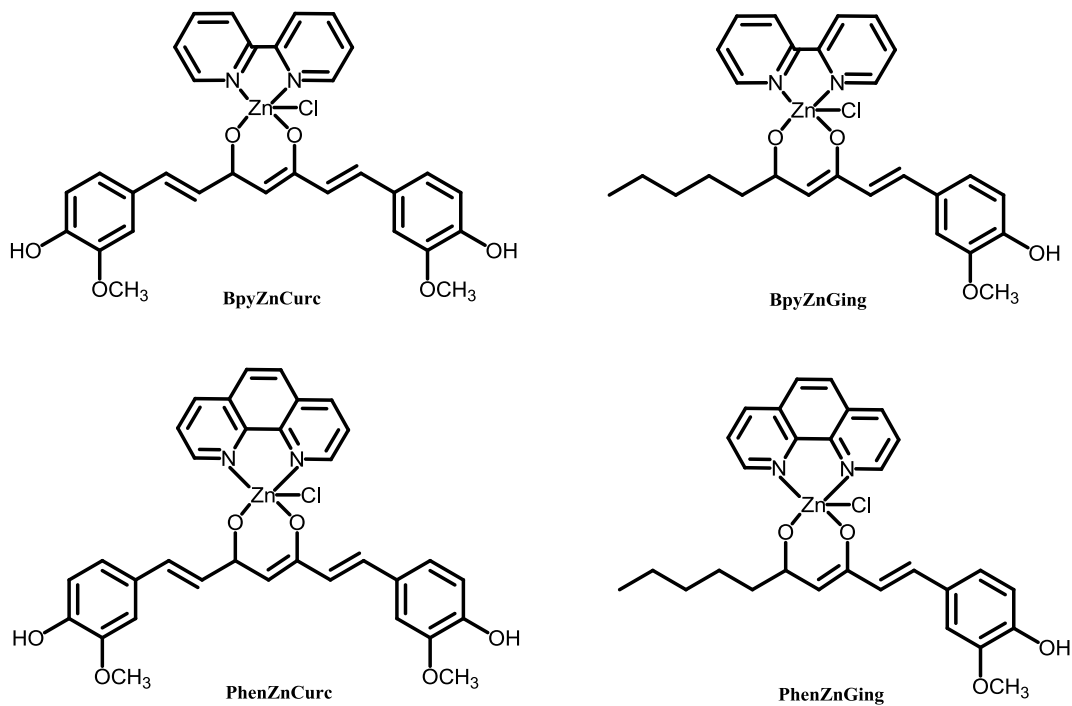


Figure 14: Synthesized Zn(II) complexes

In particular the use of the easily accessible zinc instead of iridium is a deliberate choice towards a green approach to OLED manufacturing.

All the synthesized complexes were completely characterized and tested as emitting materials in a standard OLED devices structure.

~RESULTS AND DISCUSSION~

○ SYNTHESIS OF DOPAMINE-INSPIRED IRIIDIUM (III) COMPLEXES AND APPLICATION IN OLED DEVICES

➤ Synthesis of C^N dopamine-inspired ligands

For the synthesis of the dopamine-inspired C^N cyclometalating ligands, the Bischler-Napieralski reaction was exploited in order to get a set of 6,7-dimethoxy-3,4-dihydroisoquinolines substituted on the 1 position with phenyl residues, functionalized on the para-position with different groups (PHQs).

In detail, for the synthesis of PHQs, the selected benzoic acid derivative (benzoic acid, 4-fluorobenzoic acid, 4-methoxybenzoic acid or 4-cyanobenzoic acid) was treated first with ethylchloroformate and triethylamine (TEA) in anhydrous dimethylformamide (DMF) at 0 °C, and then with *O,O*-dimethyldopamine at 60 °C. This afforded the amides *Am*_1-4 with yields ranging from 91 to 98% (Figure 15).

In the second step, the amides *Am*_1-4 were treated with POCl₃ in a mixture of ethanol/dichloromethane (EtOH/DCM) under reflux conditions to give the corresponding 1-phenyl-6,7-dimethoxy-3,4-dihydroisoquinoline derivative.

The identity of all the isolated compounds has been confirmed by ¹H and ¹³C NMR spectroscopy and ESI⁺ MS spectra.

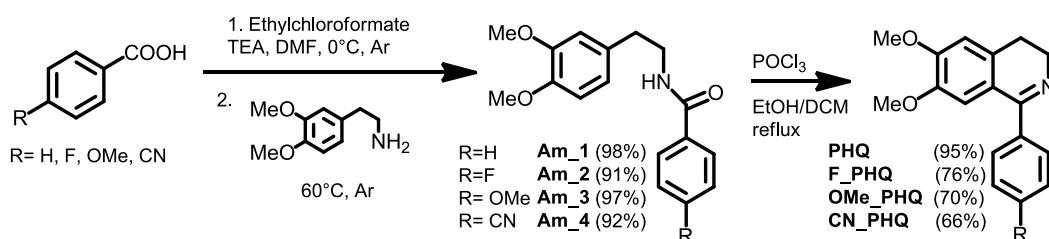


Figure 15: C^N ligands synthesis

➤ Synthesis of iridium complexes with C[^]N ligands (Ir_PHQs)

The iridium(III) complexes were obtained via the synthetic strategy developed by Nonoyama. This involves the intermediate formation of a dinuclear chloro-bridged iridium complex by reacting IrCl₃·nH₂O with stoichiometric amounts of the selected ligand under very mild conditions. The dinuclear chloro-bridged iridium complex can evolve toward the formation of the corresponding homoleptic iridium complex Ir(C[^]N)₃ by reacting with another C[^]N ligand or can lead to the formation of the heteroleptic iridium complex Ir(C[^]N)₂(C[^]N') by reacting with a different C[^]N' ligand.

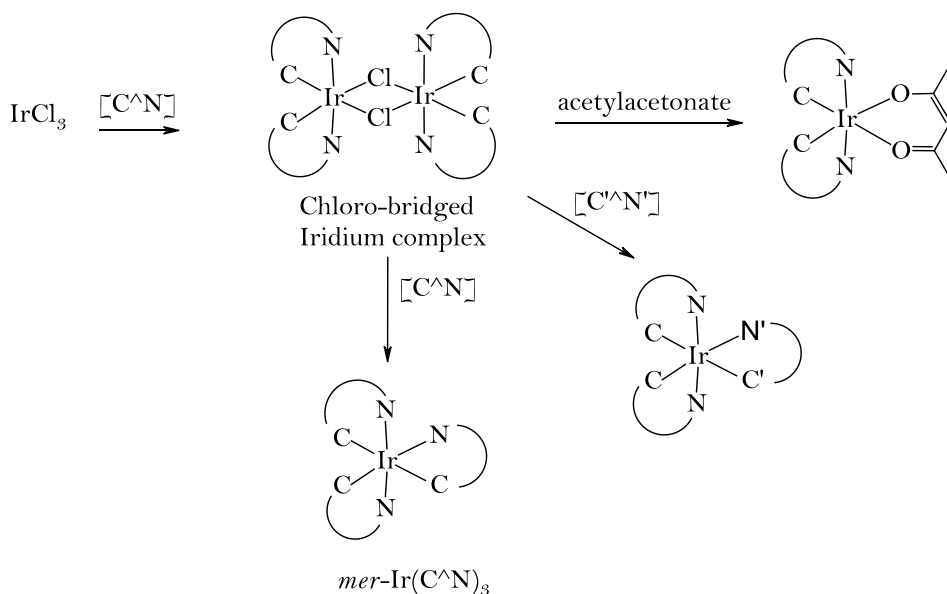


Figure 16: Synthetic pathways usually used for the synthesis of homoleptic or heteroleptic iridium (III) complexes

The synthesis of the chloro-bridged dinuclear complex was carried out by treating the iridium trichloride with 2.5 molar equivalents of 2-phenylpyridine in an ethoxyethanol/water mixture under an argon atmosphere and reflux conditions (Figure 17).¹⁷

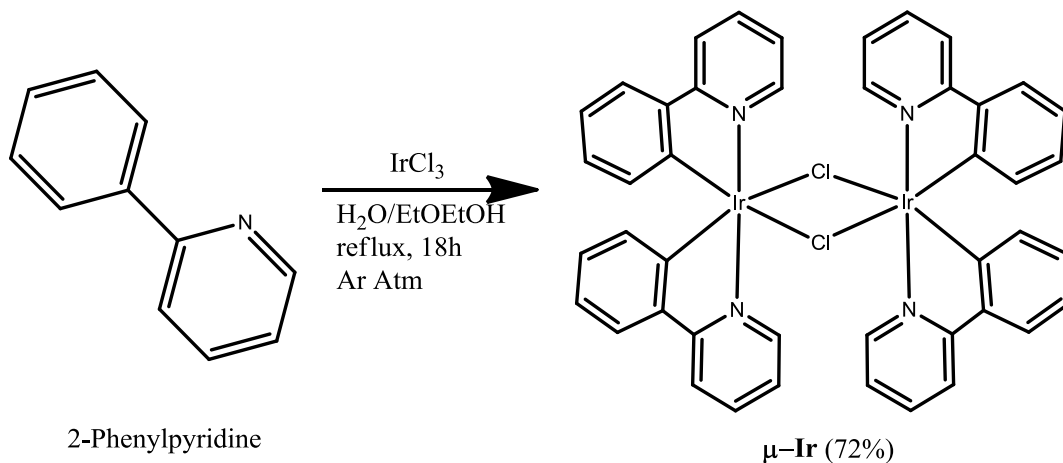


Figure 17: Synthesis of the dichloro-bridged dinuclear complex ($\mu\text{-Ir}$)

The complex $\mu\text{-Ir}$ was isolated after the addition of water to the reaction mixture as a yellow solid by filtration. Its identity and purity was checked by ^1H NMR; this latter showed a single pattern of resonances in the aromatic proton region accounting for the four ppy units, suggesting a trans arrangement of the ligands. Once obtained, the iridium complex $\mu\text{-Ir}$ was treated with the corresponding ligand previously synthesized.

When using the PHQ series of ligands, the complex $\mu\text{-Ir}$ was dissolved in dry DMF and treated with an excess of the proper ligand in presence of TEA and acetylacetonone under reflux conditions and in an argon atmosphere (Figure 18). After 48 h the reaction mixture was cooled to room temperature and the solvent was evaporated under reduced pressure to afford a solid constituted by a mixture of three complexes differing for the ratio between the PHQ and the ppy ligands. All the complexes were isolated in pure form by silica gel chromatography and subjected to mono- and bi-dimensional NMR spectroscopy and ESI⁺ MS analysis in order to confirm the structure of the compounds. In the case of the ligand CN-PHQ only two complexes were isolated with a mono and bis substitution of the PHQ ligand.

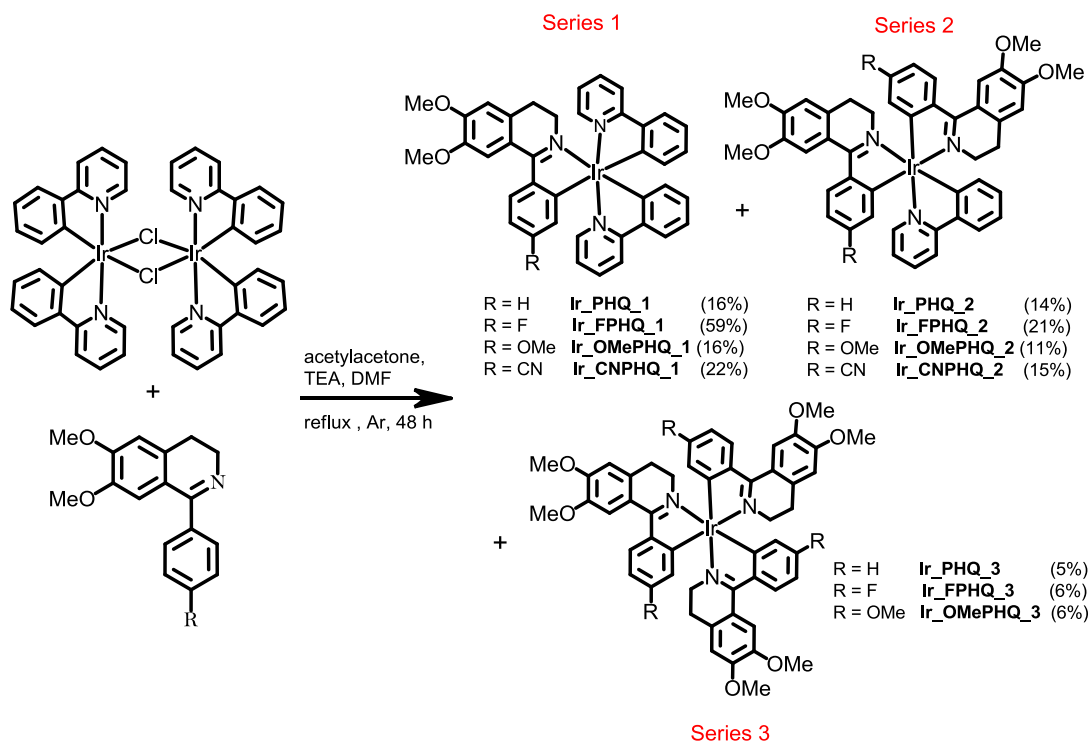


Figure 18: Synthesis of the Ir_PHQ complexes

All the synthesized complexes were fully characterized by ^1H and ^{13}C NMR analysis confirming the structures. ^{19}F NMR spectroscopy was also used to confirm that the *fac*-isomer of the homoleptic iridium complexes trisubstituted with PHQ_F-type ligands was formed.

➤ Photophysical Characterization of Ir_PHQ complexes

A comparative analysis of the photo-physical properties of the synthesized complexes was carried out by UV-vis and emission spectroscopy to assess: 1) the absorption and emission properties of the complexes; 2) the eventual role played by oxygen in quenching the emission radiation of the complexes; 3) the role played by the different ligands; 4) the influence of the different ratio between the

ppy and phenyl-3,4-dihydroisoquinoline units within the same series of complexes; 5) the effects of the nature of the functional groups on the phenyl ring of the phenyl-3,4-dihydroisoquinoline ligands.

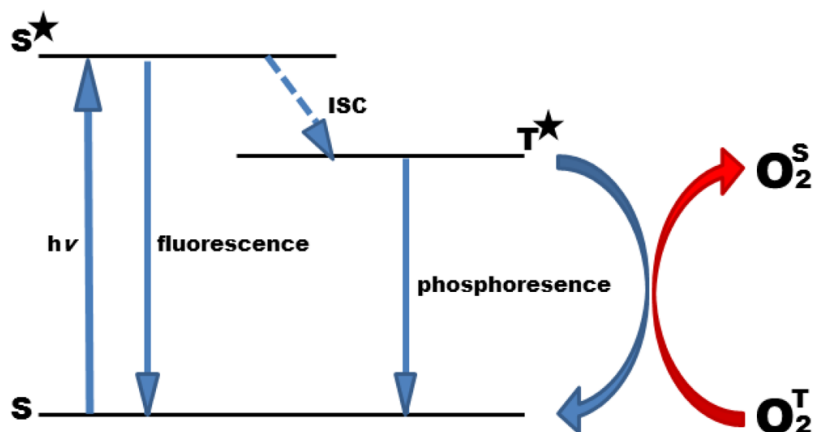


Figure 19: Jablonski diagram showing the oxygen quenching

Dilute solutions (1×10^{-6} M) of each of the complexes were prepared. For all the compounds, the molar extinction coefficients (ϵ) were calculated according to the Lambert-Beer Law

$$A = \epsilon lc$$

with:

ϵ = molar extinction coefficient

l = optical path length

c = molar concentration

The quantum yields (Φ) for all the complexes are reported in air and in oxygen depleted conditions referred to fluorescein, selected as standard ($\Phi = 0.9$ in a 0.1 M solution of NaOH), and were calculated using the following formula:

$$\phi_x = \Phi_{st} \cdot \frac{B_x}{B_{st}} \cdot \frac{n^2 \text{ solv}_x}{n^2 \text{ solv}_{st}}$$

where:

Φ_{st} = quantum yield of the reference standard

B_x = integral of the emission spectrum of the compound / absorbance of the compound at λ_{exc}

B_{st} = integral of the emission spectrum of the standard / absorbance of standard at λ_{exc}

η_{solv_x} = refractive index of the solvent in which the compound has been dissolved

$\eta_{solv_{st}}$ = refractive index of the solvent in which the standard has been dissolved

The overall photo-physical data are listed in Table 1.

Table 1: Photo-physical data of compounds Ir_PHQ_1-3, Ir_FPHQ_1-3, Ir_OMePHQ_1-3 and Ir_CNPHQ_1-2

Compound	UV-vis λ_{max} , nm ($\log \epsilon$, $M^{-1}cm^{-1}$) ^a	PL λ_{em} , nm (λ_{ecc} , nm) ^a	Φ (λ_{em} , nm) ^b	Φ (λ_{em} , nm) ^c (no O ₂)	UV-vis λ_{max} , nm ^d	PL λ_{em} , nm (λ_{ecc} , nm) ^a	E_g opt, eV
	SOLUTION				FILM		
<i>Ir_PHQ_1</i>	283 (4.15), 332 (sh), 391 (3.73), 480 (2.99)	626 (480)	0.41% (626)	0.30% (620)	342 393 449	610, 662 (480)	2.46
<i>Ir_PHQ_2</i>	283 (4.58), 320 (sh), 400 (4.17), 500 (3.39)	630 (500)	0.14% (630)	0.26% (628)	311 400 507	530, 616, 632, 671 (500)	2.43
<i>Ir_PHQ_3</i>	280 (4.56), 330 (sh), 400 (4.10), 500 (3.36)	627 (500)	0.18% (627)	0.23% (625)	342 397 505	611, 671, 685 (500)	2.42
<i>Ir_FPHQ_1</i>	280 (4.40), 330 (sh), 382 (3.96), 480 (3.19)	613 (480)	0.24% (613)	0.70% (604)	362 390 485	615, 639, 671 (480)	2.44
<i>Ir_FPHQ_2</i>	280 (4.35), 325 (3.91), 385 (4.04), 480 (3.28)	613 (480)	0.15% (613)	0.40% (595)	341 391 478	517, 604, 664 (480)	2.38
<i>Ir_FPHQ_3</i>	275 (4.11), 325 (sh), 383 (3.73), 480 (2.95)	605 (480)	0.19% (605)	0.22% (603)	339 387 475	509, 526, 594, 660 (480)	2.37
<i>Ir_OMePHQ_1</i>	284 (6.62), 382 (4.11), 490 (3.27)	617 (490)	0.21% (617)	0.61% (603)	340 388 468	603, 661 (490)	2.60

<i>Ir_OMePHQ_2</i>	288 (4.31), 386 (3.92), 490 (3.17)	617 (490)	0.15% (617)	0.23% (615)	335 367 388 492	606, 663 (490)	2.54
<i>Ir_OMePHQ_3</i>	295 (4.73), 390 (4.42), 490 (3.67)	617 (490)	0.13% (617)	0.19% (616)	332 370 393 500	609,658 (490)	2.54
<i>Ir_CNPHQ_1</i>	340 (4.13), 405 (4.00), 420 (4.02),540 (3.18)	656, 712 (540)	0.11% (656)	0.14% (653)	341 420 545	643, 661 (540)	2.14
<i>Ir_CNPHQ_2</i>	340 (4.10), 416 (4.04), 540 (3.17)	648, 710 (540)	0.14% (648)	0.15% (649)	341 394 422 535	635, 667 (540)	2.11

[a] Determined in diluted solutions in dichloromethane (1×10^{-6} M); [b] determined relatively to fluorescein $\Phi=0.9$ in a 0.1 M solution of NaOH); [c] determined in oxygen free solutions of DCM; [d] determined as thin film on glass substrates.

The absorption profiles of the iridium(III) complexes were quite similar within each series (Figure 20a). The intense maxima below 300 nm can be assigned to the spin-allowed $^1\pi-\pi^*$ transition of the cyclometalating ligand with high molar extinction coefficient ($\log\epsilon > 10000 \text{ M}^{-1}\text{cm}^{-1}$); for the homoleptic complexes, these bands account for the transitions within the PHQ ligands, while in the heteroleptic complexes these bands are composed by a mixture of π and π^* orbitals of both PHQ and ppy ligands.

Bands below 450 nm can be assigned to the spin-allowed metal-ligand charge transfer ($^1\text{MLCT}$) characterized by values of $\log\epsilon > 5000 \text{ M}^{-1}\text{cm}^{-1}$. The small bands ranging between 450 nm and 550 nm can be assigned to the spin-forbidden $^3\text{MLCT}$ band; the relatively high intensity of these bands indicates an efficient spin-orbit coupling that is a prerequisite for good phosphorescent emission.

Within each series, the absorption maxima of the complexes did not suffer any significant shift except for bands at around 300 nm confirming the nature of these states; fixing the ratio between the ppy and the PHQ units, the insertion of the fluorine and the methoxy group on the phenyl ring induced a small hypsochromic

effect on the absorption maxima while the cyano group produced a bathochromic shift.

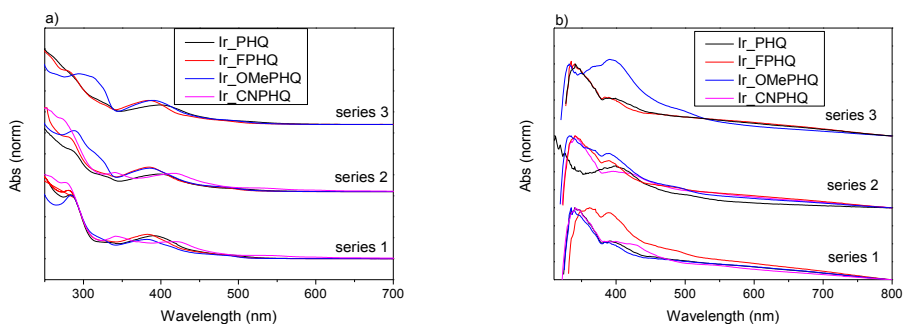


Figure 20: a) Normalized absorption spectra of complexes IrPHQs from DCM solution; b) Normalized absorption spectra of complexes IrPHQs from thin film on glass substrates

The emission spectra registered in dilute solutions of DCM showed for all the complexes a red emission, with maxima ranging from 600 to 660 nm. Also in this case, similar emission maxima within each series of complexes were observed (Figure 21). Worthy of note is the effect of the substituent on the phenyl ring on the emission wavelength of the complexes. Phosphorescence quantum yields proved quite high and consistent with those reported in the literature for similar iridium(III) complexes. For most of the complexes it was observed higher quantum yields and a significant quenching effect exerted by oxygen, with quantum yields that in some cases tripled when the emission spectrum was registered on oxygen free solutions of the complexes.

UV-vis and emission spectra of all the characterized complexes registered in thin films (Figure 20b-Figure 21b) indicated an appreciable bathochromic shift (red shift) of the absorption and emission maxima with respect to spectra obtained in solution and long tails at the lower energy edge suggesting aggregation of these complexes in the solid state.

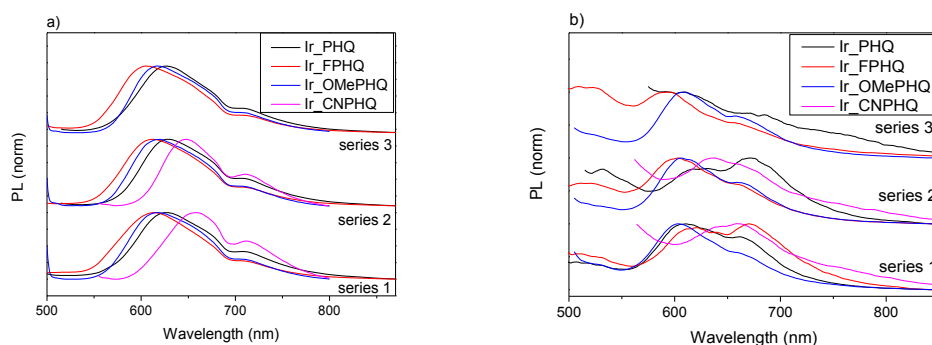


Figure 21: a) Normalized emission spectra of complexes IrPHQs from DCM solution; b) Normalized emission spectra of complexes IrPHQs from thin film on glass substrates

➤ Cyclic Voltammetry Ir_PHQ complexes

Cyclic voltammetry is a very suitable method for a wide range of applications and it is considered one of the most useful methods to characterize organic materials and estimate the energy band diagram

Redox processes can be recognized using cyclic voltammetry method by measuring the potentials of reduction and oxidation processes. Ferrocene is used as a known reference to calculate the energy of the HOMO and LUMO levels.

The cyclic voltammetry measurements and a summary table are reported.

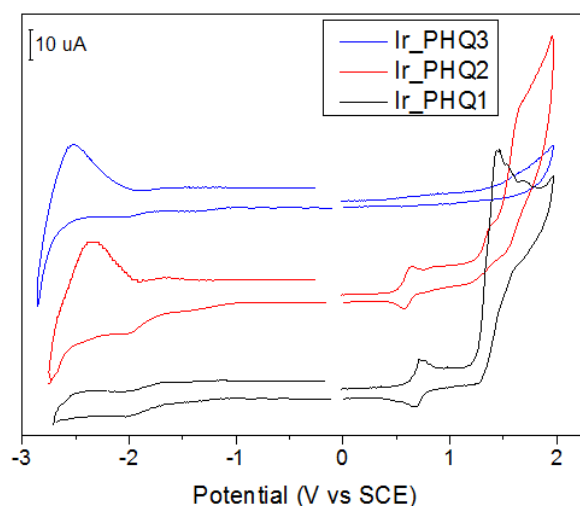


Figure 22: Cyclic voltammetry of Ir_PHQ_1-3

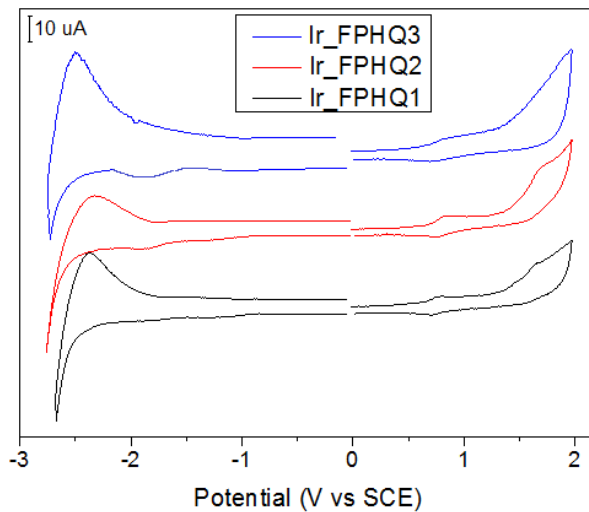


Figure 23: Cyclic Voltammetry Ir_FPHQ_1-3

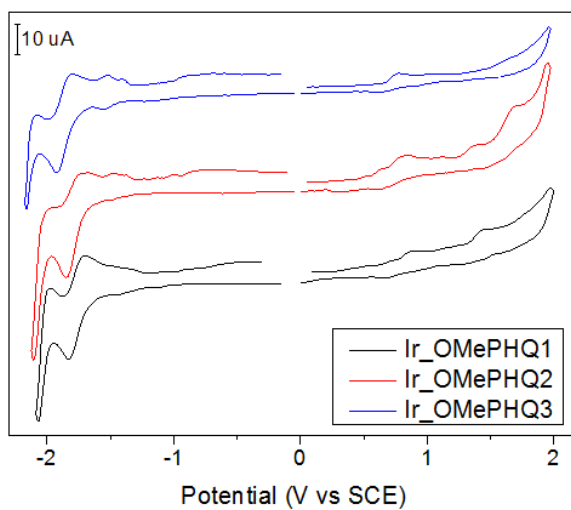


Figure 24: Cyclic Voltammetry Ir_OMePHQ_1-3

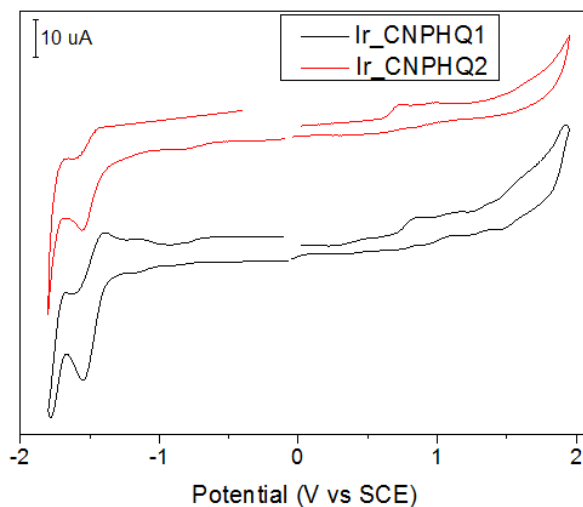


Figure 25: Cyclic Voltammetry Ir_CNPHQ_1-2

Table 2: Cyclic Voltammetry data IrPHQs

Compound	$E_{\text{onset}}^{\text{Ox}}$ (SCE) (V)	HOMO level (eV)	$E_{\text{onset}}^{\text{Red}}$ (SCE) (V)	LUMO level (eV)	HOMO-LUMO gap (eV)	Optical E_g (eV)
Ir_PHQ_1	0.61	-5.31	-1.72	-2.98	2.33	2.46
Ir_PHQ_2	0.51	-5.21	-1.74	-2.96	2.25	2.43
Ir_PHQ_3	0.41	-5.11	-1.77	-2.93	2.18	2.42
Ir_FPHQ_1	0.59	-5.29	-1.69	-3.01	2.28	2.44
Ir_FPHQ_2	0.64	-5.34	-1.60	-3.10	2.24	2.38
Ir_FPHQ_3	0.64	-5.34	-1.52	-3.18	2.16	2.37
Ir_OMePHQ_1	0.74	-5.44	-1.65	-3.05	2.39	2.60
Ir_OMePHQ_2	0.6	-5.3	-1.70	-3.00	2.30	2.54
Ir_OMePHQ_3	0.68	-5.38	-1.68	-3.02	2.36	2.54
Ir_CNPHQ_1	0.69	-5.39	-1.38	-3.32	2.07	2.14
Ir_CNPHQ_2	0.64	-5.34	-1.39	-3.31	2.03	2.11

The complexes are under investigation with computational methods to determine where are located the HOMO and LUMO levels, furthermore is difficult to give a complete explanation about the variation of the HOMO and LUMO values with the different substituents.

Otherwise, important observations result from the analysis of the energy gap values. Usually the gap obtained by cyclic voltammetry is smaller than that evaluated by optical measurements, but it is clear that the nature of the substituents strongly influence the electronic layout of the complexes. To explain this effect, the plots of the energy gap against the Hammett constant σ is reported for both optical and cyclic voltammetry gaps. The good correlation shown in this plots suggested that it is possible to tune in a predicted manner energy values of these kind of iridium complexes by introducing the proper functional group. In particular, it has been possible to rise the optical band gap by selecting electron releasing groups or to reduce it by inserting electron withdrawing groups.

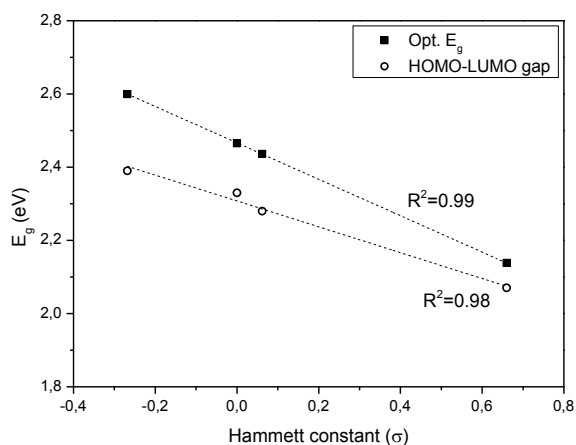


Figure 26: Correlation between E_g and Hammett constant for $\text{Ir}(\text{ppy})_2\text{PHQ}$ complexes

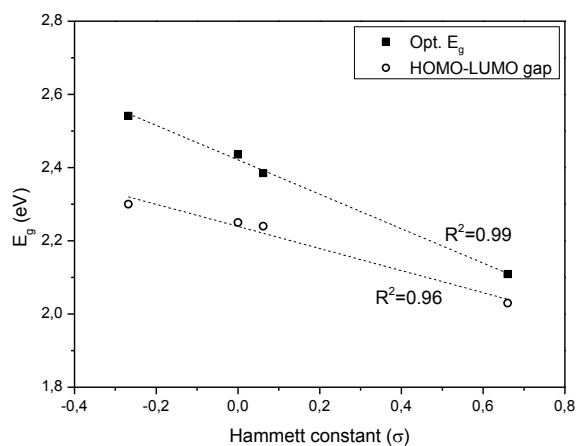


Figure 27: Correlation between E_g and Hammett constant for Ir(ppy)(PHQ)₂ complexes

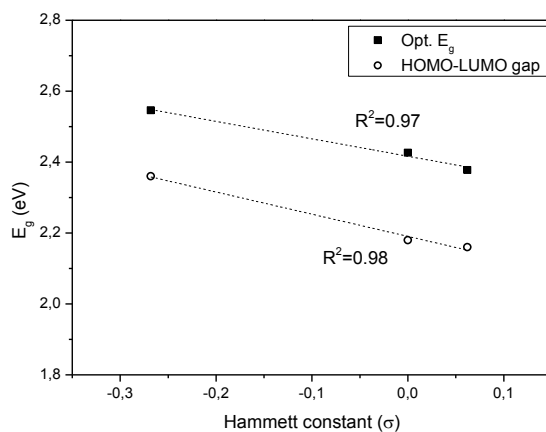


Figure 28: Correlation between E_g and Hammett constant for Ir(PHQ)₃ complexes

➤ OLED devices with Ir_PHQ complexes

The data obtained from the photo-physical analysis proved very encouraging, so that the Ir_PHQs complexes were tested as organic emitters in OLED devices.

According to data reported in the literature on the fabrication of OLED devices by using similar iridium(III) complexes, the complexes were used as “guest” by mixing

them at different percentage (2%, 6% and 12% w/w) with the 4,4'-bis(N-carbazolyl)-1,1'-biphenyl (CBP) selected as the "host".

As described, the use of emitting layers doped with organic phosphorescent transition metal complexes affords high efficient OLED devices due to specific mechanisms of energy transfer (see Introduction).

The scheme reported in fFigure 29 shows the configuration of the OLED devices fabricated.

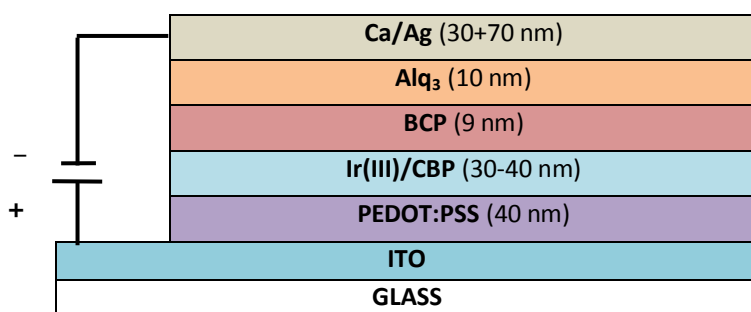


Figure 29: OLED multilayer structure fabricated using the synthesized complexes

The structure of the fabricated OLED devices is: *ITO/PEDOT:PSS/Ir:CBP(%)/BCP/Alq₃/Ca/Ag*.

OLED devices were fabricated on ITO (indium tin oxide) sputtered glass substrates used as anode; ITO was patterned by photolithography and wet chemical etching. These glass/ITO substrates were then cleaned with deionized water and detergent in an ultrasonic bath, then rinsed with acetone and isopropyl alcohol, and dried in oven at 130 °C for at least two hours. An UV/O₃ treatment was applied to remove organic residues and improve wettability of the ITO surface. A hole injection layer (HIL) of poly(3,4-ethylenedioxythiophene): polystyrenesulfonate (PEDOT:PSS) was spin coated and baked in oven at 115°C (thickness 40 nm). Subsequently, the organic emitting layer constituted by a blend of the iridium complex in CBP was spin coated onto the HIL layer. The samples were finally placed on a hot plate at a

temperature of 80 °C for 30 min in a glove box for the curing of the active material. Substrates were then loaded into a glove box system, integrated with the evaporation system (Kurt J. Lesker Company® SPECTROS 150) before being loaded in the process chamber; functional organic layers and cathodes were deposited. The evaporated organic materials were: 2,9-Dimethyl-4,7-diphenyl-1,10-phenanthroline (BCP) as hole blocking layer (HBL), tris-(8-hydroxyquinoline) aluminium (Alq₃) as electron transport layer (ETL), and finally a bilayer of calcium and silver as the cathode.

In Table 3 and Table 4 are listed the devices and the relative performances.

Table 3: OLED devices realized with IrPHQs

Entry	Complex (% in CBP)	Entry	Complex (% in CBP)	Entry	Complex (% in CBP)
1a	Ir_PHQ_1 (2%)	1b	Ir_PHQ_1 (6%)	1c	Ir_PHQ_1 (12%)
2a	Ir_PHQ_2 (2%)	2b	Ir_PHQ_2 (6%)	2c	Ir_PHQ_2 (12%)
3a	Ir_PHQ_3 (2%)	3b	Ir_PHQ_3 (6%)	3c	Ir_PHQ_3 (12%)
4a	Ir_FPHQ_1 (2%)	4b	Ir_FPHQ_1 (6%)	4c	Ir_FPHQ_1 (12%)
5a	Ir_FPHQ_2 (2%)	5b	Ir_FPHQ_2 (6%)	5c	Ir_FPHQ_2 (12%)
6a	Ir_FPHQ_3 (2%)	6b	Ir_FPHQ_3 (6%)	6c	Ir_FPHQ_3 (12%)
7a	Ir_OMePHQ_1 (2%)	7b	Ir_OMePHQ_1 (6%)	7c	Ir_OMePHQ_1 (12%)
8a	Ir_OMePHQ_2 (2%)	8b	Ir_OMePHQ_2 (6%)	8c	Ir_OMePHQ_2 (12%)
9a	Ir_OMePHQ_3 (2%)	9b	Ir_OMePHQ_3 (6%)	9c	Ir_OMePHQ_3 (12%)
10a	Ir_CNPHQ_1 (2%)	10b	Ir_CNPHQ_1 (6%)	10c	Ir_CNPHQ_1 (12%)
11a	Ir_CNPHQ_2 (2%)	11b	Ir_CNPHQ_2 (6%)	11c	Ir_CNPHQ_2 (12%)

Table 4: Performances of OLED devices realized with IrPHQs

Device	Luminance (cd/m ²) @ 10-11 V	Efficiency (cd/A) @ 10-11 V	Lum. Max (cd/m ²)	Eff. max (cd/A)	Power Efficiency max (lm/W)	λ_{\max} EL (nm)	CIE (1931)
1a	449.5	0.39	527.75@11V	0.49@9V	0.17 @9V	610	0.51 0.40
1b	39.6	0.92	718.9@15V	0.92 @10V	0.30 @10V	610	0.56 0.40
1c	388.5	0.54	709.3@12V	0.54 @10V	0.16 @10V	615	0.56 0.40
2a	628	0.29	682.4 @11V	0.29@10V	0.11@7.5V	620	0.55 0.38
2b	159.2	0.56	495.9@15.5V	0.56 @10V	0.17 @10.3V	620	0.60 0.37
2c	215.5	0.3	483.6@12V	0.32 @9V	0.10 @9V	624	0.60 0.37
3a	509.6	0.24	600.6@10V	0.64@7.8V	0.26 @7.8V	620	0.47 0.39
3b	72	0.5	435@16V	0.55 @11.5V	0.15 @11.5V	625	0.58 0.37
3c	359.4	0.42	518.7@12V	0.44@10.5V	0.13@9.7V	625	0.59 0.38
4a	261	0.18	261@10.5V	0.25 @8.3V	0.09 @8.3V	600	0.46 0.44
4b	764	0.59	764@10V	0.92@8.5V	0.34@8.5V	605	0.54 0.42
4c	450.9	0.13	687@13.5V	0.17 @13.5V	0.04 @13.5V	605	0.55 0.43
5a	1092	0.35	1092@11V	0.35@11V	0.1@11V	585	0.48 0.46
5b	317	0.55	384.9@12.2V	0.55 @10V	0.16 @10V	605	0.54 0.41
5c	149.3	0.35	472.2@13V	0.35@11V	0.1@11V	627	0.59 0.39
6a	559.6	0.39	591.5@10.7V	0.55 @8V	0.22@8V	580	0.43 0.40
6b	343.5	0.2	343@10.7V	0.27 @9.2V	0.1 @8.2V	602	0.48 0.41
6c	175	0.07	175 @10V	0.07 @10V	0.023 @9V	602	0.40 0.38
7a	468.61	1.64	2475.43 @14V	1.78 @13V	0.42 @13V	606	0.57 0.39
7b	319.43	0.064	319.43 @10V	0.064 @10V	0.02 @10V	603	0.56 0.40
7c	466.79	0.18	580.53 @12V	0.18 @12V	0.05 @9V	608	0.57 0.41
8a	606.61	0.81	1008 @13V	0.81 @11V	0.23 @11V	612	0.57 0.39
8b	453.69	0.26	524.11 @13V	0.29 @9V	0.10 @9V	618	0.60 0.37
8c	334.94	0.47	620.56 @13V	0.52 @10V	0.16 @11V	618	0.61 0.38
9a	497.73	0.23	583.71 @12V	0.34 @9V	0.12 @9V	615	0.54 0.36
9b	416.38	0.24	745.68 @13V	0.24 @11V	0.07 @11V	616	0.60 0.37
9c	260.92	0.18	425.57 @13V	0.18 @11V	0.053 @11V	619	0.60 0.38
10a	236	0.33	469.06 @14V	0.33 @10V	0.099 @10V	628	0.47

							0.36
10b	177.43	0.062	256.69 @13V	0.065 @12V	0.018 @11V	638	0.53
							0.34
10c	35.6	0.05	385.62 @13V	0.17 @12V	0.044 @12V	635	0.57
							0.37
11a	323.48	0.15	323.48 @10V	0.15 @10V	0.047 @10V	635	0.39
							0.32
11b	131.76	0.051	159.74 @13V	0.051 @11V	0.014 @11V	639	0.56
							0.35
11c	67.56	0.047	161.1 @12V	0.056 @12V	0.015 @10V	640	0.57
							0.36

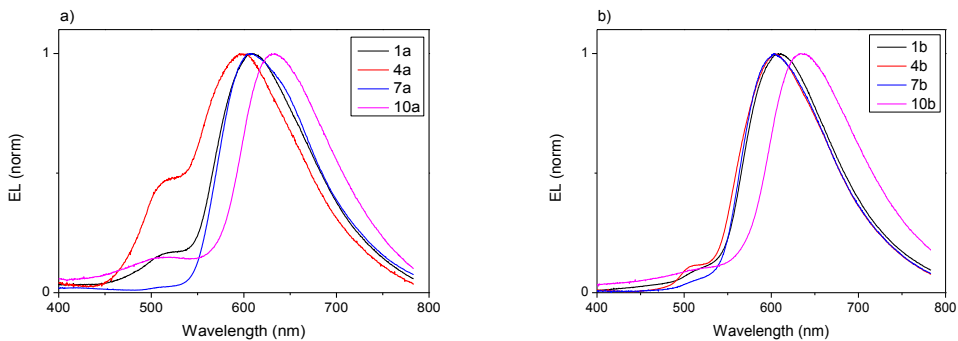


Figure 30: a) Normalized electroluminescence spectra of devices 1a, 4a, 7a and 10a; b) Normalized electroluminescence spectra of devices 1b, 4b, 7b and 10b

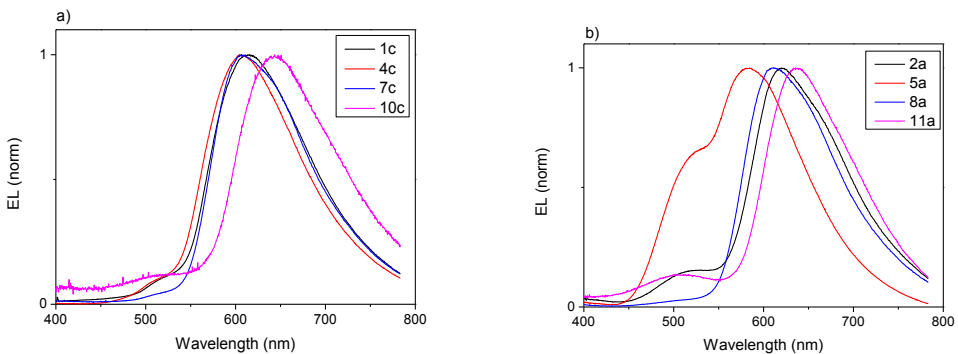


Figure 31: a) Normalized electroluminescence spectra of devices 1c, 4c, 7c and 10c; b) Normalized electroluminescence spectra of devices 2a, 5a, 8a and 11a

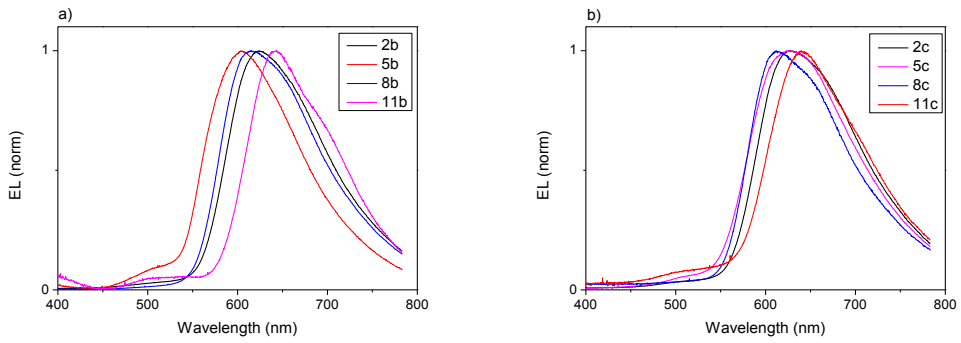


Figure 32: a) Normalized electroluminescence spectra of devices 2b, 5b, 8b and 11b; b) Normalized electroluminescence spectra of devices 2c, 5c, 8c and 11c

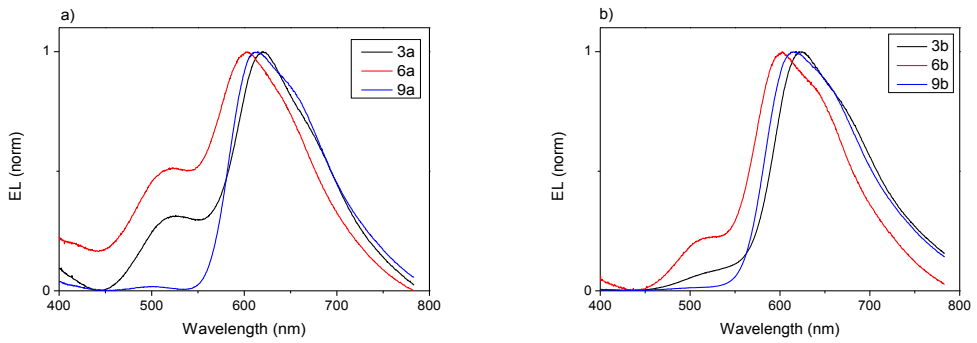


Figure 33: a) Normalized electroluminescence spectra of devices 3a, 6a and 9a; b) Normalized electroluminescence spectra of devices 3b, 6b and 9b

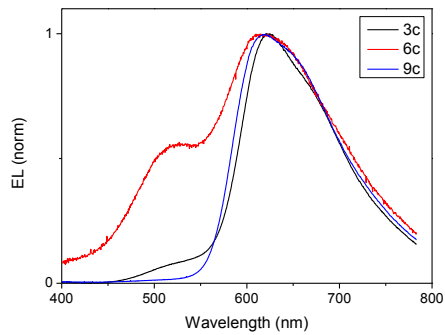


Figure 34: Normalized electroluminescence spectra of devices 3c, 6c and 9c

By analyzing the data reported in Table 4, it is possible to deduce that all the fabricated OLED devices exhibit an intense electroluminescence ranging from the red/orange to the purple ascribable to the iridium(III) complexes.

The best devices in terms of luminance and turn-on voltage resulted those prepared by using a 2% wt of the iridium(III) complexes, reaching a maximum luminance of 1092 cd/m^2 with the device 5a and 2474 cd/m^2 with the device 7a; only in the case of the *Ir_FPHQ-1* the best results were obtained with the 6% wt blend (device 4b).

In terms of maximum luminance, in the case of the *Ir_PHQ* and *Ir_FPHQ* series the best results were obtained in complexes built up with two phenylisoquinoline units, whereas for the *Ir_OMePHQ* series the best results were given by complex *Ir_OMePHQ_1*. For the *Ir_CNPHQ* series there is no appreciable influence of the number of phenylisoquinoline ligands on the maximum luminance.

Analyzing the electroluminescence of the devices it is possible to identify some general trends. When fixing either the structure of the complex and the nature of the substituent, the emission maximum shows a slight red shift when increasing the percentage of the complex. Instead, along each series, the emission maximum remains unaffected. The overall substituent effect on the emission maximum is:

F \rightarrow OMe \rightarrow H \rightarrow CN, with the minimum emission λ observed at 580 nm with fluorine and the maximum emission λ observed at 639 nm with the cyano group (Figure 35).

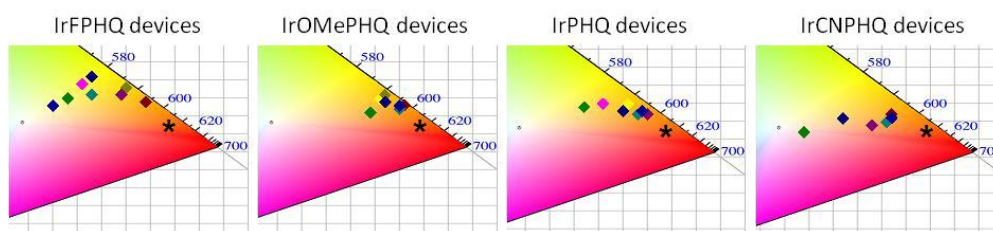


Figure 35: CIE coordinates of OLED devices with IrPHQs

➤ Synthesis of N[^]O dopamine-inspired ligands

The synthesis of the N[^]O ligands (CHQ and CQ) was carried out starting from *O,O*-dimethyldopamine in analogy with the synthesis of the PHQs. This latter was treated in the first step with diethyloxalate in toluene under reflux conditions to give the amide *Am_5*.¹⁸ The amide *Am_5* underwent the intramolecular cyclization by treatment with POCl₃ under reflux conditions, affording **1** (78% yields). To obtain CHQ, the 3,4-dihydroisoquinoline **1** was subjected to acid hydrolysis, whereas to afford the isoquinoline CQ, **1** was first oxidized using palladium on carbon (Pd/C 10%) in glacial acetic acid at 80 °C,¹⁹ and then subjected to acid hydrolysis under the same conditions previously described (Figure 36).

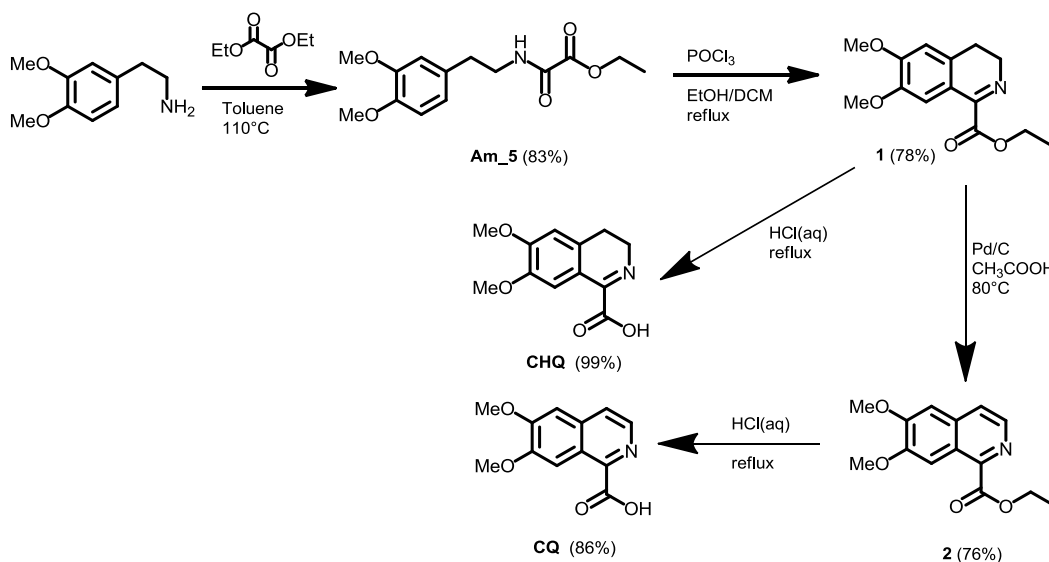


Figure 36: Synthesis of CHQ and CQ ligands

➤ Synthesis of iridium complexes with N[^]O ligands (Ir_CHQ and Ir_CQ)

As for the Ir_PHQ complexes, the synthesis of the complexes with CHQ and CQ as ligands was carried out starting from the dichloro-bridged dinuclear iridium complex. The complex μ -Ir was dissolved in presence of the base K₂CO₃ in

ethoxyethanol at 50 °C and under oxygen depleted conditions to afford the complexes Ir_CHQ and Ir_CQ (Figure 37).²⁰

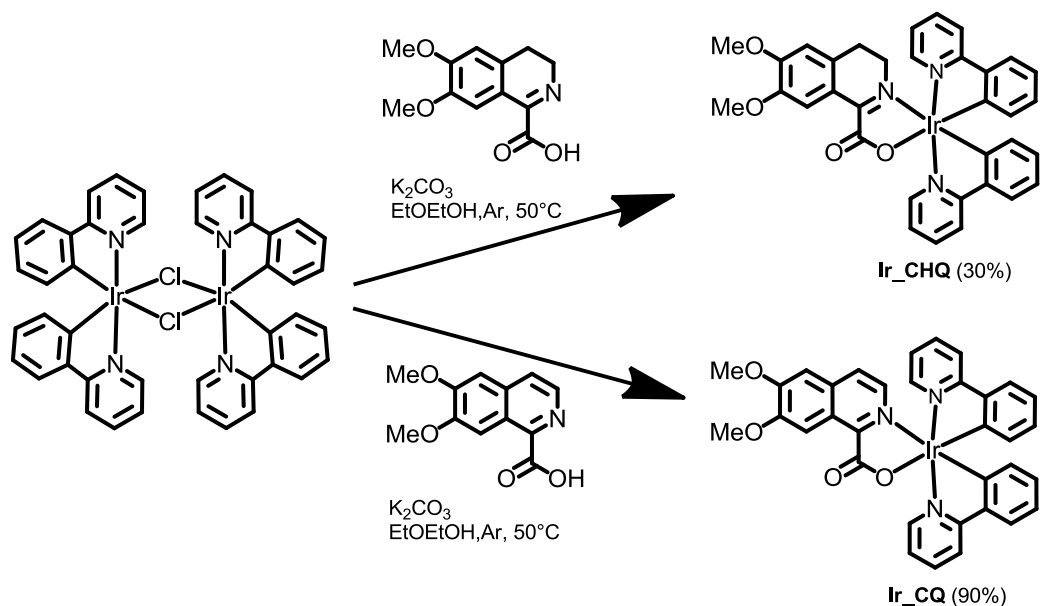


Figure 37: Synthesis of Ir_CHQ and Ir_CQ

The identity of the complexes Ir_CHQ and Ir_CQ was supported by mono- and bi-dimensional NMR spectroscopy and mass spectrometry.

➤ Photophysical Characterization of Ir_CHQ and Ir_CQ

The photophysical characterization of the Ir_CHQ and Ir_CQ complexes was carried out as for the IrPHQ complexes.

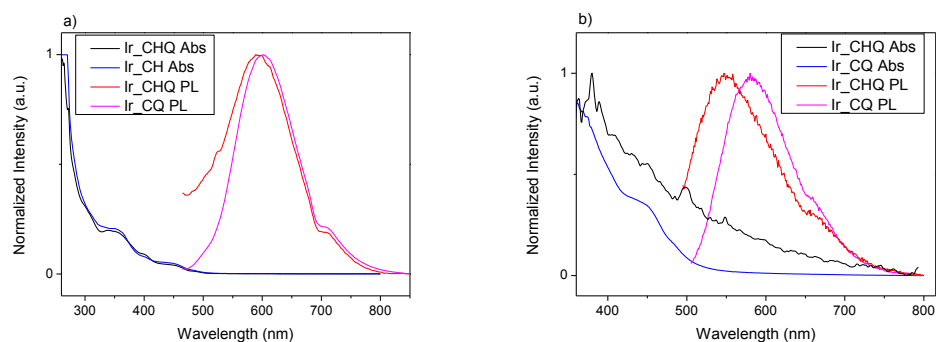


Figure 38: a) Absorption and Emission spectra of Ir_CHQ and Ir_CQ from solution; b) Absorption and Emission spectra of Ir_CHQ and Ir_CQ from thin film

Table 5: Photo-physical data of compounds Ir_CHQ and Ir_CQ

Compound	UV-vis λ_{\max} , nm ($\log \epsilon_r$, $M^{-1}cm^{-1}$) ^a	PL λ_{em} , nm (λ_{eccr} , nm) ^a	Φ (λ_{em} , nm) ^b	Φ (λ_{em} , nm) ^c	UV-vis λ_{\max} , nm ^d	PL λ_{em} , nm (λ_{eccr} , nm) ^a	Eq opt, eV
SOLUTION				FILM			
<i>Ir_CHQ</i>	292 (sh), 355 (4.08), 450 (sh), 484 (sh)	602 (480)	0.14%	0.39%	380 498	551 662	2.56
<i>Ir_CQ</i>	280 (sh), 349 (4.05), 400 (sh), 450 (sh), 493 (sh)	606 (490)	0.45%	0.46%	370 453	551 660	2.52

[a] Determined in diluted solutions in dichloromethane (1×10^{-6} M); [b] determined relatively to fluorescein $\Phi=0.9$ in a 0.1 M solution of NaOH); [c] determined in oxygen free solutions of DCM; [d] determined as thin film on glass substrates.

Both complexes show absorption maxima set in the 200-400 nm region. In detail, it is visible a shoulder set at 292 and 280 nm, respectively, due to spin allowed π - π^* ligand-centered (LC) transitions for the cyclometallating ppy and ancillary (dihydro)isoquinoline ligands, and in the range 300-400 nm a maximum centered at 355 and 349 nm, assigned to metal-to-ligand charge transfer (1MLCT). The weak and broad absorption maxima at longer wavelengths (400-500 nm) is ascribable to the spin forbidden metal-to-ligand charge transfer transitions (3MLCT). The

emission spectra of complexes Ir_CHQ and Ir_CQ proved quite similar, with a single broad maximum centered at 589 nm for Ir_CHQ and at 602 nm for Ir_CQ. The bathochromic shift observed for the emission maxima of the isoquinoline-based complexes may be due to the structure of CQ characterized by a conjugated double bond system extending over the entire heterocyclic skeleton. This allows the stabilization of the LUMO of the complex and so a reduction of the HOMO-LUMO gap. This hypothesis is under investigation by theoretical calculations. The emission quantum yields are similar to that reported for the complexes with PHQ series ligands and a quenching effect of the oxygen was also observed. Spectra from thin film indicate the formation of aggregate as already reported for IrPHQs.

➤ Cyclic Voltammetry Ir_CHQ and Ir_CQ

The HOMO and LUMO levels and the energy gap of the Ir_CHQ and Ir_CQ complexes were estimated by cyclic voltammetry.

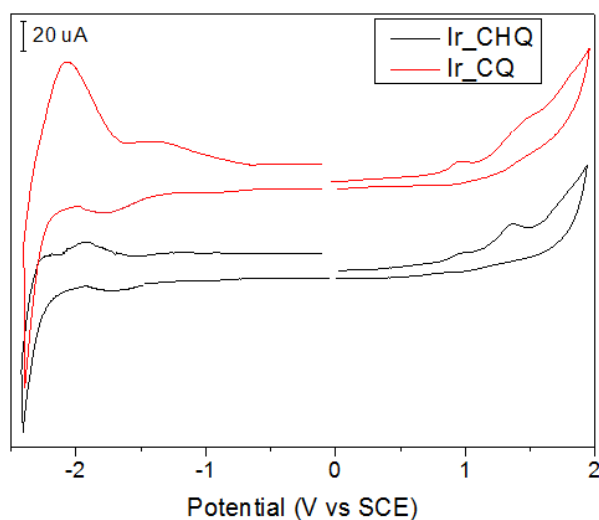


Figure 39: Cyclic voltammetry Ir_CHQ and Ir_CQ

Table 6: Cyclic Voltammetry data Ir_CHQ and Ir_CQ

Compound	$E_{\text{onset}}^{\text{Ox}}$ (SCE) (V)	HOMO level (eV)	$E_{\text{onset}}^{\text{Red}}$ (SCE) (V)	LUMO level (eV)	HOMO-LUMO gap (eV)	Optical E_g (eV)
IrCHQ	0.83	-5.53	-1.42	-3.28	2.25	2.56
IrCQ	0.80	-5.49	-1.44	-3.26	2.24	2.52

The energy gap calculated from cyclic voltammetry is smaller than the optical band gap for both complexes.

From a comparison of the two complexes, the Ir_CQ complex have a smaller band gap respect Ir_CHQ. As already mentioned in the previous paragraph, probably the higher degree of conjugation of the ligand CQ can induce a stabilization of the LUMO level and a reduction of the energy gap. Computational studies are necessary to confirm such hypothesis.

➤ OLED devices with Ir_CHQ and Ir_CQ

The complexes Ir_CHQ and Ir_CQ were tested as phosphorescent emitting layer in the following OLED structure: *ITO/PEDOT:PSS/Ir:CBP(%)/BCP/Alq₃/Ca/Ag*.

The OLED performances and the electroluminescence spectra are reported.

Table 7: OLED devices realized with Ir_CHQ and Ir_CQ

Entry	Complex (% in CBP)	Entry	Complex (% in CBP)
12a	Ir_CHQ (6%)	12b	Ir_CHQ (12%)
13a	Ir_CQ (6%)	13b	Ir_CQ (12%)

Table 8: Performances of OLED devices realized with Ir_CHQ and Ir_CQ

Device	Luminance (cd/m ²) @ 10-11 V	Efficiency (cd/A) @ 10-11 V	Lum. Max (cd/m ²)	Eff. max (cd/A)	Power Efficiency max (lm/W)	λ_{max} EL (nm)	CIE (1931)
12a	2719	0.95	3031 @ 11.2V	1.09 @ 8.4V	0.42 @ 7.8V	563	0.44 0.51

12b	996 @ 9.5V	0.35 @ 9.5V	996 @ 9.5V	0.44 @ 8.5V	0.17 @ 8.1V	576	0.46 0.51
13a	1074	0.50	2403 @ 8.4V	1.75 @ 7.8V	0.70 @ 7.8V	548	0.43 0.52
13b	927	0.32	7161 @ 9.3V	3.64 @ 8.2V	1.43 @ 7.8V	567	0.42 0.54

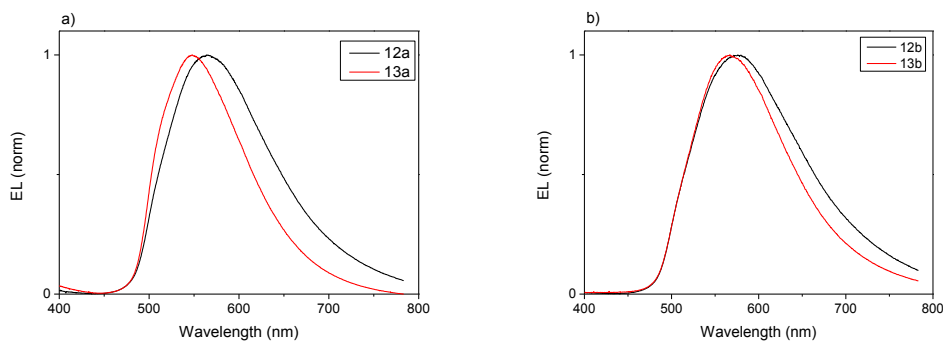


Figure 40: a) Normalized electroluminescence spectra of devices 12a and 13a; b) Normalized electroluminescence spectra of devices 12b and 13b

OLED devices show an intense electroluminescence in the yellow region of the spectrum ascribable to the iridium complexes. The performances for these devices result really higher than that reported for the complexes of the PHQ series, in particular maximum luminance range between 1000 and 7000 cd/m^2 and maximum efficiency range between 0.44 and 3.64 cd/A . The best performances are reported for the OLED with the 12% of complex in the host-guest layer and a red shift of the electroluminescence is observed for the devices at the 12% respect to that at 6%.

The big differences in the performances of the OLED realized with complexes of the PHQ series and that realized with Ir_CHQ and Ir_CQ can be due to the energy levels and structural differences that probably lead to a best energy transfer between host and guest and a better morphological arrangement of the emitting layer.

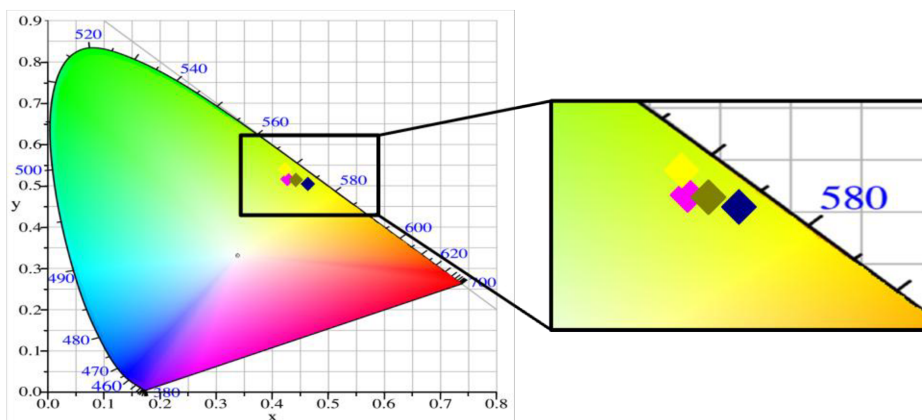


Figure 41: CIE coordinates OLED devices with Ir_CHQ and Ir_CQ

○ SYNTHESIS OF TRANSITION METAL COMPLEXES WITH NATURAL β -DIKETONES AND APPLICATION IN OLED DEVICES

➤ Synthesis of 6-dehydrogingerdione

6-Dehydrogingerdione was prepared according to a procedure reported in the literature²¹ with slight modifications. The procedure is based on the aldol condensation of 2,4-nonanedione with vanillin. To induce the regioselective formation of the carbanion on the C-1 position, 2,4-nonanedione was first treated with boron trioxide in *N,N*-dimethylformamide (DMF) at 90 °C to allow the formation of the complex *I*. The treatment of this latter with isobutylamine (*i*-BuNH₂) and vanillin led to the formation of the desired 6-dehydrogingerdione, isolated after treatment with HCl 1M to promote boron decomplexation and chromatographic purification on silica gel (Figure 42).

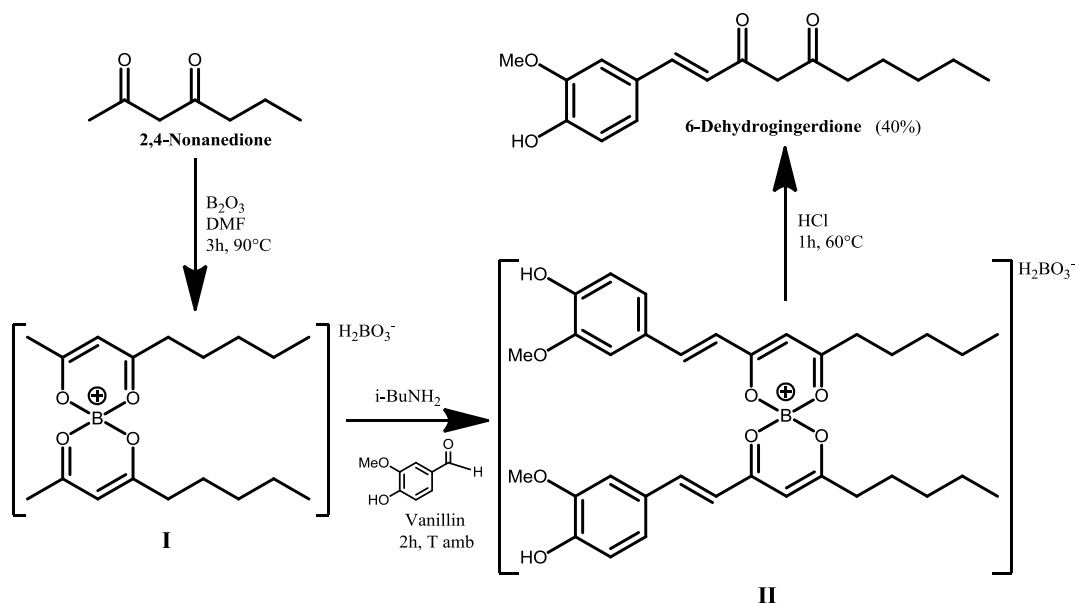


Figure 42: Synthesis of 6-dehydrogingerdione

The identity of 6-dehydrogingerdione was confirmed by mono- and bi-dimensional NMR spectroscopy.

➤ Synthesis of Ir(III) complexes

The insertion of the β -diketone ligand curcumin or 6-dehydrogingerdione was pursued by treating a solution of μ -Ir in dichloromethane with an ethanol solution of the proper ligand in presence of the base tetrabutylammonium hydroxide (Bu_4NOH) under reflux conditions (Figure 43).

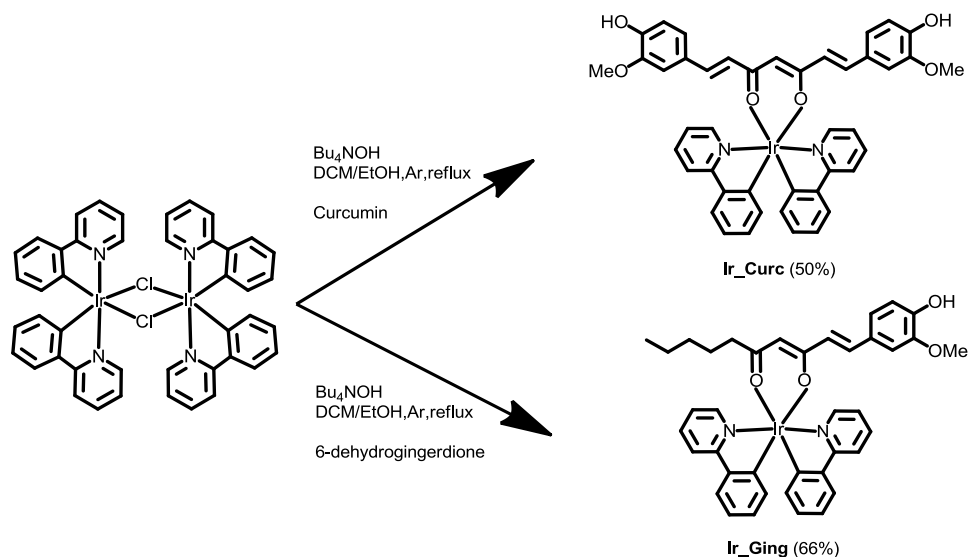


Figure 43: Synthesis of Ir_Curc e Ir_Ging

In both cases, the crude reaction mixture was subjected to a first chromatographic step on silica gel allowing the isolation of a mixture of isomeric iridium(III) complexes. Further purification steps allowed the isolation of Ir_Curc and Ir_Ging in pure form. For comparative purposes, the iridium(III) complex $\text{Ir}(\text{ppy})_2\text{acac}$ (acac = acetylacetonate), widely described in the literature as efficient emitting layer for OLED devices,²² was synthesized by using the same procedure used for Ir_Curc and Ir_Ging (Figure 44).

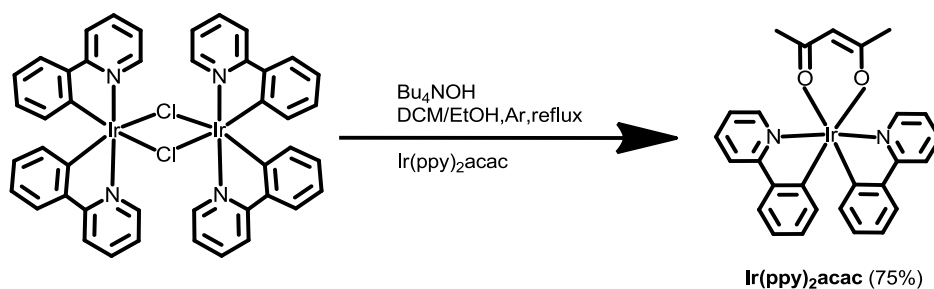


Figure 44: Synthesis of Ir(ppy)₂acac

➤ Synthesis of Zn(II) complexes

The synthesis of the zinc complexes was carried out according to a procedure previously reported in the literature.²³

The complexes BpyZnCurc and BpyZnGing were prepared starting from the precursor **3** obtained from bpy and ZnCl₂, whereas the complexes PhenZnCurc and PhenZnGing were prepared starting from the precursor **4** obtained from phen and ZnCl₂ (Figure 45).

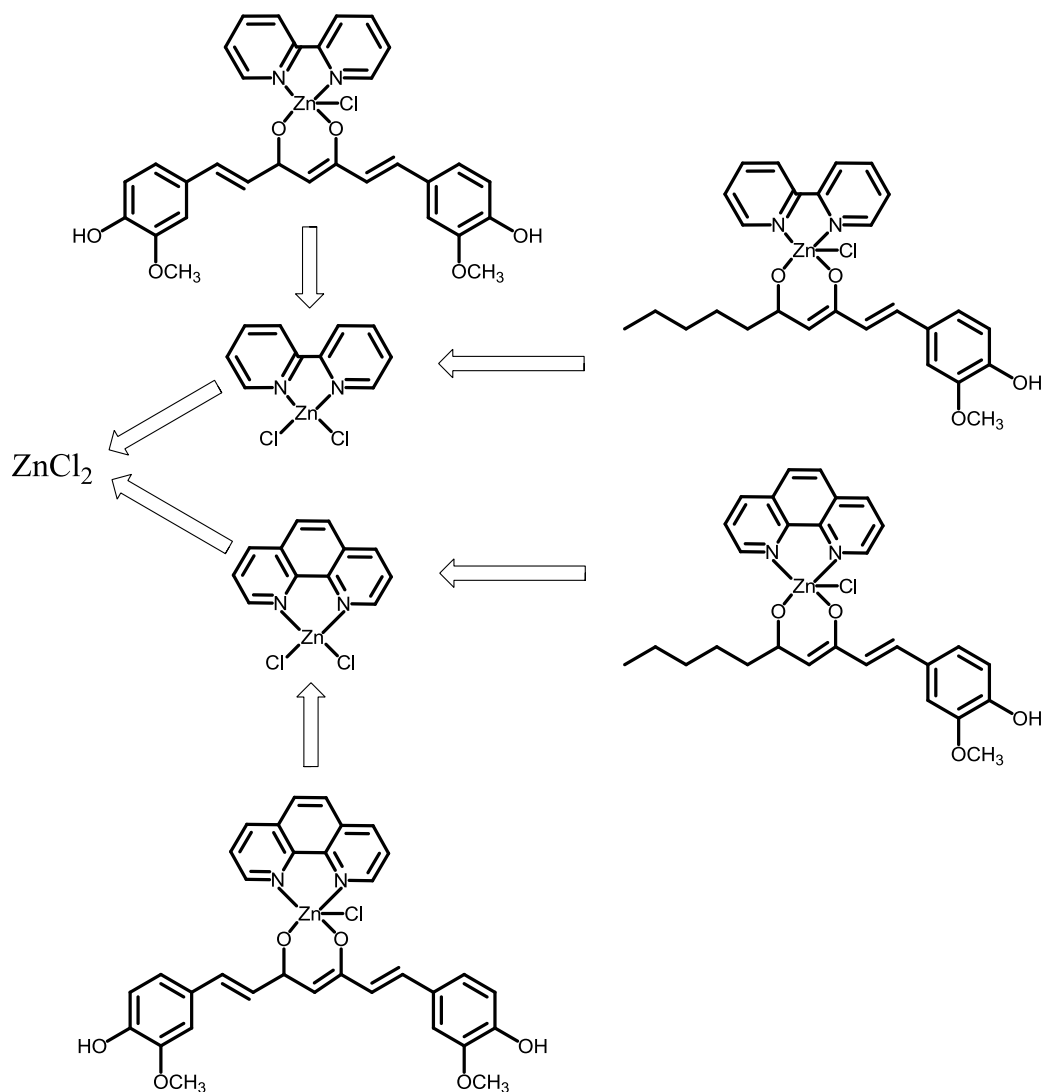


Figure 45: Retro-synthetic scheme for Zn(II) complexes with β-diketone ligands

The precursor **3** was prepared by treating ZnCl_2 with bpy in methanol at room temperature (Figure 46). After 48h a white solid was recovered by filtration, washed with ethanol and dried under reduced pressure. The identity of the solid as the complex **3** was deduced by comparison of NMR data with those reported in the literature.

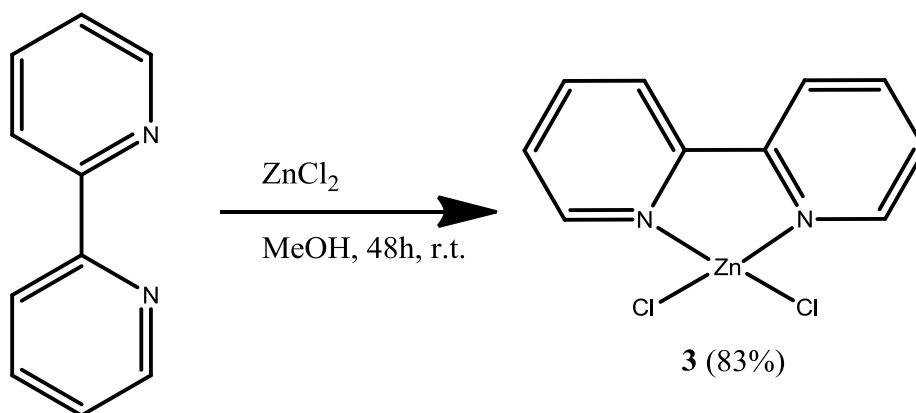


Figure 46: Synthesis of precursor **3**

For the synthesis of the complex BpyZnCurc (Figure 47), an orange solution of curcumin in MeOH was added to triethylamine (TEA) under an argon atmosphere at room temperature. After ten minutes the resulting red solution was added to a solution of **3** in water. After 24 hours, a dark orange solid was obtained by filtration, washed with water and MeOH and dried under reduced pressure.

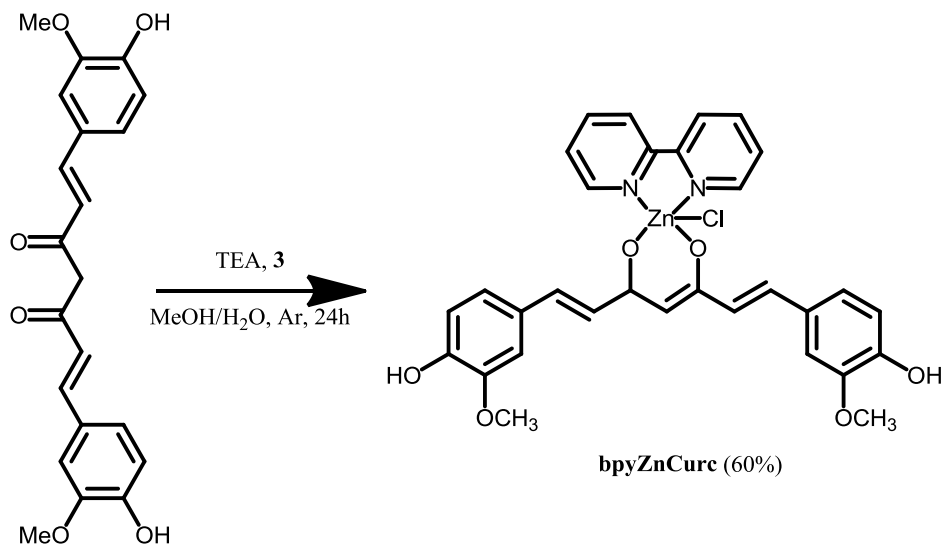


Figure 47: Synthesis of bpyZnCurc

A similar procedure was used for the synthesis of the complex BpyZnGing, by using 6- dehydrogingerdione instead of curcumin (Figure 48). In this case, after 24 hours an orange solid was obtained by filtration, washed with water and MeOH and dried under reduced pressure.

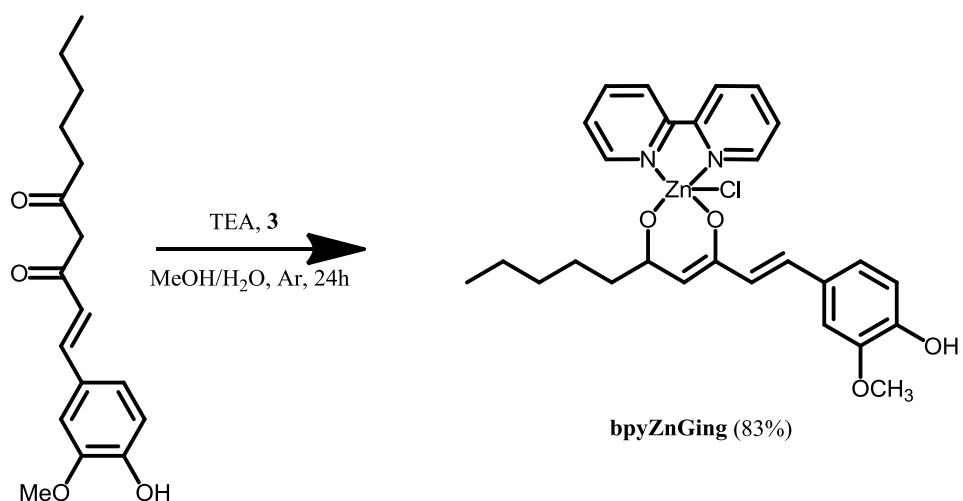


Figure 48: Synthesis of bpyZnGing

A more conjugated and rigid N^N ligand was introduced with the use of phenanthroline (phen). By treating ZnCl₂ with a chloroform solution of phen it was possible to obtain, as white solid, the complex **4** in high yields (Figure 49).

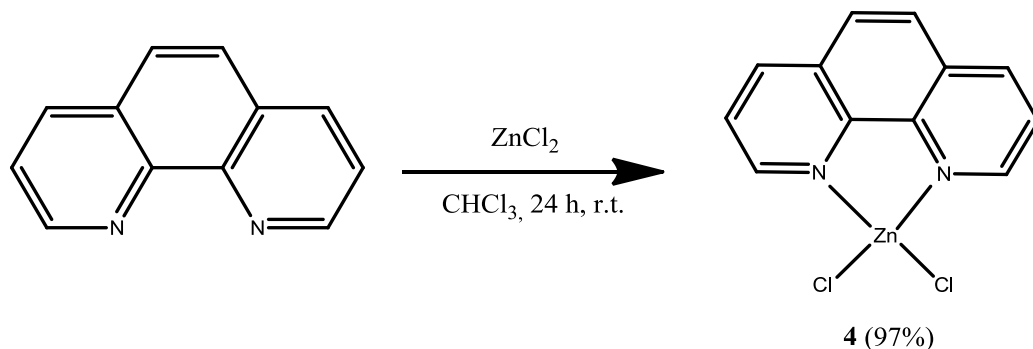


Figure 49: Synthesis of precursor **4**

For the synthesis of the complex PhenZnCurc (Figure 50), an orange solution of curcumin in MeOH was treated first with triethylamine and then with a DMSO solution of the complex **4** under an argon atmosphere. After 24 h an orange solid was obtained by filtration, washed with methanol and dried under reduced pressure.

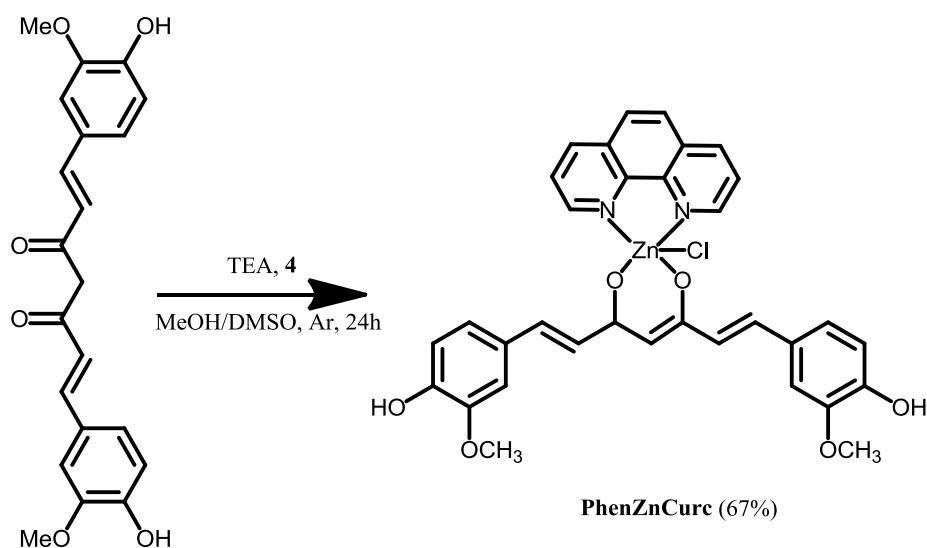


Figure 50: Synthesis of PhenZnCurc

A similar procedure was used for the synthesis of complex PhenZnGing (Figure 51). In brief, a solution of 6-dehydrogingerdione in MeOH was treated with triethylamine and then with the complex **4** under argon at room temperature. After 24 hours a yellow solid was isolated and dried under reduced pressure.

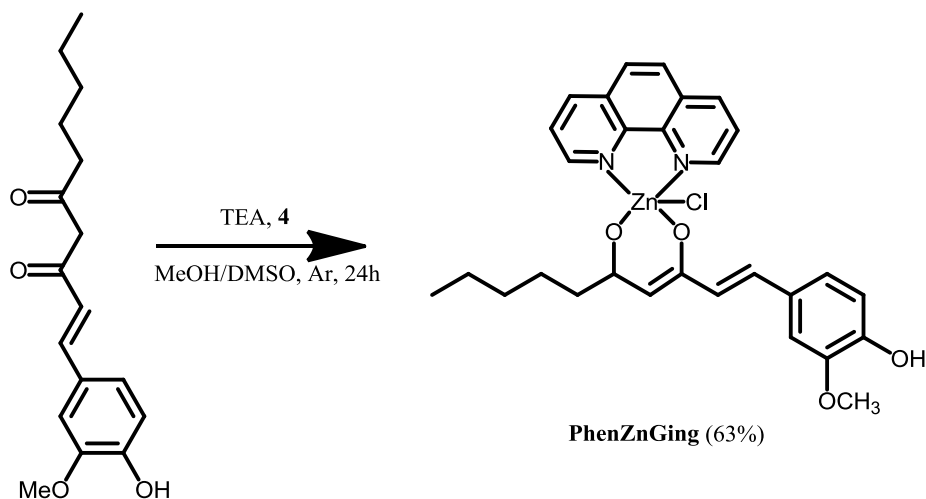


Figure 51: Synthesis of PhenZnGing

➤ Photophysical Characterization

In this paragraph the photophysical characterization of the Ir(III) and Zn(II) complexes synthesized by using curcumin and 6-dehydrogingerdione as β -diketones ligands is reported.

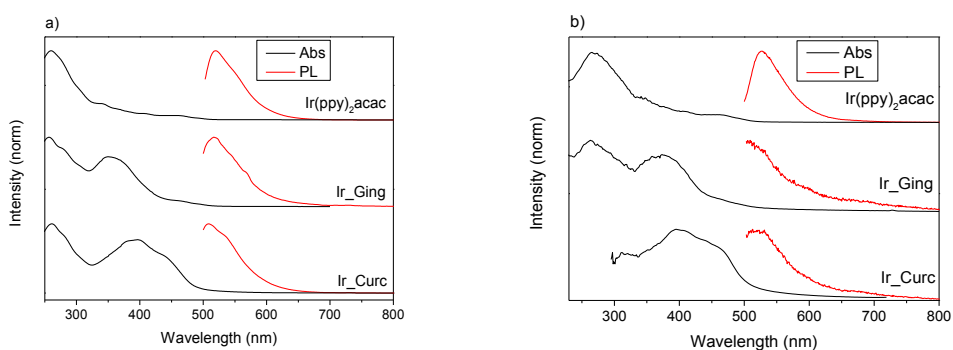


Figure 52: a) Absorption and emission spectra from solution; b) Absorption and emission spectra from thin film

Table 9: Photo-physical data of compounds Ir_Ging, Ir_Curc and Ir(ppy)₂acac

Compound	UV-vis λ_{max} , nm ($\log \epsilon$, $M^{-1}cm^{-1}$) ^a	PL λ_{em} , nm (λ_{ecc} , nm) ^a	Φ (λ_{em} , nm) ^b	Φ (λ_{em} , nm) ^c	UV-vis λ_{max} , nm ^d	PL λ_{em} , nm (λ_{ecc} , nm) ^a	E_g opt, eV
	SOLUTION				FILM		
<i>Ir(ppy)₂acac</i>	259(4.81), 342 (sh), 363 (sh), 407 (sh), 455 (3.62), 490 (sh)	519 (485)	2.4% (485)	16.9% (485)	265, 337 (sh), 350 (sh), 375 (sh), 410 (sh), 460, 490 (sh)	527 (485)	2.46
<i>Ir_Ging</i>	255(4.54), 280 (sh), 348(4.40), 370 (sh), 467 (sh)	516 (485)	0.3% (485)	1.7% (485)	367, 470 (sh), 500 (sh)	524 (485)	2.39
<i>Ir_Curc</i>	260 (4.6) 378 (sh) 395 (4.5) 440 (sh)	508 (485),	0.3% (485)	0.2% (485)	395, 410 (sh) 442 (sh) 465 (sh)	516, 523 (485),	2.32

[a] Determined in diluted solutions in dichloromethane (1×10^{-6} M); [b] determined relatively to fluorescein $\Phi=0.9$ in a 0.1 M solution of NaOH; [c] determined in oxygen free solutions of DCM; [d] determined as thin film on glass substrates.

The UV-vis spectrum of Ir(ppy)₂acac showed the typical profile of cyclometallated iridium(III) complexes. In detail, it is possible to note the presence of an intense maximum below 300 nm assigned to the spin-allowed $\pi-\pi^*$ ligand-centered (LC) transition for the cyclometallating ppy ligands with high molar extinction coefficient ($\log \epsilon > 4 M^{-1}cm^{-1}$); featureless bands between 300 nm and 450 nm assigned to the spin-allowed metal-to-ligand charge transfer (¹MLCT) characterized by values of $\log \epsilon > 3 M^{-1}cm^{-1}$; weak and broad absorption maxima at longer wavelengths (450-550 nm) ascribable to spin forbidden metal-to-ligand charge transfer transitions (³MLCT).

The UV-visible profile resulted significantly modified in the case of the complexes Ir_Curc and Ir_Ging by the presence of the absorption maxima of the ligands curcumin or 6-dehydrogindione (Figure 52a) at 395 nm and 348 nm, which

partially covered, in the case of Ir_Ging, or almost completely covered, in the case of Ir_Curc, the maxima due to metal-to-ligand charge transfer transitions.

The emission quantum yields of the iridium(III) complexes Ir_Curc and Ir_Ging has been proved to be in good agreement with those reported in the literature for similar complexes (0.3%) , but lower than that exhibited by Ir(ppy)₂acac (2.4%).

Only in the case of Ir(ppy)₂acac a marked quenching effect exerted by oxygen was observed, with higher quantum yields obtained when the emission spectrum was registered on oxygen free solutions (from 2.4% to 16.9%).

About the spectra from thin film, the aggregation effects proved more evident in the case of Ir_Curc and Ir_Ging respect Ir(ppy)₂acac suggesting that the long chains of the ligands curcumin and 6-dehydrogingerdione play a key role in favoring aggregation.

The photo-physical properties of zinc(II) complexes both in dilute solution (DMSO (1×10^{-5} M)) and in thin films were investigated by UV-vis and emission spectroscopy. The overall data are listed in Table 10.

Table 10: Photo-physical data of compounds PhenZnCurc, PhenZnGing, BpyZnCurc and BpyZnGing

Compound	UV-vis λ_{\max} , nm ($\log \epsilon$, $M^{-1}cm^{-1}$) ^a	PL λ_{em} , nm (λ_{ecc} , nm) ^a	Φ (λ_{em} , nm) ^b	UV-vis λ_{\max} , nm ^c	PL λ_{em} , nm (λ_{ecc} , nm) ^a	E_g opt, eV
	SOLUTION			FILM		
PhenZnCurc	405 (sh), 429 (4.65), 452 (4.61)	523 (452)	78.0% (452)	388, 410 (sh), 431, 456	527, 670 (456)	2.52
PhenZnGing	365 (sh), 381 (4.46), 403 (sh)	484 (381)	3.0% (381)	384	522 (384)	2.87
BpyZnCurc	400 (sh), 427 (4.58), 451 (4.62)	520 (451)	64.4% (451)	407 (sh), 431, 460 (sh)	523 (460)	2.55
BpyZnGing	362 (sh), 381 (4.48), 397 (sh)	485 (397)	13.8% (397)	370 (sh), 385 (sh), 398	468, 515, 670 (398)	2.91

[a] Determined in diluted solutions in dichloromethane (1×10^{-6} M); [b] determined relatively to fluorescein $\Phi = 0.9$ in a 0.1 M solution of NaOH; [c] determined as thin film on glass substrates.

The absorption profiles show maxima in the 300-500 nm region, ascribable to transitions involving the ligands curcumin and 6-dehydrogingerdione.

The emission spectra showed maxima centered at 520-523 nm for the curcumin-based complexes and maxima centered at 484-485 nm for the 6-dehydrogingerdione-based complexes. The quantum yields of the curcumin-based complexes is very high (64.4% and 78.0%), while the 6-dehydrogingerdione based complexes show smaller quantum yields.

UV-vis and emission spectra of the complexes registered in thin films (Figure 54) indicated an appreciable bathochromic shift of the absorption and emission maxima with respect to spectra obtained in solution and long tails at the lower energy edge suggesting aggregation of these complexes in the solid state.

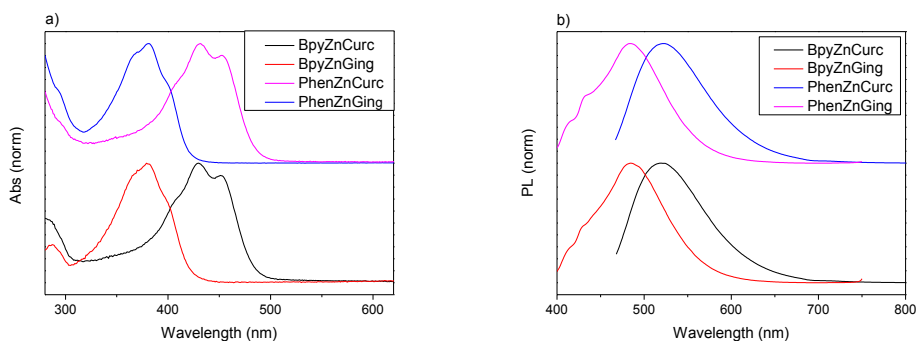


Figure 53: a) Absorbance spectra of Zn(II) complexes from solution; b) Emission spectra of Zn(II) complexes from solution

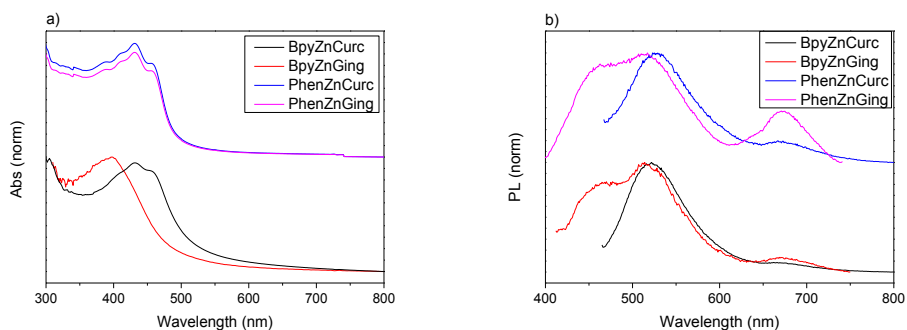


Figure 54: a) Absorbance spectra of Zn(II) complexes from thin film; b) Emission spectra of Zn(II) complexes from thin film

➤ Cyclic Voltammetry

The cyclic voltammetry characterization of the Ir(III) and Zn(II) complexes with β -diketones were carried out.

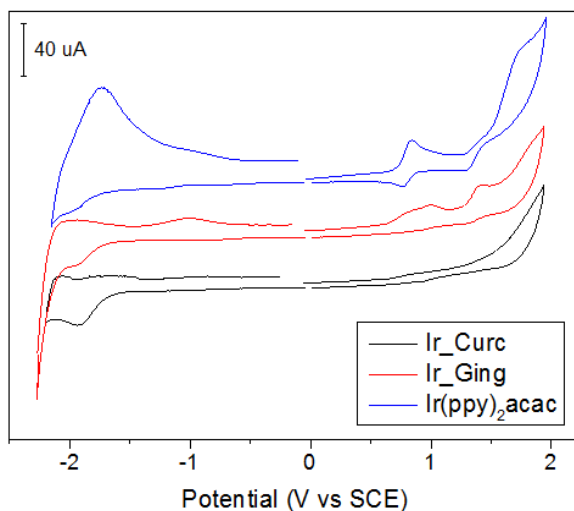


Figure 55: Cyclic voltammetry Ir_Curc, Ir_Ging and Ir(ppy)₂acac

Table 11: Cyclic Voltammetry data Ir_Curc, Ir_Ging and Ir(ppy)₂acac

Compound	$E_{\text{onset}}^{\text{Ox}}$ (SCE) (V)	HOMO level (eV)	$E_{\text{onset}}^{\text{Red}}$ (SCE) (V)	LUMO level (eV)	HOMO-LUMO gap(eV)	Optical E_g (eV)
Ir(ppy) ₂ acac	0.69	-5.39	-1.76	-2.94	2.45	2.46
IrGing	0.66	-5.35	-1.71	-2.99	2.38	2.39
IrCurc	0.66	-5.35	-1.65	-3.05	2.31	2.32

The energy gap values calculated by cyclic voltammetry and absorption spectra are comparable. From Ir(ppy)₂acac to Ir_Curc there is an increase in the conjugation length that seems to stabilize the LUMO level with a consequent reduction of the energy gap.

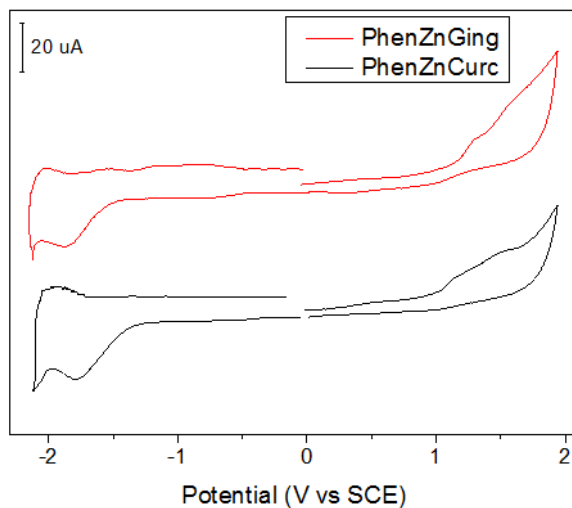


Figure 56: Cyclic voltammetry PhenZnGing and PhenZnCurc

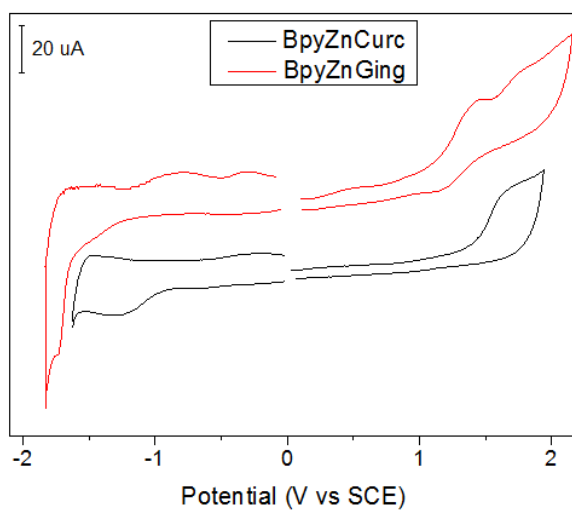


Figure 57: Cyclic voltammetry BpyZnCurc and BpyZnGing

Table 12: Cyclic Voltammetry data PhenZnCurc, PhenZnGing, BpyZnCurc and BpyZnGing

	$E_{\text{onset}}^{\text{Ox}}$ (SCE) (V)	HOMO level (eV)	$E_{\text{onset}}^{\text{Red}}$ (SCE) (V)	LUMO level (eV)	HOMO-LUMO gap (eV)	Optical E_g (eV)
PhenZnCurc	1.00	-5.7	-1.30	-3.40	2.30	2.52
PhenZnGing	1.12	-5.82	-1.50	-3.20	2.62	2.87
BpyZnCurc	1.38	-6.08	-0.93	-3.77	2.31	2.55
BpyZnGing	1.17	-5.87	-1.51	-3.19	2.68	2.91

About the cyclic voltammetry characterization of the Zn(II) complexes, the energy gap is smaller than the optical gap but with similar trends. In particular, the energy gap decrease with the increase of the conjugation length for both the typology of ligands (O[^]O and N[^]N).

Computational calculations are necessary to confirm the information obtained through cyclic voltammetry.

➤ OLED devices

The iridium complexes with β -diketone ligands were tested as emitting materials in the same OLED structure reported for the other synthesized Ir(III) complexes. The prepared OLED devices, the performances and the electroluminescence spectra are reported.

Table 13: OLED devices with Ir_Ging, Ir_Curc and Ir(ppy)₂acac

Entry	Complex (% in CBP)	Entry	Complex (% in CBP)	Entry	Complex (% in CBP)
14a	Ir_Ging (2%)	14b	Ir_Ging (6%)	14c	Ir_Ging (12%)
15a	Ir_Curc (2%)	15b	Ir_Curc (6%)	15c	Ir_Curc (12%)
16a	Ir(ppy) ₂ acac (2%)	16b	Ir(ppy) ₂ acac (6%)	16c	Ir(ppy) ₂ acac (12%)

Table 14: Performances of OLED devices realized with Ir_Ging, Ir_Curc and Ir(ppy)₂acac

Device	Luminance (cd/m ²) @ 10-11 V	Efficiency (cd/A) @ 10-11 V	Lum. Max (cd/m ²)	Eff. max (cd/A)	Power Efficiency max (lm/W)	λ_{max} EL (nm)	CIE (1931)
14a	482	0.13	482 @ 10.7V	0.14 @ 9.7V	0.052 @ 8V	517	0.32 0.54
14b	390	0.18	491 @ 11.2V	0.19 @ 9.6V	0.061 @ 9.6V	522	0.35 0.56
14c	195	0.34	336 @ 13 V	0.34 @ 11V	0.11 @ 10.15V	525	0.37 0.55
15a	142	0.067	210 @ 7.6V	0.18 @ 7.6V	0.076 @ 7.6V	507	0.27 0.35
15b	143.7	0.17	143.7 @ 11.5V	0.17 @ 11.5V	0.046 @ 11.5V	521	0.33 0.45

15c	78	0.14	116 @ 14.4V	0.15 @ 10.2V	0.045 @ 10.2	534	0.38 0.47
16a	883 @ 8.5V	0.22 @ 8.5V	883 @ 8.5V	0.22 @ 8.5V	0.081 @ 8.5V	519	0.31 0.63
16b	807	0.56	915 @ 8.5V	1.28 @ 8.5V	0.49 @ 7.2V	521	0.32 0.62
16c	673	0.47	2586 @ 8.6V	2.26 @ 8.6V	0.83 @ 8.6V	523	0.32 0.63

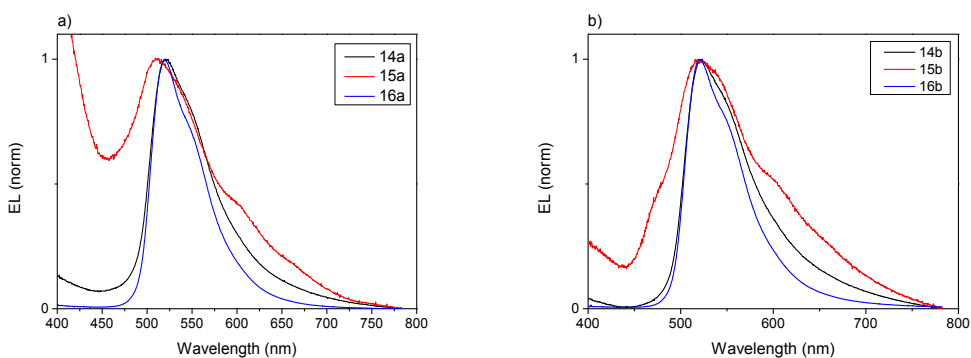


Figure 58: a) Normalized electroluminescence spectra of devices 14a, 15a and 16a; b) Normalized electroluminescence spectra of devices 14b, 15b and 16b

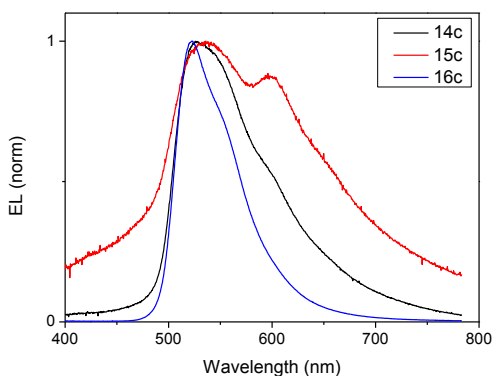


Figure 59: Normalized electroluminescence spectra of devices 14c, 15c and 16c

OLEDs prepared with iridium complex having the acac ligand show a green electroluminescence ascribable to the synthesized complex. The electroluminescence maxima of all the devices with 2% of complexes correspond to the emission maxima registered in solution. These EL maxima emission

underwent a red-shift along with the increasing concentration of the iridium complex due to aggregation processes. This effect proved more consistent in the case of the complex Ir_Curc for which a 27 nm red-shift is observed, suggesting that the molecules of Ir_Curc are more prone to form aggregates.

This phenomenon strongly influences the performance of the devices. As shown in Table 14, in the case of Ir_Curc the luminance and the efficiency of the devices decrease with the growth of the percentage of the complex. This trend is less evident in the case of the devices fabricated with Ir_Ging; in this case while the luminance values decrease with the content of Ir_Ging, the efficiency tends to grow in a moderate manner.

The devices fabricated with Ir(ppy)₂acac exhibited a completely opposite behavior with both luminance and efficiency growing with the amount of iridium complex. Overall these data suggest that the aggregation induced by the aromatic side chain in curcumin, and in minor extent in 6-dehydrogingerdione, compromise the performances of the corresponding OLED devices.

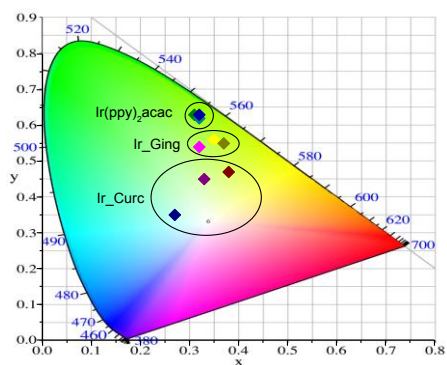


Figure 60: CIE coordinates OLED devices with Ir_Ging, Ir_Curc and Ir(ppy)₂acac

~CONCLUSIONS~

In conclusion, this section reports on the first example of nature-inspired iridium complexes for applications in OLEDs. In particular, the reactivity of a dopamine derivative was exploited, the O,O-dimethyldopamine, in order to synthesize a novel set of bio-inspired ligands for iridium(III) complexes. The synthesis of the complexes with a set of phenyldihydroisoquinolines (PHQ) as C^N ligands produced in a one-pot reaction a set of three different complexes with different ratio between the two cyclometalating selected ligands, ppy and PHQ. All the synthesized complexes showed a red emission in solution with good quantum efficiencies. The encouraging photo-physical properties prompted us to fabricate OLED devices by incorporating the synthesized neutral dopamine-inspired iridium(III) complexes as dopant in the emitting layer. In particular, the complexes were tested in blend with CBP (2% or 6% or 12% wt) in the emitting layer. The devices exhibited a red electroluminescence with luminance values up to 2475 cd/m².

Two different N[^]O ligands were also synthesized starting from dopamine and differing each other for the conjugation extension. The heteroleptic iridium complexes obtained with these ligands show very high luminance in an OLED device structure (more than 7000 cd/m²) and an electroluminescence wavelength in the yellow region of the spectrum.

Finally iridium and zinc complexes were synthesized by using natural β-diketone ligands, respectively curcumin and 6-dehydrogingerdione.

OLED devices realized with the iridium complexes show an emission in the green region of the spectrum and the performances are very limited by the effect of aggregation phenomena. Zinc complexes show very poor solubility in the common used organic solvents and with some difficulties they were tested as fluorescent

emitters in a standard device structure (*ITO/PEDOT:PSS/Zn complex/BCP/Alq₃/Ca/Ag*). Deposition of the zinc complexes were performed from solution and with a thermal vacuum deposition; unfortunately in both cases, although devices show a diode electrical behavior, the emission of the zinc complexes was not observed. As future development, the synthesized zinc complexes can be structural modified to improve the solubility and they can be tested as host and/or electron transport material.

It is possible to conclude that, these data pointed out the potentiality of these new nature-based complexes as organic materials for optoelectronic application and represent the first step toward the development of more sustainable OLED devices.

~EXPERIMENTAL SECTION~

○ MATERIALS AND METHODS

O,O-Dimethyldopamine, diethyloxalate, potassium carbonate, POCl₃, palladium on carbon, ethoxyethanol, 2-phenylpyridine, iridium trichloride, benzoic acid, 4-fluorobenzoic acid, 4-methoxybenzoic acid, 4-cyanobenzoic acid, ethyl chloroformate, acetylacetone, triethylamine (TEA), vanillin, 2,4-nonanedione, boron trioxide, isobutylamine, tetrabutylammonium hydroxide, curcumin, 2,2'-bipyridine, zinc chloride, 1,10-phenanthroline, CBP and BCP were purchased from Sigma-Aldrich, PEDOT:PSS was purchased from HeraeusClevios.

Analytical and preparative TLC were performed on silica gel plates F₂₅₄ (0.25 and 0.5 mm, respectively) and were visualized using a UV lamp ($\lambda = 254$ nm) and a fluorescence lamp ($\lambda = 356$ nm).

Liquid chromatography was performed on silica gel (60-230 mesh).

¹H, ¹³C and ¹⁹F spectra were acquired on a Bruker DRX (400 MHz) spectrometer. Chemical shifts are given in ppm relative to the internal standard tetramethylsilane (Me₄Si) and *J* values are given in Hz. ¹H,¹H COSY, ¹H,¹³C HSQC, ¹H,¹³C HMBC, ¹H, and NOESY experiments were run at 400.1 MHz using standard pulse programs.

Mass spectra were recorded in positive ion mode using a 1100 VL LC/MSD Agilent instrument.

MALDI mass spectra have been recorded on a AB Sciex TOF/TOF 5800 instrument using 2,5-dihydroxybenzoic acid as the matrix. Spectra represent the sum of 15000 laser pulses from randomly chosen spots per sample position.

ATR spectra of the powders in transmission mode have been recorded with a Nicolet 5700 spectrometer. FT-IR spectra on thin films have been performed on CaF₂ slide by using a Perkin Elmer GX instrument.

UV-visible and emission spectra were recorded on a Jasco V-560 and a Jasco FP-750 instruments. Quantum efficiencies (Φ) were calculated using fluorescein ($\Phi = 0.9$ in a 0.1 M solution of NaOH) as reference.

Cyclic voltammetry was carried out in a 3 electrode configuration; Pt electrodes have been used as working and counter electrode and Ag/AgCl as reference electrode. CV experiments were performed at a scan rate of 50 mV/s at room temperature under nitrogen flux in anhydrous acetonitrile with TBAPF6 as electrolyte (0.1M) (analyte concentration 10^{-3} M).

The optical characterization of the OLED devices was performed using a Gooch&Housego OL770 spectroradiometer coupled with an integrating sphere and a camera telescope. The electrical measurements of the OLED devices were performed with a Keithley 2400 SourceMeter.

Several devices (4-5 per type) were tested to verify the reproducibility of the results and the reported data are related to the best performances.

- *Synthesis of Am_1*

A solution of benzoic acid (500 mg, 3.47 mmol) in 28 mL of dry dimethylformamide (DMF) was cooled with an ice bath, TEA (403 mg, 3.47 mmol) and ethyl chloroformate (394 mg, 3.47 mmol) were added and under stirring and an argon atmosphere. After 1 h, *O,O*-dimethyldopamine (634 mg, 3.47 mmol) was added dropwise. The mixture was stirred at room temperature for 1 h and then heated at 50–60 °C for 1 h. The mixture was evaporated under reduced pressure and the residue extracted with an aqueous solution of NH_4Cl (10% w/w) and chloroform and then with phosphate buffer (0.1 M, pH 7.4) and chloroform. The organic layers were collected, dried over anhydrous sodium sulphate, filtered and evaporated under reduced pressure to afford the pure *N*-(3,4-

dimethoxyphenethyl)benzamide *Am_1* (969 mg, 98%, $R_f = 0.8$ chloroform/methanol 95:5 (v/v)).

^1H NMR (400 MHz, CDCl_3) δ ppm: 7.83 (dd, $J = 8.2, 2.3$ Hz, 2H), 7.71 (t, $J = 8.2$ Hz, 1H), 7.59 (t, $J = 8.2$ Hz, 2H), 6.56 (bs, 1H), 4.31 (s, 3H, $-\text{OCH}_3$), 4.28 (s, 3H, $-\text{OCH}_3$), 4.12 (dt, $J = 6.4, 6.0$ Hz, 2H), 3.32 (t, $J = 6.4$ Hz, 2H).

- *Synthesis of **Am_2***

A solution of 4-fluorobenzoic acid (140 mg, 1 mmol) in 8 mL of dry DMF was cooled with an ice bath and TEA (116 mg, 1 mmol) and ethyl chloroformate (114 mg, 1 mmol) were added under stirring and an argon atmosphere. After 1 h, *O,O*-dimethyldopamine (182 mg, 1 mmol) was added dropwise. The mixture was stirred at room temperature for 1 h and then heated at 50–60 °C for 1 h. The mixture was evaporated to dryness under reduced pressure and the residue worked-up as described above. The procedure afforded the pure *N*-(3,4-dimethoxyphenethyl)4-fluorobenzamide (*Am_2*) (275 mg, 91%, $R_f = 0.81$ chloroform/methanol 95:5 (v/v)).

^1H NMR (400 MHz, CDCl_3) δ ppm: 7.70 (dd, $J = 8.6, 5.3$ Hz, 2H), 7.05 (t, $J = 8.5$ Hz, 2H), 6.7-6.85 (m, 3H), 6.28 (bs, 1H), 3.85 (s, 3H, $-\text{OCH}_3$), 3.82 (s, 3H, $-\text{OCH}_3$), 3.6 (dt, $J = 6.7, 6.0$ Hz, 2H), 2.85 (t, $J = 6.72$ Hz, 2H).

- *Synthesis of **Am_3***

A solution of 4-methoxybenzoic acid (152 mg, 1 mmol) in 8 mL of dry DMFdimethylformamide (DMF) was cooled with an ice bath and TEA (116 mg, 1 mmol) and ethyl chloroformate (114 mg, 1 mmol) were added under stirring and an argon atmosphere. After 1 h, *O,O*-dimethyldopamine (182 mg, 1 mmol) was added dropwise. The mixture was stirred at room temperature for 1 h and then heated at 50–60 °C for 1 h. The mixture was evaporated under reduced pressure

and the residue worked-up as described above. The procedure afforded the pure *N*-(3,4-dimethoxyphenethyl)-4-methoxybenzamide *Am_3* (295 mg, 97%, $R_f = 0.8$ CHCl₃/MeOH 95:5 (v/v)).

¹H NMR (400 MHz, CDCl₃) δ ppm: 7.65 (d, $J = 8.4$ Hz, 2H), 6.87 (d, $J = 8.4$ Hz, 2H), 6.8-6.6 (m, 3H) 6.56 (bs, 1H), 3.85 (s, 6H, -OCH₃), 3.81 (s, 3H, -OCH₃), 3.65 (m, 2H), 2.85 (t, $J = 6.8$ Hz, 2H).

¹³C NMR (100 MHz, CDCl₃) δ ppm: 167.0, 148.9, 147.5, 142.6, 133.3, 131.5, 128.6 (2C), 120.6, 113.7 (2C), 111.9, 111.3, 55.9, 55.8, 55.3, 41.2, 35.2.

- *Synthesis of Am_4*

A solution of 4-cyanobenzoic acid (147 mg, 1 mmol) in 8 mL of dry DMF was cooled with an ice bath, and under stirring and an argon atmosphere, TEA (116 mg, 1 mmol) and ethyl chloroformate (114 mg, 1 mmol) were added. After 1 h, *O,O*-dimethyldopamine (182 mg, 1 mmol) was added dropwise. The mixture was stirred at room temperature for 1 h and then heated at 50–60 °C for 1 h. The mixture was evaporated to dryness under reduced pressure and the residue worked-up as described above. The procedure afforded the pure *N*-(3,4-dimethoxyphenethyl)-4-cyanobenzamide (**7c**) (275 mg, 92%, $R_f = 0.78$ CHCl₃/MeOH 95:5 (v/v)).

¹H NMR (400 MHz, CDCl₃) δ ppm: 7.79 (d, $J = 4$ Hz, 2H), 7.70 (d, $J = 8$ Hz, 2H), 6.83 (d, $J = 8$ Hz 1H), 6.76 (d, $J = 12$ Hz, 2H), 6.34 (bs, 1H), 3.87 (s, 3H, -OCH₃), 3.85 (s, 3H, -OCH₃), 3.71 (dt, $J = 6.4, 6.0$ Hz, 2H), 2.89 (t, $J = 6.4$ Hz, 2H).

¹³C NMR (100 MHz, CDCl₃) δ ppm: 132.40, 127.51, 120.63, 111.82 (2C), 111.37 (2C), 55.88 (2C), 41.38, 34.99.

- *Synthesis of PHQ*

A solution of the amide *Am_1* (989 mg, 3.47 mmol) in 11.7 mL of a mixture 3:11 (v/v) of ethanol/dichloromethane was treated under stirring with POCl₃ (3.28 mL, 34 mmol) and kept under reflux. After 4 h, 8 mL of petroleum ether were added and the mixture was kept under reflux. After 12 h the reaction mixture was filtered and the solid was rinsed with water and treated with an aqueous solution of K₂CO₃ until pH 10 was reached. Then the mixture was extracted with chloroform and the organic layers were dried with anhydrous sodium sulphate, filtered and evaporated under reduced pressure. The crude solid was purified by liquid chromatography on silica gel using dichloromethane/methanol 95:5 (v/v) as eluent to give the pure 6,7-dimethoxy-1-phenyl-3,4-dihydroisoquinoline *PHQ* (885 mg, 95%, R_f = 0.25, chloroform/methanol 95:5 (v/v)).

¹H NMR (400 MHz, CDCl₃) δ ppm: 7.61 (m, 2H), 7.43 (m, 3H), 6.78 (m, 2H), 3.93 (s, 3H, -OCH₃), 3.82 (t, *J* = 7.28 Hz, 2H), 3.7 (s, 3H, -OCH₃), 2.75 (t, *J* = 7.28 Hz, 2H).

¹³C NMR (100 MHz, CDCl₃) δ ppm: 167.0, 151.3, 147.2, 138.5, 132.8, 129.6, 128.9, 128.2, 121.3, 111.9, 110.4, 56.2, 56.1, 47.2, 26.0.

ESI⁺ MS: *m/z* 268.2.

- *Synthesis of FPHQ*

A solution of the amide *Am_2* (261 mg, 0.86 mmol) in 2.1 mL of a mixture 3:11 (v/v) of ethanol/dichloromethane was treated under stirring with POCl₃ (0.8 mL, 8.6 mmol) and kept under reflux. After 4 h, 8 mL of petroleum ether were added and the mixture was kept under reflux. After 12 h the reaction mixture was filtered and the solid was rinsed with water and worked-up as reported above. The crude solid was purified by liquid chromatography on silica gel using chloroform/methanol 95:5 (v/v) as eluent to give the pure 6,7-dimethoxy-1-

phenyl-3,4-dihydroisoquinoline (*FPHQ*) (187 mg, 76%, $R_f = 0.24$, chloroform/methanol 95:5 (v/v)).

^1H NMR (400 MHz, CDCl_3) δ ppm: 7.60 (dd, $J=8.4, 5.6$ Hz, 2H), 7.11 (t, $J = 8.4$, 2H), 6.78 (s, 1H), 6.74 (s, 1H), 3.94 (s, 3H, $-\text{OCH}_3$), 3.79 (t, $J = 7.4$, 2H), 3.73 (s, 3H, $-\text{OCH}_3$), 2.73 (t, $J=7.4$ Hz, 2H).

ESI⁺ MS: m/z 286.1.

- *Synthesis of OMePHQ*

A solution of the amide *Am_3* (295 mg, 0.97mmol) in 3.1 mL of a mixture 3:11 (v/v) of ethanol/dichloromethane was treated under stirring with POCl_3 (0.86 mL, 9.4 mmol) and kept under reflux. After 4 h, 2 mL of petroleum ether were added and the mixture was kept under reflux. After 12 h the reaction mixture was filtered and the solid was rinsed with water and worked-up as reported above. The crude solid was purified by liquid chromatography on silica gel using ether/ethyl acetate 1:1 (v/v) as eluent to give the pure 1-(4-methoxyphenyl)-6,7-dimethoxy-3,4-dihydroisoquinoline (*OMePHQ*) (200 mg, 70%, $R_f = 0.75$, DCM/MeOH95:5 (v/v)).

^1H NMR (400 MHz, CDCl_3) δ ppm: 7.59 (d, $J = 8.8$ Hz, 2H), 6.95 (d, $J = 8.8$ Hz, 2H), 6.84 (s, 1H), 6.78 (s, 1H), 3.95 (s, 3H, $-\text{OCH}_3$), 3.86 (s, 3H, $-\text{OCH}_3$), 3.82 (t, $J = 7.28$ Hz, 2H), 3.74 (s, 3H, $-\text{OCH}_3$), 2.55 (t, $J = 7.28$ Hz, 2H).

^{13}C NMR (100 MHz, CDCl_3) δ ppm: 166.5, 160.9, 151.3, 147.2 (2C), 133.0, 130.5 (2C), 121.3, 113.6 (2C), 112.0, 110.3 (2C), 56.2, 56.1, 55.4, 46.9, 26.1.

- *Synthesis of CNPHQ*

A solution of the amide *Am_4* (275 mg, 0.92mmol) in 3.1 mL of a mixture 3:11 (v/v) of ethanol/dichloromethane was treated under stirring with POCl_3 (0.86 mL, 9.4 mmol) and kept under reflux. After 4 h, 2 mL of petroleum ether were added

and the mixture was kept under reflux. After 12 h the reaction mixture was filtered and the solid was rinsed with water and worked-up as reported above. The crude solid was purified by liquid chromatography on silica gel using ether/ethyl acetate 1:1 (v/v) as eluent to give the pure 1-(4-cyanophenyl)-6,7-dimethoxy-3,4-dihydroisoquinoline (*CNPHQ*) (193 mg, 66%, $R_f = 0.8$, AcOEt/CE 7:3 (v/v)).

^1H NMR (400 MHz, CDCl_3) δ ppm: 7.74 (s, 4H), 6.84 (s, 2H), 6.65 (s, 2H), 3.96 (s, 3H, -OCH₃), 3.85 (t, $J = 8$ Hz, 2H), 3.74 (s, 3H, -OCH₃), 2.76 (t, $J = 8$ Hz).

^{13}C NMR (100 MHz, CDCl_3) δ ppm: 165.39, 151.39, 147.33, 143.60, 132.62, 132.09 (2C), 129.47 (2C), 120.72, 118.63, 112.98, 110.52, 56.21, 56.09, 47.93, 25.84.

- *Synthesis of Am_5*

A solution of O,O-Dimethyldopamine (500mg, 2.76 mmol) in 20.8 mL of toluene was treated with a solution of diethyloxalate (1.825 mg, 12.49 mmol) in 4.2 mL of toluene. The mixture was kept under reflux for 5 h and then cooled at room temperature and evaporated under reduced pressure. The residue was purified by liquid chromatography on silica gel (eluent: chloroform/methanol 99:1 (v/v)), to afford the amide 9 (644 mg, 83%, R_f 0.52 chloroform/methanol 98:2 (v/v)).

^1H NMR (400 MHz, CDCl_3) δ ppm: 7.44 (bs, 1H), 6.51 (m, 3H), 4.03 (q, $J = 6.8$ Hz, 2H), 3.59 (s, 3H, -OCH₃), 3.57 (s, 3H, -OCH₃), 3.32 (? , $J = 6.4$ Hz, 2H), 2.58 (t, $J = 6.8$ Hz, 2H), 1.08 (t, $J = 6.8$ Hz, 3H).

^{13}C NMR (100 MHz, solv) δ ppm: 160.4, 156.5, 148.8, 147.5, 130.7, 120.4, 111.8, 111.3, 62.6, 55.6, 55.5, 40.9, 34.4, 13.6.

- Synthesis of **1**

A solution of Am_5 (644 mg, 2.29 mmol) in 6 mL of a 3:11 (v/v) mixture of ethanol/dichloromethane was treated with POCl₃ (1.84 mL, 19.68 mmol) under reflux conditions.

After 5 h light petroleum (7 mL) was added and the mixture was kept under reflux and vigorous stirring overnight. The mixture was then evaporated under reduced pressure and the residue was dissolved in a water/methanol mixture (25 mL/1 mL). The resulting solution was brought to pH 10 with K₂CO₃ and extracted with chloroform. The collected organic layers were dried over anhydrous sodium sulphate, filtered and then evaporated under reduced pressure. The solid was purified by liquid chromatography on silica gel (eluent: chloroform) to afford compound **10** (469 mg, 77%, R_f 0.46 chloroform/methanol 98:2 (v/v))

¹H NMR (400 MHz, CD₃OD) δ ppm: 7.24 (s, 1H), 6.87 (s, 1H), 4.40 (q, J = 7.2 Hz, 2H), 3.88 (s, 3H, -OCH₃), 3.81 (s, 3H, -OCH₃), 3.73 (t, J = 8.0 Hz, 2H), 2.71 (t, J = 8.0 Hz, 2H), 1.40 (t, J=7.2 Hz, 3H).

¹³C NMR (100 MHz, CD₃OD) δ ppm:165.5, 161.1, 153.9, 148.9, 133.4, 119.5, 111.8, 111.7, 63.0, 56.6, 56.4, 48.0, 25.7, 14.4.

- Synthesis of **CHQ**

A solution of compound **1** (155 mg, 0.588 mmol) in 1mL of methanol was treated with HCl 6M (10 mL) under reflux conditions overnight. The reaction mixture was evaporated under reduced pressure affording pure **1** (138 mg, 99%, R_f 0.47 chloroform/methanol 8:2 (v/v)).

¹H NMR (400 MHz, CD₃OD) δ ppm: 7.87 (s, 1H), 7.12 (s, 1H), 4.00 (s, 3H, -OCH₃), 3.92 (t, J = 8.4 Hz, 2H), 3.86 (s, 3H, -OCH₃), 3.16 (t, J = 8.4, 2H).

¹³C NMR (100 MHz, CD₃OD) δ ppm: 163.7, 161.2, 159.3, 149.5, 137.8, 116.0, 115.7, 112.8, 57.6, 56.7, 42.5, 25.8.

- Synthesis of **2**

A solution of compound 1 (190 mg, 0.722 mmol) in 3.2 mL of glacial acetic acid was treated with palladium on carbon (Pd/C 10%, 38 mg). The resulting suspension was kept at 80 °C for 4h and then filtered on celite and added dropwise to a saturated aqueous NaHCO₃ solution (100 mL). The solution was extracted with ethyl acetate and the collected organic layers were dried over anhydrous sodium sulphate, then filtered and evaporated under reduced pressure providing compound 2 (144 mg, 76%, R_f 0.64 chloroform/methanol 98:2 (v/v)).

¹H NMR (400 MHz, acetone-d₆) δ ppm: 8.40 (d, J = 4.8 Hz, 1H), 8.01 (s, 1H), 7.82 (d, J = 4.8 Hz, 1H), 7.41 (s, 1H), 4.49 (q, J = 6.8 Hz, 2H), 4.01 (s, 3H, -OCH₃), 3.99 (s, 3H, -OCH₃), 1.44 (t, J = 6.8Hz, 3H).

¹³C NMR (100 MHz, acetone-d₆) δ ppm: 167.0, 154.0, 152.0, 148.0, 140.8, 134.5, 124.5, 122.6, 105.5, 104.2, 61.4, 55.7, 55.6, 14.1.

- Synthesis of **CQ**

A solution of compound 2 (144 mg, 0.552 mmol) in 1mL of methanol was treated with HCl 6M (9.4 mL) under reflux conditions overnight. The resulting mixture was filtered and rinsed with ethanol. The filtered solution was evaporated under reduced pressure to obtain ligand CQ (111mg, 86%, R_f 0.45 chloroform/methanol 8:2 (v/v))

¹H NMR (400 MHz, CD₃OD) δ ppm: 8.41 (d, J = 5.2 Hz, 1H), 8.02 (s,1H), 7.83 (d, J = 5.2 Hz, 1H), 7.42 (s, 1H), 4.025 (s, 3H, -OCH₃), 3.998 (s, 3H, -OCH₃)

¹³C NMR (100 MHz, CD₃OD) δ ppm: 167.0, 153.0, 152.0, 147.0, 140.82, 135.0, 124.0, 122.6, 105.5, 104.2, 55.8, 55.6.

- Synthesis of **6-Dehydrogingerdione**

Vanillin (1 g, 6.6 mmol), 2,4-nonanedione (2 g, 12.8 mmol) and boron trioxide (1.4 g, 20 mmol) have been mixed with 8 mL of *N,N*-dimethylformamide (DMF) and warmed to 90 °C for 3h. A solution of isobutylamine (400 mg, 4 mmol) in 7 mL of DMF has been added dropwise for 2 h at room temperature. After stirring at 85–90 °C for 1 h, has been added HCl 1M until pH=5. The resulting mixture has been stirred at 60 °C for 1 h and at room temperature for 12 h. The reaction mixture has been extracted with ethyl acetate, and the solvents have been evaporated under reduced pressure. The residue has been purified by column chromatography on silica gel (eluent: gradient from cyclohexane to cyclohexane/ethyl acetate 7:3 (v/v)) to afford **2** (766 mg, 40% Rf 0.54 cyclohexane/ethyl acetate 7:3 (v/v)).

¹H NMR (CDCl₃, 400 MHz). δ ppm: 15.54 (br s, 1H), 7.54 (d, J = 16 Hz, 1H), 7.09 (dd, J= 1.6, J=8Hz, 1H), 7.02 (d, J = 1.6 Hz, 1H), 6.93 (d, J = 8 Hz, 1H), 6.35 (d, J = 16 Hz, 1H), 5.64 (s, 1H), 3.93 (s, 3H, OCH₃), 2.39 (t, J=8 Hz, 2H), 1.70–1.63 (m, 2H), 1.27–1.36 (m, 4H), 0.92 (t, J= 4 Hz, 3H).

¹³C NMR (CDCl₃, 100 MHz). δ ppm: 200.22, 178.14, 147.76, 146.99, 139.91, 127.69, 122.63, 120.51, 114.37, 109.53, 110.15, 55.1, 40.09, 31.48, 25.34, 22.46, 13.94.

- Synthesis of **μ₂Ir**

Iridium trichloride hydrate (500 mg, 1.67 mmol) was dissolved in a mixture of 32 mL of 2-ethoxyethanol and water 3:1 (v/v) and treated with 480 μL (3.6 mmol) of 2-phenylpyridine under reflux and argon atmosphere. After 24 h the reaction mixture was cooled and filtered on a glass filter frit to obtain **μ₂Ir** as a yellow precipitate (644 mg, 72%).

^1H NMR (400 MHz, DMSO- d_6) δ ppm: 9.81 (d, $J = 5.6$ Hz), 9.53 (d, $J = 5.6$ Hz), 8.26 (d, $J = 8.0$ Hz), 8.18 (d, $J = 8.0$ Hz), 8.11 (t, $J = 8.0$ Hz), 8.02 (t, $J = 8.0$ Hz), 7.79 (d, $J = 8.0$ Hz), 7.73 (d, $J = 8.0$ Hz), 7.56 (t, $J = 5.6$ Hz), 7.44 (t, $J = 5.6$ Hz), 6.89 (t, $J = 8.0$ Hz), 6.83 (t, $J = 8.0$ Hz), 6.76 (t, $J = 8.0$ Hz), 6.69 (t, $J = 8.0$ Hz), 6.25 (d, $J = 8.0$ Hz), 5.66 (d, $J = 8.0$ Hz).

- Synthesis of the iridium complexes ***Ir_PHQ_1-3***

A solution of the iridium complex $\mu\text{-Ir}$ (119 mg, 0.11 mmol) in DMF dry (15 mL) was treated under an argon atmosphere with *PHQ* (276 mg, 0.89 mmol), acetylacetone (22 mg, 0.22 mmol) and TEA (22 mg, 0.22 mmol) and kept under reflux for 48 h. The solvent was evaporated under reduced pressure and the solid was subjected to liquid chromatography on silica gel (eluent ethyl acetate/cyclohexane 3:7 (v/v)) to afford complexes *Ir_PHQ_1-3* in pure form (*Ir_PHQ_1*: 21.4 mg, 16%, $R_f = 0.67$; *Ir_PHQ_2*: 26.4 mg, 14%, $R_f = 0.6$; *Ir_PHQ_3*: 10.8 mg, 5%, $R_f = 0.48$, ethyl acetate/cyclohexane 7:3 (v/v)).

Ir_PHQ_1: ^1H NMR (400 MHz, CD_2Cl_2) δ ppm: 8.17 (d, $J = 5.2$ Hz, 1H), 7.94 (d, $J = 8.4$ Hz, 1H), 7.89 (d, $J = 8.4$ Hz, 1H), 7.80 (d, $J = 8.4$ Hz, 1H), 7.67-7.72 (m, 4H), 7.61 (t, $J = 8.0$ Hz, 1H), 7.56 (d, $J = 5.2$ Hz, 1H), 7.53 (s, 1H), 7.05 (t, $J = 6.4$ Hz, 1H), 6.6-7.0 (m, 10H), 3.89 (s, 3H, $-\text{OCH}_3$), 3.88 (s, 3H, $-\text{OCH}_3$), 3.42 (m, 1H), 3.00 (m, 1H), 2.67 (m, 1H), 2.41 (m, 1H).

^{13}C NMR (100 MHz, CD_2Cl_2) δ ppm: 175.4, 166.5, 166.2, 165.5, 162.5, 161.1, 151.4, 148.3, 147.7, 144.5, 143.0, 136.8, 136.7, 136.6, 136.1, 135.8, 129.6, 129.5, 129.1, 124.0, 123.6, 122.1, 121.7, 119.8, 119.5, 118.9, 118.8, 118.5, 112.0, 110.5, 56.2, 55.8, 47.7, 27.8.

ESI $^+$ MS: m/z 767.2.

Ir_PHQ_2: ^1H NMR (400 MHz, CD_2Cl_2) δ ppm: 8.15 (d, $J = 5.2$ Hz, 1H), 7.90 (d, $J = 8.0$ Hz, 1H), 7.6-7.85 (m, 4H), 7.54 (s, 1H), 7.51 (s, 1H), 6.99 (t, $J = 6.4$ Hz, 1H), 6.65-

6.95 (m, 1H), 3.93 (s, 9H, -OCH₃), 3.92 (s, 3H, -OCH₃), 3.71 (m, 1H), 3.46 (m, 1H), 3.40 (m, 1H), 2.69 (m, 1H), 2.62 (m, 1H), 2.46 (m, 1H), 2.38 (m, 1H).

¹³C NMR (100 MHz, CD₂Cl₂) δ ppm: 174.5, 174.2, 167.6, 166.6, 165.0, 162.9, 150.8, 150.7, 148.1, 147.2, 145.4, 145.3, 144.5, 137.3, 137.06, 137.01, 136.2, 132.2, 132.1, 130.1, 129.9, 129.8, 129.7, 126.7, 125.1, 124.1, 122.6, 122.3, 120.0, 119.3, 119.1, 119.0, 114.1, 112.3, 110.9, 56.6, 56.2, 49.1, 48.3, 28.0, 28.2.

ESI⁺ MS: *m/z* 879.3.

Ir_PHQ_3: ¹H NMR (400 MHz, CD₂Cl₂) δ ppm: 7.78 (d, *J* = 8.0 Hz, 1H), 7.51 (s, 1H), 6.7-6.9 (m, 4H), 3.88 (s, 3H, -OCH₃), 3.87 (s, 3H, -OCH₃), 3.68 (m, 1H), 3.38 (m, 1H), 2.68 (m, 1H), 2.43 (m, 1H).

¹³C NMR (100 MHz, CD₂Cl₂) δ ppm: 174.4, 166.5, 150.9, 147.6, 145.4, 136.8, 131.9, 129.9, 129.7, 122.5, 119.2, 57.8, 54.9, 48.4, 27.9.

ESI⁺ MS: *m/z* 991.3.

- Synthesis of the iridium complexes ***Ir_FPHQ_1-3***

A solution of the iridium complex μ -Ir (40 mg, 0.037 mmol) in DMF dry (5 mL) was treated under an argon atmosphere with *FPHQ* (44.4 mg, 0.15 mmol), acetylacetone (7.6 mg, 0.074 mmol) and TEA (7.7 mg, 0.074 mmol) and kept under reflux for 48 h. The solvent was evaporated under reduced pressure and the solid was subjected to liquid chromatography on silica gel (eluent chloroform/ethyl acetate 6:4 (v/v)) to afford complexes *Ir_FPHQ_1-3* in pure form (*Ir_FPHQ_1*: 34 mg, 59%, *R_f* = 0.76; *Ir_FPHQ_2*: 14.2 mg, 21%, *R_f* = 0.7; *Ir_FPHQ_3*: 4.6 mg, 6%, *R_f* = 0.65, chloroform/acetate 6:4 (v/v)).

Ir_FPHQ_1: ¹H NMR (400 MHz, CD₂Cl₂) δ ppm: 8.20 (d, *J* = 6.2 Hz, 1H), 7.99 (d, *J* = 8.0, 1H), 7.93 (d, *J* = 8.0 Hz, 1H), 7.82 (dd, *J* = 8.0, 6.2 Hz, 1H), 7.5-7.7 (m, 4H), 7.65 (t, *J* = 8.0 Hz, 1H), 7.57 (d, *J* = 5.5 Hz, 1H), 7.49 (s, 1H), 7.08 (t, *J* = 6.4 Hz, 1H), 6.85-7.0 (m, 5H), 6.79 (t, *J* = 8.0 Hz, 1H), 6.8 (s, 1H), 6.76-6.72 (m, 2H), 6.60 (t, *J* = 8.0 Hz,

1H), 6.48 (dd, J = 8.0 Hz, 1H), 3.92 (s, 3H, -OCH₃), 3.91 (s, 3H, -OCH₃), 3.43 (m, 1H), 3.00 (m, 1H), 2.69 (m, 1H), 2.45 (m, 1H).

¹³C NMR (100 MHz, CD₂Cl₂) δ ppm: 176.6, 171.5, 168.47, 168.41, 166.3, 167.1, 164.7, 164.3, 162.3, 153.9, 151.0, 148.3, 145.3, 145.1, 138.5, 138.1, 134.0, 131.9, 126.4, 125.8, 124.3, 123.9, 121.9, 120.9, 56.2, 55.8, 47.6, 27.9.

¹⁹F NMR (376 MHz, CD₂Cl₂) δ ppm: -112.01.

ESI⁺ MS: *m/z* 785.3.

Ir_FPHQ_2: ¹H NMR (400 MHz, CD₂Cl₂) δ ppm: 8.15 (d, J = 6.4 Hz, 1H), 7.95 (d, J = 8.0 Hz, 1H), 7.75-8.0 (m, 2H), 7.69 (d, J = 8.0, 1H), 7.66 (t, J = 7.28 Hz, 1H), 7.47 (s, 1H), 7.43 (s, 1H), 6.93 (t, J = 7.28 Hz, 1H), 6.87 (t, J = 7.28 Hz, 1H), 6.80 (t, J = 7.28 Hz, 1H), 6.73 (s, 1H), 6.71 (s, 1H), 6.74 (d, J = 7.28 Hz, 1H), 6.55-6.65 (m, 2H), 6.35-6.45 (m, 2H), 3.93 (s, 3H, -OCH₃), 3.93 (s, 3H, -OCH₃), 3.92 (s, 3H, -OCH₃), 3.89 (s, 3H, -OCH₃), 3.88 (s, 3H, -OCH₃), 3.70 (m, 1H), 3.47 (m, 1H), 3.40 (m, 1H), 2.94 (m, 1H), 2.74 (m, 1H), 2.66 (m, 1H), 2.51 (m, 1H), 2.41 (m, 1H).

¹³C NMR (100 MHz, CD₂Cl₂) δ ppm: 174.2, 173.1, 170.6, 168.2, 166.3, 165.2, 162.3, 161.1, 151.1, 150.9, 148.3, 147.3, 147.2, 144.0, 141.4, 136.7, 136.1, 131.9, 131.8, 131.2, 131.1, 129.9, 123.8, 122.0, 121.7, 120.0, 118.8, 111.8, 110.5, 56.2, 55.9, 48.6, 47.7, 28.0, 27.7.

¹⁹F NMR (376 MHz, CD₂Cl₂) δ ppm: -11.75, -112.07.

ESI⁺ MS: *m/z* 915.5.

Ir_FPHQ_3: ¹H NMR (400 MHz, CD₂Cl₂) δ ppm: 7.83 (dd, J = 8.0, 6.4 Hz, 1H), 7.49 (s, 1H), 6.82 (s, 1H), 6.65 (dt, J = 8.0, 2.7 Hz, 1H), 6.42 (dd, J = 8.0, 2.7 Hz, 1H), 3.93 (s, 3H, -OCH₃), 3.91 (s, 3H, -OCH₃), 3.69 (m, 1H), 3.40 (m, 1H), 2.71 (m, 1H), 2.49 (m, 1H).

¹³C NMR (100 MHz, CD₂Cl₂) δ ppm: 173.4, 169.3, 165.3, 163.1, 151.0, 147.3, 141.4, 131.8, 130.8, 121.9, 121.6, 111.7, 110.5, 106.2, 56.2, 55.9, 48.8, 27.9.

¹⁹F NMR (376 MHz, CD₂Cl₂) δ ppm: -111.77.

ESI⁺ MS: *m/z* 1045.3.

- Synthesis of the iridium complexes **Ir_OMePHQ_1-3**

A solution of the iridium complex μ -Ir (67 mg, 0.064mmol) in DMFdry (4 mL) was treated under an argon atmosphere with OMePHQ (150 mg, 0.5mmol), acetylacetone (25 mg, 0.25mmol) and TEA (26 mg, 0.25mmol) and kept under reflux for 48 h. The solvent was evaporated under reduced pressure and the solid was subjected to liquid chromatography on silica gel (eluent cyclohexane/ethyl acetate 4:6 (v/v)) to afford complexes Ir_OMePHQ_1-3 in pure form (Ir_OMePHQ_1: 15.7 mg, 16%, *R_f* = 0.76; Ir_OMePHQ_2: 12.1 mg, 11%, *R_f* = 0.66; Ir_OMePHQ_3: 12.4 mg, 6%, cyclohexane/acetate 4:6 (v/v)).

Ir_OMePHQ_1: ¹H NMR (400 MHz, CDCl₃) δ ppm: 8.15 (d, *J* = 5.2 Hz, 1H), 7.89 (d, *J* = 8.4 Hz, 1H), 7.84 (d, *J* = 8.4 Hz, 1H), 7.71 (d, *J* = 8.4 Hz, 1H), 7.6-7.7 (m, 4H), 7.53 (m, 1H), 7.51 (s, 1H), 6.6-7.0 (m, 8H), 6.72 (s, 1H), 6.4-6.5 (m, 2H), 3.89 (s, 3H, -OCH₃), 3.88 (s, 3H, -OCH₃), 3.54 (s, 3H, -OCH₃), 3.41 (m, 1H), 3.00 (m, 1H), 2.63 (m, 1H), 2.52 (m, 1H).

¹³C NMR (100 MHz, CDCl₃) δ ppm: 173.6, 172.9, 170.5, 167.9, 166.8, 162.8, 160.5 (2C), 150.4, 150.2, 148.4, 147.0 (2C), 143.9, 137.9, 137.8, 137.3, 135.5, 131.9, 131.7, 130.4, 129.9, 129.8, 123.5, 122.7, 122.6, 121.7, 120.5, 119.5, 118.5 (2C), 111.7, 110.2, 105.9, 56.4, 56.1, 56.0, 54.5, 47.3, 28.1.

Ir_OMePHQ_2: ¹H NMR (400 MHz, CDCl₃) δ ppm: 8.12 (d, *J* = 5.2 Hz, 1H), 7.85 (d, *J* = 8.0 Hz, 1H), 7.7 (d = 8.0 Hz, 2H), 7.64 (d, *J* = 7.6 Hz, 1H), 7.58 (t, *J* = 7.6 Hz, 1H), 7.52 (s, 1H), 7.50 (s, 1H), 6.8-6.9 (m, 4H), 6.72 (s, 1H), 6.69 (s, 1H), 6.4-6.5 (m, 3H), 6.36 (d, *J* = 8.4 Hz, 1H), 3.89 (s, 9H, -OCH₃), 3.86 (s, 3H, -OCH₃), 3.57 (s, 3H, -OCH₃), 3.5 (m, 1H), 3.3-3.4 (m, 2H), 2.9-3.0 (m, 2H), 2.6 (m, 1H), 2.4-2.5 (m, 2H).

¹³C NMR (100 MHz, CDCl₃) δ ppm: 173.6, 172.9, 170.5, 167.9, 166.8, 162.8, 160.5 (2C), 150.4, 150.2, 148.4, 147.0 (2C), 143.9, 137.9, 137.8, 137.3, 135.5, 131.9,

131.7, 130.4, 129.9, 129.8, 123.5, 122.7, 122.6, 121.7, 120.5, 120.3, 119.5, 118.5 (2C), 111.7, 110.3, 110.2, 105.9, 105.2, 56.4, 56.3, 56.1, 56.0, 54.6, 54.5, 48.1, 47.3, 28.4, 28.1.

Ir_OMePHQ_3: ^1H NMR (400 MHz, CDCl_3) δ ppm: 7.68 (d, $J = 8.0$ Hz, 1H), 7.50 (s, 1H), 6.74 (s, 1H), 6.43 (dd, $J = 8.0, 1.3$ Hz, 1H), 6.41 (d, $J = 8.0$ Hz, 1H), 3.89 (s, 3H, -OCH₃), 3.86 (s, 3H, -OCH₃), 3.71 (m, 1H), 3.64 (s, 3H, -OCH₃), 3.41 (m, 1H), 2.63 (m, 1H), 2.42 (m, 1H).

^{13}C NMR (100 MHz, CDCl_3) δ ppm: 166.5, 164.4, 150.9, 147.6, 145.4, 136.8, 131.9, 129.9, 125.7, 122.5, 121.3, 112.0, 110.3, 57.8, 57.2, 54.9, 48.4, 27.9.

- Synthesis of the iridium complexes ***Ir_CNPHQ_1-2***

A solution of the iridium complex $\mu\text{-Ir}$ (46 mg, 0.043 mmol) in DMF dry (4 mL) was treated under an argon atmosphere with *CNPHQ* (100 mg, 0.34 mmol), acetylacetonone (17 mg, 0.17 mmol) and TEA (17.8 mg, 0.17 mmol) and kept under reflux for 48 h. The solvent was evaporated under reduced pressure and the solid was subjected to liquid chromatography on silica gel (eluent cyclohexane/DCM/ethyl acetate 1.5:1.5:7 (v/v)) to afford complexes *Ir_CNPHQ_1-2* in pure form (*Ir_CNPHQ_1*: 14 mg, 22%, $R_f = 0.75$; *Ir_CNPHQ_2*: 12 mg, 15%, $R_f = 0.5$; cyclohexane/DCM/ethyl acetate 1.5:1.5:7 (v/v)).

Ir_CNPHQ_1: ^1H NMR (400 MHz CD_2Cl_2) δ ppm: 8.14 (d, $J = 5.6$ Hz, 1H), 8.00 (d, $J = 7.7$ Hz, 1H), 7.93 (d, $J = 7.4$ Hz, 1H), 7.87 (d, $J = 8$ Hz, 1H), 7.75-7.71 (m, 3H), 7.66 (t, $J = 7.8$ Hz, 1H), 7.56 (d, $J = 5.4$ Hz, 1H), 7.45 (s, 1H), 7.17 (d, $J = 8$ Hz, 1H), 7.13 (s, 1H), 7.07 (t, $J = 6$ Hz, 1H), 6.95-8.85 (m, 6H), 6.81 (s, 1H), 6.70 (d, $J = 8$ Hz, 1H), 6.63 (d, $J = 7.3$, 1H), 3.9 (s, 6H, -OCH₃), 3.52 (m, 1H), 3.41 (m, 1H), 2.79 (m, 1H), 2.47 (m, 1H).

^{13}C NMR (125 MHz CD_2Cl_2) δ ppm: 139.65, 136.84, 136.52, 136.20, 129.95, 128.57, 124.36, 123.75, 122.39, 122.31, 121.95, 120.49, 120.05, 119.21, 118.78, 112.02, 111.59, 110.63, 47.50, 29.67.

Ir_CNPHQ_2: ^1H NMR (400 MHz CD_2Cl_2) δ ppm: 8.11 (d, $J = 4$ Hz, 1H), 7.98 (d, $J = 8$ Hz, 1H), 7.91 (d, $J = 8$ Hz, 1H), 7.88-7.85 (m, 3H), 7.77-7.71 (m, 3H), 7.62 (d, $J = 4$ Hz, 1H), 7.48 (s, 1H), 7.42 (s, 1H), 7.27-7.22 (m, 3H), 7.20 (d, $J = 2$ Hz, 1H), 7.05 (d, $J = 4$ Hz, 1H), 6.96 (d, $J = 2$ Hz, 1H), 6.85 (s, 1H), 6.79 (s, 1H), 3.94 (s, 3H, $-\text{OCH}_3$), 3.93 (s, 3H, $-\text{OCH}_3$), 3.93 (s, 3H, $-\text{OCH}_3$), 3.9 (s, 3H, $-\text{OCH}_3$), 3.48-2.34 (m, 8H)

^{13}C NMR (100 MHz CD_2Cl_2) δ ppm: 173.9, 151.8, 151.4, 147.4, 143.9, 139.5, 136.6, 136.5, 132.2, 131.8, 130.4, 119.1, 112.4, 111.5, 110.6, 66.3, 56.3, 55.9, 33.9, 31.9, 29.7, 29.6, 29.4, 28.9, 27.7, 23.8, 22.7, 13.8.

- Synthesis of the iridium complexes **Ir_CHQ**

A solution of iridium complex μ_Ir (96 mg, 0.0895 mmol) in ethoxyethanol (3.5 mL) was purged with argon for 20 minutes and then ligand CHQ (65 mg, 0.277 mmol) and K_2CO_3 (124 mg, 0.897 mmol) were added. The mixture was kept at 50 $^\circ\text{C}$ under vigorous stirring and argon atmosphere overnight.

The mixture was then cooled to room temperature and water (20 mL) was added; the resulting mixture was extracted with dichloromethane, the collected organic layers were dried over anhydrous sodium sulphate, filtered and evaporated under reduced pressure. This organic fraction was purified by liquid chromatography on silica gel (eluent dichloromethane/ethyl acetate 6:4 (v/v)) affording pure complex Ir_CHQ (40 mg, 30%, R_f 0.20 dichloromethane/ethyl acetate 7:3 (v/v))

^1H NMR (400 MHz, CD_2Cl_2) δ ppm: 8.73 (d, $J = 7.2$ Hz, 1H), 8.66 (s, 1H), 8.23 (d, $J = 7.2$ Hz, 1H), 7.88 (d, $J = 7.2$ Hz, 1H), 7.85 (d, $J = 7.2$ Hz, 1H), 7.75 (d, $J = 7.2$ Hz, 2H), 7.57-7.60 (m, 2H), 7.20 (t, $J = 7.2$ Hz, 1H), 7.07 (t, $J = 7.2$ Hz, 1H), 6.81-6.89 (m, 2H), 6.72-6.77 (m, 2H), 6.58 (s, 1H), 6.36 (d, $J = 7.2$ Hz, 1H), 6.11 (d, $J = 7.2$, 1H), 3.95 (s,

3H, -OCH₃), 3.88 (s, 3H, -OCH₃), 3.66 (m, 1H), 3.15 (m, 1H), 2.64 (m, 1H), 2.36 (m, 1H).

¹³C NMR (100 MHz, CD₂Cl₂) δ ppm: 172.4 169.3, 169.2, 167.8, 167.7, 162.5, 152.2, 148.9, 148.0, 147.5, 144.1, 143.8, 137.2, 137.1, 132.5, 132.3, 130.7, 129.9, 129.6, 127.3, 124.3, 124.2, 122.3, 122.1, 121.5, 121.5, 119.1, 118.2, 112.8, 109.5, 56.3, 56.2, 49.4, 26.8

MALDI MS: *m/z* 501.1 [Ir(ppy)₂ + H]⁺, 757.2 [M + Na]⁺, 773.2 [M + K]⁺.

- Synthesis of the iridium complexes **Ir_CQ**

A solution of iridium complex μ _Ir (94 mg, 0.0877 mmol) in ethoxyethanol (3.5 mL) was purged with argon for 20 minutes and then ligand CQ (62 mg, 0.266 mmol) and K₂CO₃ (122 mg, 0.883 mmol) were added. The mixture was kept at 50 °C under vigorous stirring and argon atmosphere overnight.

The mixture was then cooled to room temperature and water (20 mL) was added; the resulting mixture was extracted with dichloromethane, the collected organic layers were dried over anhydrous sodium sulphate, filtered and evaporated under reduced pressure to afford complex Ir_CQ (177 mg, 90%, R_f 0.20 dichloromethane/ethyl acetate 7:3 (v/v))

¹H NMR (400 MHz, CD₂Cl₂) δ ppm: 9.54 (s, 1H), 8.65 (d, J = 7.6 Hz, 1H), 7.82 (t, J = 7.6 Hz, 1H), 7.77 (d, J = 7.6 Hz, 1H), 7.50-7.67 (m, 4H), 7.47 (d, J = 5.6 Hz, 1H), 7.42 (d, J = 7.6 Hz, 1H), 7.38 (d, J = 5.6 Hz, 1H), 7.03 (t, J = 7.6 Hz, 1H), 6.97 (s, 1H), 6.81-6.87 (m, 3H), 6.73 (t, J = 7.6 Hz, 1H), 6.71 (t, J = 7.6 Hz, 1H), 6.31 (d, J = 7.6 Hz, 1H), 6.12 (d, J = 7.6 Hz, 1H), 3.95 (s, 3H, -OCH₃), 3.87 (s, 3H, -OCH₃).

¹³C NMR (100 MHz, CD₂Cl₂) δ ppm: 174.1, 168.9, 167.9, 154.4, 152.1, 150.6, 149.3, 148.9, 148.8, 147.2, 144.6, 144.4, 139.8, 137.3, 137.2, 134.9, 129.9, 129.5, 126.7, 124.9, 124.6, 124.2, 122.4 (2C), 122.3 (2C), 121.5, 121.0, 119.2, 118.6, 106.0, 104.6, 56.1, 56.0

MALDI MS: m/z 501.1 $[\text{Ir}(\text{ppy})_2 + \text{H}]^+$, 755.2 $[\text{M} + \text{Na}]^+$, 771.2 $[\text{M} + \text{K}]^+$.

- Synthesis of the iridium complexes **$\text{Ir}(\text{ppy})_2\text{acac}$**

To a solution of the iridium complex $\mu\text{-Ir}$ (32.1 mg, 0.03 mmol) in 5 mL of dichloromethane has been added acetylacetone (8.23 μL , 0.08 mmol) in 0.5 mL of EtOH.

To this mixture has been added tetrabutylammonium hydroxide as a 20% w/w aqueous solution (106 μL , 0.51 mmol). The mixture has been kept at 30 °C under vigorous stirring and argon atmosphere for 5 hours. After cooling to room temperature the reaction mixture has been purified by liquid chromatography on silica gel (eluent dichloromethane) affording pure complex $\text{Ir}(\text{ppy})_2\text{acac}$ (27 mg, 75%, Rf 0.8 dichloromethane/ethyl acetate 9:1 (v/v)).

^1H NMR (CDCl_3 , 400 MHz). δ ppm: 8.53 (d, $J = 4$ Hz, 2 H), 7.86 (d, $J = 8$ Hz, 2 H), 7.75 (t, $J = 8$ Hz, 2 H), 7.57 (d, $J = 8$ Hz, 2 H), 7.36 (t, $J = 8$ Hz, 2 H), 6.83 (t, $J = 8$ Hz, 2 H), 6.72 (t, $J = 8$ Hz, 2 H), 6.3 (d, $J = 8$ Hz, 2H), 5.24 (s, 1 H), 1.81 (s, 6 H).

^{13}C NMR (CDCl_3 , 100 MHz). δ ppm: 196.40, 158.58, 137.46, 124.77, 100.03, 57.23, 36.09.

- Synthesis of the iridium complexes **Ir_Curc**

To a solution of the iridium complex $\mu\text{-Ir}$ (32.1 mg, 0.03 mmol) in 5 mL of dichloromethane has been added curcumin (29.4 mg, 0.08 mmol) in 0.5 mL of EtOH.

To this mixture has been added tetrabutylammonium hydroxide as a 20% w/w aqueous solution (106 μL , 0.51 mmol). The mixture has been kept at 30 °C under vigorous stirring and argon atmosphere for 5 hours. After cooling to room temperature the reaction mixture has been purified three times by liquid

chromatography on silica gel (eluent dichloromethane) affording pure complex Ir_Curc (24 mg, 50%, Rf 0.55 dichloromethane/ethyl acetate 9:1 (v/v)).

¹H NMR (CDCl₃, 400 MHz). δ ppm: 8.61 (d, J=8 Hz, 2H), 7.86 (d, J=8 Hz, 2H), 7.69 (t, J=8 Hz, 2H), 7.62 (d, J=8 Hz, 2H), 7.30-7.26 (m, 2H), 7.13 (br s, 2H), 6.9 (br s, 2H), 6.87 (br s, 2H), 6.76 (t, J=8 Hz, 2H), 6.50 (d, J=16 Hz, 2H), 6.35 (d, J=8 Hz, 2H), 5.64 (s, 1H), 3.95 (s, 3H, OCH₃).

¹³C NMR (CDCl₃, 100 MHz). δ ppm: 176.4, 168.6, 148.1, 147.8, 146.8, 145.0, 136.8, 136.2, 133.2, 128.8, 128.4, 123.7, 122.9, 121.5, 120.5, 118.4, 114.7, 109.3, 103.0, 56.06.

ESI+ MS: *m/z* 869.

- Synthesis of the iridium complexes **Ir_Ging**

To a solution of the iridium complex μ_Ir (32.1 mg, 0.03 mmol) in 5 mL of dichloromethane has been added 6-Dehydrogingerdione (23.2 mg, 0.08 mmol) in 0.5 mL of EtOH. To this mixture has been added tetrabutylammonium hydroxide as a 20% w/w aqueous solution (106 μL, 0.51 mmol). The mixture has been kept at 30 °C under vigorous stirring and argon atmosphere for 5 hours. After cooling to room temperature the reaction mixture has been purified three times by liquid chromatography on silica gel (eluent dichloromethane) affording pure complex Ir_Ging (31 mg, 66%, Rf 0.86 dichloromethane/ethyl acetate 9:1 (v/v)).

¹H NMR (CDCl₃, 400 MHz). δ ppm: 8.57 (br s, 2H), 7.89 (t, J=8 Hz, 2H), 7.72 (t, J=8 Hz, 2H), 7.61- 7.55 (m, 2H), 7.26 (br s, 1H), 7.11 (t, J=8 Hz, 2H), 7.00 (br s, 1H), 6.99 (br s, 1H), 6.96 (br s, 1H), 6.87-6.83 (m, 2H), 6.75 -6.72 (m, 2H), 6.43 (br s, 1H), 6.39 (br s, 1H), 6.31 (d, J=8 Hz, 1H), 5.43 (s, 1H), 3.9 (s, 3H, OCH₃), 2.11-2.08 (m, 2H), 1.38 (br s, 2H), 1.16-1.12 (m, 2H), 0.95-0.93 (m, 2H), 0.78 (t, J= 7 Hz, 3H).

¹³C NMR (CDCl₃, 100 MHz). δ ppm: 190.02, 176.5, 169.0, 149.1, 149.0, 148.9, 147.4, 146.6, 145.7, 145.5, 137.5, 137.0, 134.4, 134.1, 129.3, 129.4, 128.2, 124.7, 122.5, 122.1, 121.1, 120.9, 119.2, 115.7, 101.9, 109.8, 42.9, 31.9, 27.7, 23.9, 14.3.

ESI+ MS: m/z 791.

- Synthesis of **3**

ZnCl₂ (188 mg, 1.38 mmol) has been added to a solution of 2,2'-bipyridine (145 mg, 0.93 mmol) in water (60 ml). After stirring for 48 h at room temperature the suspension has been filtered and the white solid has been washed with ethanol (226 mg, 83%).

¹H NMR (D₂O, 400 MHz). δ ppm: 8.56 (br s, 2H), 8.44-8.42 (d, $J=8$ Hz, 2H), 8.18 (t, $J=8$ Hz, 2H), 7.64 (br s, 2H).

- Synthesis of **4**

ZnCl₂ (567 mg, 4.16 mmol) has been added to a solution of 1,10phenanthroline (500 mg, 2.77 mmol) in CHCl₃ (50 ml). After stirring for 24 h at room temperature the white suspension has been filtered and the solid has been washed with CHCl₃ (584.5 mg 97%).

¹H NMR (D₂O, 400 MHz). δ ppm: 8.78 (d, $J=8$ Hz, 4H), 8.19 (br s, 2H), 7.96 (br s, 1H).

- Synthesis of the zinc complex **bpyZnCurc**

An orange solution of curcumin (80 mg, 0.215 mmol) in MeOH (15 ml) has been added to triethylamine (20 mg, 0.215 mmol) under nitrogen at room temperature. After ten minutes the resulting red solution has been added to a solution of **3** (63 mg, 0.215 mmol) in water (5 ml). The resulting yellow–orange suspension has

been stirred under nitrogen for 24 hours, at room temperature. After filtration, the dark orange solid has been washed with water and MeOH (80 mg, 60%).

¹H NMR (DMSO-d₆, 400 MHz). δ ppm: 8.75 (br s, 2H), 8.49 (d, J= 8Hz, 2H), 8.07 (t, J= 8Hz, 2H), 7.61 (br s, 2H), 7.45 (d, J= 15Hz, 2H), 7.14 (br s, 2H), 7.03 (br s, 2H), 6.67 (br s, 2H), 6.55 (br s, 2H), 5.65 (br s, 1H), 3.79 (br s, 6H, OCH₃).

¹³C NMR (DMSO-d₆, 100 MHz). δ ppm: 184.5, 156.2, 149.3, 148.8, 148.4, 139.2, 138.9, 128.5, 125.8, 125.3, 122.8, 121.5, 117.0, 111.0, 103.0, 56.1.

MALDI MS: *m/z* 649 [M(37Cl)+Na]⁺, 647 [M(35Cl)+Na]⁺, 589 [M-Cl]⁺. 80

- Synthesis of the zinc complex **phenZnCurc**

An orange solution of curcumin (25 mg, 0.068 mmol) in MeOH (0.72 ml) has been added to triethylamine (6 mg, 0.068 mmol) under nitrogen at room temperature, giving rise to a red solution which has been added to a solution of 4(20 mg, 0.068 mmol) in DMSO (0.33 ml). The resulting orange suspension has been stirred under nitrogen for 24 hours at room temperature. After filtration, the orange solid has been washed with MeOH (29.5 mg, 67%).

¹H NMR (DMSO-d₆, 400 MHz). δ ppm : 9.40 (br s, 2H), 8.85 (d, J=8 Hz, 2H), 8.24 (s, 2H), 8.12 (br s, 2H), 7.40-7.53 (m, 1H), 7.22 (br s, 2H), 7.13 (br s, 2H), 6.78 (d, J=8 Hz, 2H), 6.69 (d, J=16 Hz, 1H), 5.72 (br s, 1H), 3.78 (s, 6H, OCH₃).

¹³C NMR (DMSO-d₆, 100 MHz). δ ppm: 183.90, 149.9, 148.84, 148.40, 140.40, 140.1, 138.63, 129.07, 128.70, 127.53, 126.83, 126.22, 122.79, 116.07, 111.31, 103.58, 56.08.

MALDI MS: *m/z* 672 [M(37Cl)+Na]⁺, 670 [M(35Cl)+Na]⁺, 612 [M-Cl]⁺

- Synthesis of the zinc complex **bpyZnGing**

A yellow solution of 6-Dehydrogingerdione (62 mg, 0.215 mmol) in MeOH (15 ml) has been added to triethylamine (20 mg, 0.215 mmol) under nitrogen at room

temperature. After ten minutes the resulting orange solution has been added to a solution of 3 (63 mg, 0.215 mmol) in water (5 ml). The resulting yellow suspension has been stirred under nitrogen for 24 hours, at room temperature. After filtration, the solid has been washed with water and MeOH (97 mg, 82.6%).

¹H NMR (DMSO-d₆, 400 MHz). δ ppm: 8.69 (d, J=8 Hz, 2H), 8.41 (d, J=8 Hz, 2H), 7.97 (t, J=8 Hz, 2H), 7.49 (t, J=8 Hz, 2H), 7.39 (br s, 2H), 7.05 (br s, 1H), 6.95 (br s, 1H), 6.50 (br s, 1H), 6.37 (br s, 2H), 5.43 (br s, 1H), 3.77 (s, 3H, OCH₃), 2.10 (br s, 2H), 1.49 (br s, 2H), 1.23 (br s, 2H), 0.79 (t, J=8 Hz, 3H).

¹³C NMR (DMSO-d₆, 100 MHz). δ ppm: 205.8, 175.3, 156.4, 149.5, 148.8, 148.4, 138.0, 137.8, 128.2, 126.1, 124.5, 122.3, 120.1, 111.5, 100.7, 55.9, 41.6, 31.8, 26.6, 22.4, 14.4.

MALDI MS: *m/z* 570 [M(37Cl)+Na]⁺, 568 [M(35Cl)+Na]⁺, 510 [M-Cl]⁺. 81

- Synthesis of the zinc complex **phenZnGing**

A yellow solution of 6-Dehydrogingerdione (40 mg, 0.136 mmol) in MeOH (1.44 ml) has been added to triethylamine (12mg, 0.136 mmol) under nitrogen at room temperature, giving rise to a orange solution which has been added to a solution of 4 (43 mg, 0.136 mmol) in DMSO (0.7 ml). The resulting suspension has been stirred under nitrogen for 24 hours at room temperature. After filtration, the yellow solid has been washed with MeOH (48.6 mg, 63%).

¹H NMR (DMSO-d₆, 400 MHz). δ ppm: 9.41 (br s, 2H), 8.88 (d, J=8 Hz, 2H), 8.29 (s, 2H), 8.11 (br s, 2H), 7.46 (br s, 1H), 7.26 (br s, 1H), 7.06 (br s, 1H), 6.75 (d, J=8 Hz, 1H), 6.60 (d, J=16 Hz, 1H), 5.49 (s, 1H), 3.80 (s, 3H, OCH₃), 2.16 (br s, 2H), 1.52 (br s, 2H), 1.25 (br s, 4H), 0.86 (br s, 3H).

¹³C NMR (DMSO-d₆, 100 MHz). δ ppm: 206.8, 175.1, 149.9, 148.4, 140.4, 140.0, 138.1, 129.3, 128.0, 127.2, 125.7, 126.6, 122.5, 116.0, 111.2, 100.8, 56.1, 40.9, 31.1, 26.1, 21.9, 13.9.

MALDI MS: m/z 574 [M(37Cl)+Na]⁺, 572 [M(35Cl)+Na]⁺, 514 [M-Cl]⁺.

○ DEVICE FABRICATION

Indium tin oxide ITO-coated glass plates ($15 \Omega \cdot \text{sq}^{-1}$) were patterned by conventional photolithography. The substrates were cleaned with deionized water and detergent (deconex) at 80 °C in a ultrasonic bath, then rinsed with water, acetone and isopropyl alcohol and dried in oven at 130 °C for two hours. After drying, the substrates were placed in a UV-ozone cleaner (Jelight 42-220) for 5 min before spin coating a water solution of PEDOT:PSS, previously filtered through a 0.2 μm PVDF filter. To afford a 40 nm thick layer, the following spin-coating parameters were used: 3000 rpm, 500 rpm^{-1} for 30 sec.

The PEDOT:PSS layer was patterned and baked in a vacuum oven at 110 °C for 2 h. OLED devices were fabricated as follows.

For the deposition of the complexes iridium complexes as emitting layer, a 10mg/ml solution of CBP in chlorobenzene was added with the proper amount of the complex (2%, 6% or 12% wt). Each solution was filtered through a 0.45 μm PTFE filter and spin coated on the glass/ITO/PEDOT:PSS substrate using the following parameters: 3000 rpm, 500 rpm^{-1} for 30 seconds. Samples were then loaded in the evaporator process chamber for BCP, Alq₃ and calcium/silver deposition.

The area of the device was 6.534 mm^2 . The devices were not encapsulated and were characterized inside the glovebox at room temperature.

REFERENCES

- ¹ H. Xu et al, *Chem. Soc. Rev.*, 2014, 43, 3207-3812
- ² S. Sprouse et al, *J. Am. Chem. Soc.*, 1984, 106, 6647-6653
- ³ A. B. Tamayo et al, *J. Am. Chem. Soc.*, 2003, 125, 7377
- ⁴ S. Lamansky et al, *J. Am. Chem. Soc.*, 2001, 123, 4304
- ⁵ P.J. Hay, *J. Phys. Chem. A*, 2002, 106, 1634
- ⁶ E. Baranoff et al, *Journal of Organometallic Chemistry*, 2009, 694, 2661-2670
- ⁷ F. Dumur, *Synthetic metals.*, 2014, 195, 241-251
- ⁸ T. Sano et al, *J. Mater. Chem.*, 2000, 10, 157
- ⁹ I.O. Balashova et al, *Mol. Cryst. Liq. Cryst.*, 2007, 467, 295
- ¹⁰ R. Wang et al, *J. Mater. Chem.*, 2012, 22, 23454
- ¹¹ B.-S. Kim et al, *J. Electr. Eng. Technol.*, 2009, 4, 418
- ¹² S. Banerjee et al, *Acc. Chem. Res.*, 2015, 48, 2075–2083.
- ¹³ J. Yao et al, *J. Agric. Food Chem.*, 2014, 62, 5507–5518
- ¹⁴ M. N. Soltani Rad et al, *IJST*, 2015, 39A3, 297-304
- ¹⁵ C.C. Carmona-Vargas et al, *The Royal Society of Chemistry*, 2017
- ¹⁶ B. Groblacher et al, *J. Nat. Prod.*, 2012, 75, 1393–1399
- ¹⁷ S. Sprouse et al, *J. Am. Chem. Soc.*, 1984, 106, 6647
- ¹⁸ P. Manini et al, *Chem. Res. Toxicol.*, 2004, 17, 1190-1198
- ¹⁹ N. Nakamichi et al, *Org. Lett.*, 2002, 4, 3955–3957
- ²⁰ Y.-J. Cho et al., *J. of Photochemistry and Photobiology A: Chemistry*, 2018, 356, 673-780
- ²¹ J. Yao et al, *J. Agric. Food Chem.*, 2014, 62, 5507–5518
- ²² Md. K. Nazeeruddin et al, *J. Am. Chem. Soc.*, 2003, 125, 29, 8797
- ²³ D. Pucci et al, *Dalton Trans.*, 2013, 42, 9679

SECTION 4

SYNTHESIS AND PROCESSING TECHNIQUES OF BIOCOMPATIBLE AND LOW COST MATERIALS FOR ENCAPSULATING LAYERS IN OLED DEVICES

~INTRODUCTION~

○ DEVICES DEGRADATION AND ENCAPSULATION PRINCIPLES

To ensure suitable performances and lifetime of the organic electronic devices for their commercial applications, it is necessary to overcome their ageing, which is caused by the poor stability and degradation of the organic materials and of the low work function cathode metals.¹ The degradation phenomena can be intrinsic and/or extrinsic. Intrinsic phenomena² occur when there are changes in the basic properties of the materials and their interactions in the device, therefore an accurate selection of the used materials and an optimization of the deposition processes can minimize intrinsic degradation mechanisms.

On the contrary, extrinsic degradation³ is strictly connected to the rapid modification into some other substances of both organic layers and low work-function metals that suffer when they are exposed to harsh environmental conditions and to atmospheric oxygen and water vapor. The results of degradation processes are: dark spots formation and decrease in light emission intensity and efficiency in OLED devices, decrease of generated electric current and reduced lifetime in OPV, worsening of the threshold voltage and sharp decrease of the on/off ratio in OTFT.⁴

Nowadays, don't exist materials to realize organic electronic devices that are completely immune to the exposition to water vapor and oxygen (i.e. that don't chemically react with). For such reason, it is necessary to protect the devices from atmospheric conditions, so their encapsulation and protection are fundamental.⁵

In the design of an encapsulation for organic electronic devices, two important aspects need to be considered: the barrier properties of the encapsulating materials and the compatibility with the devices of the processes used to deposit the encapsulating materials.

About the barrier properties, as said, the main degrading agents are water vapour and oxygen, so a good encapsulating material is selected according to its Water Vapor Transmission Rate (WVTR) and/or its Oxygen Transmission Rate (OTR). In Figure 1, the barrier requirements are reported for various organic electronic devices.⁶

About the process compatibility, for example the temperature reached during the encapsulation process might cause the device degradation so it represents another critical parameter.

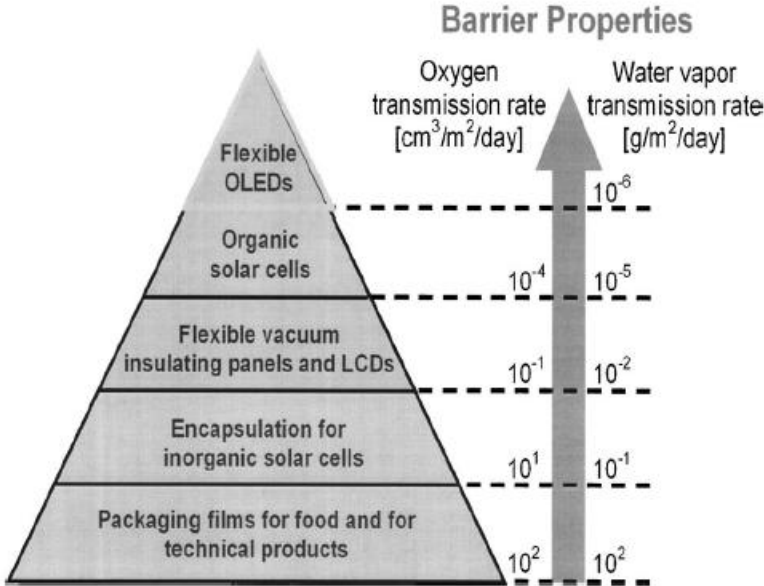


Figure 1: Barrier requirements for different applications

The encapsulation process depends also on the type of the substrate on which the device is realized. When the substrate is rigid (usually glass), a glass lids is often used and it is sealed by using an UV epoxy resin (Figure 2).⁷

Glass show negligible permeability to water and oxygen⁸ and by using specifically designed glue, water vapour barrier properties of 10⁻⁴-10⁻⁵ g/m²/day can be reached,⁹ so this is a very performing encapsulation solution for rigid devices. In

addition, desiccant materials such as calcium and barium are used to absorb water vapor diffusing from the resin so removing water traces. However, the high costs of this approach and the demand for cheap, flexible and roll-to-roll processable systems are steadily pushing the demand for alternative high-barrier systems. In this case, a thin-film barrier is usually used as coating of a flexible substrate, since bare plastic materials are permeable to water and oxygen.

Encapsulation of flexible devices is still a great challenge for academic and industrial researchers.

Two main approaches are studied, in the first case barrier films can be laminated on the device (foil-to-foil encapsulation), in the second case a thin film is applied directly on the organic devices (thin film encapsulation, TFE) (Figure 2).¹⁰ A huge advantage of the foil-to-foil technology is the possibility to manufacture the barrier films in advance, so their production conditions are not limited by the sensible organic device. All the known deposition techniques can be used, limited only by the substrate compatibility. For example, higher temperature, radiation, chemical baths, solvent and gases can be applied to deposit the films.

The lamination of the barrier films occurs by roll-to-roll technology and it can cause mechanical stress with defects formation in the barrier layers and therefore a reduction of the barrier properties. In general, flexible barrier coatings are thin and sensitive to mechanical strain and surface damage, so large area manufacturing, handling and lamination represent important issues to solve.

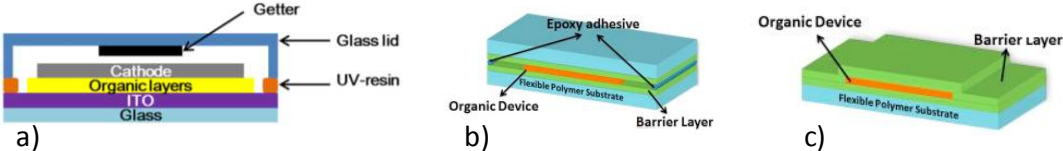


Figure 2: a) encapsulation layout of rigid devices; b) Foil-to-foil flexible encapsulation; c) Thin film flexible encapsulation

A thin-film encapsulation (TFE) is desirable to keep the mechanical stress of the barrier as low as possible, to position it as close as possible to the sensitive layers and to reduce the number of the process steps and costs. The main problem of TFE is the presence of the already completed organic device during the process, that limits the processing conditions. Typical TFE processes involve deposition of inorganic barrier films (oxides and nitrides) with PECVD, sputtering, ALD and other similar technologies.¹⁰

Anyway, in all the cases the encapsulating materials must be opportunely designed to optimize the barrier properties. As reported in Figure 1, an encapsulating layer must have excellent water and oxygen blocking behavior, because of the sensitive nature of the materials used for organic electronic devices, in particular OLED devices show the major sensitivity. For this reason, the packed crystal structure of the inorganic films seems the perfect solution to reduce water and oxygen penetration. SiO_x , SiN_x and alumina are the most commonly used inorganic encapsulating films.¹⁰ The barrier capability of course is strongly dependent of the quality of the inorganic thin film, water and oxygen are able to penetrate through surface pinhole and defects with an increment of the layer permeability. The quality of the inorganic thin film is strictly related to the deposition techniques and so its choice represent a fundamental step towards the best encapsulation process. Different methods are applied in thin film fabrication. Reactive thermal evaporation of aluminum and electron-beam evaporation of SiO_x can deposit transparent layers with medium barrier performances.¹¹ These techniques show very high deposition rate and very low deposition costs for producing large areas of barrier film. It is also reported that the addition of a plasma to the evaporation leads to a better barrier film quality with a reduction of the gas transmission rates and improved process stability.¹² Nevertheless, the

barrier properties obtained by using such techniques are not yet suitable for application in organic electronic devices.

Permeation barrier properties superior to evaporated layers can be achieved by using a sputtering process. In particular for the deposition of transparent oxide layers, often metallic material targets are used and the oxides are formed by a reactive sputtering process. Good barrier properties were reported with this technologies but it is also reported that it can't be utilize for the direct encapsulation since it cause damaging of the device.¹³

A method for the deposition of barrier layers directly on the devices is the plasma assisted chemical vapor deposition,¹⁴ in the PECVD method, a plasma is used to provide the activation energy for a chemical reaction between different precursors that finally will precipitate on the substrate as a thin film. Plasma is able to reduce the process temperature in comparison with other CVD technologies (hot-wire, thermal. etc). Typical barrier layer materials deposited by PECVD are SiO₂ and SiN_x, with a very good permeation properties suitable for organic electronic devices.¹⁴ Unfortunately, the barrier thickness is in the range between 100 and 700 nm and in this case mechanical stress in the layers does not allow a further improvement of the barrier performances.

The most promising deposition technique for the production of very dens almost defect-free thin films is the atomic layer deposition.¹⁵ One of the most important properties of the ALD technology is the self-limitation of the reaction, which means that the deposition rate is equal to or less than a monolayer for each cycle, leading to an ideal layer-by-layer growth. Because of this, ALD layers have a very high density and a very low number of defects. In the same way, the very low deposition rate and productivity represent the major drawbacks of the ALD process.

The most often ALD-deposited barrier material is Al_2O_3 , and a WVTR of 10^{-4} $\text{g}/\text{m}^2/\text{day}$ or even less has been achieved using a 10 nm to 25 nm thick Al_2O_3 .¹⁶ Of course the quality of the substrate plays an important role for the ALD process.^{17,18}

Also with the best choice of the deposition techniques and with the best design of the barrier layer, once a defect is formed during the growth of a film it will propagate and duplicate, creating a perforation channel through the film rather than disappearing with the increase of film thickness.

To compensate defects and pinholes formation in inorganic thin layers and to improve the flexibility of the barriers, it is used the strategy to alternate inorganic and organic layers, to create multilayer encapsulating thin films.¹⁹

The inorganic layer constitutes the main barrier against water and oxygen permeation, while the organic layer is able to smooth the surface, to decouple the defects on the surface of the inorganic layer and to improve the flexibility of the overall multilayer (Figure 3).

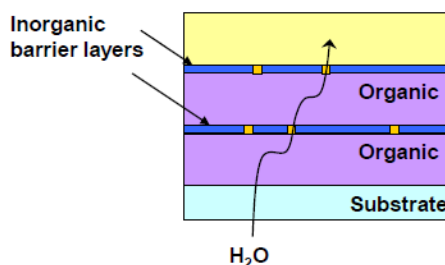


Figure 3: Diffusion path of a water molecule showing the inorganic-organic multilayer barrier approach.

Organic and inorganic materials used in the multilayer structure show different permeation mechanisms.

Permeation process through polymer films used as the substrate or the decoupling layer can be well described using Fick's laws of diffusion.²⁰ Unfortunately, as is widely known, polymers do not have a sufficiently low water

vapor and oxygen permeation to be used as sole encapsulation for organic device. Typical values of WVTR, of polymer films at 38°C and 90% RH, range from 1 to 10^{-2} g/m²/day. These values are far from requirements for organic electronics devices. On the other hand inorganic materials are in principle completely impermeable, although they have other disadvantages such as mechanical rigidity, and the costly vacuum deposition processes. As a result, real permeation through inorganic material is several order of magnitude higher than the theoretical value due to the presence of defects in the material structure; these defects are considered as almost solely responsible for the permeation of gases through the thin films, while the Fickian solid state diffusion is negligible.²¹

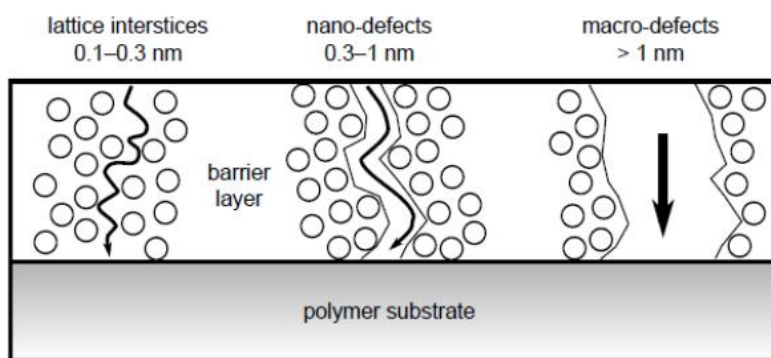


Figure 4: Classification of defects: permeation of water and oxygen through barrier layers is dominated by nano- and macro-defects

Defects of inorganic materials result from the substrate surface roughness and the quality of its cleaning procedure,¹⁷ or particles generated during the deposition process¹⁸. Using the Arrhenius dependence of permeation from temperature, it is possible to investigate how the defects dominate the barrier performances. If the activation energy of the barrier-coated substrate is equal or similar to the one of the bare substrate, the barrier layer acts simply as a block reducing the effective area for permeation, while in case of an interaction with the inorganic layer,

elevated activation energy is expected for the coated substrate. In particular, if the activation energy is the same for the barrier material as for permeation through the bare substrate, permeating molecules flow through the macro defects and there is no interaction with the barrier material.²²

○ THIN FILM PERMEATION PHYSICS

Permeation is the mass transport of a gas or liquid, the permeate, through a solid. Permeation is a very complex process consisting of sequential phases²³ known as: adsorption/dissolution, diffusion and desorption (Figure 5).

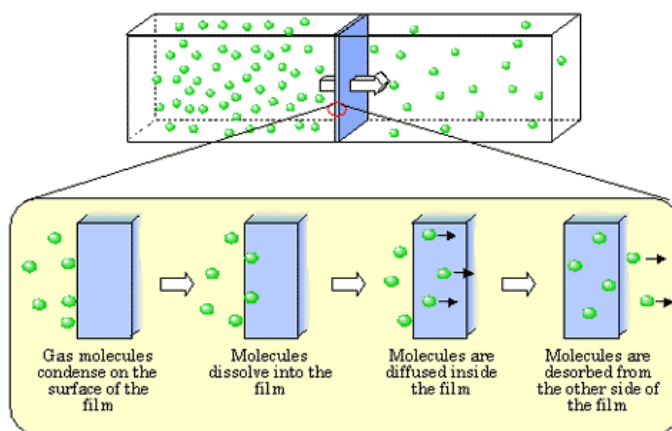


Figure 5: Schematic representation of the permeation process

In the first step, the permeating gas is adsorbed on the surface of the solid and, if it is soluble in this material, it is dissolved into the solid.

In the second step, diffusion occur and it consists in the mass transport through the solid of randomly moving particles induced by a gradient of concentration. Diffusion can occur via defects, like micro-cracks, or through the bulk material itself. In theory, diffusion through the bulk is negligible for inorganic materials, but the presence of defects in the material structure brings to a relevant increase of

the diffusion coefficients respects to the theoretical values. On the other hand, diffusion through the bulk material is an important issue for polymers and is described by Fick's law.

Finally, the gas particles are released from the backside of the solid surface (desorption).

As result, the quantity of permeated gas is proportional to the permeation coefficient (P) that is the product of the diffusion coefficient (D) and the sorption coefficient (S).

$$P = D \cdot S \quad (1)$$

➤ First Fick's law

Fick's first law describes the gas and liquid diffusion through a solid material under a concentration gradient. In the case of permeation through a thin film, first Fick's law can be simplified to a one-dimensional equation with a concentration gradient only perpendicular to the solid surface. In this assumption, the permeate flux (J) can be described as:

$$J = \frac{\partial n}{\partial t} \cdot \frac{1}{A} = -D \cdot \frac{c_1 - c_2}{d} = -D \cdot \frac{\partial c}{\partial z} \quad (2)$$

where n is the quantity of the permeating gas, A is the surface area of the solid, D (cm^2/s) is the diffusion coefficient, d is the solid thickness, c_1 and c_2 are the concentration values of the permeant at the two sides of the permeation process and z is the direction of the permeation process.

➤ Sorption

The sorption is a set of processes related with the accumulation and the removal of gases and liquids on a solid surface or within a solid material and it is correlated with the adsorption and desorption processes.

The sorption process is described by Henry's law:

$$c = S \cdot p_g \quad (3)$$

where S is the sorption coefficient, c is the concentration of a permeating gas and p_g is the permeating partial pressure.

Combining Henry's law with the First Fick's law, it is possible to obtain the following equation:

$$J = -D \cdot S \cdot \frac{p_1 - p_2}{d} = -P \cdot \frac{p_1 - p_2}{d} = -P \cdot \frac{\partial p}{\partial z} \quad (4)$$

Henry's law can be applied only when physisorption takes place (no chemisorption) and when the permeating gas cannot condensate on the solid surface at the given temperature. In the case of the water vapor, Henry's law can be applied.

➤ Temperature dependence

Diffusion and sorption process are both thermally activated and the Arrhenius equation describes the exponential dependence from the temperature.

$$P = P_0 \cdot e^{-\frac{E_A}{RT}} \quad (5)$$

where the permeation activation energy E_A is the sum of the activation energy of the gas diffusion and the heat of solution of sorption process ($E_A = E_D + \Delta H_S$).

As previously mentioned the permeation through defects in thin films is not ruled by the fickian diffusion. When macro-defects are present, the thin film doesn't contribute to the barrier properties and the activation energy doesn't change respect the bare substrate. With the decreasing of the defects size the permeation mechanisms change.

➤ Second Fick's law

The time dependence of the permeation process can be described by the Second Fick's law that is derived from the combination of Fick's first law with the continuity equation.

$$\frac{\partial c}{\partial t} = D \frac{\partial^2 c}{\partial z^2} \quad (6)$$

This equation is valid for the one-dimensional case in which the permeation is only taking place perpendicularly to the substrate's surface.

Within the sample during the experiment, the permeate concentration will increase until reaching a constant concentration profile. With the assumptions that the concentration of the permeating gas is kept constant on the top and on the bottom surfaces of the barrier sample and that the measurement is started with a fully dry sample (correct assumption for encapsulated organic electronic devices), the second Fick's law is solved to give the time-dependent amount of gas permeating through the solid:

$$N(t \rightarrow \infty) = \frac{Dc_1}{d} \left(t - \frac{d^2}{6D} \right) \quad (7)$$

for large value of t .²⁴

After a certain time, the concentration profile will become constant leading to a steady state diffusion, this specific time is called lag time and is equal to:

$$t_0 = \frac{d^2}{6D} \quad (8)$$

Here a typical permeation curve is shown (Figure 6). The first part indicates the transient regime, in which the concentration profile changes with time through the layer; in the second part the concentration profile approaches the linear steady state.

The first region accounts for the kinetics of the phenomenon allowing the estimation of the lag time, a parameter strictly related with the diffusion coefficient. The second part accounts for the permeation flux according to the first Fick's law.

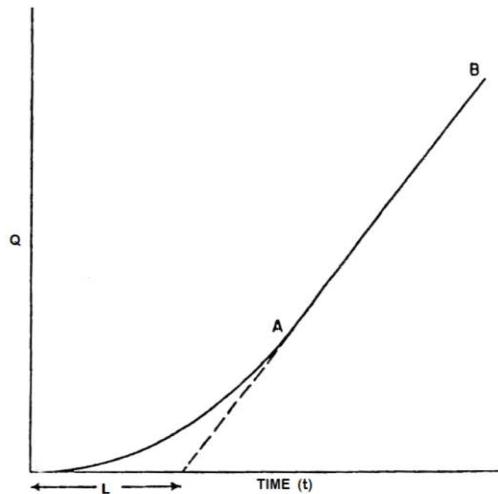


Figure 6: Typical permeation curve: amount of permeated penetrant Q , as a function of time, t

○ PERMEATION MEASUREMENTS

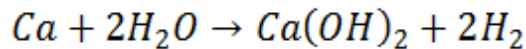
An accurate permeation measurement is fundamental to correctly choose the best barrier layer, in particular when the required barriers are extremely high as for organic electronic devices.

The barrier measurement can be performed by direct detection of the permeate or by exploiting a chemical interaction of the permeating species with a well-chosen material. Different signals can be detected to define different measurement methods: electric, optical, mass differences, mass spectroscopy, pressure differences, etc.

In any case, all measurements require a close control of the process conditions, in particular temperature and relative humidity.

➤ Calcium Corrosion Tests

Calcium test²⁵ is probably the most frequently used permeation test for water vapor for ultrahigh barriers. The test is based on the observation of the chemical transformation of a thin film of metallic calcium as a consequence of its interaction with water vapour. In presence of water the conductive and opaque calcium becomes the insulating and transparent calcium hydroxide.



The permeation can be tested evaporating on a substrate the Calcium thin film and immediately protecting it (encapsulation process) using the barrier material of which we want to know the permeability, and measuring the change in the electrical or optical properties of the Calcium film.

Leaving the prepared device exposed to known and constant environmental conditions, metallic calcium becomes calcium hydroxide with the progress of time (and consequently the permeation of water vapor within the encapsulation system), passing from to be a reflective (and conductive) to a transparent (and insulating) material. Therefore, monitoring the variation of these properties over time, it is possible to calculate, by means of suitable mathematical models, the amount of water permeated through the barrier material. So, by measuring changes in the electrical resistivity or in the optical absorption coefficient of the calcium layer, it is possible to discern between electrical or optical calcium corrosion tests respectively.

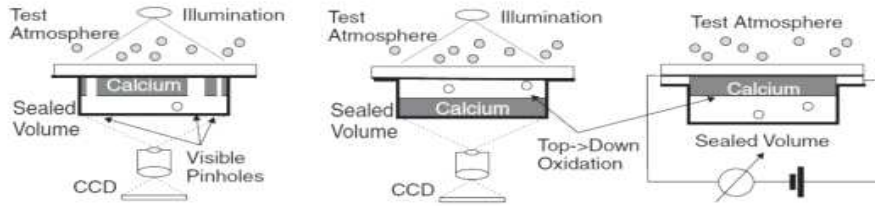


Figure 7: Different calcium test setups. The conversion of calcium (Ca) can be monitored by optical transmission (left and center) or by electrical resistance measurements (right). For both principles, two variants are possible: placing the Ca layer directly on the barrier (left) causes local Ca conversion at barrier pinholes and thereby allows the characterization of pinhole sizes and densities. Placing the calcium layer with a connecting gas volume causes evenly distributed Ca consumption (center and right)

This method is ideal for the long-lasting experiments, able to evaluate the effective WVTR (including the macro-defects caused by the processing of the barrier, fundamental to check the quality and hence improve the process itself) with very good accuracy and at relatively low cost setup. Another advantage of measurement devices based on this principle it is the high versatility: theoretically calcium test can be used with a huge variety of geometries. It also offers the possibility to perform the test in a configuration similar to that of the device. The major drawback is the difficulty to compare results from different research groups or laboratories.

The limit of the calcium test sensitivity depends on the setup, but it is assumed to be in the $10^{-6} \text{ g/m}^2/\text{day}$ range.²⁶

- AIMS

The aim of this thesis section is to realize a low cost flexible encapsulating layer by using easily accessible materials and fast deposition processes.

As discussed previously, the permeation process is a very complex set of phenomena and different mechanisms are involved. As a consequence, different approaches can be used to realize an effective barrier layer.

The use of oxides seems one of the most used solution for the realization of high performances barrier layers by using vacuum deposition techniques. However, vacuum techniques are expensive and often very slow. In this work, ZnO nanoparticles deposited by solution based processes were used as an alternative to inorganic barrier films realized by vacuum techniques. Thanks to the small dimension of the nanoparticles, they are able to form packed structure with reduced defect dimensions, when compared with microparticles.

To improve the barrier properties of the thin film realized with ZnO nanoparticles, a multilayer approach was used. Activation energy of the adsorption phase, for example, can be increased by reducing the surface interactions between the penetrant and the barrier materials. Hydrophobic and/or oleophobic treatments of surfaces reduce the wettability and slow down the adsorption process. Stearic acid was selected as hydrophobic material, and deposited by solution based processes.

The use of "sacrificial" water absorbing layers is another approach to improve the barrier performances. An hydrogel thin film was tested as absorbing material in a multilayer structure.

~RESULTS AND DISCUSSION~

○ NANOPARTICLES BASED OXIDES THIN FILM

➤ Ceramic Thin Film

Ceramics have been widely recognized as important materials for both structural and electrical applications.

Structural ceramics based on oxides, nitrides and carbides are used as component in engines and other machinery.²⁷ Passive oxides such as alumina and silica are employed as substrates and insulators in electronic circuits.²⁸ "Active" ceramics like zirconia are used in high temperature oxygen sensors²⁹ and perovskite compounds (BaTiO_3 and lead zirconate titanate), find application in capacitors, electrically driven mechanical resonators or electrically controlled optical switches.³⁰ Ceramic coatings based on alumina, silica and titanium nitride are also able to improve corrosion resistance.^{31,32}

Different methods have been developed for the deposition of ceramic thin films. The target is to obtain crystalline and densified films with superior functions such as electronic conductivity, piezoelectricity, mechanical strength, etc. Atomic diffusion usually ensures these kind of properties and this phenomenon is activated at high temperatures (greater than 500°C, sintering process). In order to reduce the working temperature, since 1970 different deposition techniques have been developed.^{33,34,35} The use of plastic substrates is one of the fundamental reason that asks for the reduction of the working temperatures.

The technologies for thin film fabrication fall into two broad areas; physical techniques, which include thermal and electron beam evaporation, sputtering, laser ablation, etc; and chemical techniques which include spray pyrolysis, chemical vapor deposition, atomic layer deposition and sol-gel processes.

Most of the mentioned methods are vacuum vapor phase deposition based, in this case crystallization may be achieved by high activities of atomic and molecular species in vapor phase. As all the vacuum techniques, these are expensive and require a time to reach the vacuum. Furthermore, the area of the thin film is limited by the dimensions of the deposition chamber. This represents a limitation in a vision in which large area thin films on plastic substrates are a demand for the future of the electronics.

Liquid phase depositions can be more versatile if compared to vapor depositions. Sol-gel represents an inexpensive and industrially convenient method for the realization of ceramic powder and thin films. In this method, organometallic precursors are deposited and a firing process is performed to eliminate the organic and liquid phase and to leave the ceramic coating.^{36,37} Several techniques have been proposed to crystallize sol-gel-derived amorphous gel films on plastics without firing. The exposure to laser beams³⁸ and humid vapors³⁹ and the soaking in hot water⁴⁰ are reported to induce crystallization of gel films. However, neither high crystallinity nor high density (low porosity) is expected because of the low processing temperatures, which limit the atomic diffusion for crystal growth and densification.

Deposition of crystalline oxide nanoparticles by spin coating and dip coating are also reported.^{41,42} A firing process in this case can eliminate porosity resulting from the nanoparticles deposition. Furthermore, nanoparticles show the great advantage that can be used to reduce the porosity respect a deposition from micro-particles, because they are able to agglomerate in a closed packed structure.

For the realization of a continuous ceramic thin film starting from nanoparticles suspension, gravure printing and airbrushing were here explored as high throughput deposition techniques.

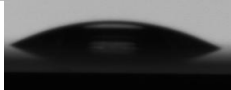
➤ Ceramic Thin Film realization with gravure printing and airbrushing

A thin film of inorganic layer was realized on PEN substrate starting from an ethanol suspension of ZnO nanoparticles by using gravure printing⁴³ and airbrushing technology.

The deposition strategy were separately optimized and after that the characteristics of the obtained thin films were compared, in terms of uniformity, wettability and barrier properties.

In Table 1, the transmittance values of the thin films in the visible region of the spectrum, the thickness, the roughness and the water contact angle are reported.

Table 1: Morphological and optical characteristics of the ZnO layers

	%T 400-800 nm	Thickness (nm)	Roughness Sq (nm)	Contact Angle (°)	
PEN	99-98	≅	12.3 ± 2.2	68 ± 5	
Printed ZnO	99-98	232 ± 10	10.6 ± 1.6	26 ± 4	
Airbrushed ZnO	99-98	115 ± 15	8.4 ± 1.2	100 ± 3	

The samples are transparent in the visible region, so they can be used for application where transparency is required. The roughness seems to be not affected from the deposition process, while the water contact angle of the airbrushed layer is much higher than one of the printed ZnO layer.

The water contact angle of the printed ZnO shows hydrophilicity as expected for oxide materials, while airbrushed ZnO layer shows hydrophobicity, maybe due to a structurization of the surface as a consequence of the deposition techniques.

Scanning electron microscopy measurements were carried out to confirm such experimental evidences. In particular, the printed ZnO layer results particularly smooth and uniform while the ZnO airbrushed surface is heterogeneous and a large number of aggregates is visible that probably reduce the surface wettability.

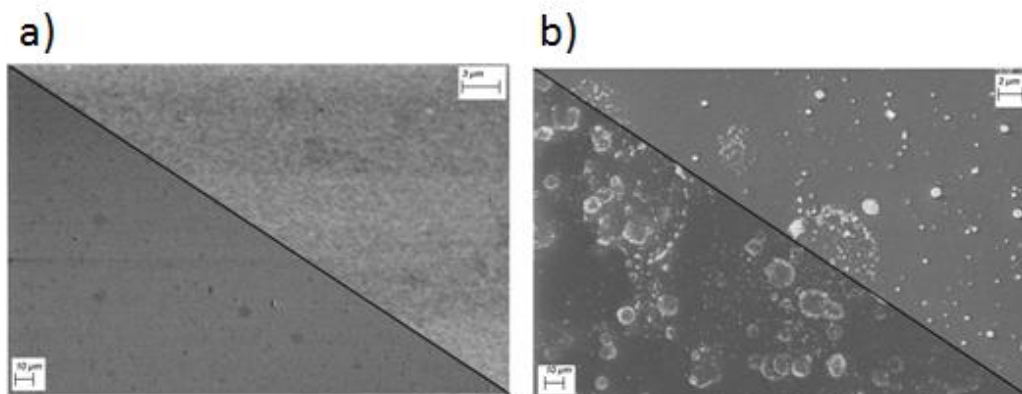


Figure 8: SEM images of printed ZnO (a) and airbrushed ZnO (b)

The barrier properties of the ZnO layers were studied through electrical calcium tests. In Figure 9 are reported the normalized conductance vs time curves of the ZnO layers and for comparison of the sole PEN substrate. In Table 2, the WVTR and the lag time values are reported.

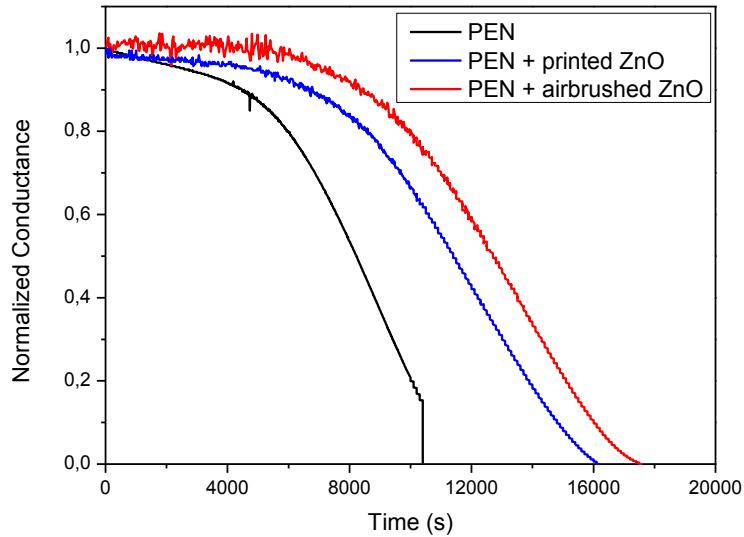


Figure 9: Normalized conductance vs time for electrical calcium tests carried out on PEN substrates and PEN/ZnO samples.

Table 2: WVTR and lag time values for calcium tests carried out on PEN and PEN/ZnO samples

Sample	WVTR (g/m ² /day) @ 38°C, 90% RH	Lag time (h)
PEN	1.58 ± 0.13	1.51 ± 0.32
Printed ZnO	1.18 ± 0.11	2.13 ± 0.45
Airbrushed ZnO	1.24 ± 0.15	2.33 ± 0.41

After the deposition of the ZnO layer, an improvement of the barrier characteristics have been observed respect to the sole PEN, corresponding to a reduction of the WVTR value and an increase of the lag time. Although printed and airbrushed ZnO layers have comparable WVTR and lag time values, on the basis of the observed microstructures different permeation mechanisms can be drawn for these samples: the compact printed ZnO layer works as an excluded

area to the water vapor permeation process, while airbrushed ZnO layer has pores that can act as specific interactions sites, slowing down the permeation.

- HYDROPHOBIC THIN FILM

- Hydrophobicity

Hydrophobicity is the physical property of a material that is repelled from a mass of water. Such property is ruled by the intermolecular interactions resulting from contact between a liquid and a solid, specifically the phenomenon is determined considering the combination of adhesive and cohesive forces. Adhesive forces between a liquid and a solid cause a liquid drop to spread when in contact with a surface, cohesion is the force that holds the molecules together and it can limit the spreading of a liquid on a solid surface. When the adhesion is greater than the cohesion the surface is wettable by a given liquid, otherwise the surface is not or poorly wettable, i.e. hydrophobic.

The key parameter that is used to evaluate wettability is the contact angle (CA); a surface can be considered hydrophobic if the water CA (WCA) is $> 90^\circ$. Potential applications can be found in microfluidic devices, self-cleaning, anti-corrosion, anti-friction, building exteriors, fabrics, etc.

The wettability of a surface can be manipulated through a combination of chemical and/or morphological modifications.⁴⁴ To reach hydrophobic behavior, molecules with low surface energy are usually involved, such as fluoro compounds, polymers, wax, fats, oils, alkanes, etc, furthermore the combination of micro- and nano-scale surface structures is able to influence hydrophobicity.

Such aspects are well explained by Wenzel⁴⁵ and Cassie⁴⁶ who showed the correlation between hydrophobicity and surface morphology.

The Wenzel regime is usually recognized as a homogeneous wetting, since the liquid completely penetrates into the surface grooves (Figure 10). While under

some circumstances, especially the increase of the surface roughness, vapor pockets may be trapped underneath the liquid, yielding a composite interface. This heterogeneous wetting is usually described by the Cassie-Baxter (CB) model.

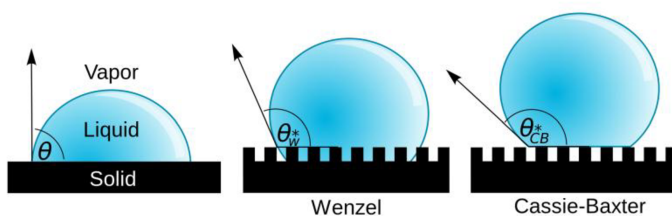


Figure 10: Wenzel and Cassie-Baxter model for hydrophobicity

➤ Hydrophobic thin film realization with printing and airbrushing techniques
In this thesis, ZnO nanoparticles were functionalized with stearic acid, in order to obtain an hydrophobic barrier layer. For the samples preparation, two different approaches were used. The first one consists of a two-steps deposition process: at first, the inorganic material is deposited by printing or airbrushing from an ethanol suspension of zinc oxide nanoparticles; then the external hydrophobic layer is realized by printing or airbrushing a solution of stearic acid.

The second approach is based on an one-step process. Zinc oxide nanoparticles and stearic acid are mixed together for 1h at 50°C to induce functionalization,⁴⁷ then the obtained suspension is directly deposited on the substrate by printing or air-brushing.

The SEM images of the realized layer are reported. Sample realized by two printing steps is particularly smooth, probably the printing process of the stearic acid is able to uniformly cover the ZnO surface. For the 2-steps airbrushed sample, the stearic acid doesn't cover all the ZnO surface and aggregates are visible.

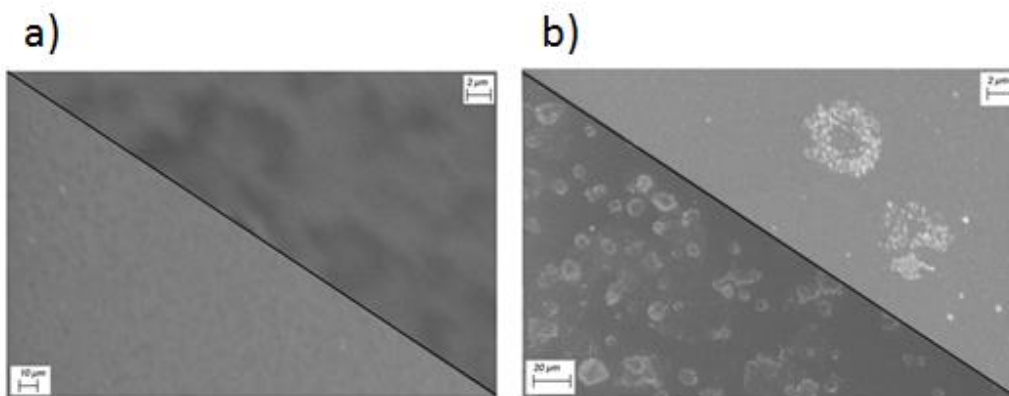


Figure 11: SEM images of the printed 2-steps sample (a) and airbrushed 2-steps sample (b)

About samples realized with a 1-step process, the functionalization process of ZnO nanoparticles with stearic acid before the deposition, probably is able to stabilize the suspension and reduce the aggregates formation. SEM images of these samples seems to confirm this theory (Figure 12).

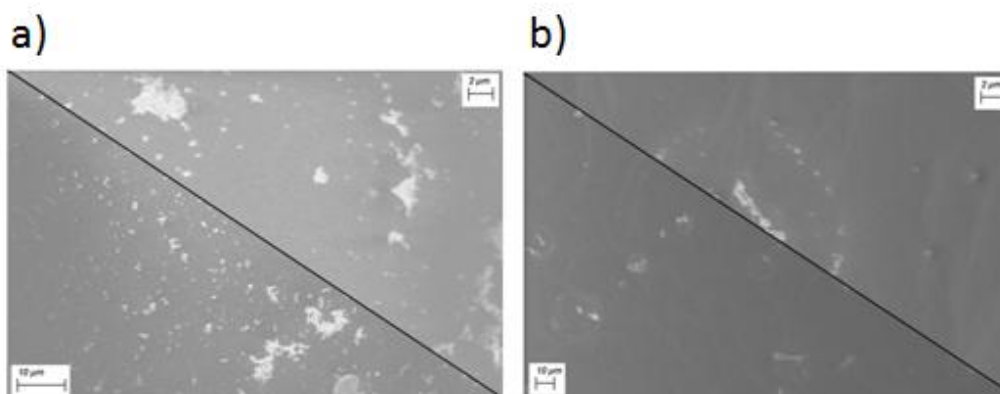


Figure 12: SEM images of the printed 1-step sample (a) and airbrushed 1-step sample (b)

In order to investigate the functionalization of the nanoparticles, the FTIR characterization was performed. Since the low thickness of the produced layers, an IR transparent substrate is necessary to improve the sensitivity of the measurements. For this reason, the measurements were performed on CaF₂ substrates airbrushed with the materials under investigation, since the

impossibility of printing on such rigid substrates. FTIR spectra of the one-step and two-steps airbrushed layers are compared in Figure 13, and they are considered as reference to understand the chemical differences between the layers prepared by one-step and two-steps processes. For comparison, the ATR spectra of stearic acid and zinc stearate are also reported.

The ATR spectrum of the stearic acid shows the typical stretching C=O of the carboxylic group at 1700 cm^{-1} , that disappears in the IR spectrum of the corresponding stearate. In the spectrum of the stearate there is a shift of the carboxylic peak toward low wave numbers due to electron acceptance from Zn atoms (COO-Zn).⁴⁸ In particular, there are two absorption peaks at 1538 cm^{-1} and 1461 cm^{-1} resulting from the asymmetric and symmetric stretches of the carboxyl group.

About the FTIR spectra of the deposited thin film, even if the signals have very low intensity, since this kind of measurement is not suitable for thin films characterization, nevertheless it is possible to do some evaluation about the process. The spectrum of the ZnO nanoparticles shows a typical broad signal at 3500 cm^{-1} of the O-H stretching and some signals in the range $1700\text{-}1500\text{ cm}^{-1}$ usually due to carbonyl and carboxylic species, these latter are due to organic residues deriving from the nanoparticles synthesis process.

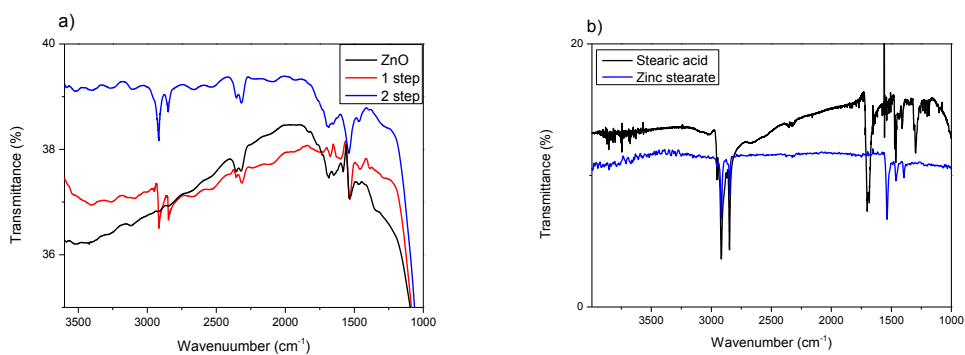


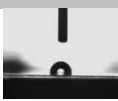
Figure 13: a) FTIR spectra of ZnO, one-step and two-steps layer on CaF_2 substrates; b) ATR spectra of stearic acid and zinc stearate powders

About the spectrum of the ZnO/stearic acid thin films, the absorption peaks in the region 2900–3000 cm^{-1} correspond to the CH_2 and CH_3 groups stretching vibration from the alkyl chain. The absorption bands at 1700 cm^{-1} , that is the characteristic peak of carboxylic acid, is only slightly visible in the 2-steps sample and it is visible the COO-Zn signal at 1534 cm^{-1} . From these evidences, it is possible to suppose that stearic acid is not just adsorbed on the nanoparticles surface but it is anchored on the surface of ZnO nanoparticles .

About the morphological and optical characterization of the prepared thin films, the samples show good transparency in the visible region of the spectrum and a low roughness, between 8 and 14 nm (Table 3).

As expected, the water contact angle (WCA) measurements confirm the hydrophobic character. In particular, WCA of the two-steps layer is slightly larger than the corresponding WCA of the one-step layer; this difference can be simply explained considering the higher quantity of stearic acid on the surface of the two-steps layers, closely related to the deposition process.

Table 3: Morphological and optical characteristics of the ZnO_stearic acid samples

	%T@	Thickness	Roughness	Contact	
	400-800	(nm)	Sq (nm)	Angle (°)	
	nm				
Printed 2-steps	98-97	305 ± 12	12 ± 1.5	115 ± 4	
Airbrushed 2-steps	99-98	160 ± 24	10 ± 2.2	102 ± 6	
Printed 1-step	100-99	240 ± 11	13 ± 1.8	99 ± 3	

Airbrushed	100-99	140 ± 21	14 ± 1.7	95 ± 6
1-step				



Water vapor barrier properties were investigated through electrical calcium test. The addition of the stearic acid leads to a significant increase in the lag time values, while no great differences in the WVTR values are observed respect to the non-functionalized ZnO layers.

As expected, the hydrophobic character of the stearic acid is able to slow down the permeation process affecting the adsorption stage thus increasing the lag time, that is the time necessary to reach the steady state of the permeation process. Since the steady state of the permeation process is essentially controlled by the substrate bulk characteristics, the WVTR values remain quite similar.

The worst barrier properties observed for the two-steps printed layer is probably due to printing of the stearic acid on the ZnO surface, provoking crack formation in this layer with an inevitable reduction of the barrier properties.

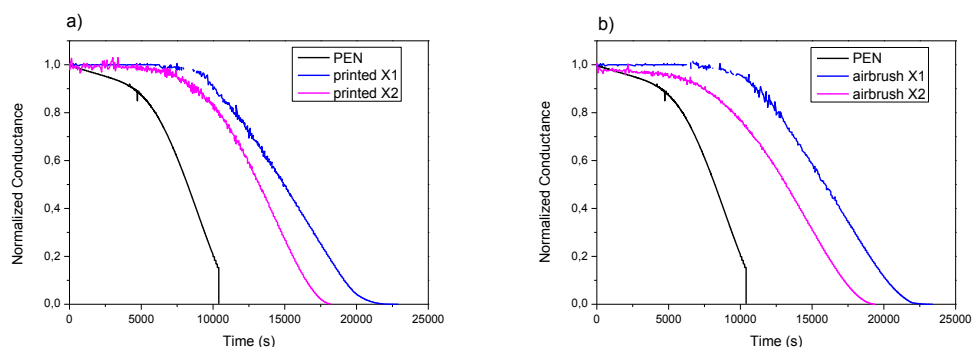


Figure 14: Normalized conductance vs time for electrical calcium tests carried out on a) ZnO_stearic acid printed and b) ZnO_stearic acid airbrushed samples

Table 4: WVTR and lag time values for calcium tests carried out on PEN/ZnO_stearic acid samples

	WVTR (g/m ² /day) @ 38°C, 90% RH	Lag time (h)
PEN	1.58 ± 0.13	1.51 ± 0.32
Printed ZnO	1.18 ± 0.11	2.13 ± 0.45
Airbrushed ZnO	1.24 ± 0.15	2.33 ± 0.41
Printed 2-steps	1.27 ± 0.18	2.47 ± 0.28
Airbrushed 2-steps	1.02 ± 0.20	2.26 ± 0.33
Printed 1-step	0.89 ± 0.16	2.63 ± 0.38
Airbrushed 1-step	0.96 ± 0.21	2.98 ± 0.42

The one-step process results the most effective in terms of the barrier properties and simplicity of the preparation/deposition process.

The reported data demonstrate the great potential of the used approach to obtain functional thin films with low cost materials and techniques. With a careful choice of the materials and the appropriate nanoparticles/materials engineering it is possible to realize a variety of “green” functional surfaces.

- WATER ABSORBING MULTILAYER

- Hydrogel materials

An hydrogel is a cross-linked polymeric network produced by the reaction of one or more monomers that exhibit the ability to swell and retain a significant fraction of water within their structure, but not dissolving in water.⁴⁹

Hydrogels possess a degree of flexibility very similar to the natural biological tissues due to the large water content of both these types of materials. The ability of hydrogels to absorb water arises from hydrophilic functional groups attached to the polymeric backbone, while crosslinking confers the insolubility in water. This

kind of materials can be of natural origin or synthetic. With the establishment of the first synthetic hydrogel by Wichterle and Lim in 1954,⁵⁰ the hydrogel technologies have been applied to hygienic products, agriculture, drug delivery systems, sealing, coal dewatering, artificial snow, food additives, pharmaceuticals, biomedical applications, tissue engineering and regenerative medicines, diagnostics, wound dressing, barrier materials to regulate biological adhesion, biosensors, etc.

There are different types of synthetic strategy:

- one-step procedures, like polymerization and parallel cross-linking of multifunctional monomers;
- multiple step procedures, involving synthesis of the polymers and subsequent cross-linking by using suitable cross-linking agents.

In both cases, the three integral parts for hydrogel preparation are monomers, initiator and cross-linkers. Hydrogels are generally prepared based on hydrophilic monomers to allow water absorption, hydrophobic monomers are sometimes used in hydrogel preparation to modulate the properties for specific applications.

The polymerization reaction is normally thermally initiated, or by UV-irradiation or by chemical catalysis. The choice of the suitable initiator depends upon the type of monomers and solvent being used.

The polymerized hydrogels may be produced in a wide variety of forms, including films and membranes, rods, particles and emulsions by accurately choosing the starting materials and the process conditions.

Bulk polymerization involves only monomer and monomer soluble initiators and crosslinker. High rate of polymerization and degree of polymerization occur because of the high concentration of the monomer. This methods produce a glassy, transparent polymeric matrix which is very hard. When immersed in water the glassy matrix swells to become soft and flexible.

By using a solution polymerization, monomers and crosslinking agent are mixed together with a solvent and the polymerization is initiated thermally, by UV irradiation or by a redox initiator. The presence of solvent serves as a heat sink and it represents the major advantage of this method. Typical solvents are: water, water-ethanol mixtures and benzyl alcohol.

Generally, hydrogels prepared by bulk polymerization and/or solution polymerization have inherent weak structure. To improve the mechanical properties of an hydrogel, it can be grafted on a surface coated onto a stronger support; it consists in a direct polymerization of the monomers on the support surface.

Hydrogels realized by standard methods have a shape that depends on the shape of the container in which they are prepared and with a minimum thickness of a few millimeters. The possibility to realize hydrogel thin films combines the advantages of both hydrogels and films. Despite their huge potential, hydrogel films are still scarcely investigated, except for very specific uses.⁵¹

In this thesis, some preliminary results are reported about the exploitation of a simple hydrogel thin film as water absorbing layer for the realization of a low cost barrier.

➤ Water absorbing thin film for an active multilayer encapsulation approach
One of the simplest strategy for the realization of an hydrogel thin film consists in the deposition of a non-crosslinked polymer that is usually soluble in water and a subsequent crosslinking process.

For this purpose, poly(acrylamide-co-acrylic acid) partial sodium salt and N,N'-methylenebis(acrylamide) were selected respectively as linear polymer and crosslinking agent.

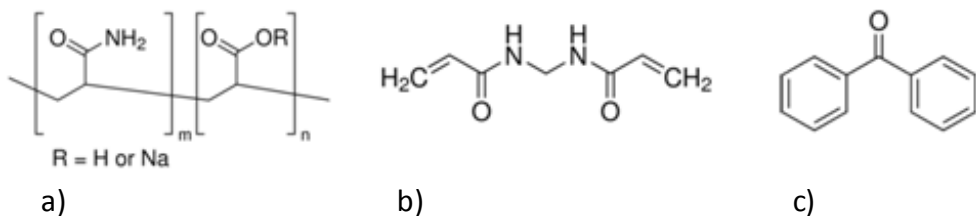


Figure 15: a) poly(acrylamide-co-acrylic acid) partial sodium salt; b) N,N'-methylenebis(acrylamide); c) benzophenone (UV initiator)

Chosen polymer, crosslinker and UV initiator were mixed together in a water-isopropanol mixture and then deposited on a PEN substrate using a k-bar.

The k-bar is a simple and effective means for the application of a variety of coating materials and it can be used for the deposition of materials with thickness in the order of hundreds of microns.

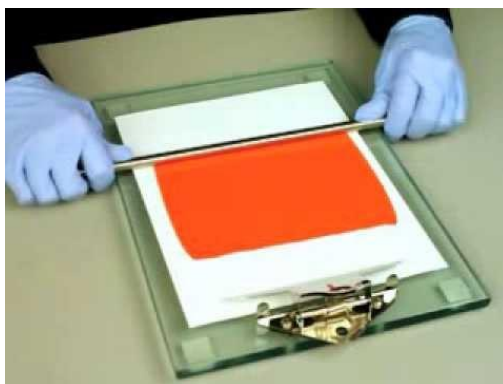


Figure 16: k-bar deposition

The deposited layer was exposed to UV-radiation (10') to perform the crosslinking process.

The mixture and the material after exposition to UV-radiation were analyzed through differential scanning calorimetry (DSC) (Figure 17).

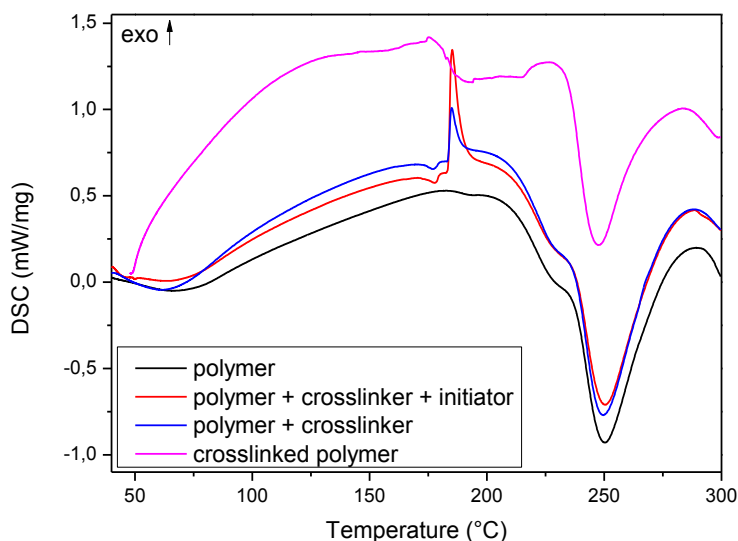


Figure 17: DSC analysis of the reaction mixture before and after UV exposition

The DSC analysis of the linear polymer shows an intense endothermic peak at about 250°C due to the fusion process. In the mixture with the crosslinker, it is possible to observe an additional exothermic peak at about 180°C that can be due to the crosslinking process.

The DSC curve of the mixture after UV exposition shows a step signal at about 180°C, a fusion at 250°C and it is not visible the exothermic peak observed in the no-crosslinked mixture.

From such evidences it is possible to hypothesize that a crosslinking process occur, in particular the methylenebis(acrylamide) is able to react with himself and with the polymer backbone and/or with the carboxylic functionality; as a result, the exothermic peak due to the curing process is not anymore visible after the reticulation, and a glass transition is visible. Probably the crosslinking degree is very low since the fusion temperature doesn't change and/or disappear, but for our application this doesn't represent a problem because the water uptake of an

hydrogel is inversely proportional to the crosslinking degree. Further investigation are necessary to confirm the crosslinking process.

Principal objective of the study is to understand if an hydrogel thin film can be used as water absorbing material in a multilayer barrier. For this reason, the preliminary hydrogel thin film realized was tested by using an electrical calcium test. In Figure 18 and in Table 5 are reported the data of an electrical calcium test carried out on a double layer hydrogel/ZnO nanoparticles deposited on PEN substrates. Two different double layers were realized, in one case the ZnO layer was deposited by gravure printing and in the other case by airbrushing, to test the two different technologies and obtain the best multilayer structure.

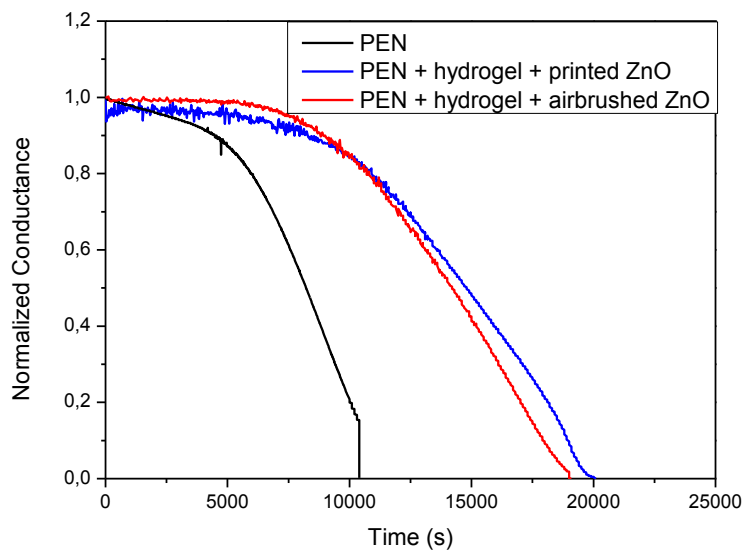


Figure 18: Normalized conductance vs time for electrical calcium tests carried out on Hydrogel/ZnO samples

Table 5: WVTR and lag time values for calcium tests carried out on Hydrogel/ZnO samples

	WVTR(g/m²/day)	Lag time (h)
	@ 38°C, 90% RH	
PEN	1.58 ± 0.13	1.51 ± 0.32
Printed ZnO	1.18 ± 0.11	2.13 ± 0.45
Airbrushed ZnO	1.24 ± 0.15	2.33 ± 0.41
Hydrogel + printed ZnO	0.86 ± 0.12	2.68 ± 0.37
Hydrogel + Airbrushed ZnO	0.99 ± 0.11	2.52 ± 0.33

The barrier properties of the hydrogel/ZnO samples are better than ones of ZnO single layer samples, in terms of the increment of the lag time as observed for the hydrophobic layers. This data demonstrate the effective capacity of the hydrogel layer to trap water and to slow down the permeation process improving the barrier properties. The optimization of the hydrogel structure, morphology and crosslinking degree can further improve this barrier mechanism.

~CONCLUSIONS~

Different functional thin film were realized by using solution based deposition techniques, demonstrating how it is possible to easily confer some characteristics to a layer.

In particular ceramic, hydrophobic and absorbing thin films were prepared, to test the possibility to realize a water permeation barrier multilayer.

ZnO nanoparticles were used for the realization of the ceramic thin films and two different deposition techniques were compared. The obtained ceramic thin films show different permeation mechanisms in relation to their microstructure. The impossibility to use high temperatures to proceed with sintering process is the main obstacle to further improve the barrier properties of these layers.

Hydrophobic layers were prepared by using functionalized ZnO with stearic acid deposited on PEN substrates. An improvement of the barrier properties respect to the only ZnO layers was observed. It was demonstrated how the hydrophobicity is capable to slow down the permeation process and to improve the multilayer barrier performances. It was also demonstrated that it is possible to merge the use of a ceramic and a hydrophobic material in a single step deposition process to obtain interesting surface properties.

Finally an hydrogel thin film was realized, to prove the possibility to use a water absorbing material in a multilayer structure to improve the barrier properties.

The double layer hydrogel/ZnO shows better barrier properties respect the single ZnO layer and comparable performances with the hydrophobic layers.

Although the hydrophobic and hydrogel layers act according to different mechanisms, both solutions can be exploited to improve the ceramic layer barrier properties.

The proposed methods can be used for preparing multilayer structures that can be very attractive for packaging applications and encapsulation of moisture sensitive devices.

~EXPERIMENTAL SECTION~

○ MATERIALS AND METHODS

The ZnO nanoparticles suspension and its powder, the stearic acid, the poly(acrylamide-co-acrylic acid) partial sodium salt, the N,N'-methylenebis(acrylamide), the benzophenone and all the solvents were purchased from Sigma Aldrich. Polyethylene naphthalate (PEN) substrates (Teonex® with a thickness of 125 μm) having a pretreated side with improved adhesion were used.

The employed gravure was a lab-scale printer (8G1-5, IGT, Amsterdam, The Netherlands) equipped with a cylinder having line density of 70 lines/cm, stylus angle of 120° and screen angle of 53° (cell depth 45 μm for ZnO and printed_1step). The ZnO nanoparticles and the blend ZnO nanoparticles and stearic acid were printed by using a printing force of 500 N at a speed of 60 m/min, while the stearic acid solution was printed using by using a printing force of 100 N.

The employed airbrush was a Iwata mod. Neo with a 0,35 mm nozzle, used at 3 bar of pressure and with a working distance from substrate of about 20 cm.

ATR spectra of the powders in transmission mode have been recorded with a Nicolet 5700 spectrometer. FT-IR spectra on thin films have been performed on CaF_2 slide by using a Perkin Elmer GX instrument.

The produced films on PEN substrates were also characterized by performing UV-visible transmission measurements (Lambda 900, Perkin Elmer, Waltham MA, USA).

The thickness and surface roughness of the layers were investigated by interferometry based optical profilometer (Talysurf CCI HD, Taylor Hobson, Leicester, UK). The root mean square surface roughness was obtained according

to the ISO 25178 standard; the reported values are the average results of several measurements.

Water contact angles were measured by using a OCA20 Dataphysics instrument and the reported values of WCA are the average of several measurements.

The barrier properties of the prepared films were evaluated by estimation of the water vapour transmission rate (WVTR) and the lag time through electrical calcium test. The calcium patch and the silver electrodes were directly evaporated under vacuum on the prepared films. A back encapsulation of the calcium patch with a glass lid sealed with an UV-curable epoxy resin (SAES getters, Zeoglue HV-SEU10) was made. Successively, the calcium test sensor is placed in a climate chamber to perform the electrical measurements at 38°C and 90% relative humidity (RH). The electrical measurements of the Calcium test sensor were performed with a Keithley 2400 SourceMeter.

The reproducibility of the WVTR and lag time were tested (3-4 samples for each kind of coating).

The morphology of the samples was also investigated through electron scanning microscopy (1530, LEO Elektronenmikroskopie GmbH, Zeiss, Germany).

DSC measurements have been carried out by using a DSC/TGA Jupiter STA449F3 instrument (Netzsch).

○ SAMPLE PREPARATION

	1st deposition	Treatment	2nd deposition	Treatment
Printed ZnO	ZnO nanoparticles 10% w/w in EtOH	140°C 1h		
Airbrushed ZnO	ZnO Nanoparticles 5 mg/ml in EtOH	140°C 1h		
Printed 2-steps	ZnO nanoparticles 10% w/w in EtOH	140°C 1h	Stearic acid in EtOH 30 mg/ml	60°C overnight - solvent printing

				with toluene
Airbrushed 2-steps	ZnO nanoparticles 5 mg/ml in EtOH	140°C 1h	Stearic acid in EtOH 20 mg/ml	60°C overnight - solvent printing with toluene
Printed 1-step	ZnO+20% stearic acid in EtOH (10 mg/ml)	60°C 1h		
Airbrushed 1-step	ZnO+20% stearic acid in EtOH (2.5 mg/ml)	60°C 1h		
Hydrogel/printed ZnO	Polymer + 5% w/w crosslinker + 1% initiator in in H ₂ O/IPA (1/1 v/v) (conc. Respect pol5% w/v)	UV exposition 10'	ZnO nanoparticles 10% w/w in EtOH	140°C 1h
Hydrogel/airbrushed ZnO	Polymer + 5% w/w crosslinker + 1% initiator in in H ₂ O/IPA (1/1 v/v) (conc. Respect pol5% w/v)	UV exposition 10'	ZnO Nanoparticles 5 mg/ml in EtOH	140°C 1h

REFERENCES

- ¹ W. Su, Chapter 8: "*Encapsulation Technology for Organic Electronic Devices*", Printed Electronics: Materials, Technologies and Applications, Wiley 2016.
- ² J. Shen et al, *Synthetic Metals*, 2000, 111–112, 233-236
- ³ M. Schaer et al, *Adv. Funct. Mater.*, 2001, 11, 2, 116-121
- ⁴ S. Scholtz et al, *Chem. Rev.*, 2015, 115, 16, 8449-8503
- ⁵ H. Ardebili, M. Pecht, "*Encapsulation Technologies for Electronic Applications*", Elsevier Inc. 2009
- ⁶ S. Logothetidis et al, *Materials Science and Engineering: B*, 2008, 152,1–3, 96-104.
- ⁷ P.E. Burrows et al, *Appl. Phys. Lett.*, 1994, 65, 2922.
- ⁸ J. J. Perez-Buenon et al, *Thin Solid Films*, 2000, 379, 57–63.
- ⁹ E. Santoro, PhD thesis: "*Degradation of OLEDs devices: study methods and solutions*", 2016
- ¹⁰ Duan Yu et al. *Optics Communications*, 2016, 362, 43–49
- ¹¹ G. Hoffmann et al, *Proceedings of the 37th Annual Technical Conference of the Society of Vacuum Coaters*, 1994, 155–160.
- ¹² S. Schiller et al, *Surf. Coat. Technol.*, 2000, 125, 354–360
- ¹³ C. Charton et al, *Thin Solid Films*, 2006, 502, 99–103
- ¹⁴ F. Duerinckx et al, *Sol. Energy Mater. Sol. Cells*, 2002, 72, 231
- ¹⁵ P. F. Carcia et al, *Journal of Applied Physics*, 2009, 106, 023533
- ¹⁶ E. Langereis et al, *Applied Physics Letters*, 2006, 89, 081915
- ¹⁷ A. Dameron et al, *The Journal of Physical Chemistry C*, 2008, 112, 4573–4580
- ¹⁸ L. Moro, R. Jan Visser, Chapter 18: "*Barrier Films for Photovoltaics Applications*", Organic Photovoltaics: Materials, Device Physics, and Manufacturing Technologies, WILEY-VCH Verlag GmbH & Co, 2008
- ¹⁹ J.D. Affinito et al, *Thin Solid Films*, 1996, 290, 63
- ²⁰ F. Krebs, "*Stability and Degradation of Organic and Polymer Solar Cells*", Wiley 2012
- ²¹ W. Decker et al, *Proceedings of the 45th Annual Technical Conference of the Society of Vacuum Coaters*, 2002
- ²² Y. G. Tropsha et al, *Journal of Physical Chemistry B*, 11997, 5647, 2259–2266
- ²³ G. L. Graff et al, *Journal of Applied Physics*, 2004, 96,1840
- ²⁴ J. Crank, "*The Mathematics of Diffusion*", Oxford University Press, 1979
- ²⁵ G. Nisato, *White Paper For The Use Of OE-A Members*, 2013
- ²⁶ S. Schubert et al, *Rev. Sci. Instrum.*, 2011, 82
- ²⁷ F. S. Lange et al, "*Fracture Mechanics of Ceramics*", Plenum, New York, 1973.
- ²⁸ R. R. Tummala, *Ceram. Bull*, 1988, 67, 752
- ²⁹ G. Fisher, *ibid.*, 1986, 65, 622

- ³⁰ V. E. Wood, *Proceedings of the Sixth IEEE International Symposium on Applications of Ferroelectrics*, 1987
- ³¹ W. J. Lackey et al., *Ceramic Coatings for Heat Engine Materials-Status and future Needs*, ORNL/TM-8959, 1989
- ³² K. Shi et al., *J. Am. Ceram. Soc.*, 1988, 71, 924
- ³³ Sobajima, S. et al, *Jpn. J. Appl. Phys.*, 1974, 2, 475–478
- ³⁴ Itoyama, K. J. *Electrochem. Soc.* 1979, 126, 691–694
- ³⁵ Howson, R. P. *Appl. Phys. Lett.* 1979, 35, 161–162
- ³⁶ S. K. Dey et al, *IEEE Trans. Ultrason., Ferroelectr. Freq. Control*, 1988, 35, 80
- ³⁷ G. Yi et al, *J. Appl. Phys.*, 1989, 64, 2717
- ³⁸ N. Asakuma et al, *J. Sol–Gel Sci. Technol.*, 2003, 27, 91–94
- ³⁹ M. Langlet et al, *J. Sol–Gel Sci. Technol.*, 2002, 25, 223–234
- ⁴⁰ A. Matsuda et al, *J. Sol–Gel Sci. Technol.*, 2003, 27, 61–69
- ⁴¹ M. A. Aegerter et al, *J. Sol–Gel Sci. Technol.*, 2003, 27, 81–89
- ⁴² M. Langlet et al, *Thin Solid Films*, 2003, 429, 13–21
- ⁴³ G. Sico et al, *Ceramics International*, 2018, 44(16), 19526-19534
- ⁴⁴ M. Yamamoto, *Langmuir*, 2015, 31, 26, 7355–7363
- ⁴⁵ R. N. Wenzel, *Ind. Eng. Chem.*, 1936, 28, 988–994
- ⁴⁶ A.B.D. Cassie, S. Baxter, *Trans. Fraday Soc.*, 1944, 40, 546–551
- ⁴⁷ M. Lashanizadegan et al, *Journal of Ceramic Processing Research*, 2014, 15, 5, 316-319
- ⁴⁸ E. Tang et al, *Powder Technology*, 2006, 161, 209-214
- ⁴⁹ E. M. Ahmed et al, *Journal of Advanced Research*, 2015, 6, 105-121
- ⁵⁰ O. Wichterle et al, *Nature*, 1960, 185, 117
- ⁵¹ B. Chollet et al, *ACS Appl. Mater. Interfaces*, 2016, 8, 11729–11738

~LIST OF PUBLICATIONS~

- ⊕ *Eumelanin-Based Organic Bioelectronics: Myth or Reality?* M. Barra, I. Bonadies, C. Carfagna, A. Cassinese, F. Cimino, O. Crescenzi, V. Criscuolo, M. d'Ischia, M.G. Maglione, P. Manini, L. Migliaccio, A. Musto, A. Napolitano, A. Navarra, L. Panzella, S. Parisi, A. Pezzella, C.T. Prontera and P. Tassini. **MRS Advances**, 1, 57 (2016) 3801-3810
- ⊕ *Study of the electroluminescence of highly stereoregular poly(N-pentenyl-carbazole) for blue and white OLEDs.* R. Liguori, A. Botta, S. Pragliola, A. Rubino, V. Venditto, A. Velardo, S. Aprano, M.G. Maglione, C.T. Prontera, A. De Girolamo Del mauro, T. Fasolino, C. Minarini. **Semiconductor Science and Technology**, 32 (2017) 065006
- ⊕ *PEDOT:PSS as anode for flexible ITO-free organic light emitting diodes.* M. Montanino, G. Sico, C.T. Prontera, A. De Girolamo Del Mauro, S. Aprano, M.G. Maglione, C. Minarini. **eXPRESS Polymer Letters**, Vol. 11, No. 6 (2017) 518-523
- ⊕ *An electrochemical study of natural and chemically controlled eumelanin.* R. Xu, C.T. Prontera, E. Di Mauro, A. Pezzella, F. Soavi, C. Santato. **APL Materials**, 5 (2017) 126108
- ⊕ *Gravure printing for thin film ceramics manufacturing from nanoparticles.* G. Sico, M. Montanino, C.T. Prontera, A. De Girolamo Del Mauro, C. Minarini. **Ceramics International**, 44, 16 (2018) 19526-19534

~COMMUNICATIONS AT MEETINGS~

- ⊕ *A Reaction-Based Fluorescence Turn-On Organic Platform for Smart Biomaterials and Coatings.* M. Iacomino, C.T. Prontera, O. Crescenzi, A. Napolitano, M. d'Ischia. **E-WISPOC16**, Bressanone, Italy.
- ⊕ *Eumelanin-Porous Silicon Hybrids: towards stable photocurrents.* G. Mula, E. Pinna, C. Melis, L. Colombo, C.T. Prontera, A. Pezzella, M. d'Ischia. **PSST 2016**, Tarragona, Spain.
- ⊕ *Melanin-inspired electroluminescent materials for OLED applications.* P. Manini, V. Criscuolo, C.T. Prontera, L. Migliaccio, A. Pezzella, M. d'Ischia, M. Barra, A. Cassinese, S. Lettieri, P. Maddalena, M.G. Maglione, P. Tassini, C. Minarini. **SINFO III 2016**, Napoli, Italy.
- ⊕ *Highly stereoregular poly (N-pentenyl-carbazole)s as OLED emitting layers.* A. Botta, S. Pragliola, V. Venditto, R. Liguori, A. Rubino, S. Aprano, C.T. Prontera, M.G. Maglione, C. Minarini, **SINFO III 2016**, Napoli, Italy.
- ⊕ *Bio-Inspired Luminescent Transition Metal Complexes: from Nature to Iridium Based OLED Devices.* V. Criscuolo, C.T. Prontera, A. Pezzella, M.G. Maglione, P. Tassini, C. Minarini, S. Pedatella, M. De Nisco, M. Manfra, P. Manini. **IASOC 2016**, Ischia (Napoli), Italy.
- ⊕ *Shedding Light on the Hydration-Dependent Electrical Conductivity in Melanin Thin Films.* Ri Xu, L.G. Simao Albano, E. Di Mauro, S. Zhang, P. Kumar, C. Santato, C.T. Prontera. **MRS fall 2016**, Boston, USA.
- ⊕ *From natural systems to lighting electronics: designing melanin-inspired electroluminescent materials.* V. Criscuolo, P. Manin, C.T. Prontera, A.

Pezzella, M.G. Maglione, P. Tassini, C. Minarini. **BioEL2017**, Kirchberg in Tirol, Austria.

- ⊕ *Advancing the Knowledge of the Structural Properties of the Biocompatible and Biodegradable Electroactive Eumelanin Polymer.* D Boisvert, C.T. Prontera, S. Francoeur, A. Badia, C. Santato. **MRS spring 2017**, Phoenix, USA.
- ⊕ *Controlling of (supra)Molecular Structure of Polymers from Natural Sources to Assess their Electrical Properties.* Ri Xu, C.T. Prontera, L.G. Simao Albano, E. Di Mauro, P. Kumar, P. Manini, C. Santato, F. Soavi. **MRS spring 2017**, Phoenix, USA.
- ⊕ *Melanins in bioelectronics: a survey of the role of these natural pigments from bio-interfaces to (opto)electronic devices.* P. Manini, V. Criscuolo, L. Migliaccio, C.T. Prontera, A. Pezzella, O. Crescenzi, M. d'Ischia, S. Parisi, M. Barra, A. Cassinese, P. Maddalena, M.G. Maglione, P. Tassini, C. Minarini. **E-MRS spring 2017**, Strasbourg, France.
- ⊕ *Designing dopamine-based electroluminescent complexes for innovative melanin-inspired OLED devices.* C.T. Prontera, P. Manini, V. Criscuolo, A. Pezzella, O. Crescenzi, M. Pavone, M. d'Ischia, M.G. Maglione, P. Tassini, C. Minarini. **ISNSC9 (2017)**, Napoli, Italy. Poster presentation
- ⊕ *Synthesis and Photo-Physical Properties of Dopamine-Inspired Iridium Complexes for OLED Applications.* C.T. Prontera, V. Criscuolo, A. Pezzella, M.G. Maglione, P. Tassini, C. Minarini, M. d'Ischia, P. Manini. **SCI 2017**, Paestum (SA), Italy. Poster presentation

- ⊕ *From Melanins to OLED Devices: Taking Inspiration from the Black Human Pigments for the Design of Innovative Electroluminescent Materials.* P. Manini, C. T. Prontera, V. Criscuolo, A. Pezzella, O. Crescenzi, M. Pavone, M. d'Ischia, M. G. Maglione, P. Tassini, C. Minarini. **SCI 2017**, Paestum (SA), Italy.

- ⊕ *Green and low-cost hydrophobic ZnO NPs as water-barrier layer encapsulating flexible electronic devices.* C.T. Prontera, G. Sico, M. Montanino, P. Tassini, A. Pezzella, C. Minarini, P. Manini. **Nanoinnovation 2017**, Roma, Italy. Oral presentation

- ⊕ *Electrochemical Properties of Chemically Controlled Eumelanin.* Ri Xu, C.T. Prontera, E. Di Mauro, F. Soavi, A. Pezzella, C. Santato. **MRS fall 2017**, Boston, USA

- ⊕ *New insights into the Electronic-Ionic conduction model for eumelanin thin films.* C.T. Prontera, P. Manini, A. Pezzella, V. Criscuolo, C. Santato, Ri Xu, M. Rolandi, R. Di Capua, G. De Luca. **BioEL2018**, Kirchberg in Tirol, Austria. Poster presentation and flash oral presentation

- ⊕ *En Route Towards Eumelanin Photocapacitors.* Ri Xu, C.T. Prontera, E. Di Mauro, A. Pezzella, F. Soavi, C. Santato. **MRS spring 2018**, Phoenix, USA.

- ⊕ *Oxygen Reduction Reaction Catalysed by the Eumelanin Pigment.* Ri Xu, C.T. Prontera, E. Di Mauro, A. Pezzella, F. Soavi, C. Santato. **MRS spring 2018**, Phoenix, USA.

- ⊕ *From Melanins to OLED Devices: Designing Electroluminescent Materials Inspired to Human Pigments.* P. Manini, C.T. Prontera, V. Criscuolo, A.

Pezzella, O. Crescenzi, M. Pavone, M. d'Ischia, M.G. Maglione, P. Tassini, C. Minarini. **CIMTEC 2018**, 8th Forum on New Materials, Perugia (2018).

- ⊕ *Green and low-cost hydrophobic coating based on ZnO NPs and stearic acid.* C.T. Prontera, G. Sico, M. Montanino, M.G. Maglione, P. Tassini, A. Pezzella, C. Minarini, P. Manini. **IASOC 2018**, Napoli, Italy. Poster presentation

~COURSES AND SCHOOLS~

- ⊕ *La fotochimica: principi e applicazioni.* Prof. Maria Rosaria Iesce, **2016**.
- ⊕ *Metodi di struttura elettronica per materiali allo stato solido.* Prof. Ana Belen Muñoz-Garcia, **2016**.
- ⊕ *Le tecniche di estrazione solido-liquido impiegate nella preparazione del campione per l'analisi chimica e produzione di estratti per usi industriali.* Prof. Daniele Naviglio, **2017**.
- ⊕ *Reazioni organiche nei sistemi biologici.* Prof. Alfonso Iadonisi, **2018**.
- ⊕ *Circular Economy Entrepreneurship in System Integrated Metals Processing (CEE SIMP).* Aalto University School of Chemical Technology. Online lectures February-March, Group assignments April-May, Summer Camp 28-30 June **2016**, Otaniemi, Finland.
- ⊕ *Prima Scuola Nazionale Sensori Chimici.* 26-26 May **2017**, Napoli, Italy.

- ⊕ *Conventional and high-energy spectroscopies for inorganic, organic and biomolecular surfaces and interfaces (CHESS2017)*. 27-30 November **2017**, Florence, Italy.
- ⊕ *5th International Winterschool on Bioelectronics (BioEI 2018)*. 10-17 March **2018**, Kirchberg in Tyrol, Austria.
- ⊕ *School on Advanced Materials for Sustainable Energy Technologies (Samset 2018)*. 11-15 June **2018**, Lecce, Italy.
- ⊕ *Ischia advanced school of organic chemistry (IASOC 2018)*. 22-25 September **2018**, Napoli, Italy.